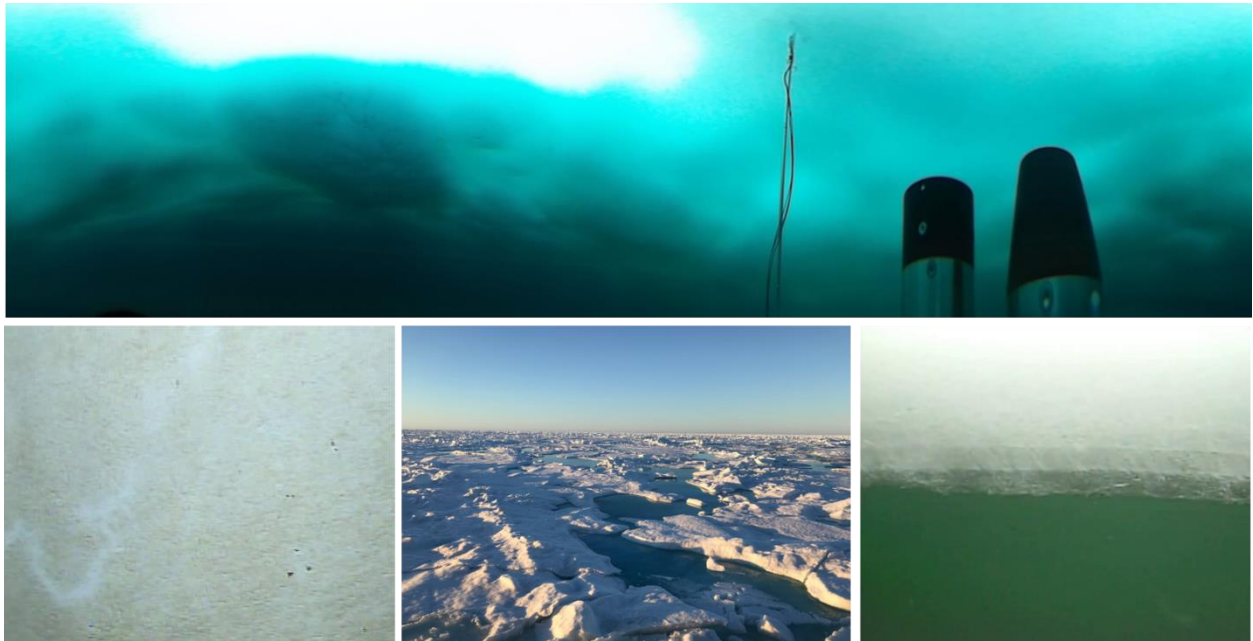Lisa C. Matthes

Light propagation in ice-covered environments: Seasonal progression and biological implications

A thesis submitted to the Faculty of Graduate Studies of
The University of Manitoba
in partial fulfillment of the degree of

DOCTOR OF PHILOSOPHY

Department of Environment and Geography
University of Manitoba
Winnipeg, Manitoba, Canada

Supervised by

Assoc. Prof. Dr. **CJ Mundy**
Department of Environment and Geography
Clayton H. Riddell Faculty of Environment,
Earth, and Resources
University of Manitoba
Winnipeg, MB R3T 2N2, Canada

Co-supervised by

Assoc. Prof. Dr. **Jens Ehn**
Department of Environment and Geography
Clayton H. Riddell Faculty of Environment,
Earth, and Resources
University of Manitoba
Winnipeg, MB R3T 2N2, Canada

Advisory committee

Assoc. Prof. Dr. **Gordon Goldsborough**
Department of Biological Sciences
Faculty of Science
University of Manitoba
Winnipeg, MB R3T 2N2, Canada

Prof. Dr. **Simon Bélanger**
Départment de Biologie, Chimie et
Géographie
Université du Québec à Rimouski
Rimouski, QC G5L 3A1, Canada

External Examiner

Prof. Dr. **Rolf Gradinger**
Department of Arctic and Marine Biology
UiT The Arctic University of Norway
Tromsø, Norway

Cover pictures
Photo credit: Laura Dalman (sea ice surface) and Lisa C. Matthes (remaining pictures of under-ice light field, ice bottom colonized by ice algae, under-ice phytoplankton bloom)

Abstract

Arctic under-ice phytoplankton blooms are initiated by a sudden increase in the transmission of photosynthetically active radiation (PAR; 400 – 700 nm) as a result of the formation of surface melt ponds in late spring. However, the more pronounced spatial variability in irradiance levels beneath ponded and white ice compared to snow-covered ice create difficulties in measuring light availability for primary production. In this thesis, the impact of spatiotemporal variability in transmitted irradiance on under-ice light field parameters is examined and later applied to produce the first estimate of late spring production in the ice-covered Hudson Bay.

Phytoplankton production is estimated based on PAR availability at the ice bottom and its vertical attenuation with increasing water depth. I demonstrated that spatially averaged transmittance from large-scale continuous measurements provides more representative estimates of under-ice PAR relative to single point irradiance measurements due to large variations in transmitted PAR. Vertical irradiance profiles in the first meters of the water column are greatly influenced by these spatial variations and the horizontal spreading of light in the overlying ice cover. Therefore, it is recommended to derive the diffuse vertical attenuation coefficient from deeper depths. To further account for the shift from a diffuse to a more-downward directed light field with ongoing ice surface melt, these measurements should be performed with scalar radiometers with a spherical collector. Otherwise measured downwelling irradiance can be converted into scalar irradiance by using under-ice downwelling average cosine values, for which direct measurements are first reported in this thesis.

Applying this improved parametrization of the apparent optical properties in the investigation of microalgal primary production in Hudson Bay, I estimate that 32% of annual biomass is produced during the sea ice melt period. Under-ice phytoplankton reach high production rates due to a large plasticity of their photosynthetic machinery to acclimate to variable light conditions over large spatial scales. The findings from this thesis provide new information on the parametrization of the complex under-ice light field to minimize errors in production estimates and model development of PAR availability, and to ultimately improve our general understanding of under-ice bloom phenology.

Acknowledgements

Table of Contents

List of Tables

List of Figures

XVII

List of Acronyms

AO	Arctic Ocean
AUV	Autonomous underwater vehicle
CDOM	Coloured dissolved organic matter
Chl	Chlorophyll
Chlide	Chlorophyllide
CIS	Canadian Ice Service
CV	Coefficient of variance
D-transect	Destructive transect
DIC	Dissolved inorganic carbon
DOW	Days of open water
FB	Freeboard
FSW	Filtered seawater
FYI	First-year ice
GPP	Gross primary production
HPLC	High-performance liquid chromatography
I	Ice
IR	Infrared radiation
MP	Melt pond
MYI	Multiyear ice
ND-transect	Non-Destructive transect
NPP	Net primary production
NPQ	Non-photochemical quenching
PAR	Photosynthetically active radiation (400 – 700 nm)
PE	Photosynthesis-irradiance relationship
POC	Particulate organic carbon
PE curve	Photosynthesis versus irradiance curve
PON	Particulate organic nitrogen
PPC	Photoprotective carotenoids
PP	Primary production

PSC	Photosynthetic carotenoids
ROV	Remotely operated vehicle
RPAS	Remotely piloted airborne system (similar to UAV)
S	Snow
SAT	Surface air temperatures
SCM	Subsurface chlorophyll maximum
TChl *a*	Total chlorophyll *a* (Chlorophyll *a* and its derivates) concentration
UIB	Under-ice phytoplankton bloom
UVR	Ultraviolet radiation (280 – 400 nm)
UAV	Unmanned aerial vehicle
WI	White ice

Use of Copyrighted Material

Figure 2.3A: Modified from Light B, Maykut G, Grenfell T. 2003. Effects of temperature on the microstructure of first-year Arctic sea ice. *Journal of Geophysical Research: Oceans* **108**(C2). Copyright (2003) American Geophysical Union, reprinted with permission from John Wiley and Sons.

Figure 2.4B: Perovich DK. 1996. The optical properties of sea ice. This monograph has no copyright restriction. Credit should be given to US Army Corps of Engineers (USACE)/Engineer Research and Development Center (ERDC) for the original work. This is in accordance with Copyright Law of the United States, Chapter 1, Section 105, https://www.copyright.gov/title17/92chap1.html, and Chapter 4, Section 403, https://www.copyright.gov/title17/chapter4.pdf. More information can be found at USA.gov, https://www.usa.gov/government-works.

Figure 2.7: Coello-Camba A, Agustí S, Vaqué D, Holding J, Arrieta JM, Wassmann P, Duarte CM. 2015. Experimental Assessment of Temperature Thresholds for Arctic Phytoplankton Communities. *Estuaries and Coasts* **38**(3): 873–885. doi: 10.1007/s12237-014-9849-7. Copyright (2015), reprinted with permission from Springer.

Figure 2.12: Bélanger S, Babin M, Tremblay J-É. 2013. Increasing cloudiness in Arctic damps the increase in phytoplankton PP due to sea ice receding. *Biogeosciences* **10**(6): 4087. Copyright (2013), Copernicus Publications. Copyrighted under Creative Common Licence: Attribution - 3.0 Unported (CC BY 3.0)

Figure 2.13: Ardyna M, Babin M, Gosselin M, Devred E, Rainville L, Tremblay J. 2014. Recent Arctic Ocean sea ice loss triggers novel fall phytoplankton blooms. *Geophysical Research Letters* **41**(17): 6207–6212. Copyright (2014) American Geophysical Union, reprinted with permission from John Wiley and Sons.

Chapter 3 of this thesis is reproduced with minor modifications from Matthes et al. (2019): *Average cosine coefficient and spectral distribution of the light field under sea ice: Implications for primary production*. Elem Sci Anth, 7(1), p.25. DOI: http://doi.org/10.1525/elementa.363].

Chapter 4 of this thesis is reproduced with minor modifications from Matthes et al. (2020): *Spatial heterogeneity as a key variable influencing spring-summer progression in UVR and PAR transmission through Arctic sea ice.* Front Mar Sci **7**. Frontiers. doi: 10.3389/fmars.2020.00183.

Chapter 5 of this thesis is reproduced with minor modifications from Matthes et al. (Under review): *Environmental drivers of spring primary production in Hudson Bay*. This manuscript was submitted to the special issue on the BaySys Study in the journal *Elementa: Science of the Anthropocene*.

1. Chapter – Introduction

1.1. Motivation

The Arctic Ocean (AO) has seen a rapid loss in sea ice extent and volume in the past decades (Comiso et al., 2008; Kwok, 2018; Stroeve and Notz, 2018) with the 10 lowest summer sea ice extents all occurring within the last 12 years (www.nsidc.org, website accessed: Sept 2020). The loss in volume is particularly evident in the thinning of the mobile ice pack and the replacement of multiyear ice (MYI) with first-year ice (FYI) as dominant ice type (Kwok, 2018; Stroeve and Notz, 2018). This long-term decline in sea ice is attributed to an increased ice export out of the Arctic (Kwok and Rothrock, 1999; Babb et al., 2013; Kwok et al., 2013), an increased movement of warm water into the Arctic from the Atlantic Ocean (Spielhagen et al., 2011; Årthun et al., 2012; Oziel et al., 2016; Polyakov et al., 2020) and the Pacific Ocean (Shimada et al., 2006; Woodgate et al., 2012), an increased surface air temperature due to greenhouse warming (Rothrock and Zhang, 2005; Comiso, 2012) and the accelerating ice-albedo feedback (Perovich et al., 2007; Serreze and Barry, 2011; Stroeve et al., 2012). The ice-albedo feedback results from the large contrast between the high albedo of sea ice (>0.5) and low albedo of open water (<0.05, Perovich, 1996). Increasing air temperatures contributed to a shrinking ice cover and more open water, which enhances absorption of solar radiation and further melts the ice.

The decrease in sea ice thickness and extent have also altered the habitat characteristics for phytoplankton, which represents the bottom of the Arctic marine food web. Annual phytoplankton net primary production (NPP) has increased by 30% over the open Arctic Ocean between 1998 and 2012 due to an extended open water period (Arrigo and van Dijken, 2015). Additionally, phytoplankton in the ice-covered water column profit from enhanced lead formation (Assmy et al., 2017) and enhanced light transmission through thinner and more transparent FYI (Ardyna et al., 2020a, and citations therein). As a result, large under-ice blooms (UIBs) develop under a fully consolidated ice cover after the snowmelt onset significantly increased under-ice light availability. These blooms are dominated by diatoms or the colonial haptophyte *Phaeocystis pouchetii* depending on the relative availability of silicic acid for diatom frustule formation (Ardyna et al., 2020b). Under-ice phytoplankton communities are aslo well acclimated to low light levels, which

enables them to reach high rates of carbon fixation and to utilize the limited nutrient reservoir immediately once light levels increase during the spring melt (e. g. Palmer et al., 2013; Lewis et al., 2019; Kauko et al., 2019).

The strongest increase in light transmission through the ice layer is driven by the formation of ponds of melt water from the snow melt, which cover a significant fraction of the ice surface and lower its regional albedo (Nicolaus et al., 2012). Simultaneously, the shift from a relatively homogeneous high-albedo snow cover to a less reflective mosaic of white ice (drained bare surface ice layer) and melt ponds in combination with the lateral spreading of radiation within the ice layer increase the complexity of the under-ice light field (Frey et al., 2011; Katlein et al., 2016; Laney et al., 2017; Massicotte et al., 2018; Horvat et al., 2020). As discussed in these studies, the higher light transmittance through more transparent melt ponds influences the vertical radiation transfer causing edge effects at the ice bottom of less transparent white ice and subsurface irradiance maxima in the underlying water column. These phenomena affect point measurements of light transmission beneath ice of different melt stages and need to be parametrized correctly for the estimation of under-ice light availability for marine primary production (PP) assessments.

Understanding the relationship between the increase in light transmission during the sea ice melt, the termination of the ice algal bloom in the ice bottom and the start of an UIB is of key importance to make predictions regarding productivity of the AO under a rapidly warming climate. However, the inaccessibility of vast areas of the Arctic and sub-Arctic during the spring ice melt as well as the lack of satellite-derived chlorophyll *a* observations in ice-covered regions has left large knowledge gaps on the seasonal progression in underwater light availability and the corresponding timing and magnitude of ice-algal and phytoplankton growth. The sub-Arctic sea Hudson Bay is only one example of sparse *in situ* data of spring PP, which is limited to observations on landfast ice in the periphery of the inland sea.

1.2. Thesis Objectives

The first goal of this thesis is to quantify the spatial variability of the increase in the transmission of ultraviolet (UV, 280 – 400 nm) and photosynthetically active radiation (PAR, 400 – 700 nm) through a melting FYI cover and to improve the parametrization of the complex under-ice light field when a phytoplankton bloom commences beneath a still fully consolidated ice cover. To

achieve this goal, *in situ* optical measurements are performed beneath seasonal sea ice during a land-based field campaign in late spring in a fjord in southern Baffin Bay. The second goal of this thesis was to apply the established knowledge about light propagation and availability during the spring ice melt during a research cruise in Hudson Bay to investigate the interactions between environmental parameters, with an emphasis on light availability, and primary producers in spring. Part 1 and Part 2 are subdivided into the following objectives:

Research Objectives – Part 1

1.1. Quantify the increase in spectral light transmission through sea ice as a function of changing quantities of snow, sea ice, melt ponds and ice algae

1.2. Examine the spatial variability of surface albedo and PAR transmission during sea ice melt

1.3. Investigate the impact of spatial heterogeneity in PAR transmission on the under-ice light field and calculation of the euphotic depth

1.4. Evaluate the use of different sensor types to measure under-ice PAR availability for PP estimates

Research Objectives – Part 2

2.1. Investigate the role of light availability on the onset and magnitude of spring PP with a retreating seasonal sea ice cover in Hudson Bay

2.2. Assess the acclimation of ice algae, open-water and under-ice phytoplankton to the prevailing light conditions in Hudson Bay

1.3. Thesis Outline

This thesis includes six chapters. **Chapter 2** provides background on (2.1.–2.3.) the physical characteristics of sea ice and how it influences light propagation in the underlying water column, (2.4.) Arctic marine PP and its controlling factors, and (2.5.) on the impact of climate change on the AO and regional PP patterns. **Chapter 3** and **4** contain separate original full-length research papers that are published in peer-reviewed journals. **Chapter 5** contains an original full research paper that has been submitted to a peer-reviewed journal. **Chapter 6** summarizes the key findings

of this thesis with respect to the above stated objectives and offers recommendations for future work.

Chapter 3 addresses the thesis objectives 1.1.–1.3. by collecting a large-scale data set of sea ice surface properties and spectral radiation beneath melting landfast sea ice to investigate local spatial variability in light transmission through ice of different melt stages. This work was carried out with the help of a remotely operated vehicle (ROV) as part of the multidisciplinary Green Edge project. Findings are presented in a peer-reviewed research paper in the journal *Frontiers of Marine Science:*

Matthes, L.C., Mundy, C.J., L.-Girard, S., Babin, M., Verin, G. and Ehn, J.K. (2020). *Spatial heterogeneity as a key variable influencing spring-summer progression in UVR and PAR transmission through Arctic sea ice.* Front Mar Sci 7. Frontiers. doi: 10.3389/fmars.2020.00183

Chapter 4 addresses the objectives 1.3.–1.4. by exploring the variations in the apparent optical properties such as the diffuse attenuation coefficient and average cosine of downwelling radiation of the under-ice light field, its impacts on frequently used hyperspectral radiometer types and the error in production calculations resulting from varying PAR input. This work is also part of the Green Edge project and was peer-reviewed and published in the journal *Elementa: Science of the Anthropocene*:

Matthes, L.C., Ehn, J.K., L.-Girard, S., Pogorzelec, N.M., Babin, M. and Mundy, C.J. (2019). *Average cosine coefficient and spectral distribution of the light field under sea ice: Implications for primary production*. Elem Sci Anth, 7(1), p.25. DOI: http://doi.org/10.1525/elementa.363

Chapter 5 addresses all objectives 2.1.–2.2. of Part 2 by investigating the environmental parameters driving PP in the open and ice-covered water column, the structure of microalgal communities and their photophysiological response to changing light conditions in spring in Hudson Bay. This work represents the first measurement of late spring PP in central Hudson Bay and was part of the larger Hudson Bay System Study (BaySys). Findings are presented in a research paper, which was submitted to the journal *Elementa: Science of the Anthropocene*:

Matthes, L.C., Ehn, J.K., Dalman, L.A., Babb, D.G., Peeken, I., Harasyn, M., Kirillov, S., Lee, J., Bélanger, S., Tremblay, J.-É., Barber, D.G., and Mundy, C.J. *Environmental drivers of spring primary production in Hudson Bay*. Elem Sci Anth (BaySys Special Issue). Under review.

2. Chapter – Background

2.1. Physical characteristics of Arctic sea ice

2.1.1. Sea ice structure, thickness and extent

A sample of fully formed sea ice reveals distinct internal layers that characterize the growth history of the ice cover (Fig. 2.1). The top layer of granular ice represents the first stage of ice formation in which frazil ice crystals collect and congeal into a contiguous ice sheet at the surface of the ocean. Due to turbulence caused by temperature-driven density instability, wind and waves during this early stage, the small crystals are randomly oriented in this thin ice layer resulting in a granular texture. Once the ice sheet of granular ice forms, ice then accretes to the base of the sheet via thermodynamic growth, where crystals with a c-axis aligned horizontally have a growth advantage to adjacent, differently oriented crystals (Weeks, 1998). This forms a transition zone between the granular layer and the columnar layer in which horizontal directions in the c-axis dominate (Petrich and Eicken, 2010). The columnar layer tends to account for the greatest thickness of Arctic sea ice. As ice thickens, a thin permeable layer with a sub-crystal lamellar plate structure consistently forms at the accreting ice bottom, the so-called skeletal layer. Sea ice is separated into two general age classes: First-year sea ice (FYI) that forms during the freeze-up in fall/winter and is less than one year old, while multiyear sea ice (MYI) survives the summer melt and is more than one year old. Landfast sea ice refers to sea ice attached to the coastline. All sea ice can undergo dynamic growth via deformation due to strong winds and currents that can cause cracks, fractures, and leads in divergent zones versus formation of rafts as well as pressure ridges and hummocks in convergent zones.

During ice growth the major salt ions present in seawater are excluded from the crystal lattice and are mostly rejected. Only 10 – 40% remain in the ice matrix as solid salts or liquid brine (Petrich and Eicken, 2010). Brine, located in spaces, tubes and channels, determine the bulk salinity of the sea ice cover, which displays a characteristic C-shape in FYI in winter (Fig. 2.1). Within a short distance from the accreting ice bottom, lower temperatures within the ice matrix (a function of thermodynamic growth) rapidly decrease ice porosity below a 5% brine volume threshold (Golden et al., 1998). This makes the ice impermeable to fluid transport, so that brine and salts become trapped until the ice warms. As ice temperature increase in spring, porosity increases, leading to

vertical brine convection and partial desalination of the ice cover until fresher meltwater acts to slow this process by refreezing at the ice surface and decreasing ice porosity (Eicken et al., 2002). Towards advanced melt states, sea ice can eventually become isothermal and fully permeable.
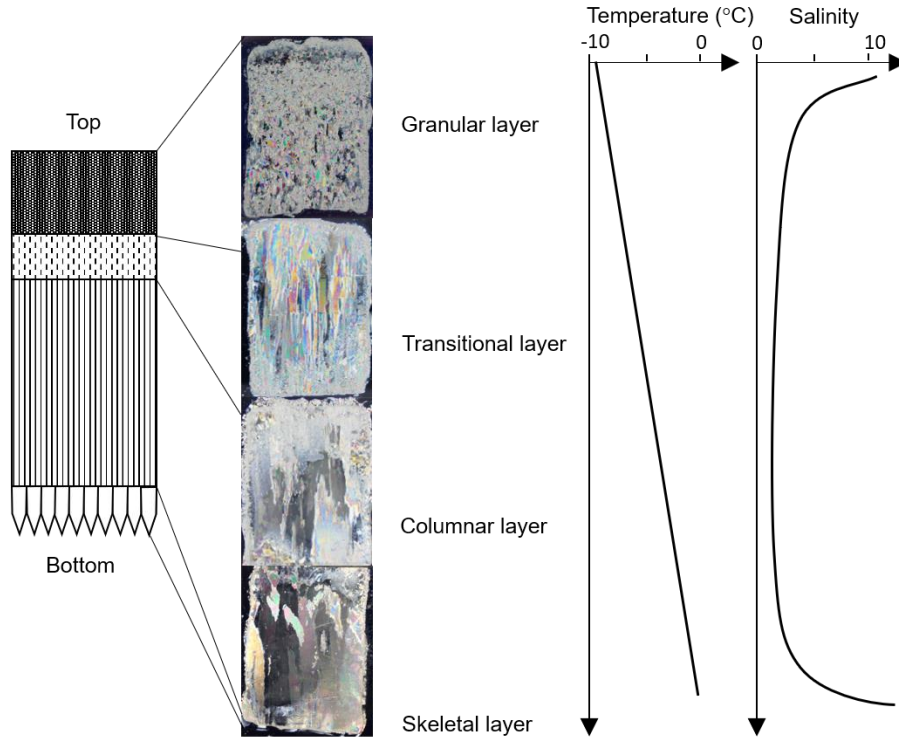
Figure 2.1: Main ice textures and idealized profiles of typical winter temperature and bulk salinity for first-year sea ice.

Variation in the sea ice age and extent (cumulative area of all pixels having at least 15% ice concentration) can be derived from passive microwave data using satellites. In the northern hemisphere, the ice extent typically fluctuates between a maximum in February/March and a minimum in September. The average maximum and minimum extent has been 15.6 and 6.1 million km^2, respectively, between 1979 – 2019 (Fetterer et al., 2017, updated daily). However, passive microwave observations showed an overall negative trend of $4.1 \pm 0.3\%$ per decade in the sea ice extent of the Northern Hemisphere (Cavalieri and Parkinson, 2012). The retreat in sea ice coverage is particularly visible in a 50% reduction in total MYI area between 1999 – 2017 (Kwok, 2018). In 2017, more than two-thirds of the Arctic ice pack consisted of FYI (Kwok, 2018; Stroeve and Notz, 2018). This shift in the dominant ice type led to an estimated decline in average ice thickness by 2 m between 1958 – 1976 and 2011 - 2018 (Kwok, 2018).

2.1.2. Temporal evolution of FYI and MYI and their surface properties

New sea ice starts to form between September in the central Arctic and November in the sub-Arctic (Markus et al., 2009) after the water surface has cooled beneath the seawater freezing point (T_{FP}). T_{FP} is a function of the seawater salinity (S) and hydrostatic pressure (P) and can be calculated following Fofonoff and Millard Jr (1983)

$$T_{FP} = \frac{-0.0575 * S + 0.001711 * S * \sqrt{S} - 0.000215 * S^2 - 0.000753 * P}{1.000024} \tag{1}$$

A surface salinity of 34 would result in a T_{FP} of –1.87°C. However, due to temperature-induced density instability as seawater cools at the atmosphere-ocean interface, the surface layer needs to reach the freezing point and potentially become supercooled before frazil ice formation starts (Fig. 2.2A). During winter, snow accumulates at the ice surface where it is rapidly redistributed by surface winds into snow drifts (Iacozza and Barber, 1999). Snow significantly influences the surface energy and mass budgets, insulating the sea ice cover from low air temperatures during fall and winter, which slows ice growth rates (Maykut and Untersteiner, 1971; Sturm and Massom, 2009). High snow loads can also depress the ice surface below the water level (negative freeboard) that can lead to flooding at the snow-ice interface and potential snow-ice formation (Arndt et al., 2017). In spring, after the sun returns above the horizon and air temperatures rise above 0°C, snow starts to melt and a slush layer (mixture of snow and water) can form at the bottom of the snow cover. Eventually patches of meltwater become visible at the ice surface, denoting melt pond onset. Due to the still impermeable (low internal temperature) sea ice cover, meltwater can flood the ice surface (Polashenski et al., 2012; Landy et al., 2014; Diaz et al., 2018) until it drains through cracks and seal breathing holes and forms discrete areas of surface-drained white ice and melt ponds. Surface melt dominates total ice melt at this stage in early summer while bottom and lateral melt dominate later in summer as the ocean heat flux increases and atmospheric heating declines (Steele et al., 2010). As ice also becomes increasingly permeable due to internal melt, melt ponds start to drain until the pond surface level matches the sea level and the ice breaks up (Eicken et al., 2002; Landy et al., 2014).

The temporal evolution of MYI and its surface properties is slightly different due to its older age and its survival through the summer months (Fig. 2.2B). As the age of MYI increases, the roughness of the ice surface topography increases due to uneven melt and ice deformation, which

leads to a lower coverage and greater depth of melt ponds compared to FYI during the melt season (Eicken et al., 2002; Nicolaus et al., 2012; Perovich and Polashenski, 2012). In summer, surface and bottom melt decrease the overall ice thickness until air and water temperatures decrease again towards fall. As air temperatures drop below 0°C, melt ponds refreeze and create a layer of superimposed ice at the interface of the newly fallen snow and ice (Granskog et al., 2006). As the surface water layer temperature reaches T_{FP}, ice growth at the bottom begins anew and increases the overall thickness of the MYI pack.
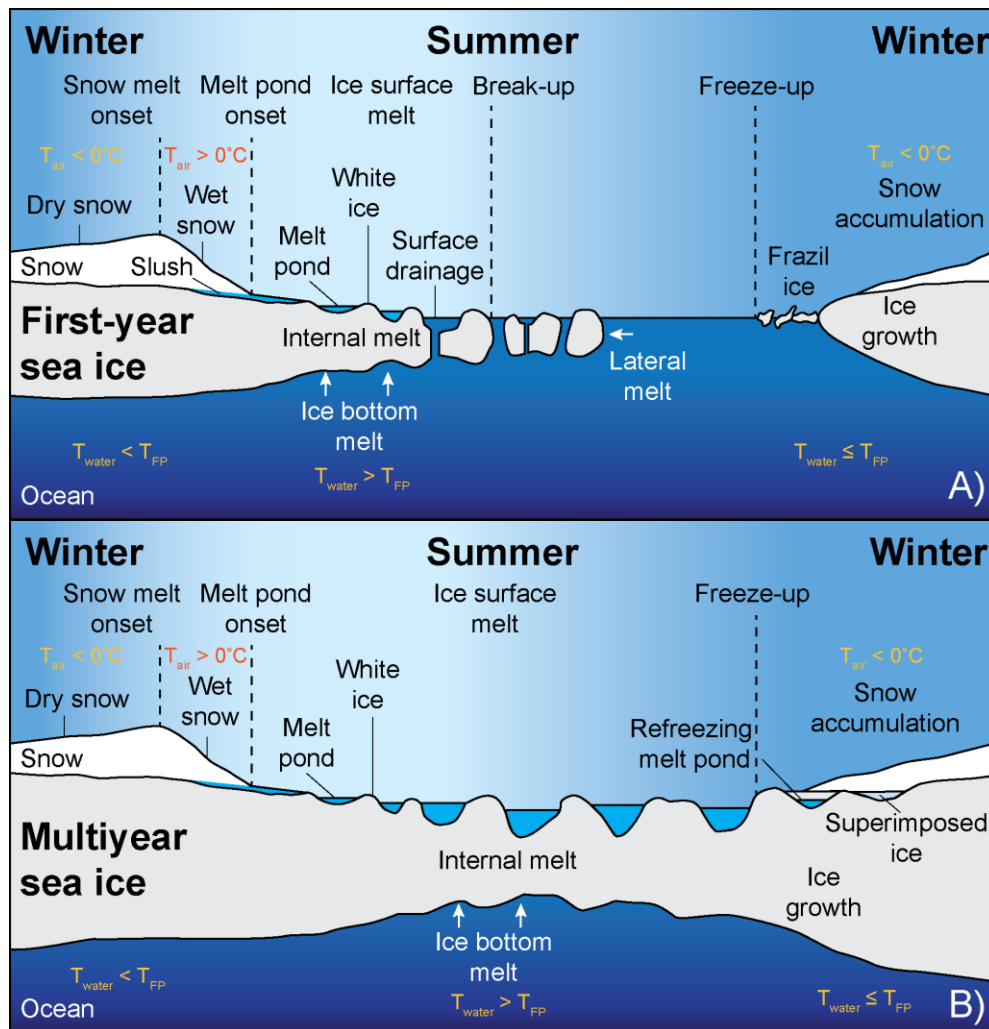
Figure 2.2: Schematic of seasonal cycle of A) first-year sea ice and B) multiyear sea ice and their surface properties. Surface air temperature (T_{air}), surface water temperature (T_{water}) and seawater freezing point (T_{FP}) relationships are provided for different seasons.

2.1.3. Inorganic inclusions in sea ice

Within the ice matrix inclusions of brine, gas, precipitated salt and other particles such as inorganic sediment can be found (Fig. 2.3). The size, concentration and spatial distribution of these inclusions impact the electromagnetic, thermal, mechanical and permeable properties of sea ice (Perovich and Gow, 1996; Golden et al., 1998; Hwang et al., 2006; Petrich and Eicken, 2010), the gas exchange (Crabeck et al., 2014) and radiative transfer through the ice cover (Light et al., 1998; Ehn et al., 2008; Light et al., 2008). The properties of inclusions themselves are affected by changes in temperature, salinity and freezing pressure of the ice (Light et al., 2003; Crabeck et al., 2019). As the ice cools, pure water from the brine inclusions freezes to the surrounding ice lattice and brine volume decreases (Light et al., 2003). At ice temperatures between –54 and –2°C, salt crystals such as ikaite, mirabilite and hydrahalite form in the existing brine channels (Fig. 2.3A, Light et al., 2003; Petrich and Eicken, 2010). Gas bubbles can be entrained in the ice matrix during ice growth or form within the matrix when gas dissolved in seawater moves out of solution (Light et al., 2003). These bubbles have been observed to shrink during cooling in response to increasing freezing pressure (Crabeck et al., 2019).
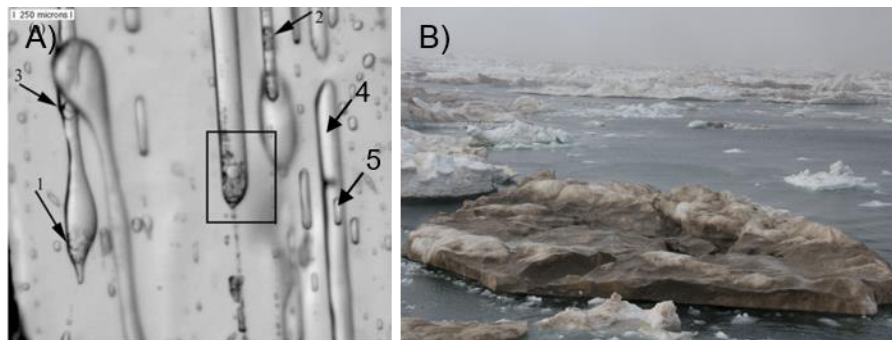
Figure 2.3: Inorganic sea ice inclusions: A) Ice microstructure with salt crystals (black rectangle, 1–3), brine channels (4) and gas bubbles (5) modified after Light et al. (2003) with permission from John Wiley & Sons, and B) sediment-laden sea ice in Hudson Bay (photo credit: L. Barber)

Inorganic sediment can be also entrained within the ice matrix when sea ice forms rapidly in turbid waters (Ledley and Pfirman, 1997) or is in repeated contact with the seafloor due to tidal movement or wind-induced ridging (Reimnitz et al., 1987; Barber et al., in press). Wind and snow can also deposit fine particles from adjacent land on the sea ice surface (Pfirman et al., 1989; Nomura et al., 2010). Heavily deformed, sediment-laden sea ice has been observed in Hudson Bay (Fig. 2.3B; Barber et al., 2021), and several shallow Arctic shelf regions (Barnes et al., 1982; Reimnitz et al., 1987; Kempama et al., 1989; Ito et al., 2019).

2.2. Light propagation in the sea ice environment

The exchange of climatically active gasses such as methane and carbon dioxide as well as the transmission of solar radiation from the atmosphere through the ice layer to the underlying water column are not completely cut off. However, the crystal structure of the ice layer, impurities and its surface components such as snow and melt water partially control and alter its permeability and transparency. This section will focus on the light propagation at the sea ice surface (2.2.2.), within the ice layer (2.2.3.) and in the water column beneath it (2.2.4.) after defining several parameters use to describe the nature of the underwater light field (2.2.1). Common technologies to perform optical measurements in the Arctic marine environment are also presented here (2.2.5).

2.2.1. The underwater light field

The term light is often used for the visible spectrum (400 – 700 nm) of solar radiation, also known as PAR. In this thesis, the term also includes ultraviolet radiation (UVR) in the UVB (280 – 315 nm) and UVA (315 – 400 nm) spectrum due to its negative effect on algae growing close to the water surface. To understand the behavior of light in water, attributes to describe the direction of radiation need to be defined. The path of a single beam is described by the angle between the beam and a vertical plane (zenith angle, θ) and the angle between the beam and a horizontal plane (azimuth angle, φ) (Kirk, 2011). The energy that this solar beam carries in a period of time is given as radiant flux (Φ). To indicate how much radiant energy is received or emitted by a point of surface (dS) from a specified direction per unit solid angle ($d\omega$) the concept of radiance (L) was introduced

$$L(\theta, \varphi) \ = \frac{d^2\,\Phi}{dS\,\cos\theta\,d\omega} \tag{2}$$

with $dS\,\cos\theta\,d\omega$ describing the flux within a small solid angle through a projected area of the surface element at a right angle to the beam. Spectral radiance of a surface is wavelength dependent and often given in the unit watt per steradian, square metre and nanometre (W sr^{-1} m^{-2} nm^{-1}). The radiant flux from all directions per unit area of a surface is called spectral irradiance (E) and is often stated in energy units (W m^{-2} nm^{-1})

$$E = \frac{d\Phi}{dS} \qquad (3)$$

Irradiance available for photosynthesis is also expressed in quantum units (µmol photons m^{-2} s^{-1}) and can be converted from energy units by using the speed of light (c), Planck's constant (h), the wavelength (λ) and Avogadro's number (NA). The conversion is performed spectrally

$$E \ [\mu mol \ photons \ m^{-2} \ s^{-1}] = \frac{E \ [Wm^{-2}] * \lambda \ [nm] * 10^{-9}}{c \ [\ ms^{-1}] * h \ [Js] * NA \ [\mu mol^{-1}]} \qquad (4)$$

Irradiance can be divided by a horizontal plane into downward (E_d) and upward (E_u) irradiance and can be measured by different radiometer types. Radiometers measuring planar irradiance record only the beam being proportional to the cosine of the angle of a flat disc at the top of the sensor. Radiometers with a spherical collector instead measure radiation from all directions, called scalar irradiance. The sum of downward (E_{0d}) and upward (E_{0u}) scalar irradiance is given as total scalar irradiance (E_0).

Apparent optical properties

The optical properties of water, which are measured under natural light and describe the radiation field, are defined as apparent optical properties (AOPs; Prisendorfer, 1961). Incident solar radiation does not entirely penetrate the ocean. A fraction is reflected at the air-sea interface depending on surface conditions and sun angle. This process is named Fresnel reflection (Born and Wolf, 1999). Another fraction is scattered back into the air after it had initially penetrated the ocean, which is described as diffuse reflection. Upward radiation represents the sum of Fresnel and diffuse reflection. The ratio of upward to downward radiation is called reflectance (R) or albedo (α) and can be calculated for irradiance following

$$R = \frac{E_u}{E_d} \qquad (5)$$

The fraction of incident solar radiation that is travelling through a medium from the surface (z_1) to a specific depth (z_2) is described as transmittance (T) and can be calculated as foll

$$T = \frac{E_d(z_2)}{E_d(z_1)} \qquad (6)$$

8

Reflectance (albedo) and transmittance are stated as ratios with values between 0 and 1. The term 'transmission' is also often used in the literature, which states the transmittance ratio in percentage (ratio*100%). Within an aquatic medium radiation is also not evenly propagated. The average cosine for downwelling light (μ_d) describes the angular distribution of the light field, specifically the cosine of the zenith angle of all photons at a specified point (Kirk, 2011). It is calculated by dividing downward planar irradiance by downward scalar irradiance

$$\mu_d = \frac{E_d}{E_{0d}} \qquad (7)$$

An average cosine of $\mu_d = 1$ indicates all radiation is propagated downward, perpendicular from the water surface. Radiation coming from all directions in an isotropic distribution equally results in a value of $\mu_d = 0.5$. Knowledge about the angular light distribution also enables the conversion of planar irradiance into scalar irradiance, which provides a more representative measurement of PAR availability for algal photosynthesis

$$E_{0d} = \frac{E_d}{\mu_d} \qquad (8)$$

PAR availability for photosynthesis decreases with depth until PAR transmission reaches the light compensation point (~0.2 to 1% of surface irradiance) at which the gains in the photosynthetic process no longer outweigh the losses associated with respiration. This point represents the depth of the euphotic zone and can be calculated with the help of the vertical diffuse attenuation coefficient for downwelling radiation (K_d) by applying Beer-Lambert's Law

$$E_d(z_2) = E_d(z_1) * e^{-K_d \, (z_2 - z_1)} \qquad (9)$$

The diffuse attenuation coefficient between the depth levels z_1 and z_2 incorporates the absorption and scattering of radiation and can vary with sun angle, depth and water body. Also note that Beer-Lambert's Law is a commonly used approximation of PAR attenuation despite the spectral nature of the downwelling irradiance in water (Wei and Lee, 2013).

Inherent optical properties

Inherent optical properties (IOPs) describe the properties of the matter itself and can be measured with a controlled light source. They are independent of the ambient light field. Dissolved or particulate substances and their corresponding composition, morphology and concentration cause

variations in the IOPs of an aquatic medium. A portion of the downwelling radiation is absorbed by the medium and its components described in the absorption coefficient *a*. Simultaneously, a fraction of radiation is scattered. The scattering coefficient *b* indicates the total number of photons diverging from their original path whereby the resulting angular distribution of scattered photons is expressed in the volume scattering function *ß(ψ)* including the scattering angle *ß*. Both coefficients are summarized in the beam attenuation coefficient

$$c(\lambda) = a(\lambda) + b(\lambda) \tag{10}$$

Water found in the clearest oceans attenuate incoming light weakly, which creates an euphotic layer of up to 200 m. On the contrary, turbid coastal waters have a high concentration of dissolved and particulate organic materials and inorganic sediment resulting in much higher absorption and scattering coefficients and shallow euphotic zones of sometimes only a few meters or centimeters.

In summary, incident solar radiation upon a medium undergoes reflection, absorption, diffusion and transmission. Applying the concept of energy conservation for a given layer such as sea ice, the sum of reflectance, absorbance and transmittance is equal to 1. The strength of these parameters in the equation varies largely in the sea ice-covered environment due to the freeze-thaw cycles of snow and sea ice, the changing concentration of ice impurities, and biological activity in and beneath the ice.

2.2.2. At the sea ice surface

Snow controls the amount of light reaching the ice and underlying water layer significantly. Surface *α(PAR)* ranges from 0.75 for melting snow to 0.87 for fresh snow and changes little with wavelength in the visible light spectrum (Perovich, 1996). A low (optically thin) snow depth, large grain size, high concentration of absorptive impurities and a high moisture content can decrease *α(PAR)* while an increase in the solar zenith angle can increase the snow albedo (Warren, 1982). A high cloud cover can also increase the albedo due to a more diffuse incident light field and the stronger absorption of near-infrared (IR) radiation, leaving shorter wavelength to reach the surface (Grenfell et al., 1981; Warren, 1982). Light transfer through the snowpack is also influenced by the scattering and absorption properties of snow grains and impurities resulting in an exponential decline of downward radiation with depth. UVR and IR are attenuated strongest in the snowpack (Perovich, 1996). PAR is absorbed weakly if the concentration of impurities such as soot is low

(Sturm and Massom, 2009). The high attenuation coefficient of snow, approximately an order of magnitude greater than that of sea ice (Perovich, 1996), is mainly caused via scattering by snow grains. Small grains at the surface scatter light significantly and increase travel of photons in the medium (i.e. the optical pathlengths) and consequently the probability of radiation being absorbed. Deeper in the snow pack, larger crystals are formed by kinetic growth (temperature-gradient) snow metamorphism, which decreases attenuation in the lower layers of the snowpack (Mundy et al., 2005). For the spatial variability of light transmission through snow-covered sea ice, these differences in the attenuation coefficient are negligible. Overall, snow depth primarily controls the amount of *T(PAR)* and scale of its spatial variability, and greatly reduces transmitted PAR at the ice bottom (Iacozza and Barber, 1999; Nicolaus et al., 2013).

During the melt season, the transformation from a homogeneous snow cover to a mixture of white ice and melt ponds affects the optical properties of the sea ice surface drastically. Surface albedo declines to 0.5 – 0.7 for white ice and to 0.2 – 0.6 for melt ponds while *T(PAR)* increases up to a factor of twenty (Fig. 2.4, Perovich, 1996; Nicolaus et al., 2012; 2013; Katlein et al., 2015a). However, the decrease in surface albedo and the related increase in transmittance is not a steady process (Fig. 2.4A). When the snow starts to melt, freshwater is trapped at the surface due to an impermeable ice cover and forms large flooded surface areas. The albedo continuously decreases during this stage (Perovich and Polashenski, 2012). With progressive melt, ice becomes more permeable and surface water starts to drain resulting in melt ponds with sharp edges connected through channels. At this time, the regional albedo increases due to emerging drained white ice. In the last stage of melt, pond surface levels are equal to the sea water level while the albedo decreases with thinning ice cover until break-up (Landy et al., 2014).
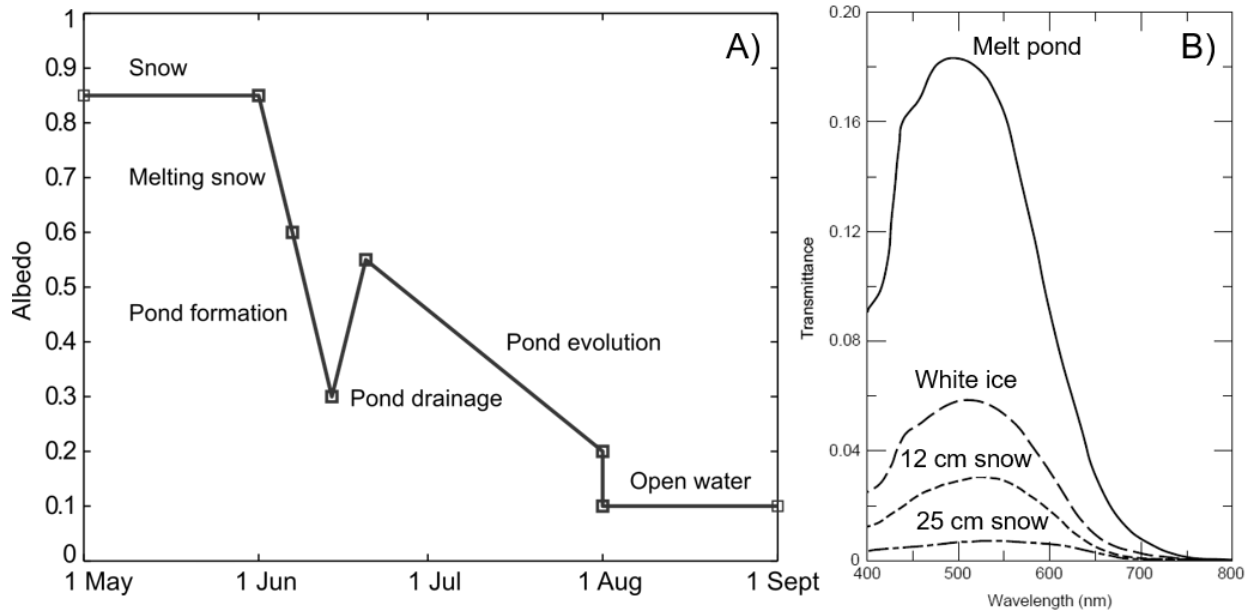
Figure 2.4: Seasonal progression of first-year ice A) surface albedo and B) spectral transmittance during the melt period. A) Created after Perovich and Polashenski (2012). B) Modified after Perovich (1996) with permission from USACE/ERDC.

2.2.3. Within the ice layer

Wavelength-specific light attenuation is one order of magnitude lower in the underlying sea ice, but also highly variable over time. Light propagation is affected by the microstructure of ice including its crystal matrix, brine and air bubbles as well as inclusions like sediments, and particulate and dissolved organic matter (Warren, 1982; Weeks and Ackley, 1986; Light et al., 1998; Belzile et al., 2000). The crystal structure shows a similar layer-influenced scattering behavior as that of snow with small granular crystals and a high scattering coefficient in the top and bottom layer and large, lamellar crystals in the interior scattering photons mainly downwards. Brine and air bubbles are the main scatterers in ice, whereas the volume scattering function of sea ice is particularly dependent on brine volume (Katlein et al., 2014). The authors of this study state that the anisotropic behavior, meaning more forward travelling photons, is particularly pronounced on larger scales when multiple scattering leads to a stronger attenuation of photons traveling horizontally. This impacts the under-ice light field significantly and will be discussed later. With warming ice in spring, air bubbles form in the brine pockets due to depressurization (Crabeck et al., 2019), which increases scattering within the ice layer. However, with ongoing melt, scattering decreases due to an increasing porosity connecting brine channels and flushing out air bubbles through incoming surface melt water (Light et al., 2008; Ehn et al., 2011).

Trapped sediments and ice biota influence scattering, but they play a more important role in the absorption of light. Pure, bubble free ice absorbs UVR moderately, PAR weakly and radiation in the longwave spectrum strongly (Perovich, 1996). Chlorophyll *a*-containing ice algae, however, have their absorption maximum in the visible light spectrum between 400 and 500 nm and 600 and 700 nm resulting in a higher attenuation of PAR when phototrophs are present. Mundy et al. (2014) reported an increase in light transmittance of 50% after most ice algae were released from the ice bottom during the spring phytoplankton bloom in the Canadian Archipelago. Additionally, the absorption coefficient of colored dissolved organic matter (CDOM) is high in the blue end of the spectrum (Kirk, 2011). CDOM concentrations are expected to be very low in sea ice (Belzile et al., 2000), but can increase rapidly at the ice bottom if ice algae are present (Xie and Gosselin, 2005; Granskog et al., 2007).

On large scales in the central Arctic, changes in the surface albedo, snow and ice thickness explain most of the variation in light transmission during the period of melt ponds covering the ice surface Nicolaus et al., 2013; Katlein et al., 2015a). The increase in melt pond coverage during melt season allows more radiation to pass through the ice into the water column. Besides the lower albedo due to the darker surface, thinner ice beneath the pond compared to white ice also contribute to a greater transmission of 13 – 67% through ponded ice versus 3 – 22% through white ice (Fig. 2.5, Ehn et al., 2011; Light et al., 2015). Additionally, summer MYI transmits less short-wave radiation with 4% compared to FYI with 11% (Nicolaus et al., 2012).

2.2.4. Beneath the sea ice layer

Variations in PAR propagation through the ice cover due to differences in snow depth, the presence of hummocks, ridges, leads and developing melt ponds, and variations in the horizontal distribution of light absorbing ice impurities create a heterogeneous light field in the first meters of the underlying water column (Fig. 2.5; Ehn et al., 2008; Light et al., 2008; Ehn et al., 2011; Frey et al., 2011; Katlein et al., 2015a; 2016; Horvat et al., 2020). In early spring, the thick snow and ice layer is associated with a diffuse under-ice light field and very low PAR levels. After the snow melt onset and melt pond formation, fluctuations in under-ice PAR levels are more pronounced as regional PAR transmission increases rapidly (Katlein et al., 2016; 2019). However, a diffuse under-ice field was assumed to prevail until ice break-up (e.g. Frey et al., 2011). The higher light transmission through more transparent near-by structures impacts the vertical radiation transfer in

the water column causing edge effects at the ice bottom and subsurface irradiance maxima beneath white ice areas with adjacent melt ponds (Ehn et al., 2011; Frey et al., 2011; Katlein et al., 2016). This increase in under-ice PAR levels in the first meters to a subsurface maximum contrasts the exponential light attenuation in the open water (Fig 2.5). The enhanced solar input further increases the heat content in the surface layer promoting ice bottom melt and a shallowing of the mixed layer depth. Simultaneously, the euphotic zone starts to deepen until increased light attenuation by under-ice phytoplankton accumulation reverses this process (Oziel et al., 2019). A shallower euphotic zone during ice-break up compared to a deeper euphotic zone beneath an ice layer with intensive melt pond formation can be further attributed to the increased cloudiness during summer when increasing surface temperatures and moisture fluxes favor cloud formation (Bélanger et al., 2013).
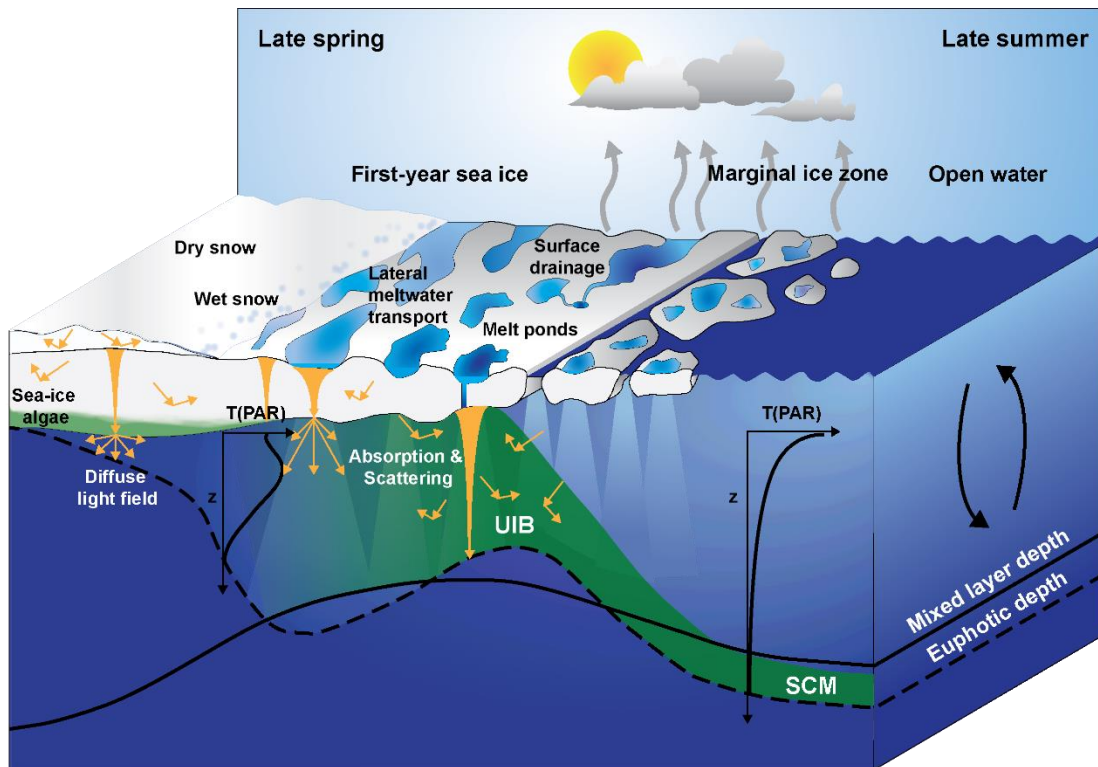
Figure 2.5: Schematic of under-ice light field during the sea ice spring melt. Changes in the depth of the euphotic zone (dashed black line) and mixed layer (solid black line) are presented in relation to the ice surface melt progression and the development of an under-ice bloom (UIB) and subsurface chlorophyll maximum (SCM) from late spring to late summer. Decrease in transmission of photosynthetically active radiation, *T(PAR)*, in the water column and regional average transmission, $\bar{T}(PAR)$, at the water surface is displayed for sea ice melt progression, marginal ice zone and open water, respectively. Modified after Ardyna et al. (2020a).

2.2.5. Optical measurements in the sea ice environment

Apparent and inherent optical properties of the water column are measured with various sensor applications (Fig. 2.6). Spectral radiance sensors record the radiant flux of specific wavelengths or, such as the hyperspectral fish-eye radiance camera (CamLum, Fig. 2.6A), measure the geometrical structure of the radiance distribution above the sensor. Irradiance is recorded with multispectral, hyperspectral (Fig. 2.6B–E) and broad-band PAR quantum sensors. Knowledge about the absorption and scattering characteristics of dissolved and particulate matter is applied through the use of bio-optical IOP sensors (Fig. 2.6F) to measure, e.g. *in situ* chlorophyll *a* concentration (Chl *a*) and colored dissolved organic matter (CDOM) via the emitted fluorescence, or the concentration of total suspended particles through the amount of light that is scattered back to the instrument.
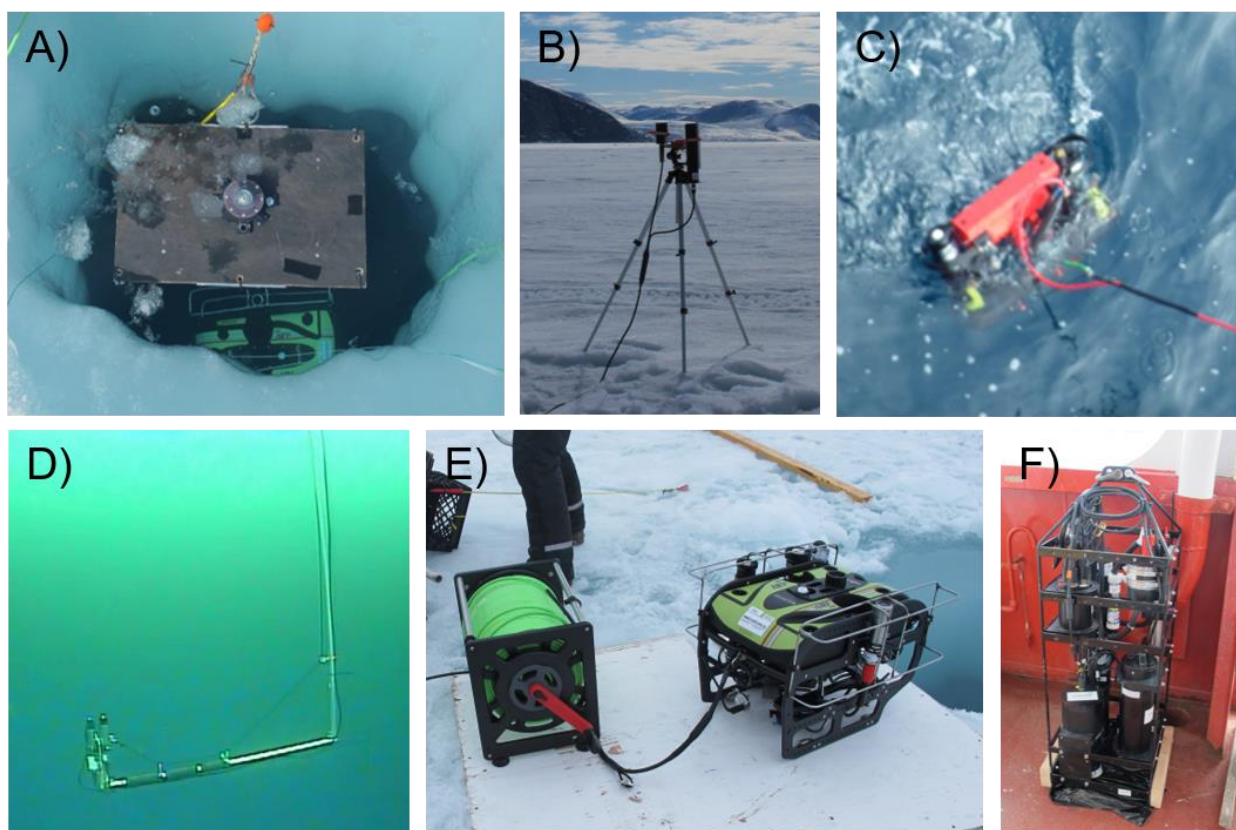
Figure 2.6: Optical sensor set-ups deployed in the ice-covered environment: A) Circular fish-eye radiance camera (CamLum) attached to under-ice sledge, B) irradiance sensors at the ice surface, C) free-floating radiance and irradiance sensors (Compact Optical Profiling System, C-OPS), D) irradiance sensors attached to custom-built double-hinged aluminum pole (L-arm), E) irradiance and radiance sensors attached to a remotely operated vehicle (ROV), F) IOP-frame with bio-optical sensors measuring absorption, scattering and fluorescence signal of dissolved and particulate matter.

Measuring light availability at the sea ice surface and the underlying water column is challenging due to the inaccessibility of the under-ice environment. Often, radiometer set-ups are deployed through small holes drilled by ice augers and are positioned beneath the ice bottom with the help of custom-build double-hinged poles, called L-arm (Fig. 2.6D). This deployment option as well as vertical profiles through small holes represent point-measurements, which can often not capture the heterogeneity in light transmission through the ice cover. Remotely operated vehicles (ROVs) equipped with different physical and bio-optical sensor arrays are capable to collect high temporal and/or spatial resolution datasets of under-ice radiance and irradiance with minimized disturbance over several hundred meters (Fig. 2.6E). Nowadays, ROVs are frequently used to perform large-scale irradiance measurements beneath landfast sea ice and moving pack ice in the Arctic Ocean (Nicolaus and Katlein, 2012; Katlein et al., 2015a; 2019), West Greenlandic fjord (Lund-Hansen et al., 2018), and in the Weddell Sea (Arndt et al., 2017). On even larger spatial scales, autonomous sampling platforms such as Argo floats carry advanced bio-optical sensors for the remotely-sensed detection of bio-geochemical parameters (IOCCG, 2011).

2.3. Environmental factors controlling algal growth in the Arctic

Several physical, biological and chemical factors regulate PP within the Arctic Ocean and will be introduced in this section. The availability of nutrients (section 2.3.1) defines the trophic status of a region (i.e. oligotrophic vs. eutrophic), and the availability of light (section 2.3.2) modulates the timing and magnitude of production within each region. Physiological processes within the algal cell are furthermore dependent on water temperature (section 2.3.3) and salinity (section 2.3.4). Temperature and salinity differences between water masses can also strengthen water column stratification and limit vertical mixing processes (section 2.3.5), which replenish inorganic nutrients in the surface layer and fuel a phytoplankton bloom in the surface water. The magnitude of a bloom is also influenced by the strength of grazing (section 2.3.6). These bottom-up and top-down controls interact with each other and reduce PP if one reaches a critical limit for continuous algal growth.

2.3.1. Nutrients

Algae utilize a variety of inorganic nutrients for sufficient growth with nitrate+nitrite (NO_3+NO_2), ammonium (NH_4), phosphate (PO_4), silicic acid ($Si(OH)_4$) and iron (Fe) defined as essential

(Taylor et al., 2013; Tremblay and Gagnon, 2009). The ratio of available nutrients controls limitations for the algal metabolism and is often referred to as the Redfield-Brzezinski Ratio, which represents the average ratios of $C:N:Si:P:O_2$ (106:16:15:1:-138) (Redfield, 1963; Brzezinski, 1985). As highlighted in this ratio, inorganic carbon is also essential for algal growth and is provided via the atmosphere-ocean gas exchange of carbon dioxide (CO_2). Nutrients are supplied to surface waters through physical processes such as atmospheric deposition, horizontal advection, vertical mixing and upwelling, and through the biological processes of remineralization.

Inorganic nutrients in the Arctic waters are laterally advected from adjacent oceans with Pacific water containing higher concentrations of N, P, and Si compared to Atlantic water (Codispoti et al., 2013; Tremblay et al., 2015), and from the terrestrial environment through rivers (e.g. Gordeev, 2000; Holmes et al., 2012; Tremblay et al., 2015). The Pacific water, entering through the Bering Strait, provides large amounts of N, P and Si and stays below the polar mixed layer, where nutrients are largely accessible for phytoplankton when the water mass mixes with surface waters along shoaled straits (Michel et al., 2006; Dalman et al., 2019) and in upwelling zones (Mundy et al., 2009; Tremblay et al., 2011; Williams and Carmack, 2015). More saline and denser Atlantic water enters through deeper channels and often remains below the other water masses, which makes the nutrient pool not fully accessible for PP (Tremblay et al., 2015). River runoff represents another, though minor source of nutrients to the Arctic Ocean due to its rapid consumption by primary producers within close proximity to estuaries (Macdonald et al., 2010; Fouest et al., 2013; Tremblay et al., 2014).

Vertical mixing due to wind stress or tides in coastal areas, and convective mixing during fall freeze-up or by ice formation in leads and polynyas in winter brings nutrients from the deeper layer up to the surface. Codispoti et al. (2013) estimated that roughly 93% of the annual nitrate consumption is driven by vertical supply processes and shallow nitrification (oxidation of NH_4 to NO_3+NO_2). Furthermore, wind-induced Ekman upwelling at the ice edge (Alexander and Niebauer, 1981; Mundy et al., 2009; Randelhoff and Sundfjord, 2018) and upwelling at the shelf break (Niebauer and Alexander, 1985; Tremblay et al., 2011; Falk-Petersen et al., 2015) also bring nutrient-rich deep water to the surface and support large phytoplankton blooms. Less studied is the role of cyclonic eddies in nutrient upwelling on the Arctic shelfs. The mechanisms behind eddy generation are still speculative (O'Brien et al., 2011 and citations therein). However, cyclonic

eddies have been observed to bring nutrients to the surface in their center (Mizobata et al., 2002; Mathis et al., 2007; O'Brien et al., 2011).

Advection, vertical mixing and upwelling prime the surface water layer for large algal growth in springtime when light levels are sufficient for positive photosynthesis (gains are higher than losses through respiration; Randelhoff et al., 2020a). In summer, the phytoplankton bloom usually terminates with the depletion of NO_3 while other essential nutrients are still available (Tremblay et al., 2015). A secondary bloom can be initiated in later summer/early fall after storm-driven mixing has replenished nutrients in the euphotic zone (Ardyna et al., 2014).

2.3.2. Light

Light determines the onset of net algal growth and influences the length of the growth season and the magnitude of production in each nutrient regime. Between 42 and 52% of the shortwave radiation that reaches the Earth's surface lies within the spectrum of PAR (Yu et al., 2015). The amount of incident surface PAR depends on absorption and scattering process by air molecules, aerosols, water vapour and other gases in the atmosphere (Kirk, 2011; Bélanger et al., 2013). But as discussed in section 2.2, only a fraction of incident PAR reaches the ice bottom and underlying water column and is available for algal photosynthesis in comparison to open water. Ice algae are shade-adapted such as that they can grow in the bottommost centimetres of sea ice with varying snow depths and low-light conditions (e.g. Cota, 1985; Cota and Smith, 1991; Gradinger, 2009; Campbell et al., 2015). Additionally, multiple scattering by sea ice inclusions and thus enhanced pathlengths of photons likely plays a role for ice algal growth in early spring after the sun returned (Ehn and Mundy, 2013). This is supported by observed lower *in situ* ice algal compensation light levels at 0.36 µmol photons m^{-2} s^{-1} (Mock and Gradinger, 1999), compared to 2 – 9 µmol photons m^{-2} s^{-1} (Horner and Schrader, 1982; Gosselin et al., 1985), measured in melted samples.

Phytoplankton can accumulate biomass in the euphotic zone of the upper ocean. The depth of the euphotic zone is not uniformly defined in the literature; it ranges from the surface to 0.1 – 1% of incident surface irradiance, or to a threshold isolume of 0.415 mol photons m^{-2} d^{-1}, below which light is assumed to be insufficient to support biomass accumulation (Letelier et al., 2004; Boss and Behrenfeld, 2010). The onset of phytoplankton growth in the euphotic zone of the AO has been studied intensively in the past years. The formation of large phytoplankton blooms has been

observed beneath fully consolidated FYI and landfast ice covers after the melt pond onset had increased PAR transmission to the underlying water column in late June (Ardyna et al., 2020a; b, and citations therein) . Re-frozen leads with little snow cover in the ice pack may promote and sustain UIBs beneath snow-covered Arctic pack-ice even earlier in late May (Assmy et al., 2017). Several studies have shown that autotrophic and mixotrophic phytoplankton maintain components of the photosynthetic apparatus even during polar night to enable rapid growth as soon as light becomes available again in spring (Kvernvik et al., 2018; Johnsen et al., 2020; Randelhoff et al., 2020b).

Very high PAR intensities or UVR can affect algal growth negatively and can inhibit photosynthesis. After snow melt onset, UVR transmission through FYI also increases significantly due to the moderate absorption by sea ice, reaching transmission levels of 2 and 19% through white and ponded ice, respectively, in the UVA spectral range (Elliott et al., 2015). High UVR intensities inhibit the photosynthetic capacity by damaging the photosystem II complex (Kirk, 2011), causing algae to acclimate with photoprotective mechanisms in microalgae. Ice algae and phytoplankton produce UV-absorbing mycosporine-like amino acids (MAAs) that absorb light in the 300 to 400 nm spectral range (Elliott et al., 2015; Piiparinen et al., 2015; Kauko et al., 2017) and other photoprotective pigments such as xanthophylls (e.g., Galindo et al., 2017; Lewis et al., 2019, also see Section 2.4.3.). However, UVR is absorbed quickly in the water column by CDOM and likely plays a more important role for surface phytoplankton blooms after the sea ice retreat than for UIBs.

2.3.3. Temperature

Temperature regulates metabolic processes and causes an exponential increase in algal growth rate until the optimal species specific temperature range is reached (Iriberri et al., 1985). Temperature above the optimum cause a decline in growth rate as well as Chl *a* of algal cells (Fig. 2.7A, Coello-Camba et al., 2015). The authors of this study performed incubation experiments of Arctic phytoplankton communities, composed of diatoms, dinoflagellates and other flagellates, under different temperature regimes. Besides the observed variation in Chl *a*, the authors also found a temperature effect on cell abundance and growth rates depending on the taxonomic group. Diatom abundance decreased with warming while small flagellates showed an increase in cell numbers with a temperature increase of 3 to 4°C from a sampling temperature of 2°C. Simultaneously with

19

the shift in dominance, an increase in the community production rate was observed until a maximum in production was reached between a water temperature of 4 to 6°C (Fig. 2.7B). Other observations report a linear relationship between temperature and respiration, photosynthetic efficiency and the light intensity at which photosynthesis is saturated (Darley, 1982).
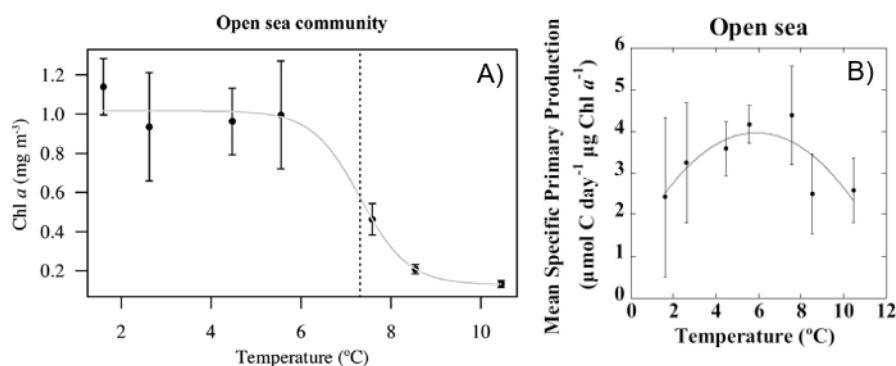
Figure 2.7: Temperature dependence of A) chlorophyll *a* concentration and B) primary production of an Arctic phytoplankton community from Coello-Camba et al. (2015). Used with permission from Springer.

2.3.4. Salinity

Osmotic stress due to very high or low salinity influences metabolic processes such as the pigment arrangement, the nutrient uptake and storage (Arrigo and Sullivan, 1992) and the cellular energy transfer (Ralph et al., 2007). Furthermore, production rates of ice algae have been noted to greatly decrease under low salinity stress (Campbell et al., 2019). Ice algae and phytoplankton communities in river estuaries must acclimate to varying salinities due to river discharge. High brine concentrations in the ice matrix and ice melt lead to additional salinity variations. Arrigo and Sullivan (1992) observed optimized photosynthetic rates of an Antarctic ice algal community between salinities of 30 – 50. Salinity tolerance also varies with species with some species showing a euryhaline response over large salinity ranges while others exhibit stenohaline responses with optima at lower (<20) or higher salinities (e.g. Hsiao, 1988; Cota and Smith, 1991; Zhang et al., 1999; Yoshida et al., 2020).

2.3.5. Vertical mixing

The replenishment of nutrients in the surface water is controlled by several physical processes that can reduce or strengthen vertical mixing. Temperature and salinity differences of the various water masses governs stratification in the AO, which form a layered halocline between the low-salinity

surface water and the saltier Pacific and Atlantic water masses beneath (Carmack, 2007). It is strongest in summer, but also present in winter. Models predict a strengthening of stratification due to an increase in freshwater inflow (Haine et al., 2015). Indeed, there is documentation of a stratification increase in the Beaufort Sea due to an enhanced river discharge (Yamamoto-Kawai et al., 2009; Morison et al., 2012). However, strong winds and tides can weaken this density-driven stratification and can keep the nutrient concentration in the surface layer high (Drinkwater and Jones, 1987; Ardyna et al., 2014).

Vertical mixing further affects phytoplankton directly by transporting it in and out of the euphotic zone. Low biomass and PP can be the result of the weakly stratified water column since phytoplankton cells do not receive a sufficient daily amount of PAR for net growth (Fig. 2.8). A study by Oziel et al. (2019) showed that the lack of a stable surface mixed layer due to cold air temperatures is typical for an early bloom stage in the ice-covered environment. Only after the mixed layer shoaled towards the depth of the euphotic zone due to freshwater input from ice melt and increased solar heating of the surface layer, phytoplankton received enough light to reach maximum production rates. However, phytoplankton in a stagnant mixed layer will draw down the available, and not replenished, macronutrient concentrations, so that PP decreases over time in a strongly stratified water column.
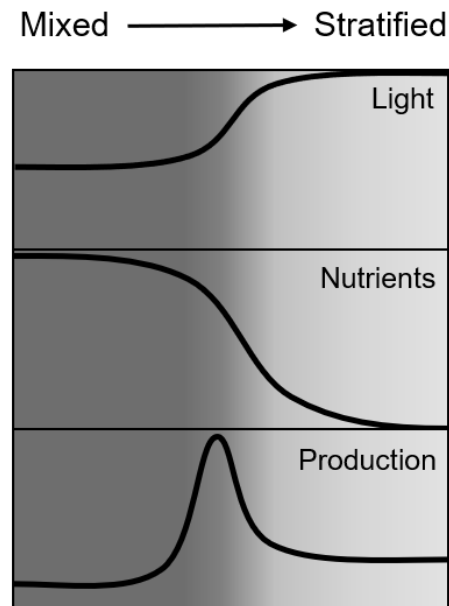
Figure 2.8: Impact of vertical mixing on nutrient and light availability, and phytoplankton PP in the surface layer. Modified after Kiørboe, (2008, p. 167).

2.3.6. Grazing

While the availability of essential nutrients and PAR control phytoplankton growth from the 'bottom up', grazing impacts microalgal abundance and biomass from the 'top down'. The timing, magnitude and duration of the spring microalgal bloom play a significant role for mesozooplankton development (Dalpadado et al., 2020). Microplankton (20 – 200 μm) such as ciliates, dinoflagellates and diatoms are consumed by mesozooplankton (200 – 20,000 μm) such as copepods, amphipods and krill. Cyanobacteria and several autotrophic and mixotrophic flagellate groups in the categories of picoplankton (0.2 – 2 μm) and nanoplankton (2 – 20 μm) are too small too be consumed by mesozooplankton directly. Instead, larger heterotrophic flagellates feed on these groups, resulting in an extended trophic level food web. With increasing phytoplankton biomass in spring, zooplankton biomass increases as well, although its seasonal peak occurs during summer stratification (Kiørboe, 2008; Dalpadado et al., 2020). High grazing pressure can limit the net population growth rate, particularly for smaller pico-and nanoplankton (Franks, 2001; Kiørboe, 2008). However, larger bloom-forming microplankton such as diatoms and raphidophytes can overwhelm their grazers if nutrients and light conditions are favorable and form large blooms until surface nutrients are exhausted (Stoyneva et al., 2007; Kiørboe, 2008; Lebret et al., 2012).

2.4. Arctic marine primary production

2.4.1. Algal photosynthesis

Primary production in the aquatic ecosystem describes the synthesis of carbohydrates from dissolved inorganic carbon to build biomass. It occurs through the process of photosynthesis by autotrophic organisms and can be stated as either net or gross production. Gross primary production (GPP) includes autotrophic respiration, the break-down of organic molecules into water and CO_2, and, thus, describes the total amount of organic matter fixed. Excluding autotrophic respiration in the calculation of production results in net primary production (NPP). Algae are important autotrophs in the marine environment and can accumulate a large amount of biomass under favorable environmental conditions.

The collection of light energy for photosynthesis is carried out by photosynthetic pigments, whose composition differs between algal groups. All algae contain chlorophyll and carotenoids. Red algae, cyanobacteria, and cryptophytes also contain biliproteins. Chlorophyll *a* is the main light

harvesting pigment, while the others are accessory pigments, which expand the absorption range of the light harvesting complex within the PAR spectrum and/or protect the photosynthetic apparatus from excessive light intensities. The presence of Chl *b* and Chl *c* as well as certain carotenoids is algal group specific and can be used for taxonomical analysis of algal communities (e.g. Mackey et al., 1996; Alou-Font et al., 2013; Coupel et al., 2015; Fragoso et al., 2017). The pigment composition also provides information on the physiological condition of communities. A large concentration of phaeopigments indicates grazing or decomposition (Geider and Osborne, 1992). Additionally, pigment ratios are used to assess the state of photoacclimation or photoprotection of algal cells.

2.4.2. Photosynthetic parameters

Information about the photosynthetic performance at varying light intensities can be examined using photosynthesis versus irradiance curves (P-E curves, Fig. 2.9). Measurements of the photosynthetic rate are performed via oxygen or radio-labelled carbon incubations of algal communities at different or natural light intensities. Fluorescence can be also used to measure photosynthetic rate via the electron transport rate (Consalvey et al., 2005). The chlorophyll *a*-normalized photosynthetic rate (P^B) can be plotted over a range of irradiances (E) to retrieve the photosynthetic parameters using a regression that best describes the plotted curve. The equations provided by Platt et al. (1980) shown in Figure 2.9 are commonly applied in PP calculations, which uses the maximum photosynthetic rate (P_s^B) with no photoinhibition (β^B), the photosynthetic efficiency (α^B), defined as the initial slope of the PE curve, and the irradiance (E) measured in the incubation chamber. If photoinhibition occurs at high light intensities during the incubation experiment, the maximum photosynthetic rate (P_{max}^B) is calculated using α^B and β^B (Fig. 2.9). The photoacclimation parameter (E_k) is calculated as P_{max}^B/α^B. Please note that the symbol α^B was chosen for photosynthetic efficiency in this thesis instead of the commonly used Greek letter α due to the use of α for surface albedo in the following chapters.
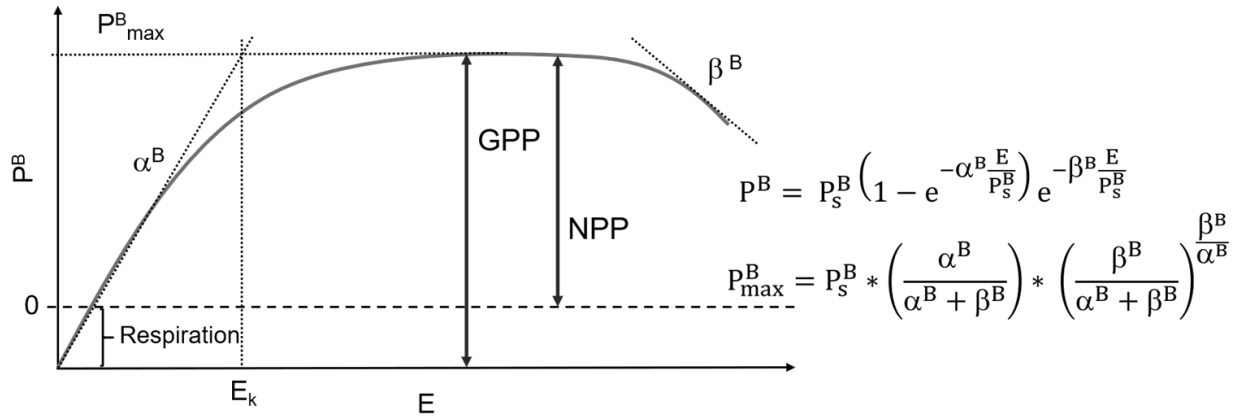
Figure 2.9: Photosynthesis versus irradiance curve and photosynthetic parameters. Gross production (GPP) and net production (NPP) excluding autotrophic respiration are highlighted as red arrows. Equations to calculate maximum photosynthetic rate with (P_s^B) and without (P_{max}^B) photoinhibition are taken from Platt et al. (1980).

2.4.3. Photoacclimation

Algae are exposed to a highly variable light regime, which is influenced by the sun angle, cloud cover, waves, water column stability or in polar regions on the presence of snow and ice (Perovich, 1996; Kirk, 2011). In response to these variations on different spatial and temporal scales, algae can modulate their P-E parameters to maximize biomass accumulation through adjusting the number of photosynthetic units, their cell volume, the functional size of light-harvesting antennae serving the photosystem reaction centers, and through changes in enzymatic activities involved in photosynthesis and respiration (Eberhard et al., 2008; Kirk, 2011; Yoshida et al., 2020; Falkowski and Raven, 2007). These short-term adjustments in response to changing light availability are called photoacclimation, while long-term genetic changes on evolutionary timescales refer to photoadaptation (Brunet et al., 2011).

If light levels reach damaging intensities, such as at the water surface, phytoplankton produce light-capturing pigments such as photoprotective carotenoids (e.g. xanthophylls) to reduce the number of photons absorbed and to minimize the inhibition of the photosynthetic apparatus (Geider and Osborne, 1992). The excess energy is diverted away by these protective pigments from the photosystem II reaction centers and dissipated as heat in the process of non-photochemical quenching (NPQ). Through these mechanisms light-acclimated algae often show a lower α^B and reach P_{max}^B at higher light levels (Kirk, 2011). Shade-acclimated algae living in turbid coastal waters, at greater water depths, in the bottom of snow-covered sea ice and in the water column beneath it are characterized by a high α^B to reach P_{max}^B at lower light levels (Zacher et al.,

2009; Kirk, 2011; Palmer et al., 2011; Huot et al., 2013; Arrigo et al., 2014; Lacour et al., 2017). In the case of phytoplankton drifting in the ice-covered water column, cells have a high concentration of Chl *a* and accessory pigments to maximize light utilization (Hill et al., 2005; Lewis et al., 2019; Kauko et al., 2019). Once light intensities increase in the under-ice environment through melt pond formation and ice melt, phytoplankton communities increasingly synthesize photoprotective carotenoids and reduce the number of functional reaction centers (Hill et al., 2005; Joy-Warren et al., 2019; Lewis et al., 2019; Kauko et al., 2019).

2.4.4. Microalgal communities in the Arctic Ocean

Ice algae

The internal sea ice matrix provides habitat for a diverse microbial community including viruses, bacteria, archaea, protists, microalgae, and meiofauna. Ice algae concentrate in the bottom 0 – 10 cm where favorable light and nutrient conditions and high surface area in the skeletal ice layer for colonization drive biomass accumulation (Fig. 2.10A, Arrigo et al., 2010). Ice algae can also inhabit the snow-ice interface, called infiltration assemblages, after a thick snow cover caused a negative freeboard and surface flooding (Buck et al., 1998; Fernández-Méndez et al., 2018). Light availability at the ice bottom drives the formation of an ice algal bloom and is itself controlled by solar insolation, ice thickness and snow depth (Gosselin et al., 1985; Mundy et al., 2005; Campbell et al., 2015). Ice algae can accumulate biomass when nutrients are constantly supplied by the water column (Leu et al., 2015). The increasing nutrient demand during a bloom can lead to nutrient limitation in the ice bottom that ultimately constrains the magnitude of the bloom (Gosselin et al., 1990; Smith et al., 1997; Leu et al., 2015). Nutrient availability further influences species composition such as larger pennate diatoms dominate the community at high nutrient concentrations and centric diatoms and flagellates dominate during nutrient-deplete conditions (Poulin et al., 2011; Campbell et al., 2018). Nevertheless, the sea ice matrix represents an extreme environment that internal ice algal communities need to adapt to, due to very low temperatures, high salinity and limited space. Ice algae living at the ice surface in melt ponds during advanced sea ice melt (Mundy et al., 2011; Fernández-Méndez et al., 2015; Sørensen et al., 2017) also need to acclimate to high light intensities and brackish water from snow melt.

Although ice algal production tends to contribute <20% total annual production in most of the Arctic Ocean (Legendre and Gosselin, 1991; Michel et al., 2006; Arrigo et al., 2010; Leu et al.,

2015), it provides an early food source for grazing zooplankton, amphipods and ice fauna and is funnelled in large amounts into the pelagic and benthic food webs (Boetius et al., 2013; Søreide et al., 2013). In the central Arctic Ocean, ice algae can contribute up to 60% to entire primary production (Gosselin et al., 1997; Fernández-Méndez et al., 2015). Particularly the sub-ice centric diatom *Melosira arctica* plays an important role in increasing local PP in the otherwise marginally productive central Arctic (Gutt, 1995; Gosselin et al., 1997; Melnikov, 1997; Fernández-Méndez et al., 2014; 2015) and in carbon export as much of their biomass sinks to the seafloor as a consequence of ice break-up and substantial under-ice melt (Gutt, 1995; Ambrose et al., 2005; Boetius et al., 2013). *M. arctica* has been observed as small clumps or in large strands, growing attached to the bottom of MYI and FYI (Fig. 2.10B) in the Arctic Ocean (Syvertsen, 1991; Gutt, 1995; Gosselin et al., 1997; Ambrose et al., 2005; Boetius et al., 2013; Fernández-Méndez et al., 2014; 2015) and the Canadian Archipelago (Poulin et al., 2014).
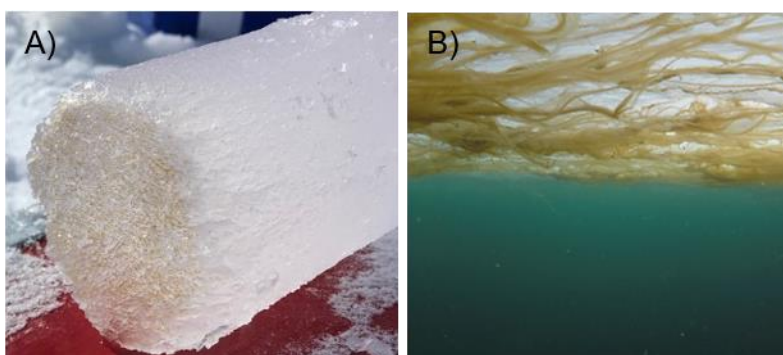
Figure 2.10: Microalgal communities of A) ice algae in the ice bottom, and B) sub-ice algae *Melosira arctica* in the Canadian Arctic (Photo credit: L. Dalman).

Phytoplankton

Phytoplankton growth in the Arctic Ocean is tightly linked to the sea ice cover. A phytoplankton bloom (Chl *a* >1 µg L^{-1}) is initiated in the surface water when the mixed layer depth (MLD) is shallow enough for the algal cells to stay in the euphotic zone during vertical mixing processes (Darley, 1982). Several studies showed that phytoplankton communities can endure polar night without entering resting stages due to low respiration rates associated with the low water temperature (Kvernvik et al., 2018; Johnsen et al., 2020; Randelhoff et al., 2020b). This behavior enables them to recover quickly and to take advantage of light immediately as the sun returns in spring. Arctic phytoplankton spring blooms are dominated by diatoms or the colonial haptophyte *Phaeocystis pouchetii* depending on the relative availability of silicic acid for diatom frustule

formation (Ardyna et al., 2020b). These blooms are also often short-lived in the surface water as they deplete the nutrient stock quickly and strong stratification prevents a nutrient replenishment from deeper waters (Tremblay and Gagnon, 2009). At this point, PP continues at the bottom of the euphotic zone where algal cells are acclimated to the low-light conditions and have access to nutrients from deeper waters through molecular diffusion through the pycnocline. This band of high Chl *a* is often called subsurface chlorophyll maximum (SCM) and can contribute significantly to PP in summer (Martin et al., 2010; Ferland et al., 2011). Ultimately, temperature and wind-induced upwelling and mixing in late fall and winter brings nutrients back to the surface and preconditions the surface water layer for PP during the spring and summer in the following year (Tremblay et al., 2011; Falk-Petersen et al., 2015).

2.4.5. Regional primary production

The central basins and marginal seas of the AO are divided into functional types based on regional geography as well as physical and biogeochemical exchange processes (Fig. 2.11, Carmack and Wassmann, 2006). This sub-section will discuss the biogeochemical properties of these functional regions. Estimates of annual pan-Arctic integrated PP from satellite observations and models range from 400 Tg C to 1100 Tg C yr^{-1} (Babin et al., 2015 and citations therein). Inflow shelves are the gateways for temperate water into the AO and account for 75% of that production due to the high nutrient load of the incoming Atlantic and Pacific water and the lower ice extent (Reigstad et al., 2002; Hill et al., 2013). The large blooms in the Barents Sea also benefit from the vertical mixing of the deeper Atlantic water to the surface layer (Oziel et al., 2017). Additionally, inflow shelves are characterized by a large amount of advected biomass from sub-Arctic regions, which fuels a diverse benthic community (Carmack and Wassmann, 2006).
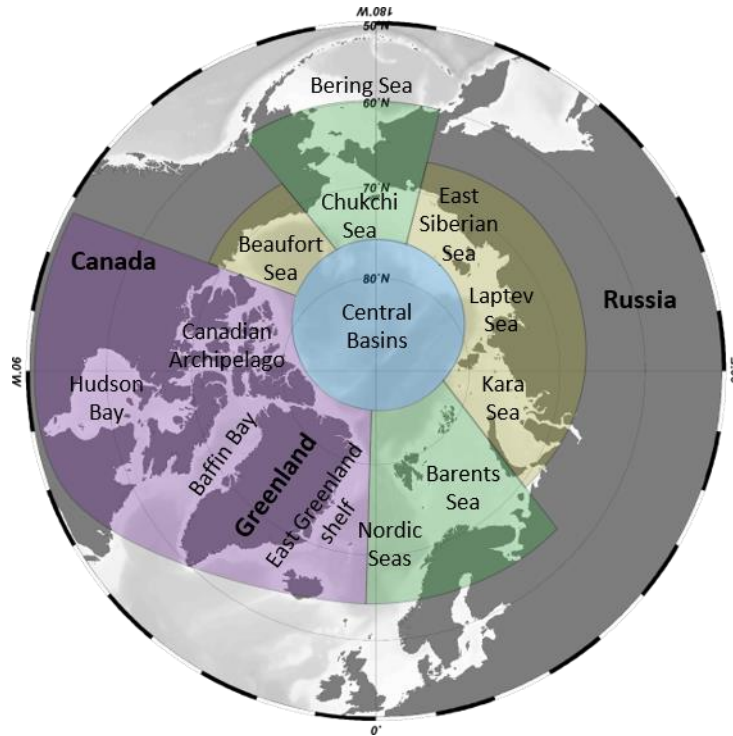
Figure 2.11: Geographical and functional regions of the Arctic Ocean. Borders of the central basins (blue), inflow shelves (green), interior shelves (yellow) and outflow shelves (purple) are schematic and do not exactly follow geographic borders.

Interior shelves are described as marginally productive and only contribute approximately 10% to the annual PP of the AO (Hill et al., 2013). The reasons for low pelagic PP are a significant riverine freshwater input causing a strong stratification as well as the large landfast and seasonal sea ice cover, which inhibits the vertical mixing of the water column. Furthermore, these shelves are shallow and often turbid due to the large river discharge, particularly in the Russian Arctic (Carmack and Wassmann, 2006). Although pelagic PP is low due to these physical processes, benthic biomass is relatively high (Carmack and Wassmann, 2006).

The central AO is characterized as persistently stratified and ice-covered for most of the year. The resulting light and nutrient limitation causes annual PP to be very low and in the case of phytoplankton, to be limited to a two to three month growth season in the surface layer of the central basins (Gosselin et al., 1997; Hill et al., 2013; Fernández-Méndez et al., 2015). Observations by Gosselin et al. (1997) and Fernández-Méndez et al. (2015) further showed that ice algae in the MYI and FYI bottom significantly contribute to total PP. However, the occasional observed high biomass of sub-ice algal aggregates formed by *Melosira arctica* are not yet included in annual PP estimates of the central basins.

Outflow shelves funnel fresher water as well as sea ice out of the central Arctic. Most of the exported MYI and FYI already melts within the shelves resulting in a strong haline stratification (Carmack and Wassmann, 2006; Michel et al., 2015). The presence of these thick MYI floes also causes light limitation for phytoplankton, particularly in the Greenland shelf region (AMAP, 2017). Overall, PP within the outflow shelves is spatially variable due to many small tidally mixed polynyas creating localized areas of high productivity in the Canadian Arctic Archipelago (CAA, Michel et al., 2015). The North Water Polynya in northern Baffin Bay is also known for its high productivity (Tremblay et al., 2006). For the other sections of these shelves, a long post-bloom phase with a low nutrient concentration in the surface water and a well-defined SCM has been frequently observed (Ferland et al., 2011; Hill et al., 2013; Barber et al., 2015).

The sub-Arctic sea Hudson Bay is included in this review due to its seasonal sea ice cover and strong haline stratification caused by a large freshwater river discharge (Prinsenberg, 1986; Stewart and Lockhart, 2005). Despite the southerly location, the continental climate of Hudson Bay keeps the seasonal ice cover in place into late spring-summer (Landy et al., 2017; Kirillov et al., 2020) and likely delays bloom onset relative to other sub-Arctic seas. Additionally, the low surface nutrient concentrations associated with the longer advective times scales of Atlantic and Pacific water and the strong stratification regime dampens productivity in the bay (Anderson and Roff, 1980; Ferland et al., 2011). Therefore, annual PP is considered to be of the same magnitude as in the interior Arctic shelves.

2.5. Observed changes in Arctic primary production patterns

2.5.1. Changes in light availability

The dominance of thinner and less snow-covered FYI, and a trend towards earlier and enhanced melt pond formation leads to an increase in light transmission to the underlying water column in spring (Agarwal et al., 2011; Nicolaus et al., 2012; Rösel and Kaleschke, 2012). Additionally, the shift in the dominant ice type reduces the freeboard height of sea ice above the sea surface (Kwok et al., 2009). Hence, the younger and thinner ice could be depressed below the water level with the heavy snow load in spring, whereas older and thicker ice would still have a positive freeboard. The resulting surface flooding creates a slush layer in the snowpack, which could potentially alter the amount of light that reaches the underlying water column in early spring due to a lower attenuation

coefficient of wet snow than that of dry snow (Arndt et al., 2017) while also creating new habitat (Fernández-Méndez et al., 2018).

The largest increase in underwater PAR is associated with the later freeze-up and earlier break-up of the seasonal ice pack resulting in an expanded open water period (Arrigo and van Dijken, 2015; Barber et al., 2015). However, more open water does not necessarily imply that more surface radiation will enter the AO. It has been shown that an increase in surface water temperatures and air moisture has led to an enhanced cloud formation during Arctic spring and summer (Schweiger, 2004; Bélanger et al., 2013). As clouds attenuate incoming radiation, Bélanger et al. (2013) was able to relate an observed reduction in incoming solar radiation by –8% per decade to an increased cloudiness in the Arctic (Fig. 2.12A). A simultaneous decline in underwater PAR was also predicted for the sub-Arctic seas (Fig. 2.12B). Only where the sea ice cover declined significantly in the marginal Arctic seas, did predictions show an increase in underwater PAR by +3.4% per decade.
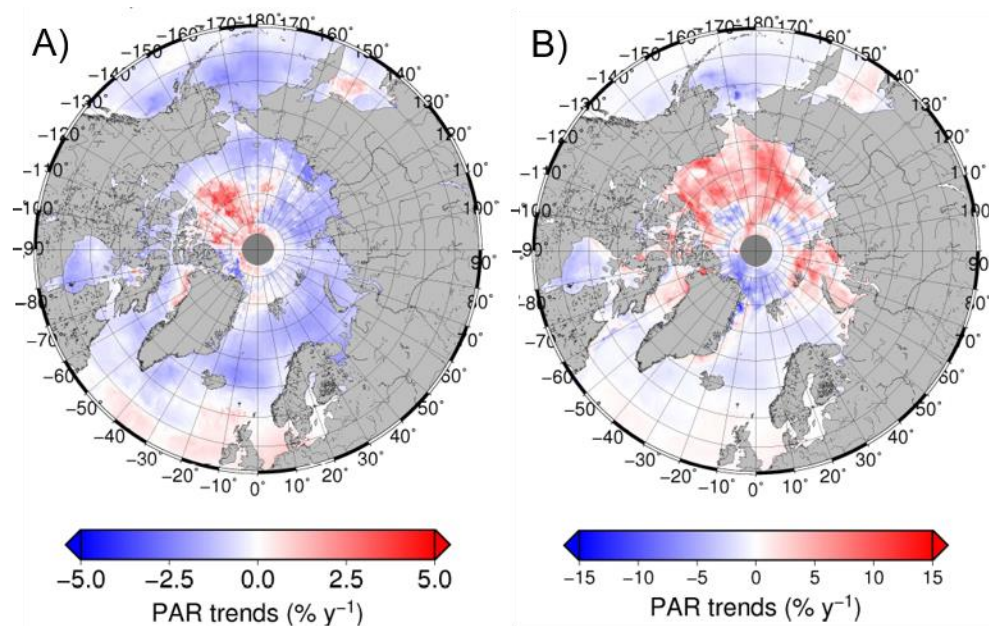
Figure 2.12: Standardized trends of A) surface PAR and B) underwater PAR in the sub-Arctic and Arctic between 1998 – 2010 (Bélanger et al., 2013). Copyrighted under Creative common licence (no permission required).

Furthermore, an increased load of dissolved and particulate matter in the coastal zone decreases water transparency. Increased river discharge also contributes, along with sediment resuspension due to tidal activity and coastal erosion, to increased turbidity in the coastal zone, which has been forecasted to reduce light penetration and thus primary production (Spencer et al., 2009; Slagstad

et al., 2011; Bélanger et al., 2013). As mentioned in section 2.2.3., CDOM absorbs PAR strongly in the blue part of the spectrum, which overlaps with one of the absorption peaks of Chl *a* at 443 nm.

2.5.2. Changes in nutrient availability

Strengthening of haline stratification due to an increased freshwater input from higher melt rates of FYI in summer negatively impacts the vertical nutrient supply (Yamamoto-Kawai et al., 2009; AMAP, 2017). Therefore, regional and local mixing events induced by tides, bathymetry (shelf breaks) and storm events will gain importance in the nutrient replenishment of the euphotic zone to fuel PP. For the last decades, meteorological data shows an increasing trend in the ocean-atmosphere exchange of moisture and heat with the retreating ice cover, which has enhanced the strength and size of Arctic storms (Simmonds and Keay, 2009; Long and Perrie, 2012; Crawford et al., 2020). These storms have the potential to mix the open water column, which will likely promote greater upwelling along the shelf edge and ice edge. The resulting increase in nutrient supply due to upwelling events has been already observed in the AO. For example, the decline in sea ice extent beneath the shelf break in combination with a high frequency of upwelling-favorable wind events led to an extended algal growth season with multiple peaks of high PP in the Beaufort Sea in 2007 and 2008 (Tremblay et al., 2011). Also observed in 2008 was a wind-induced upwelling along the ice edge that brought nutrient-rich water to the surface and fuelled a large phytoplankton bloom along the ice edge (Mundy et al., 2009). Furthermore, this positive effect of wind-mixing was also seen in polynyas and is expected to increase if polynyas widen earlier (Tremblay and Smith, 2007).

Another potential source of new nutrients into the system is the increased advection of Atlantic and Pacific waters into the AO (Shimada et al., 2006; Spielhagen et al., 2011; Årthun et al., 2012; Woodgate et al., 2012; Oziel et al., 2016). The incoming nutrient-rich Pacific waters already fuel the large summer phytoplankton blooms in the Chukchi Sea (Lowry et al., 2015) and could become an even more significant nutrient source since the Pacific inflow has increased by ~50% from 2001 to 2011 (Woodgate et al., 2012). Simultaneously, an enhanced Atlantic inflow introduces temperate phytoplankton and nutrients into the AO through the Barents Sea (Oziel et al., 2017; 2020). This additional influx of new nutrients has in combination with the longer ice free period increased total annual production in the AO by 57% between 1998 – 2018 (Lewis et al., 2020).

2.5.3. Changes in phytoplankton growth patterns

Although total Arctic pelagic production increased over the past decades, PP trends vary greatly across regions. The largest increase in PP was observed in the Atlantic inflow shelves, the Beaufort Sea and in parts of the Canadian Arctic Archipelago due to a weakening of surface stratification in the Beaufort Gyre (Giles et al., 2012; Moore et al., 2018), an increased open water season and wind-induced mixing events (Pickart et al., 2013; Arrigo and van Dijken, 2015). In turn, large sections of the outflow shelves showed a minimal increase to a decrease in PP due to an enhanced export of MYI reducing light availability in the water column (Arrigo and van Dijken, 2015; Barber et al., 2015; 2018), and enhanced stratification due to an increased freshwater input from advected melting ice floes and the Greenland ice sheet in summer. This resulted in a limited nutrient replenishment in the surface water (Arrigo and van Dijken, 2015; Barber et al., 2015; 2018, Blais et al., 2017).

Under-ice phytoplankton blooms

A new PP feature that has been found to be of common occurrence in the Arctic Ocean are under-ice phytoplankton blooms. These blooms have been observed across the AO (overview in Ardyna et al., 2020a). The magnitude of UIBs can be extremely high as a depth-integrated biomass of 28.7 to 32.5 g C m^{-2} was observed far within the ice pack during the ICESCAPE cruise in the Chukchi Sea in 2011 (Arrigo et al., 2012). Due to the inability of detecting under-ice Chl *a* via remote sensing, it is not clear if these blooms are a phenomenon of the changing Arctic or if blooms of large magnitude have occurred beneath the ice decades ago. For example, there were sporadic reports of high phytoplankton abundance beneath sea ice in a brackish environment (Legendre et al., 1981; Gradinger, 1996) and in the central AO (Apollonio, 1959; English, 1965). However, it was assumed that the former dominant MYI cover of the AO transmits an insufficient amount of surface PAR for under-ice PP, so that a bloom could only form at the ice edge. Large UIBs are now driven by the transmission of sufficient PAR levels through the melting and more transparent FYI cover with a high melt pond coverage.

Under-ice phytoplankton communities are often dominated by large diatoms that are taxonomically different from ice algae communities (Arrigo et al., 2014). The phytoplankton cells are acclimated to the low-light conditions to maximize their photosynthetic rate and have a high pigment concentration to increase light absorption (Arrigo et al., 2014; Lewis et al., 2019).

Furthermore, as mentioned in section 2.3.2, several phytoplankton species remain in a vegetative state during winter, leaving them prepared to start photosynthesizing as soon as the light returns in spring. The deeper MLD in early spring is also hypothesised to precondition phytoplankton due to the greater vertical migration from beneath the snow-covered sea ice layer to the bottom of the deep MLD increases Chl a synthesis in algal cells (Degerlund and Eilertsen, 2010). As explained in section 2.2.4., the under-ice light field is very heterogenous during the spring melt. To successfully form a bloom beneath the fully consolidated ice cover, the phytoplankton community must acclimate to these quick changes in low and high light levels.

Re-frozen leads are another characteristic of the sea ice cover that can enable early season phytoplankton blooms to develop due to a higher light penetration to the water column (Assmy et al., 2017). However, blooms can not form if the algal cells are mixed beneath the critical depth (Sverdrup, 1953), e.g. if a lead stays open where brine rejection influences density instability and resultant convective mixing of the under-ice water column (Lowry et al., 2018). Ultimately, UIBs, triggered by re-frozen leads or higher light transmission through ponded FYI (Fig. 2.5), have changed the timing of regional PP (Ardyna and Arrigo, 2020).

Fall blooms

Fall blooms are known for temperate waters in which fall storms induce vertical mixing and a replenishment of the surface nutrient pool. Ardyna et al. (2014) showed that areas with a second bloom in fall have increased between 1998 – 2001 and 2007 – 2012 in the AO (Fig. 2.13). In the past, light limitation associated with the low sun angle, the large sea ice cover and the early freeze-up made the occurrence of fall blooms unlikely. However, second bloom events in fall have become more common due to the observed extensive sea ice loss, later freeze-up dates and more open sea surface exposed to wind stress (Ardyna et al., 2014; Lebrun et al., 2019). Figure 2.13 shows the largest increase in two blooming events in the Arctic shelf seas in the Russian sector and in the Bering Strait, which is consistent with the latest sea ice loss (AMAP, 2017). Regions with a large freshwater input and strong vertical stratification, such as the Beaufort Sea, are less likely to support fall blooms (Ardyna et al., 2014).
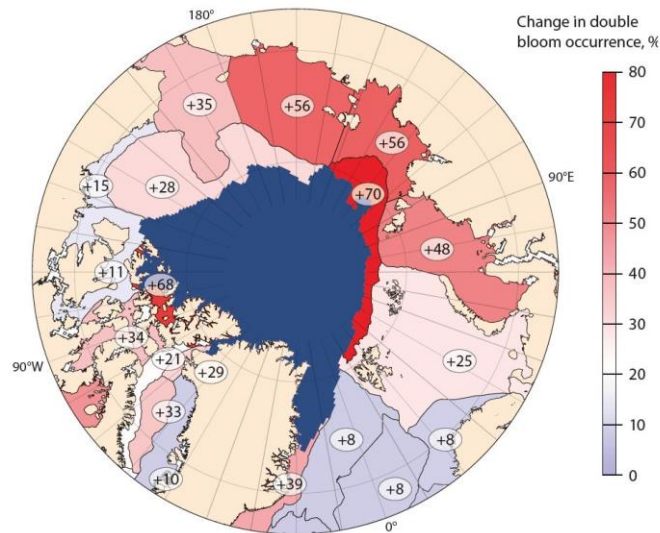
Figure 2.13: Percentage change in pan-Arctic occurrence of fall blooms between 1998 – 2001 and 2007 – 2012 (Originally published by Ardyna et al. (2014); modified in AMAP (2017). Used with permission from John Wiley and Sons.

2.5.4. The future of microalgal primary production in the Arctic Ocean

Predictions about future changes in the AO include a further increase in air and water temperatures, a nearly complete shift from a perennial to a seasonal ice cover, stronger atmospheric forcing (e.g. more storm events), increasing ocean acidification and an increasing freshwater input (AMAP, 2017). These various alterations in the physical and chemical properties of the AO will continue to have a large impact on the timing and magnitude of PP. However, the impact of the thinning and retreating sea ice cover and the intensification of the positive ice-albedo feedback loop mechanism will differ between the algal communities and from one region to another. While phytoplankton will potentially benefit from a longer open water growth season, ice algae will lose their FYI habitat earlier during the spring melt in the marginal Arctic seas (Barber et al., 2015). The inflow of warm water intensifies this process (Leu et al., 2015). Ongoing changes in the physical environment will also affect the community structure in the ice and pelagic habitat.

Expected alterations of the ice algal community

Ice algal PP is estimated to contribute approximately 5 to 20% to the total PP in the AO (Legendre and Gosselin, 1991; Michel et al., 2006; Arrigo et al., 2010). However, these estimates do not include biomass production by *Melosira arctica*, which can make a significant difference in the otherwise marginally productive central Arctic, so that predictions about an increasing or

decreasing contribution of ice algae to pan-Arctic production are difficult. Generally, seasonal sea ice will still form every winter and this ice will be inhabited by ice algae. The higher initial nutrient load and brine volume of FYI is also assumed to provide better growth conditions than MYI (Leu et al., 2015). Additionally, the lower snow depth and higher transparency of FYI will increase light availability earlier in spring (Tedesco et al., 2019). In terms of alterations in the community structure of ice algae, a study by Olsen et al. (2017) hypothesizes that the shift from a perennial to a seasonal ice cover will have an impact on community diversity. The presence of MYI has been shown to seed adjacent FYI with ice algal cells that have survived the summer melt season and were trapped in the upper ice layers during winter. Following the authors' hypothesis, a loss in MYI will prevent this seeding mechanism and potentially cause a decrease in biodiversity in the Central Arctic basins where MYI is still present as recently observed (AMAP, 2017; Hop et al., 2020).

Expected alterations of the phytoplankton community

The more frequent observations of UIBs indicate that the loss of the perennial sea ice cover, the decreasing ice thickness, and thinner snow cover provides more favorable light conditions. Simultaneously, the increased open water surface area has created a longer fetch for strong winds from migratory cyclones inducing a large swell. These waves can cause a widespread fracturing of the ice pack, which reduces floe size and creates more open water (Asplin et al., 2012). The strong winds will also lengthen the phytoplankton growth season and induce fall blooms due to the vertical mixing of the water column. However, wind-mixing is not always strong enough to overturn water bodies with persistent stratification (Tremblay et al., 2015). It is predicted that the thermohaline stratification will strengthen in several parts of the Arctic Ocean due to increased freshwater input and warming of the surface layer. Therefore, the magnitude of changes in Arctic PP will depend on the strength of these contrasting effects. Table 2.1 provides a summary of observed physical properties that currently drive the change in regional phytoplankton production.

Table 2.1: Estimated annual PP of Arctic and sub-Arctic seas and their affiliation to a functional region. For each sea, observed novel PP patterns and dominant physical factors are presented that cause the observed increase or decrease (red) of PP. PP estimates are taken from Hill et al. (2013), except for Hudson Bay *(Ferland et al., 2011)*. Arrows symbolize an increase or decrease in the magnitude of the given factor.

Arctic & Sub-Arctic Sea	Functional region	Total PP (Tg C yr⁻¹)	Factor controlling current increase/ decrease in annual PP	Novel PP pattern	Reference
Canadian Arctic Archipelago	Outflow Shelf	93	↑ Open water period ↓ MYI cover ↑ Freshwater input	Under-ice blooms Fall blooms	Fortier et al. (2002) Ardyna et al. (2011) Michel et al. (2015)
Greenland Shelf (incl. Baffin Bay)	Outflow Shelf	118	↑ MYI export ↑ Freshwater input	Under-ice blooms	Michel et al. (2015) Blais et al. (2017) Green Edge project (2016)
Beaufort Sea	Interior Shelf	3.05	↑ Open water period ↑ Wind-driven upwelling	Under-ice blooms Fall blooms	Mundy et al. (2009) Yang (2009) Blais et al. (2017)
Nordic Seas	Outflow/ Inflow Shelf	308	↑ Freshwater outflow ↑ Atlantic water inflow		Dukhovskoy et al. (2019) Nöthig et al. (2020)
Bering Sea	Inflow Shelf	134	↑ Water temperature ↑ Pacific water inflow		AMAP (2017)
Chukchi Sea	Inflow Shelf	80	↑ Open water period ↑ Wind-driven upwelling ↑ Water temperature ↑ Pacific water inflow	Under-ice blooms	Arrigo et al. (2014) AMAP (2017)
Barents Sea	Inflow Shelf	212	↑ Open water period Deepening of the MLD ↑ Water temperature ↑ Atlantic water inflow	Under-ice blooms Fall blooms	Strass and Nöthig (1996) AMAP (2017) Oziel et al. (2017) Dalpadado et al. (2020)
East Siberian Sea Laptev Sea	Interior Shelf	21.92	↑ Open water period ↑ Water temperature ↑ Freshwater input	Fall blooms	Ardyna et al. (2014) AMAP (2017)
Kara Sea	Interior Shelf	16	↑ Open water period ↑ Water temperature ↑ Freshwater input	Fall blooms	Ardyna et al. (2014) AMAP (2017) Renaut et al. (2018)
Arctic Ocean Basins	Central Basin	1.39	↑ Open water period ↓ MYI cover ↑ Freshwater input		Renaut et al. (2018)
Hudson Bay	Sub-Arctic Sea	24	↑ Open water period ↑ Freshwater input		Hochheim et al. (2010) Déry et al. (2011)

The provided summary illustrates the regional differences in the physical forcing of PP. Except for the Greenland shelf, all Arctic regions show an increase in PP driven by the current physical environment. The increasing freshwater budget and sea ice export onto the Greenland shelf is assumed to reduce light and nutrient availability, which can potentially lead to a decrease in production in future. The marginal seas and inflow shelves experience a large increase in light availability and in advected new nutrients via the enhanced inflow of Atlantic and Pacific waters, which drive the current increase in production. However, it is still unclear if vertical mixing and upwelling events will become more frequent and counteract the increasing stratification from enhanced freshwater input from ice melt, rivers, and precipitation. Additionally, the future magnitude of Arctic PP will be impacted by the circulation regime of the Beaufort Gyre, which

historically showed an anticyclonic circulation that accumulated freshwater in its center. In winter 2017, this circulation system reversed and released freshwater (Moore et al., 2018). Such a cyclonic regime is projected to become more common in the future, which would redistribute large amounts of nutrient deplete (Li et al., 2009) freshwater to other Arctic and sub-Arctic regions (Proshutinsky et al., 2015). Ultimately, this would strengthen the thermohaline stratification in the Arctic periphery, while it weakens in the Beaufort Sea. Currently, only the central Arctic has the potential for a long-term increase in PP due to enhanced light availability associated with the increasing open water period, and a nutrient pool that was not depleted by the historically too short growth season (Tremblay et al., 2015).

It is also important to note that current estimates of production are often incomplete (Babin et al., 2015). This makes a calculation of baseline values for Arctic PP difficult and hampers an evaluation of the impact of climate change. The stated annual phytoplankton production in Table 2.1 is based on remote sensing estimates that include productivity at the SCM, but excludes PP in ice-covered regions. Often, the SCM as well as ice algal and under-ice phytoplankton production are excluded from regional estimates due to the inability of remote sensing techniques to measure Chl a beneath the ice cover or at deeper water depths (Lee et al., 2015).

Predictions about an increase in pan-Arctic production are widely discussed in the literature. The current increase in PP is driven by the increased open water season and a potential increase in surface nutrient concentrations (Arrigo and van Dijken, 2015; Kahru et al., 2016; Lewis et al., 2020). If the nutrient pool is depleted quickly by new production, such as a large under-ice bloom, overall annual production of a region may not further increase. Only the length of a regenerated production will be expanded in the surface layer and at the SCM. Its magnitude will be dependent on the efficiency of remineralization of organic matter by the microbial loop. This potential change in the duration of production regimes will have an impact on the energy transfer in the food web. New production entails a high grazing capacity and an efficient energy transfer. Regenerated production often results in a longer food chain with a less efficient nutrient transfer and a smaller export of organic matter to the benthos (Randelhoff and Sundfjord, 2018). Another factor, impacting the quality of the organic material that is consumed or exported, is a change in the composition of the phytoplankton community.

Ardyna et al. (2011) reported a shift from an eutrophic into an oligotrophic regime after a long growth season with a strong stratification in the Canadian Arctic. This regime shift turned the diatom-based system, typical for new production, into a flagellate-based system of regenerated production with a high abundance of picophytoplankton (<2 µm) and nanoflagellates (2 – 20 µm). A promotion of small phytoplankton cells by warmer, fresher, and nutrient depleted surface water has been investigated in several regions of the AO (Li et al., 2009; Tremblay et al., 2012; Neeley et al., 2018). In Fram Strait, the observed shift in community dominance from diatoms to the nanoflagellate *Phaeocystis pochetii* has also been interpreted as an indication for a northward extension of these flagellate driven blooms following the distribution of warmer Atlantic water in the Arctic surface layer (Nöthig et al., 2015; Oziel et al., 2017). In parallel, heterotrophic bacterioplankton became more abundant, which increased carbon cycling within the microbial loop and is thought to limit the carbon export to the benthic communities (Li et al., 2009; Tremblay et al., 2012).

3. Chapter – Spatial heterogeneity as a key variable influencing spring-summer progression in UVR and PAR transmission through Arctic sea ice

Abstract

The transmission of ultraviolet (UVR) and photosynthetically available radiation (PAR) through sea ice is a key factor controlling under-ice phytoplankton growth in seasonally ice-covered waters. The increase towards sufficient light levels for positive net photosynthesis occurs concurrently with the sea ice melt progression in late spring when ice surface conditions shift from a relatively homogeneous high-albedo snow cover to a less reflective mosaic of bare ice and melt ponds. Here, we present a detailed dataset on the spatial and temporal progression of transmitted UVR and PAR in relation to changing quantities of snow, sea ice and melt ponds. Data were collected with a remotely operated vehicle (ROV) during the Green Edge landfast sea ice campaign in June–July 2016 in southwestern Baffin Bay. Over the course of melt progression, there was a 10-fold increase in spatially averaged UVR and PAR transmission through the sea ice cover, reaching a maximum transmission of 31% for PAR, 7% for UVB and 26% for UVA radiation. The depth under the sea ice experiencing spatial variability in light levels due to the influence of surface heterogeneity in snow, white ice and melt pond distributions increased from 7 ± 4 to 20 ± 6 m over our study. Phytoplankton drifting in under-ice surface waters were thus exposed to variations in PAR availability of up to 43%, highlighting the importance to account for spatial heterogeneity in light transmission through melting sea ice. Consequently, we demonstrate that spatial averages of PAR transmission provided more representative light availability estimates to explain under-ice bloom progression relative to single point irradiance measurements during the sea ice melt season.

Encouragingly, the strong dichotomy between white ice and melt pond PAR transmittance and surface albedo permitted a very good estimate of spatially averaged light transmission from drone imagery of the surface and point transmittance measurements beneath different ice surface types.

3.1. Introduction

In the Arctic Ocean, under-ice phytoplankton blooms can contribute significantly to spring primary production and have been documented more frequently in the last decades (e.g. Fortier et al., 2002; Mundy et al., 2009; Arrigo et al., 2014; Assmy et al., 2017; Oziel et al., 2019). During spring, surface nutrient concentrations tend to be replete and the presence of sea ice and meltwater create a low turbulence that favor the growth of diatoms (Arrigo et al., 2014; Neeley et al., 2018; Oziel et al., 2019) and the colonial haptophyte *Phaeocystis pouchetti* (Assmy et al., 2017). The onset of under-ice phytoplankton production is largely triggered by the seasonal increase in transmission of photosynthetically active radiation (PAR, 400–700 nm) through the ice layer to sufficient levels for positive net photosynthesis (Mundy et al., 2014). A study by Horvat et al. (2017) demonstrated that nearly 30% of the ice-covered Arctic Ocean in July permits PAR levels that are sufficient for under-ice algal blooms. However, in situ optical measurements beneath the sea ice cover are difficult due to spatial heterogeneity in light propagation caused by differences in snow depth, melt pond coverage, melt pond geometry and depth, ice thickness, and the horizontal distribution of light absorbing ice impurities (Ehn et al., 2008; Ehn et al., 2011; Katlein et al., 2015a; Light et al., 2015; Lu et al., 2016; Horvat et al., 2020).

Sea ice albedo has been widely studied showing that the decrease in light reflection is not a steady process (Fetterer and Untersteiner, 1998; Ehn et al., 2011; Perovich and Polashenski, 2012; Landy et al., 2014; Diaz et al., 2018). Snow melt and an impermeable ice layer cause surface flooding and thus a rapid decrease in the surface albedo. As melt progresses, the trapped water begins to drain towards flaws and seal breathing holes resulting in a short-term increase in regional albedo due to the emerging white ice (drained bare surface ice layer). In the last stage of melt, surface albedo further decreases with the thinning white ice layer and ice cover until ice break-up. During this surface melt progression, the initiation of melt pond formation is associated with the strongest increase in light levels at the ice bottom (Nicolaus et al., 2012; Zhang et al., 2015). However, the intensified differences in light transmittance through ponded vs. white ice combined with the lateral spreading of radiation within the ice layer create a more complex underwater light field

(Frey et al., 2011; Katlein et al., 2016; Massicotte et al., 2018; Matthes et al., 2019). As shown in these studies studying the under-ice light field, vertical radiation transfer can be influenced by higher light transmittance through more transparent near-by structures causing edge effects at the ice bottom and subsurface irradiance maxima. This light attenuation discrepancy affects point measurements of light transmittance under the ice with different surface types and makes regional estimates of under-ice PAR availability for marine primary production estimates difficult. Optical measurements beneath a depth of 5 to 15 m are less affected by spatially heterogenous light transmission due to a more downward directed light propagation, which is only dependent on absorption and scattering processes within the water column (Frey et al., 2011; Katlein et al., 2015a; Matthes et al., 2019). Thought from a surface perspective, Perovich (2005) defined this spatial scale of minimal variation in the propagation of solar radiation as the aggregate scale. Following this definition, the depth of spatially transmitted light independence on surface conditions is hereinafter called the 'aggregate-scale depth' of light transmission. Knowledge about the impact of the surface melt progression on this depth is still limited.

To capture regional variability of light transmission through sea ice and the underlying water column, remotely operated vehicles (ROVs) equipped with different sensor arrays are more frequently used. ROVs were deployed to perform large-scale irradiance measurements beneath landfast sea ice and moving pack ice in the Arctic Ocean (Nicolaus and Katlein, 2013; Katlein et al., 2015a; 2019), West Greenlandic fjord (Lund-Hansen et al., 2018), and in the Weddell Sea (Arndt et al., 2017). The minimized disturbance caused by ROV-based measurements compared to traditional core-based point-sampling methods also enables repeated operations within the same area throughout the melt season (Nicolaus et al., 2012). These measurements can be used to calculate regional estimates of under-ice PAR levels, which are needed in the investigation of the timing of under-ice phytoplankton growth. Large-scale sea-ice coverage sampling also minimizes statistical errors in primary production estimates caused by spatially heterogeneous light propagation (Massicotte et al., 2019). Hence, spatially averaged light transmission could represent a better estimate of light availability as phytoplankton cells often drift at a different rate and direction than that of the sea ice. This is particularly true for the case of a static landfast ice cover overlying a tide-influenced water column. Additionally, area-wide averages of light transmittance were found to cancel out edge effects caused by differences in ice surface reflection of melt ponds and white ice (Ehn et al., 2011; Taskjelle et al., 2017).

Meltwater transport and melt pond evolution at the ice surface has been described to undergo several stages throughout the sea ice spring-summer progression (Eicken et al., 2002; Polashenski et al., 2012; Landy et al., 2014). However, similar studies about the temporal increase in light transmission over the melt season are still sparse. In this paper, we hypothesize that the temporal increase in under-ice PAR and UVR levels follows the stages of melt pond evolution while the spatial heterogeneity of PAR and UVR transmission remains unchanged after the melt pond onset. We further hypothesize that including spatial heterogeneity of light transmission in the calculation of the euphotic zone depth will provide a more accurate estimate to help explain processes influencing development of an under-ice phytoplankton bloom. To quantify the increase of spectral light transmission through sea ice as a function of melt processes, a remotely operated vehicle (ROV) equipped with hyperspectral radiometers was used in June-July 2016 in Southwestern Baffin Bay. Horizontal transects and vertical profiles were repeatedly performed beneath the ice cover with changing quantities of snow, ice, melt ponds and ice algae to calculate average PAR and UVR transmittance and to investigate the interaction of increasing under-ice PAR availability and the initiation of phytoplankton growth. Simultaneously, the impact of the varying ice surface conditions on the scale of spatial variability of surface albedo and light transmission and the aggregate-scale depth are examined.

3.2. Methods

3.2.1. Sampling site

As part of the Green Edge project in 2016, measurements of spectral irradiance and environmental parameters were performed on level landfast first-year sea ice (67° 28.784' N, 63° 47.372' W) near Qikiqtarjuaq, Nunavut, Baffin Bay (Fig. 3.1). An undisturbed area east of the ice camp was chosen to repeatedly measure light transmittance through sea ice transitioning from snow-covered to shallow melt ponds and white ice surface conditions between 6 June and 2 July. Snow melt onset had already begun prior to the commencement of our study with daytime air temperatures consistently exceeding 0°C on 3 June followed by melt pond formation on 15 June (Oziel et al., 2019). Sky conditions varied between cloudy with sunny intervals, fully overcast and long periods of fog causing a decrease in incident surface PAR in June compared to the previous month (Fig. 3.2 in Oziel et al. (2019)).
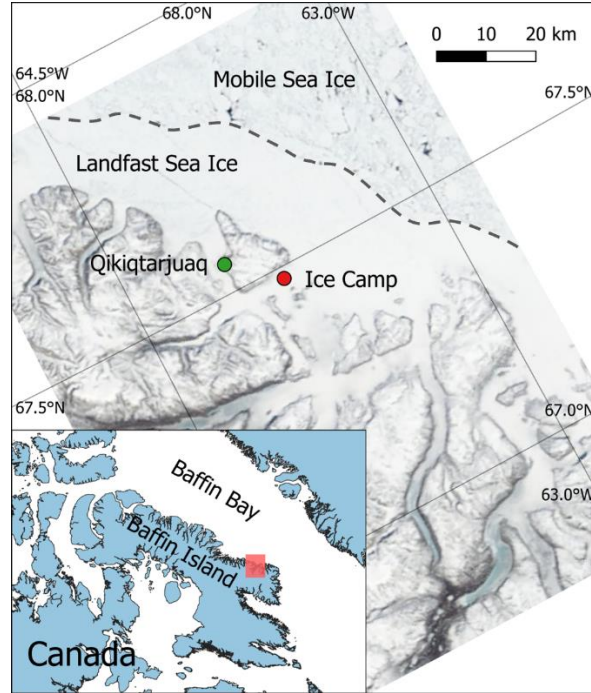
Figure 3.1. Location of the ice camp as part of the Green Edge campaign in 2016 on landfast sea ice near Qikiqtarjuaq, Southern Baffin Island, NU, Canada (MODIS image, 13 June 2016).

3.2.2. Optical measurements

Incoming solar irradiance at the sea ice surface, $E_d(\lambda, 0)$, was measured with a visible (VIS) hyperspectral radiometer (wavelength range 350 – 950 nm with 3.3 nm resolution over 256 channels) and a 4-channel multispectral ultraviolet (UV) radiometer (305, 325, 340, 379 nm; Satlantic HyperOCR and OCR-504 UV, respectively, Sea-Bird Scientific, USA), both with cosine collector and mounted on a tripod 1.5 m above the ice surface. Surface albedo measurements were made with a separate hyperspectral radiometer (wavelength range 320 – 950 nm with 3.3 nm resolution over 190 channels; Ramses-ACC, TriOS GmbH, Germany) after the under-ice light sampling. Spectral albedo, $\alpha(\lambda)$, was calculated as the ratio of five measurements of downwelling, $E_d(\lambda, 0)$, and upwelling, $E_u(\lambda, 0)$, surface irradiance measured 1 m above the ice surface

$$\alpha(\lambda) = \frac{E_u(\lambda, 0)}{E_d(\lambda, 0)} \tag{11}$$

Downwelling under-ice irradiance at 2 m water depth, $E_d(\lambda, 2)$, was measured using a remotely operated vehicle (ROV; SeaBotix vLBV300, USA), connected to a surface control unit through a tether cable of 300 m length (Fig. S3.1). The ROV was equipped with matching VIS and

43

multispectral UV surface radiometers but calibrated for underwater deployment. All sensors were triggered synchronously, and light data was binned to one measurement per second. Also attached to the ROV was a CTD probe (SBE 49 FastCAT, Seabird, USA), an altimeter (resolution: 1 mm, VA500, Valeport, USA) to measure the distance between the vehicle and the ice bottom and a 360 degree action camera (PIXPRO SP360, Kodak, USA) to record ice bottom features. The ROV was launched and recovered through ~1 m^2 holes and moved along horizontal transects by six thrusters at an average speed of 0.5 m s^{-1}. The average sinking speed for vertical profiles was 0.2 m s^{-1}. An integrated camera system at the front and back of the ROV enabled under-ice navigation along guiding lines. Prior to the field deployment, the weight distribution of ROV attachments were balanced, such that the internally measured pitch and roll of the vehicle never exceeded 7° during under-ice deployments.

To increase the spatial and temporal coverage of sampling, two transect areas were designated as shown in Figure 3.2. The change in spectral light transmission over time was measured continuously along one 150-m long horizontal transect, called non-destructive (ND) transect, at a water depth of 2 m. No destructive sampling occurred along the ND transect to guarantee an undisturbed ice surface melt progression throughout the sampling period. However, the first 20 m of the transect distance was not used in the data analysis to avoid artificial disturbances of the ice cover caused by the access hole and the ROV set-up procedures. To calculate spectral light transmittance, $T(\lambda)$, surface and under-ice irradiance in the UV and visible spectrum were measured simultaneously during the ROV deployment. Also, along the same transect vertical profiles to a water depth of 50 m were performed at 50, 100 and 150 m distance from the access hole. To navigate the ROV consistently along the transect beneath the fully consolidated ice cover, a clear nylon fishing line was stretched taut beneath the ice through holes at the start and end of the transect and secured using ice screws. Additionally, every 10 m of the line was marked to provide a reference distance for the recorded light data. In total, the ND transect was measured eight times over four weeks. Ice draft, h_I, was measured during each deployment via the ROV altimeter (mounted level with the radiometers) as the difference between the ROV depth (via the ROV CTD that was level with the radiometers) and its distance to the sea ice bottom (Fig. S3.1). Drilling through the sea ice cover to measure ice thickness was not performed to avoid artificial draining of the sampling area.

At a near-by site, identical under-ice horizontal transects, and vertical profiles were performed to study the spatial variability in light transmission caused by the differences in sea ice surface properties. Along these destructive (D) transects, every ROV deployment was followed by surface measurements. Surface properties such as snow depth, h_S, melt pond depth, h_{MP}, and the height of drained white ice above melt pond surface, h_{BI}, were measured with a ruler every 5 m of the D transect and after the eighth and final ROV deployment along the ND transect.. Surface albedo measurements were performed every 10 m when the ice was still snow-covered. After melt ponds had formed, albedo was measured at nine locations along the transect above varying ice surface structures. In total, seven D transects were performed throughout the sampling period with varying snow depth and melt pond coverage.

Changes in surface properties and melt pond coverage within both transect areas were also documented through aerial drone (Phantom 2 Vision+, USA) surveys 90 m above the ice surface. Drone images were used to retrieve information on variability of surface brightness as proxy for surface albedo along the vehicle track. Following the procedure described in Katlein et al. (2015a), pixel brightness was derived from the three RGB channels of the attached camera. The intensities of the R, G and B channels were divided by the maximum value of 255 to gain pixel brightness from a single image of each transect. Brightness values between 0 and 1 were used in the semi-variogram analysis of the spatial variability of surface albedo.
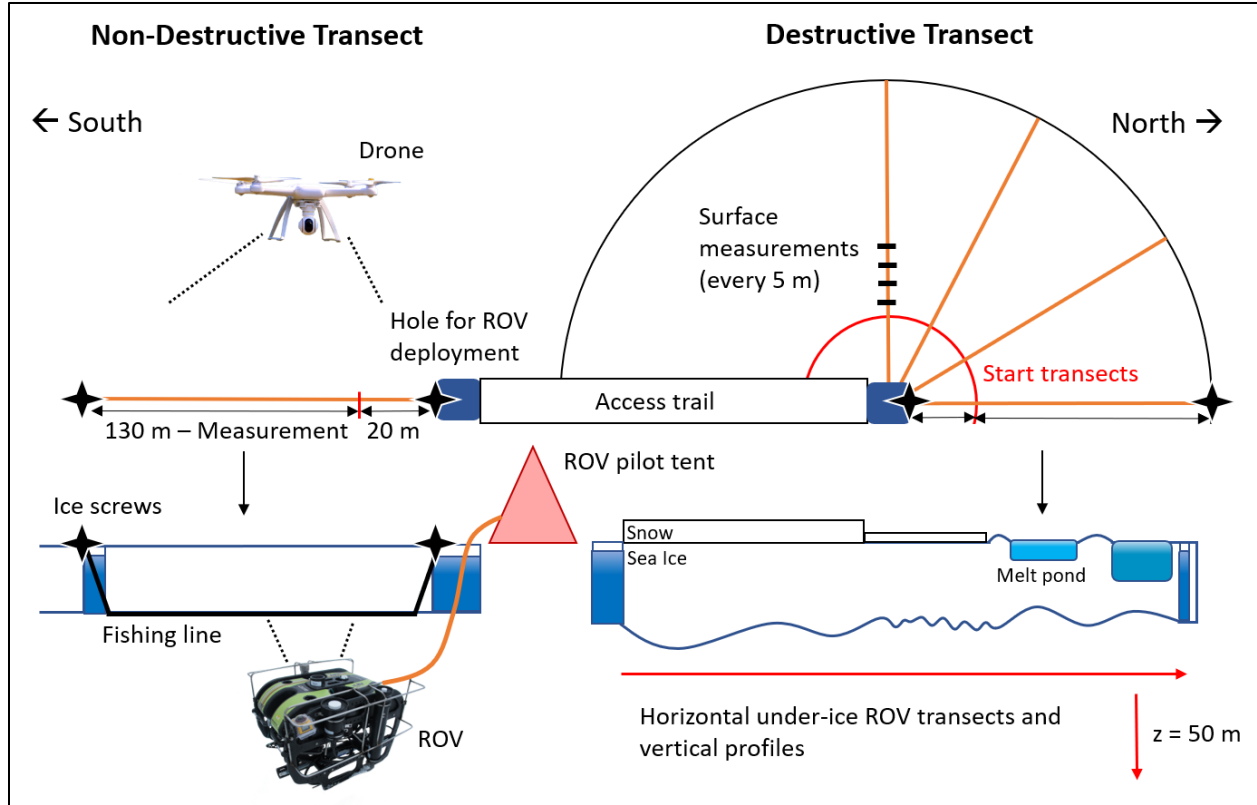
Figure 3.2: Schematic sampling set-up of under-ice ROV measurements and ice surface measurements in the two (non-destructive, destructive) transect areas.

3.2.3. Data analysis

To estimate weighted average albedo, $\overline{\alpha}_W(PAR)$, for the transect area, four replicates were measured for each surface type. Following Perovich (2005), $\overline{\alpha}_W(PAR)$ was calculated for each transect with known melt pond coverage as

$$\overline{\alpha}_W = \alpha_S A_S + \alpha_{WI} A_{WI} + \alpha_{MP} A_{MP} \tag{12}$$

where α is the albedo and A is the area fraction for snow (*S*), white ice (*WI*) and melt ponds (*MP*). Under-ice irradiance data was pre-processed with the radiometers' software ProSoft (Satlantic, USA) to perform dark corrections and immersion correction for all under-ice light measurements due to the larger refractive index of water compared to air. Recorded spectra between 320 and 700 nm were also interpolated to 1-nm steps and converted into quantum irradiance (μmol photons m^{-2} s^{-1}), which is more relevant for biological studies. Irradiance in the UVB spectrum was not interpolated due to the measurement of a single wavelength (305 nm). Based on the ROV speed, the horizontal resolution of $E_d(\lambda, 2)$ was between 1 and 2 m, while vertical profiles

of $E_d(\lambda, z)$ were calculated at 0.2-m steps from 1.6 to 50 m using linear interpolation. Spectral and PAR transmittance, $T(\lambda)$ and $T(PAR)$, respectively, as well as the diffuse vertical attenuation coefficient for downwelling irradiance, $K_d(PAR)$, were calculated as described in (Matthes et al., 2019). The vertical attenuation coefficient was calculated as the average of three vertical profiles along each horizontal transect. However, only irradiance spectra from 15 to 50 m were included to avoid the impact of variable light transmission through different surface types of the sea ice cover (Matthes et al., 2019). In order to calculate $T(PAR)$ at the ice/water interface, $K_d(PAR)$ was also used to extrapolate the transmittance data from 2 m water depth to the ice bottom following Ehn et al. (2011). Measured transmittance in the UV spectrum has not been corrected for light attenuation in the water due to irradiance values near the detection limit resulting in uncertainties in the calculation of $K_d(UVR)$. Mean transmittance, $\bar{T}(PAR, UVR)$, was calculated for each horizontal transect as the average of 164 to 1161 coincident measurements of surface and transmitted irradiance spectra. Additionally, to compare methods of calculating mean PAR transmittance of an area, length-weighted average transmittance, $\bar{T}_{LW}(PAR)$, was calculated for each D transect following Taskjelle et al. (2017)

$$\bar{T}_{LW} = \frac{L_{MP}T_{MP} + L_{WI}T_{WI}}{L_{MP} + L_{WI}} \tag{13}$$

where L_P and L_{WI} are the length of the transect covered by melt ponds or white ice, respectively, and T_P and T_{WI} are the corresponding PAR transmittances at four melt ponds and four white ice sites along the transect.

The impact of varying ice surface conditions on the aggregate scale depth was investigated by plotting change in standard deviation, SD, of the three vertical PAR profiles at each depth of the vertical profiles of each sampling day. A difference in SD below the threshold of ±1 µmol photons m^{-2} s^{-1} was chosen to identify the depth at which the under-ice light field is no longer influenced by spatial differences in light transmission through the ice cover. Repeated irradiance measurements along the ND transect and drone pictures of the same area also enabled a spatial analysis of the change in the scale of variability in surface brightness and PAR transmittance over time. Semi-variogram statistics of these two parameters provided information about the spatial distance (lag) between the first and the next measurement that is no longer correlated with the first measurement. To investigate the length scales of spatial variability the data set, a least square fit

of exponential (surface brightness) or gaussian (transmittance) theoretical variograms were used to obtain range values. The range describes the lag distance at which the model reaches 95% of the estimated semi-variance (sill) and thus measurements are spatially independent. Significant changes in the range of surface brightness, a proxy for surface albedo, and PAR transmittance were investigated using linear regression.

3.3. Results

3.3.1. Sea ice conditions

In June 2016, under-ice irradiance measurements commenced just after snow melt onset (Fig. 3.3A). Melt water became visible at the ice surface on 15 June (Fig. 3.3B), and field observations showed that the snow cover turned into large melt grain clusters. A rain event on 22 June contributed to a rapidly flooded ice surface (Fig. 3.3C). After the rain event, air temperatures decreased leading to snowfall, freezing surface water during the night and a decline in the rate of surface melt. By 27 June, large, but shallow melt ponds had formed that were separated by an elevated and drained white ice surface cover as shown for 30 June in Figure 3.3D. Increased ice surface drainage led to shrinking melt pond sizes and more prominent white ice coverage in the following days (Fig. 3.3E).
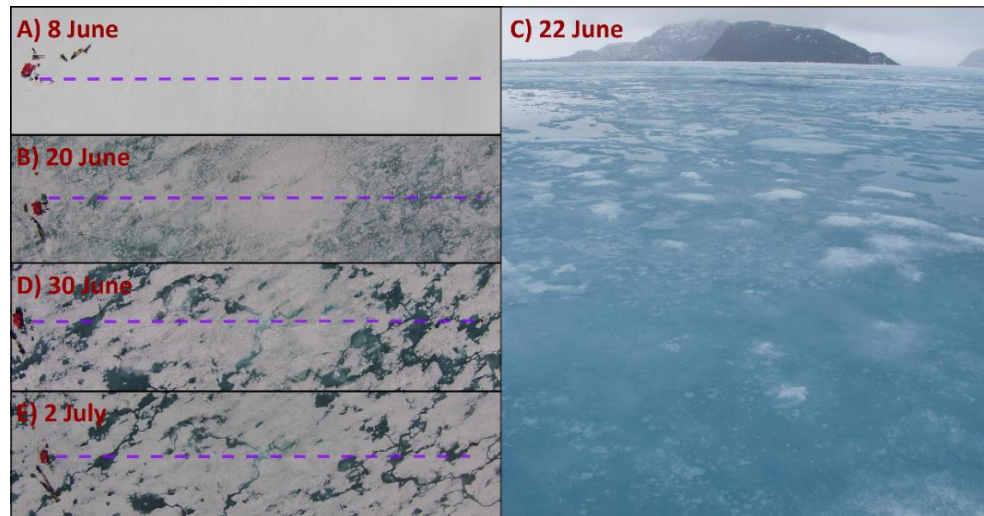
Figure 3.3: Areal images of sea ice surface conditions along the sampling transects on A) 8 June, B) 20 June, C) 22 June, D) 30 June and (E) 2 July, 2016. The ROV under-ice ND transect is indicated by the purple dashed line.

Snow depth ± standard deviation decreased from 30.1 ± 6.9 cm to 6.5 ± 3.8 cm within the first sampling week leading up to the melt pond onset on 15 June (Fig. 4A). The initial snow cover was

characterized by a high water content forming a 7.3 ± 6.1 cm thick layer of slush at its basis on 9 June. Aerial drone surveys of the D transect showed that melt pond coverage increased from 1.7% on 16 June to a maximum of 52.5% on 22 June (Fig. 3.4A). In the following days, melt pond coverage decreased gradually from 26.5% on 30 June to 16.8% on 2 July.

Ice draft decreased over the sampling period from average values of 1.47 ± 0.08 m to 1.24 ± 0.13 m along the ND transect (Fig. 3.4A). An average freeboard of 0.09 ± 0.03 m was measured at a near-by area and was within the stated standard deviation of the ice draft along the ROV transects. Temperature and salinity, measured at 2.4 m water depth and averaged for each horizontal ROV transect, shows the seasonal increase in heat content (departure from freezing temperature) and melt water content (Fig. 3.4B). Up to 13 June, measured surface water salinity and temperature remained nearly constant at 32.2 and $-1.7°C$, respectively. After melt pond onset salinity decreased to 31.7, while the difference between the freezing temperature of seawater at $-1.7°C$ and the surface water temperature at $-1.3°C$ on 2 July increased suggesting a larger energy input associated with solar radiative heating. This warming of the upper water column coincides with an alteration in sea ice bottom topography. Under-ice images taken on 6 June showed a smooth ice bottom with a brown coloration indicating the presence of ice algae and dark aggregates caught in small drainage holes (Fig. 3.4C, Video S3.1). By the beginning of July, the ice bottom appeared smoother, with larger holes and domes, and without a visible bottom coloration (Fig. 3.4D).
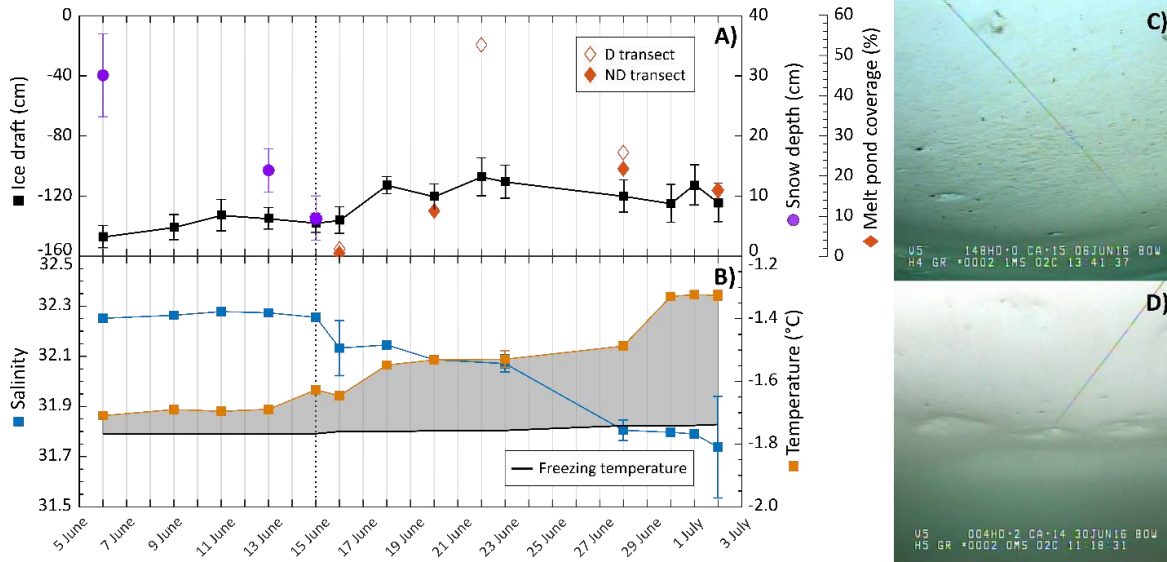
Figure 3.4: Time series of spatially averaged A) snow depth (purple circles, standard deviation error bars), ice draft (black squares), melt pond coverage (red diamonds), and averaged B) surface water salinity (blue squares), surface water temperature (orange squares) and freezing temperature of seawater for each transect at 2.4-m depth over the sampling period. Images of the ice bottom were taken at 2 m on C) 6 June and D) 30 June 2016. Melt pond coverage for the transect area is highlighted for D transects (empty diamonds) and ND transect (filled diamonds) after the melt pond onset (dotted line). The shaded area highlights the difference between water and freezing temperature.

3.3.2. PAR and UVR above and below sea ice cover

Due to clear sky conditions, incoming radiation was highest in the first half of June (Table 3.1). The second half of June was characterized by several fog events and an increasing cloud cover, which created a diffuse surface light field and reduced surface $E_d(UVA, PAR, 0)$ until the cloud cover decreased again in the beginning of July. Daily incident radiation in the UVB spectrum, $E_d(305\ nm, 0)$, reached values between $1 - 3$ mmol photons m^{-2} d^{-1} throughout the sampling period. Transmitted UVR and PAR increased with surface melt and varied along each transect (Table 3.1). This spatial variability further increased with the formation of melt ponds at the ice surface. Only at this late melt stage was a very low $E_d(305\ nm, 2)$ of 0.003 µmol photons m^{-2} s^{-1} actually measured at 2 m water depth. In the water column, diffuse vertical attenuation of PAR increased in late June, which was accompanied by an observed decrease in visibility of the guiding lines.

Table 3.1. Mean and standard deviation (SD) of incoming UVR and PAR at the sea ice surface, $E_d(0)$, and at 2 m water depth, $E_d(2)$, the daily incident UVR and PAR, and the mean vertical diffuse attenuation coefficient, $K_d(PAR)$, for four days in 2016.

		11 June	20 June	23 June	2 July
	Number of measurements	n = 306	n = 356	n = 205	n = 166
$E_d(PAR, 0)$	Mean (μmol photons m^{-2} s^{-1})	1750.0	681.2	1205.3	1268.1
	SD	111.8	15.5	29.3	53.6
	Daily (mol photons m^{-2} d^{-1})	68.6	29.3	56.5	49.9
$E_d(UVA, 0)$	Mean (μmol photons m^{-2} s^{-1})	154.8	68.3	112.1	115.1
	SD	6.0	1.0	1.7	3.0
	Daily (mol photons m^{-2} d^{-1})	6.4	3.0	5.2	4.7
$E_d(PAR, 2)$	Mean (μmol photons m^{-2} s^{-1})	29.3	108.9	241.6	202.1
	SD	10.6	50.5	99.5	100.2
$E_d(UVA, 2)$	Mean (μmol photons m^{-2} s^{-1})	2.5	11.5	26.2	21.1
	SD	1.0	5.5	10.5	10.4
$K_d(PAR)$	Mean	0.07	0.07	0.10	0.13

3.3.3. Change in light transmission with surface melt progression

Measured surface PAR albedo as well as transmittance of PAR and four wavelengths in the UV spectrum are shown over the sampling period in Figure 3.5. Concurrently with the development of melt ponds, calculated weighted $\overline{\alpha}_W(PAR)$ declined from 0.91 for snow-covered ice, to 0.58 after melt pond onset on 15 June (Fig. 3.5A). As surface melt progressed, albedo variability increased until distinct melt ponds had formed. From 22 June onward, $\overline{\alpha}_W(PAR)$ stayed relatively consistent between 0.47 and 0.53. Drone images also revealed that the prevailing landfast ice cover compromised a mosaic of smaller and larger ice floes that were frozen together (Fig. S3.2). This structural component had an impact on the color of melt ponds by creating brighter and darker ponds and thus causing a large range of melt pond albedo from 0.21 to 0.44.

Measured $T(PAR)$ and $T(UVR)$ at the ice bottom are presented as boxplots to display the variability of transmittance along the horizontal transect for each day (Fig. 3.5B,C). With the shift in surface conditions from a highly reflective snow cover to a less reflective mosaic of bare ice and melt ponds, light transmission through the ice cover increased by a factor of 30. However, a

continuous increase was only observed in the second and third week of June before mean PAR transmittance, $\bar{T}(PAR)$, levelled off to an average of 0.23 ± 0.05 (Fig. 3.5B). The observed seasonal progression of light transmittance was split into three stages defined by the state of ice surface melt and the corresponding change in the magnitude and spatial variability of light transmittance:

Stage I prior to melt pond onset on 15 June: Only 0.02 ± 0.01 of incoming PAR was transmitted through the snow-covered ice and spatial variability of light transmission did not change noticeably.

Stage II from 15 to 22 June: Once melt water became visible in large stretches at the ice surface, $\bar{T}(PAR)$ increased by an order of magnitude to 0.31 on 22 June, while under-ice irradiance became increasingly variable.

Stage III from 23 June to 2 July: A short snowfall event followed by an enhanced surface melt resulted in discrete areas of white ice and melt pond, defining stage III. PAR transmittance and its spatial variability did not increase further during this stage. In fact, $\bar{T}(PAR)$ measured along the ND transect decreased from 0.23 to 0.16.

The observed large drop in $\bar{T}(PAR)$ measured along the ND transect on 28 June was attributed to the snowfall event. Unfortunately, surface albedo was not measured that day. Repeated measurements along this transects also showed more pronounced transmittance peaks beneath melt ponds while PAR transmittance below white ice became less variable over time (Fig. S3.3). These high transmittance values of discrete surface ponds became pronounced as outliers in the boxplots after the surface flooding in stage III. The larger areas of white ice transmitting less PAR compared to ponded ice also resulted in a skewed distribution and the median to be less than the calculated mean for most of the days within stage III. On the last sampling day, the variability in measured under-ice PAR levels decreased while $\bar{T}(PAR)$ remained unchanged at 0.20. As shown in the aerial drone image of the sampling area on 2 July (Fig. 3.4E), more white ice had emerged at the surface due to ongoing drainage of melt ponds, leading to a drop in the melt pond coverage and a more uniform sea ice surface. It should be noted that the proposed stages of changes in $\bar{T}(PAR)$ are different from the stages of melt pond evolution described elsewhere (Eicken et al., 2002).

For the comparison of measured mean PAR transmittance and length-weighted average transmittance, $\overline{T}_{LW}(PAR)$ was calculated for all D transects. To do so, average $T(PAR)$ values of 0.16 to 0.24 beneath white ice and 0.25 to 0.40 beneath ponded ice, measured along four destructive transects, were used. As shown in Figure 3.5B, $\overline{T}(PAR)$ and $\overline{T}_{LW}(PAR)$ were not significantly different (t(12) = 0.005, p = 0.996) over the sampling period.
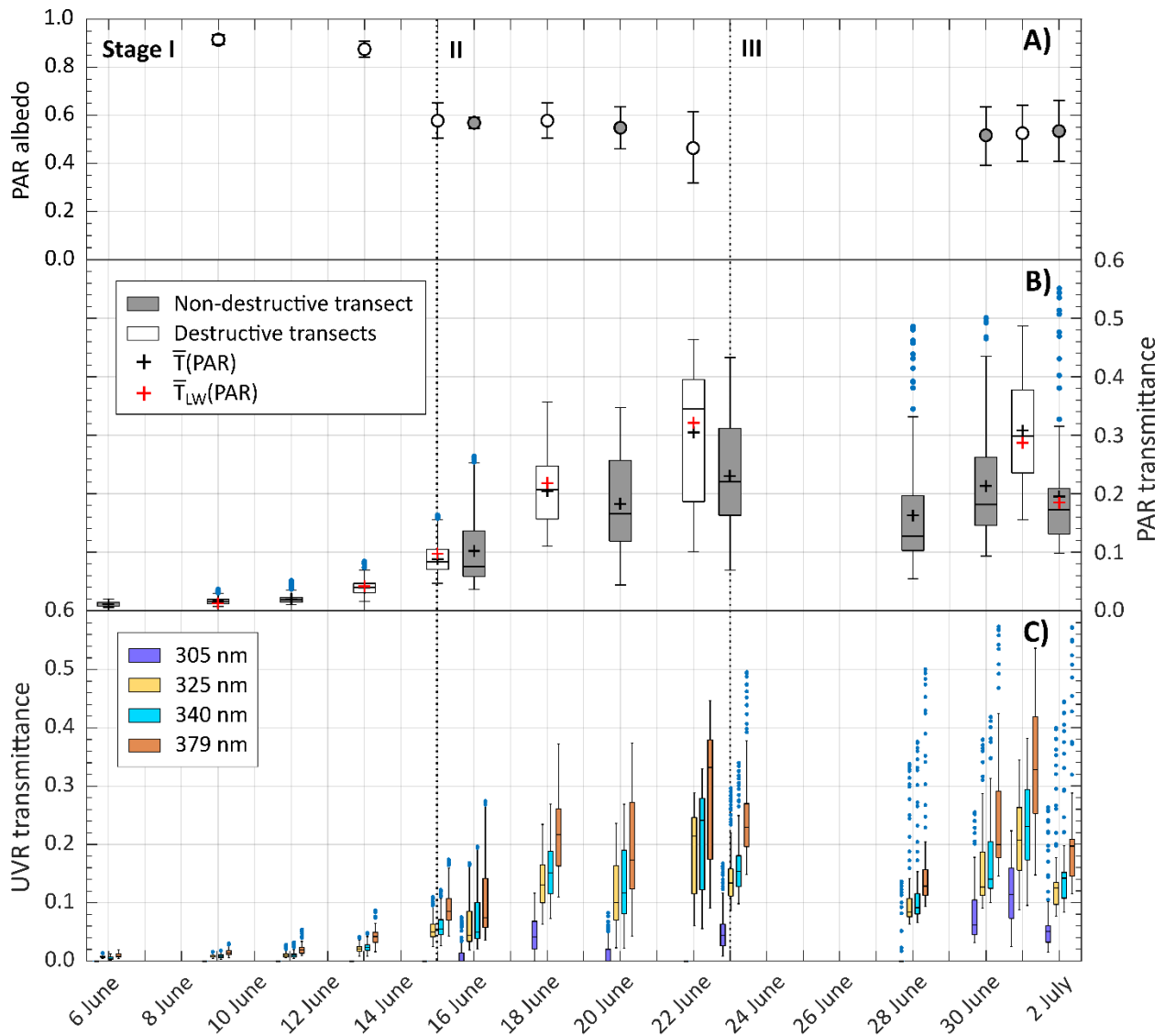
Figure 3.5: Time series of A) weighted mean PAR surface albedo, B) PAR transmittance at the sea ice bottom, and C) UVR transmittance for four wavelengths (305, 325, 340, 379 nm) at 2-m depth over the sampling period. Boxplots of PAR transmittance show median (black bar), mean (black cross), length-weighted mean (red cross) and the 25% and 75% quartiles of measurements along each D transect (grey) and the ND transect (white). Whisker length correspond to ± 2.7σ, outliers are shown as blue dots. The beginning of melt stages (I – III) is highlighted as dotted lines.

The increase in the transmission of one wavelength (305 nm) in the UVB spectrum and three wavelengths (325, 340 and 379 nm) in the UVA spectrum at 2 m is shown for all transects over the sampling period (Fig. 3.5C). Beneath snow-covered sea ice in stage I, $\bar{T}(UVA)$, ranged from 0.01 to 0.02, while UVB radiation was not detectable. It is noted that surface and transmitted irradiance were integrated over the UVA wavelength spectrum (320 – 400 nm) prior to estimating $\bar{T}(UVA)$. With melt pond onset, $\bar{T}(UVA)$ increased to 0.26 by the end of stage II on 22 June. Also, UVB radiation was detectable beneath the ice cover with a $\bar{T}(305\ nm)$ of 0.01. In stage III, transmission of UVA radiation did not increase further, displaying a mean of 0.21 ± 0.05 for D and ND transects. However, $\bar{T}(305\ nm)$ was on average greater during stage III than stage II, reaching a mean value of 0.07 ± 0.06. During stage III, UVR transmittance remained relatively consistent, while the variability in measured under-ice UVR levels decreased. Furthermore, UVR transmission through melt ponds was twice as high than through white ice. $T_{WI}(305\ nm)$ and $T_{MP}(305\ nm)$ ranged from 0.03 to 0.08 and 0.11 to 0.14, respectively. Differences in the transmission of UVA radiation through the two surface types were less pronounced with a $T_{WI}(UVA)$ and $T_{MP}(UVA)$ between 0.16 and 0.24 and 0.22 and 0.35, respectively.

To compare measured transmittance of UVR and PAR at 2-m water depth, boxplots and the spectral shape in the 400 to 700 nm range of three sampling days (11 June, 23 June, 2 July 2016), representing different ice surface types, are shown in Figure 3.6. For all presented days, $\bar{T}(PAR)$ was smaller than $\bar{T}(379\ nm)$ due to a pronounced decrease in transmittance in the 600 to 700 nm wavelength spectrum. Differences between calculated transmittance were smallest beneath snow-covered sea ice with $\bar{T}(379\ nm)$ and $\bar{T}(PAR)$ of 0.2 on 11 June. During stage I, the edges of $T(\lambda)$ were much steeper with a transmittance peak at 512 nm. With melt pond formation, $\bar{T}(379\ nm)$ exceeded $\bar{T}(PAR)$ increasingly, while the transmittance peak of the $T(\lambda)$ spectrum shifted towards the blue spectrum at 481 nm during stages II and III.
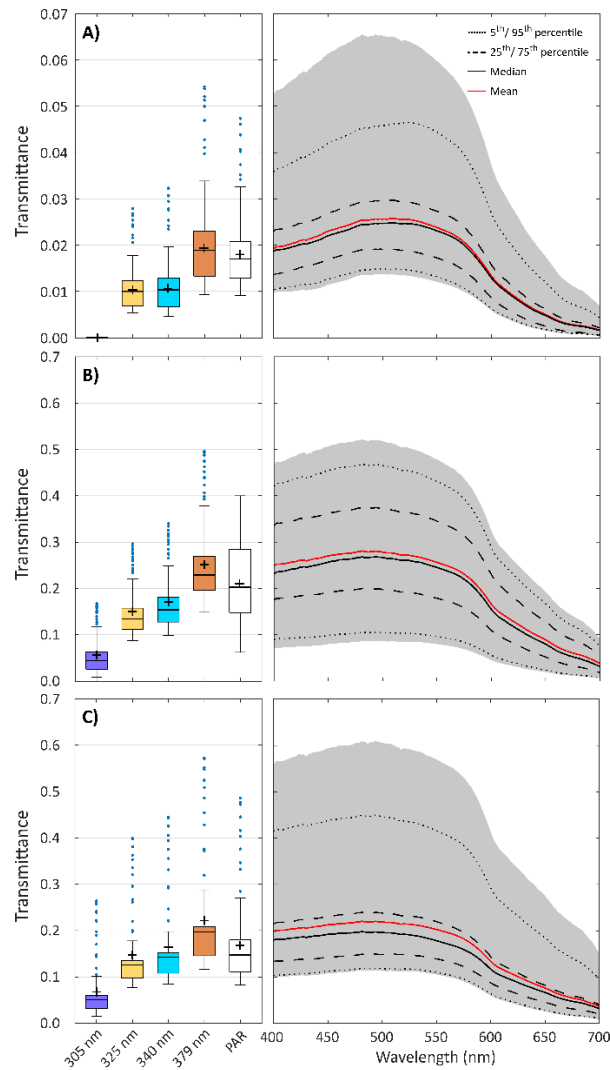
Figure 3.6: Measured transmittance of UVR (305, 325, 340, 379 nm) and PAR along ND transect at 2-m depth on A) 11 June, B) 23 June, and C) 2 July 2016. Boxplots of UVR and PAR transmittance show median (black bar), mean (cross) and the 25% and 75% quartiles of measurements along each transect. Whisker length correspond to $\pm 2.7\sigma$, outliers are shown as blue dots. Spectral irradiance in the PAR spectrum is shown for all single measurements (shaded area) along the same ND transect, and as median (black line), mean (red line), 25th/75th percentiles (dashed line) and 5th/ 95th percentile (dotted line).

3.3.4. Spatial variability of PAR propagation

The change in spatial variability of ice surface brightness, as a proxy for variability of $\alpha(PAR)$, and $T(PAR)$ at the ice bottom was investigated using semi-variances calculated for lag distances over the collected dataset (Fig. S3.4). Variograms of surface brightness were computed for eight horizontal transects of which aerial drone images were taken, while variograms of $T(PAR)$ were calculated for twelve horizontal transects (Table S3.1). The change in variogram range of variability in surface brightness did not follow any trend during the surface melt progression

55

($R^2 = 0.35$, p = 0.15). The computed mean range throughout the sampling period was 3.9 ± 1.8 m and matched well the observed length of melt ponds between 3.7 and 4.4 m along the transects. Similar to surface brightness, no temporal trend was observed in the spatial variability of $T(PAR)$ ($R^2 = 0.07$, p = 0.47). However, variability in calculated length scales of $T(PAR)$ was greater, varying between 3.9 and 7.4 m with a mean of 5.4 m.

3.3.5. Aggregate-scale depth of light transmission

During stage I, the ice surface was still characterized by a snow cover, such that only a small portion of the incident PAR was transmitted to the underlying water column (Fig. 3.6A). Vertical PAR profiles were no longer influenced by differences in surface light transmission at relatively shallow water depths between 2.0 and 13.8 m (Fig. 3.7). The influence of surface snow and melt pond distribution on the aggregate-scale depth of light transmission increased after the melt pond onset. With the occurrence of melt water at the ice surface during stage II and the formation of a more heterogenous sea ice surface during stage III, the aggregate-scale depth increased to between 14.4 and 29.0 m. This large change in depth was associated with the enhanced differences in transmittance of ponded vs. white ice. A linear regression analysis of the relationship between the aggregate scale depth and several parameters such as $\overline{\alpha}_{LW}(PAR)$, melt pond coverage (%), $\overline{T}(PAR)$ and the mean coefficient of variance, CV, of $\overline{T}(PAR)$ revealed only a significant negative trend of the aggregate-scale depth with $\overline{\alpha}_{LW}(PAR)$ ($R^2 = 0.64$, p = 0.006). This trend was mainly driven by the large decrease in surface albedo with melt pond onset between 15 and 16 June, when we observed a steep increase in aggregate-scale depth from 8.2 to 22.6 m.
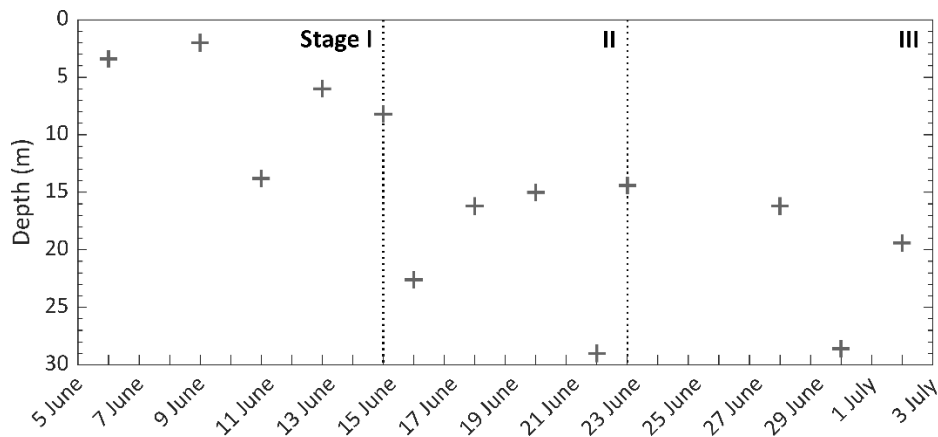
Figure 3.7: Aggregate scale depth of PAR transmission beneath landfast sea ice over the melt season. The dotted line states the beginning of each melt stage (I – III).

3.4. Discussion

3.4.1. Spatiotemporal variability of light transmission

Smooth first-year ice dominated the landfast ice study site. Our observations lacked features such as pressure ridges or leads. Variogram results revealed that the 130 m transect length was more than an order of magnitude greater than the ~4 m and ~5 m range of $\alpha(PAR)$ and $T(PAR)$ transect observations, respectively, for the typical surface features. Therefore, our spatial light transmission analysis is believed to be representative of the light available beneath landfast sea ice. Interestingly, spatial continuity in both $\alpha(PAR)$ and $T(PAR)$ did not follow any temporal trend, even though their averaged ranges matched well with surface features that developed during the melt progression. For example, the 3.9 m average range for surface reflection matched the average melt pond size, whereas the range of $T(PAR)$ was slightly larger at 5.4 m. During stage I and II, snow drifts played an important role in the scale of variability in $T(PAR)$ as ranges of spatial variability in snow distribution patterns on FYI were similar to those of $T(PAR)$ (Iacozza and Barber, 1999). During stage III, observed melt ponds were small in the sampling area, so that measured $\bar{T}(PAR)$ beneath ponds was affected by radiation propagating from the surrounding white ice patches with a mean length of 12.7 m and vice-versa (Ehn et al., 2011). Essentially, scattering by the snow and sea ice diffused the under-ice light field (Matthes et al., 2019), acting to smooth out spatial variability in light transmittance to a longer distance than that of surface melt pond size. Spatial autocorrelation analyses of PAR transmittance through mobile FYI determined even larger ranges between 7 and 30 m, which were driven by variations in the ice draft originating from ridges and refrozen leads (Katlein et al., 2015a; Lange et al., 2017). In our study, ice draft only varied by a few centimeters along the transect and thus it likely was not a significant factor in influencing the observed spatial variation in transmittance.

Overall, the variability of calculated PAR transmittance along the horizontal transects increased as discrepancy between surface characteristics (ponded vs. white ice) increased (Fig. 3.5B). To investigate the relative change in variation of PAR transmittance over time, the coefficient of variation, CV (%), as the ratio of standard deviation and mean was calculated for each transect and averaged for the three melt stages. In stage I, CV of 34 ± 3% was smallest within the sampling period, which is related to the small variability in snow depth and the overall low light levels at the ice bottom. The spatial variability increased with the ablation of snow and the exposure of

large stretches of less reflective surface melt water. This caused a 15-fold increase in $\bar{T}(PAR)$ and a mean CV of $40 \pm 11\%$ in stage II and a mean CV of $43 \pm 14\%$ in stage III. However, mean CV was not significantly different between the melt stages ($F_{2,11} = 0.876$, $p = 0.444$).

Prior to melt pond onset during stage I of the seasonal progression of light transmittance, measured snow depth and the corresponding low $\bar{T}(PAR)$ were similar to other observations on landfast and mobile FYI in the Canadian Arctic (Iacozza and Barber, 1999; Campbell et al., 2015). From the melt pond onset on 15 June, wet patches on the ice surface increased, which led to a rapid increase in $\bar{T}(PAR)$ until maximum transmittance values were reached during the largest spread of surface melt water on 22 June. Another study by Katlein et al. (2019) of the seasonal evolution of light transmission through mobile Arctic sea ice observed a similar increase of integrated $\bar{T}(320 - 900nm)$ from 0.01 through melting snow-covered ice in June to 0.25 through ponded ice in August. Katlein et al. (2019) also note that spatial variability of $\bar{T}(320 - 900nm)$ was highest after the melt pond onset. This widespread ponding in stage II due to the disappearance of snow matches as hypothesized the start of the ice ablation season described elsewhere (Eicken et al., 2002; Polashenski et al., 2012; Landy et al., 2014). In these studies, the second stage of melt pond evolution started with the complete removal of snow and an accelerated ice surface melt. Simultaneously, melt water flowed latterly towards flaws (cracks, seal breathing holes, enlarged brine drainage channels) in the ice surface while the ice was still impermeable. This led to a decrease in melt pond size and an increase in white ice patches and relates to our observed stage III of the seasonal progression of light transmittance. Also, the measured decrease in ice draft (Fig. 3.4A), the visible change in ice bottom coloration in the ROV video footage (Fig. 4C,D) and the change in shape of the transmitted PAR spectrum towards weaker attenuation at 400 and 700 nm (Fig. 3.6) indicated a sloughing of bottom ice algae during stage I and II, which contributed to the increase in light transmission. To calculate the increase in $\bar{T}(PAR)$ through this process, $E_d(PAR)$ above the ice algae layer was calculated for 15 June 2016. Following Ehn and Mundy (2013), a $K_d(PAR)$ of 10.45 m^{-1} was used for the ice algae layer of 3 cm that corresponds to the given chlorophyll *a* concentration (Chl *a*) extracted from Oziel et al. (2019). Applying Beer-Lambert's law, the loss of the ice algal layer caused an increase of 0.02 in $\bar{T}(PAR)$, which corresponds to a 34 % increase relative to $\bar{T}(PAR)$ values during stage I, but much less relative to that of stages II and III. The increase in $\bar{T}(PAR)$ of 0.2 due to snow melt was an order of magnitude

higher. Thus, changes in the snow cover played a more important role in spatiotemporal variability of light transmission to the ice bottom compared to differences in ice algal biomass. Following the increased transmittance through the ice cover in stage II after melt pond onset was an observed rise in under-ice surface water temperature by ~0.2°C (Fig. 3.4B). A rapid temperature rise by ~0.2°C was again observed in stage III concurrent with a rapid increase in phytoplankton biomass (Fig. 3.8).

The rapid change in ice surface conditions and the resulting spatial and temporal variations in PAR transmittance through the sea ice underline the importance of continuous irradiance measurements throughout the melt season for the purpose of estimating light availability for under-ice primary production. Area-averaged PAR transmittance values account for increasing spatial variability during sea ice melt progression as also discussed in Massicotte et al. (2019), who investigated the relative error in primary production estimates when averaging a certain number of single-point under-ice light measurements at random locations. The relative error was observed to drop below 10% at 99 under-ice ROV light measurements (Table 3 in Massicotte et al. (2019). However, large scale measurements by autonomous or remotely operated vehicles are expensive and logistically challenging to deploy. Hence, length-weighted mean transmittance, $\bar{T}_{LW}(PAR)$, calculated from measurements beneath melt ponds and white ice combined with aerial surveys by more affordable drones (UAVs) has shown to provide an alternative (Ehn et al., 2011; Taskjelle et al., 2017). Chosen melt ponds and white ice areas for under-ice irradiance measurements should be also sufficiently large to avoid the influence of near-by surface types on the footprint of the deployed radiometer. Following equation (1) in Nicolaus et al. (2010) we calculated the irradiance sensor bottom-ice footprint size that should encapsulate 95% of incoming light measured at the sensor. We obtained a footprint range of 1 to 2 m for the corresponding range in sensor distance from the ice bottom of 0.4 to 0.8 m, as determined from the ROV-mounted altimeter. It is noted that this footprint size is likely a maximum as the equation assumes an isotropic light field, whereas Matthes et al. (2019) concluded that the under-ice light field is downward directed with a corresponding downwelling average cosine of 0.7. Regardless, with the size of melt pond and white ice patches ranging from 3.7 to 4.4 m and 7.4 to 18.0 m in our study, respectively, our ROV transmittance measurements at the center of these surface patches should not be significantly influenced by stray light from pond/ice edges. In conclusion, a lack of statistical difference between our estimates of $\bar{T}_{LW}(PAR)$ and $\bar{T}(PAR)$ confirm the applicability of this UAV technique for future studies

requiring characterization of spatial variability in light transmission estimates through smooth first-year sea ice. Satellite-derived melt pond fraction (Rösel and Kaleschke, 2011; Zege et al., 2015) and surface albedo (Scharien et al., 2007) from optical sensors would allow even further upscaling throughout the summer melt. Although, an application on mobile pack ice would need to include a quantitative assessment of ridges and refrozen leads to account for large variations in ice draft.

3.4.2. Impact of sea ice surface melt on aggregate-scale depth

PAR availability in the upper, ice-covered water column can be estimated from incoming irradiance at the ice surface, the presented mean transmittance and the diffuse vertical attenuation coefficient, $K_d(PAR)$. However, recorded vertical irradiance profiles to derive K_d are greatly influenced within the first meters by the previously discussed differences in light transmittance through the melting snow and ice cover (Frey et al., 2011; Massicotte et al., 2018; Matthes et al., 2019). Our results showed a deepening of the aggregate-scale depth with the formation of melt ponds. During stage I, a snow layer covered the landfast sea ice, causing light transmission to be more diffuse (Matthes et al., 2019) and small variations in the range of transmitted irradiance to the ice-water interface. The resultant mean depth at which spatial irradiance levels were no longer affected by surface variability was 7 ± 4 m. After the formation of melt pond in stage II, spatial heterogeneity of $\bar{T}(PAR)$ and thus the mean aggregate-scale depth increased to 20 ± 6 m. Our observations were in the same range of those reported elsewhere that fall between 5 and 15 m beneath melt pond-covered ice (Frey et al., 2011; Katlein et al., 2015a; Matthes et al., 2019).

A correlation between the change in the aggregate-scale depth and sea ice surface properties as well as PAR transmittance was not identified. However, once an under-ice phytoplankton bloom develops, the scattering by phytoplankton may increase the diffusion of the heterogenous transmitted light and, hence, decrease the aggregate-scale depth. This was not observed during our study. In the sampling area, depth-integrated total chlorophyll *a* (TChl *a*, the sum of chlorophyll *a*, divinyl-chlorophyll *a* and chlorophyllide *a*) concentration reached 77 mg m^{-2} on 1 July over the 100-m water column (Massicotte et al., 2020). This was much less than other observations of under-ice blooms with depth-integrated Tchl *a* concentrations ranging from 450 to 1292 mg m^{-2} (Fortier et al., 2002; Arrigo et al., 2014; Mundy et al., 2014). Arrigo et al. (2014) showed a 3.5-fold increase in light absorption and a 5-fold increase in scattering that was mainly attributable to

phytoplankton cells (78%). Scattering by phytoplankton cells has also shown to decrease the degree of anisotropy of the downwelling under-ice radiation field in a radiative transfer model (Pavlov et al., 2017).

3.4.3. Seasonal increase in UVR transmission

Radiation in the UV spectrum can inhibit the photosynthetic capacity of phytoplankton (Villafañe et al., 2004) and ice algal communities (McMinn et al., 2005). Previous optical measurements beneath Arctic landfast sea ice recorded a transmittance of 0.01 – 0.02 through bare ice and 0.19 through ponded ice in the UVA (350 – 360 nm) spectral range (Elliott et al., 2015). During our investigation, we showed that UVR transmittance increased significantly with surface melt progression, reaching levels equal to PAR transmittance with $\bar{T}(UVA)$ of 0.19 beneath white ice and 0.30 beneath ponded ice by the end of June. Particularly after melt pond formation, $\bar{T}(379\,nm)$ exceeded $\bar{T}(PAR)$ because the latter is impacted by the high absorption coefficient in the red part of the visible spectrum. However, transmittance at shorter UV wavelengths remained less than $\bar{T}(PAR)$. Laboratory experiments by Perovich and Govoni (1991) demonstrated an increase in the absorption coefficient of snow and ice with decreasing wavelength within the spectrum of 250 to 400 nm, explaining the observed absence of UVB radiation during the early melt stage. However, after melt pond onset, $\bar{T}(305\,nm)$ increased to 0.05 through white ice and 0.11 through ponded ice.

Overall, $\bar{T}(UVR)$ was much larger than previously reported values obtained beneath landfast sea ice in Antarctica (Trodahl and Buckley, 1990) and from radiative transfer modelling for mobile Arctic FYI (Perovich, 2006). This greater transmission highlights the potential ecological significance of UVR transmission measurements during melt season when the spring phytoplankton bloom commences underneath sea ice. Algae in melt pond and in the ice as well as phytoplankton can synthesize mycosporine-like amino acids (MAAs) that act as UV-absorbing sun protection (Uusikivi et al., 2010; Ha et al., 2012; Elliott et al., 2015; Piiparinen et al., 2015). In particular, the study by Elliott et al. (2015) showed a modulation of the MAA concentration of an under-ice phytoplankton bloom with prevailing light conditions and stage of surface melt. Our results show that a significant portion of incoming UVA irradiance, up to 26 µmol photons m^{-2} s^{-1}, was transmitted during the spring melt when an under-ice bloom commenced beneath the ice cover. Incubation experiments of temperate phytoplankton assemblies in winter with radiation

regimes of UVR and PAR or PAR only have shown an enhanced carbon fixation rate at UVR levels <65 µmol photons m^{-2} s^{-1} and significantly lower fixation rates at higher UVR levels (Barbieri et al., 2002). The authors also concluded that the taxonomic composition and light history of the phytoplankton community plays an important role in the sensitivity of algal cells to UVR. More research is therefore needed on the acclimation and photoprotection of under-ice phytoplankton communities to know if our UVA levels < 26 µmol photons m^{-2} s^{-1} have an impact on the algal communities.

3.4.4. Implications of spatial heterogeneity on nutrient availability for under-ice phytoplankton blooms

Several studies have identified the increase in PAR availability and water column stratification associated with melt pond onset as the trigger for under-ice phytoplankton blooms (Arrigo et al., 2014; Mundy et al., 2014; Hill et al., 2018; Oziel et al., 2019). However, the relationship between the sudden change in ice surface properties, the increase in the spatial heterogeneity of PAR transmittance, and the onset of algal growth during the spring melt are still not well understood. Figure 3.8 provides an overview of the measured increase in TChl a concentration in the water column (Massicotte et al., 2020) at the ice camp site and the depth of the isolume, $z_{0.415}$, where integrated PAR$_{24h}$(z) = 0.415 mol photons m^{-2} d^{-1}, a threshold used for positive net growth (Boss and Behrenfeld, 2010). The $z_{0.415}$ was extracted from Oziel et al. (2019), and estimated from $\bar{T}(PAR)$ from our study using the same daily incident PAR data and $K_d(PAR)$. It is important to note that irradiance measurements presented in Oziel et al. (2019) were taken beneath snow-covered and later white ice at the same location throughout the entire sampling period. At this site, $T(PAR)$ increased from 0.01 to 0.09 between 6 June and 1 July, 2016. However, our ROV measurements determined $\bar{T}(PAR)$ ranged from 0.01 to 0.31 over the same period (Fig. 3.5B).

As Figure 3.8 indicates, the initiation of the observed under-ice bloom was directly related to switches in the surface melt stage. During stage I, TChl a concentration accumulated slowly although the $z_{0.415}$ deepened from 5 m to 46 m with the exponential increase over time in PAR transmission (Fig. 3.5B). Only after the switch to stage II, TChl a accumulation accelerated within the mixed surface water layer to a depth of 25 m (Oziel et al., 2019). The $z_{0.415}$ calculated from $\bar{T}(PAR)$ reached a greater maximum depth of 50 m compared to a maximum $z_{0.415}$ of 31 m obtained from the white ice point. To further account for the shape of the under-ice light field,

under-ice planar irradiance gained from $E_d(PAR, 0)$ and $\bar{T}(PAR)$ was converted to scalar irradiance by using an inverse average cosine of 1.4 (Matthes et al., 2019). Results show an even deeper maximum $z_{0.415}$ of 55 m on 18 June. These differences in calculating $z_{0.415}$ have large implications on the interpretation of nutrient availability for under-ice phytoplankton growth. A deeper $z_{0.415}$ indicates that phytoplankton had access to a much larger nutrient pool than in the previous estimate. Indeed, Oziel et al. (2019) observed an increased nutrient drawdown at 40 m on 23 June, which also matches well with the second inflection point in TChl a accumulation in the beginning of stage III. In the end of stage II, the $z_{0.415}$ shoaled due to the increased light attenuation by the phytoplankton accumulation and remained relatively constant in stage III. By the end of the sampling period, phytoplankton TChl a concentration levelled off at the maximum observed values of 77 mg m^{-2}, likely as a result of the increased light attenuation by the algal cells and depleted nutrients concentrations in the surface water layer during the melt pond period (Oziel et al., 2019).
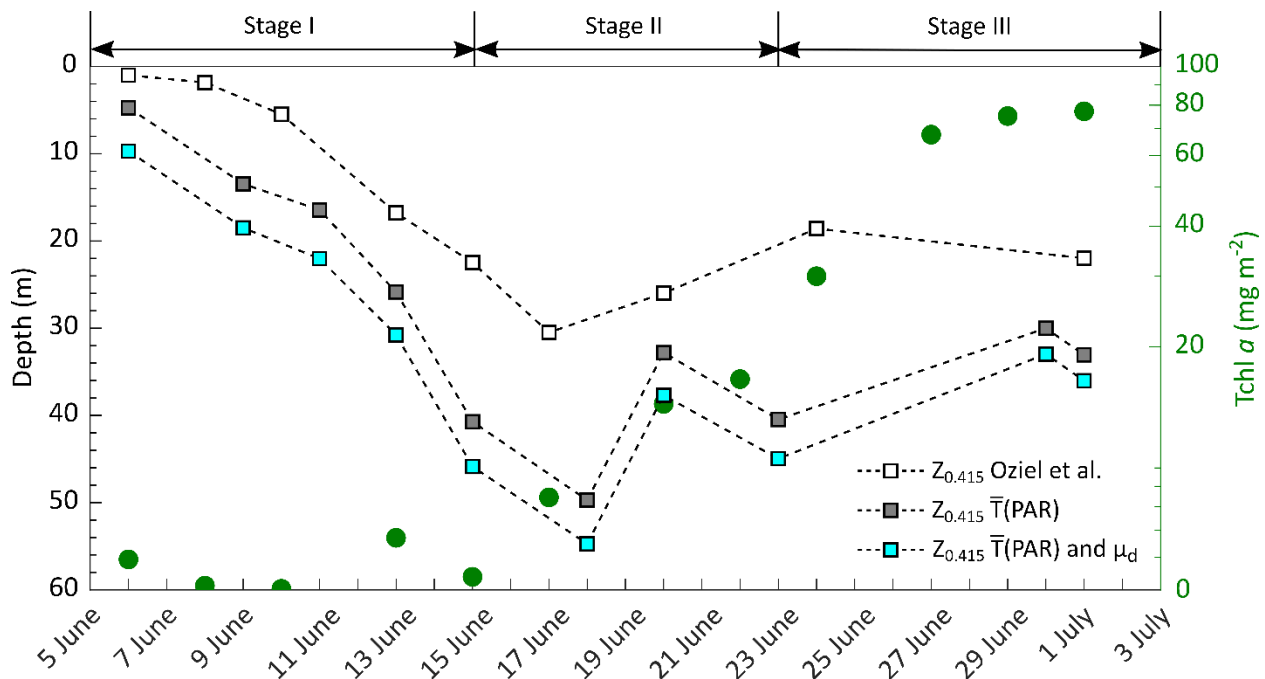
Figure 3.8: Change in total chlorophyll a (TChl a) concentration (green circles) integrated over 100-m water column (Massicotte et al., 2020), and in isolume depth ($z_{0.415}$), extracted from Oziel et al. (2019, white squares), as well as calculated from mean PAR transmittance ($\bar{T}(PAR)$, grey squares) and calculated from $\bar{T}(PAR)$ and scalar irradiance using an inverse average cosine (μ_d) of 1.4 (blue squares) for each melt stage (I – III) at the ice camp site.

3.5. Summary and conclusions

In this study, we characterized the seasonal spring progression of the transmission of UVR and PAR, and their spatial variability, in a large landfast sea ice area in southwest Baffin Bay (near the community of Qikiqtarjuaq, Nunavut) throughout the melt season in 2016. Understanding the magnitude of sunlight transmitted through the melting sea ice is of key importance to improve our understanding of the spring phytoplankton bloom. Our objectives were achieved through combined measurements of horizontal transects and vertical profiles of under-ice irradiance using a ROV, and manual and drone-based surveys of ice surface properties. This data set confirms our hypothesis of a close link between the temporal increase in under-ice PAR and UVR levels and the stages of melt pond evolution while the spatial heterogeneity of PAR and UVR transmission remained unchanged after the melt pond onset. The main findings are summarized in points $1 - 4$ below:

1. Our study area was composed of smooth landfast sea ice. Variogram results revealed that the 130 m length of our ROV transects were more than an order of magnitude greater than the $4 - 5$ m length scale of $\alpha(PAR)$ and $T(PAR)$ transect observations for typical surface types. This indicates that our spatial light transmission measurements and statistics were representative of the light available beneath the larger landfast sea ice area.

2. With melt pond formation, spatially averaged PAR transmittance increased from 0.02 to 0.31, while variations in measured under-ice PAR levels increased to up to 43%. This exposed drifting phytoplankton cells to a wide range of light conditions and highlights the importance to accurately capture spatial heterogeneity in light transmission.

3. Melt pond onset on 15 June resulted in a steep increase in aggregate scale depth for under-ice PAR levels from 7 ± 4 to 20 ± 6 m (Fig. 3.7). PAR profiles were found to be affected by surface variability to depths of 2.0 – 13.8 m during stage I prior to melt pond onset, and to depths of 14.4 – 29.0 m during stages II – III when melt water was visible present on the surface.

4. With progressing surface melt, $\bar{T}(379\,nm)$ exceeded $\bar{T}(PAR)$ due to the high absorption coefficient in the red part of the visible spectrum. Transmittance at shorter UV wavelengths remained less than $\bar{T}(PAR)$. However, after melt pond onset, $\bar{T}(305\,nm)$ increased to 0.05 through white ice and 0.11 through ponded ice.

Monitoring the increasing spatial variability in transmitted light levels even under smooth, melting landfast sea ice pose challenges in this rapidly changing environment. However, continuous observations on the spatial and temporal progression of transmitted spectral irradiance in relation to the changing quantities of snow, ice and melt ponds has proven to better explain the link between the deepening of the euphotic zone accompanied by an increased nutrient accessibility and the observed increase in the TChl *a* concentration in this area.

Supplemental material
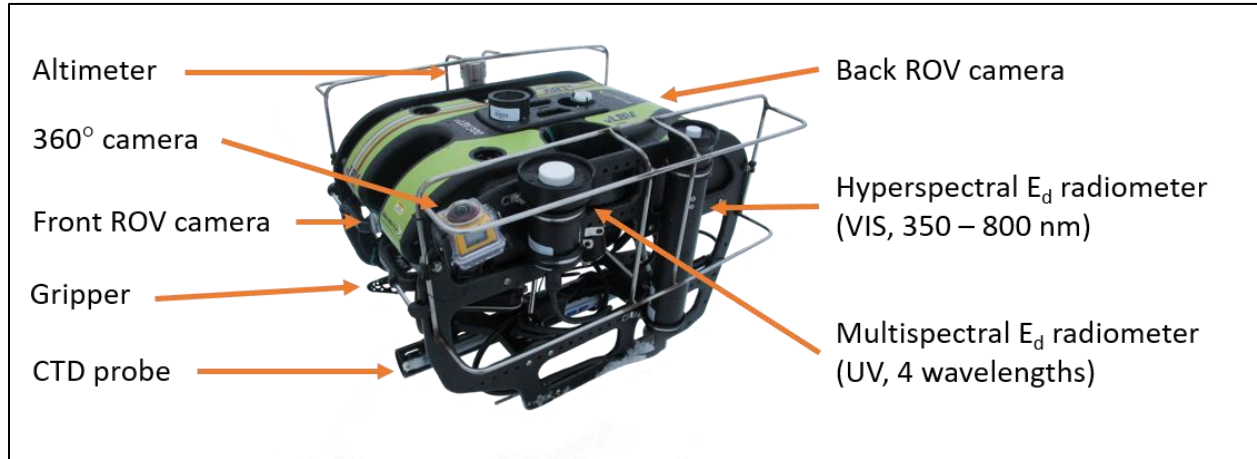
Figure S3.9: Photograph of ROV equipped with sensors, cameras and a gripper for under-ice measurements.
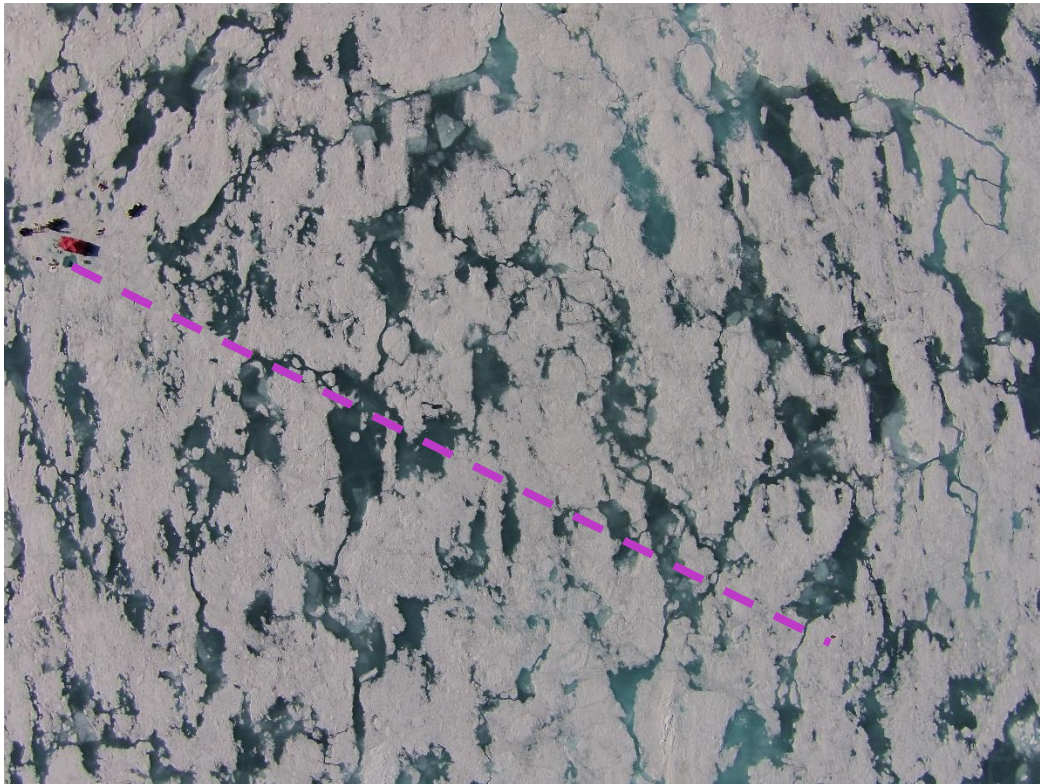
Figure S3.10: Areal drone image of sampling area taken at 90 m height on 30 June 2016. The surveyed D transect is shown as purple line.
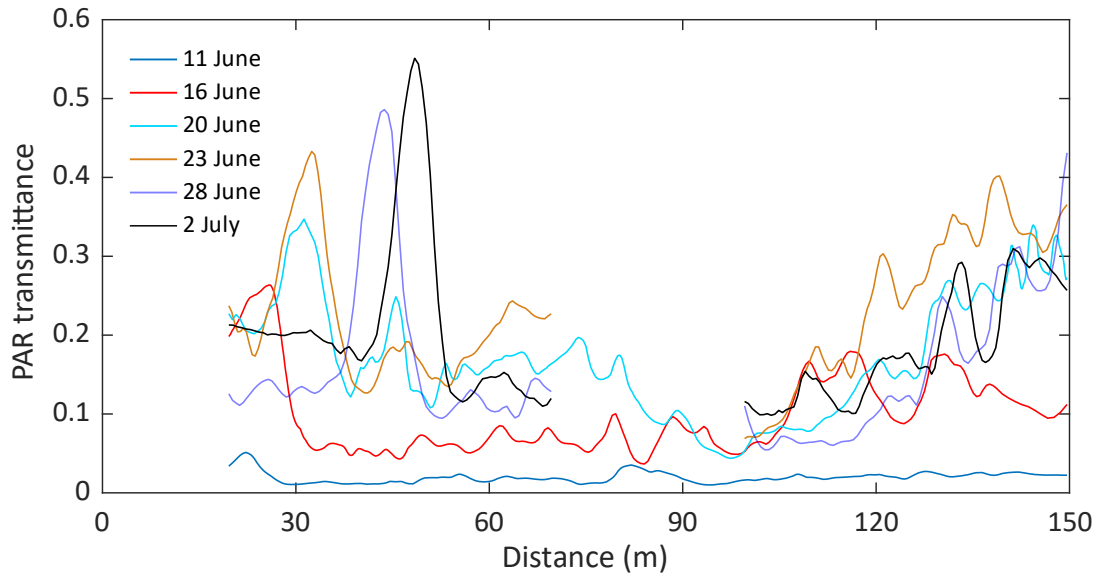
Figure S3.11: PAR transmittance calculated along the ND transect for five days over the sampling period.
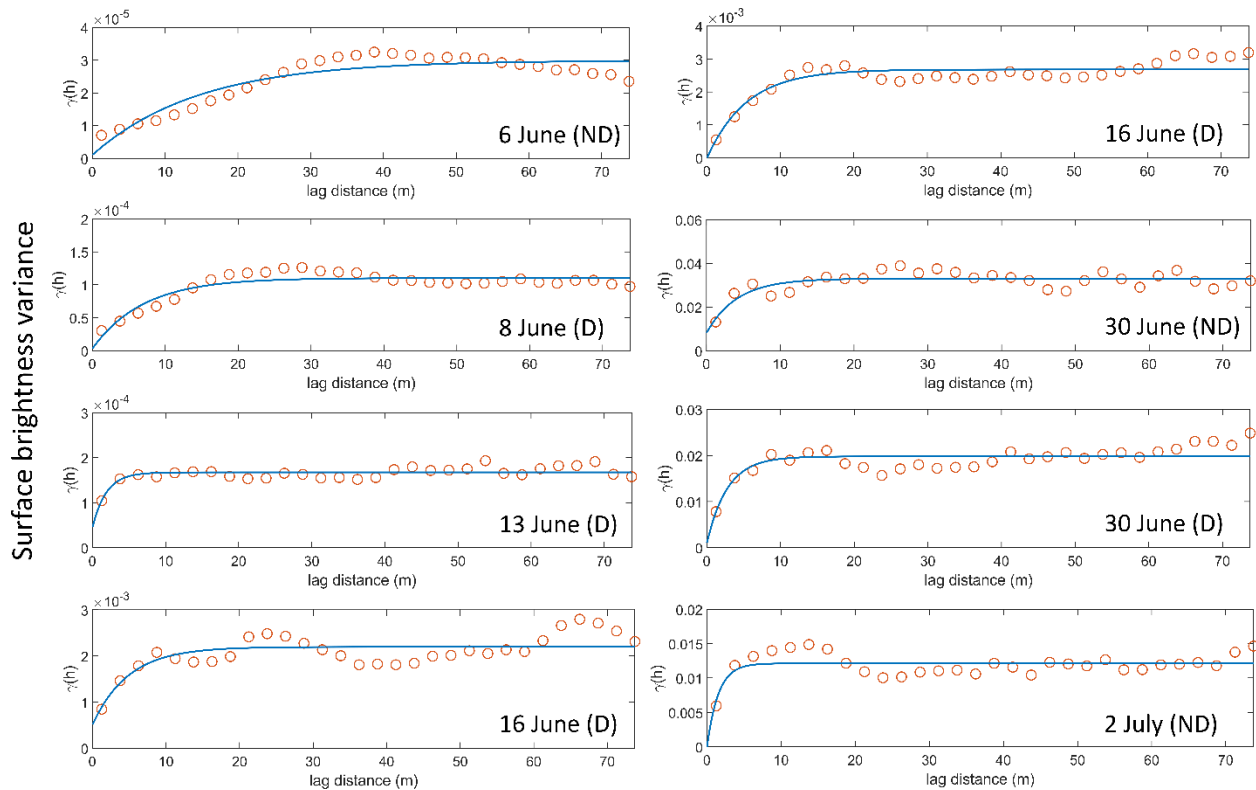
Figure S3.12: Variograms of surface brightness obtained from horizontal transects. Empirical variograms are shown as orange dots and fitted theoretical exponential variograms are shown as black lines.
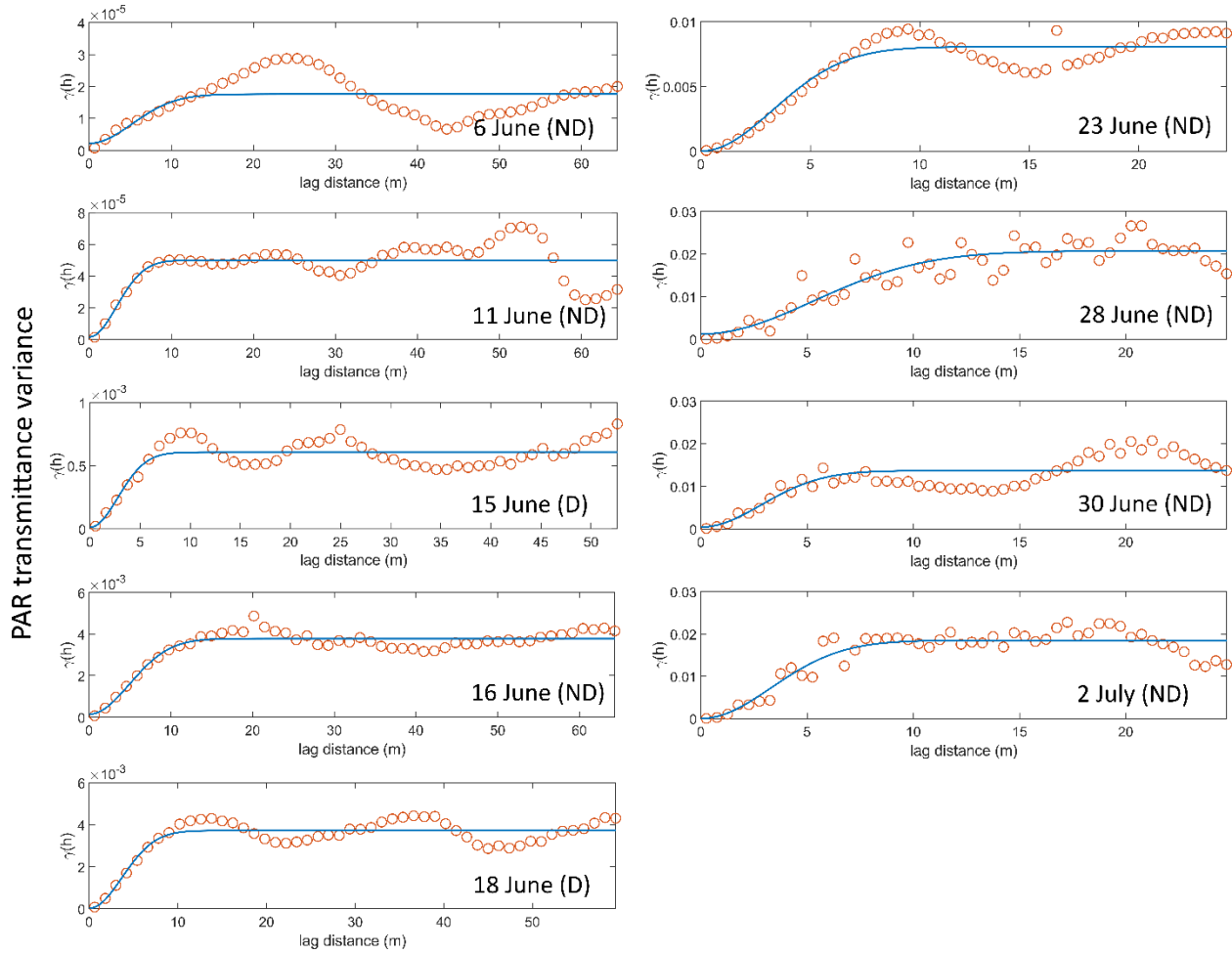
Figure S3.13: Variograms of PAR transmittance obtained from horizontal transects. Empirical variograms are shown as orange dots and fitted theoretical gaussian variograms are shown as black lines.

Table S3.2: Computed mean variogram range (m) of surface reflectance and PAR transmittance of the observed melt stages (I - III).

	Variogram range (m)	
	Surface brightness	PAR transmittance
Stage I	4.4	6.0
	n = 2	n = 2
Stage II	5.1	5.3
	n = 2	n = 3
Stage III	2.8	5.2
	n = 3	n = 4

Video S3.1. Video of ice bottom recorded at 2 m with a 360 degree action camera along horizontal D transect on 13 June.

4. Chapter – Average cosine coefficient and spectral distribution of the light field under sea ice: Implications for primary production

Abstract

The Arctic spring phytoplankton bloom has been reported to commence under a melting sea ice cover as transmission of photosynthetically active radiation (PAR; 400 – 700 nm) suddenly increases with the formation of surface melt ponds. Spatial variability in ice surface characteristics, i.e., snow thickness or melt pond distributions, and subsequent impact on transmitted PAR makes estimating light-limited primary production difficult during this time of year. Added to this difficulty is the interpretation of data from various sensor types, including hyperspectral, multispectral, and PAR-band irradiance sensors, with either cosine-corrected (planar) or spherical (scalar) sensor heads. To quantify the impact of the heterogeneous radiation field under sea ice, spectral irradiance profiles were collected beneath landfast sea ice during the Green Edge ice-camp campaigns in May–June 2015 and June–July 2016. Differences between PAR measurements are described using the downwelling average cosine, μ_d, a measure of the degree of anisotropy of the downwelling underwater radiation field, which, in practice, can be used to convert between downwelling scalar, E_{0d}, and planar, E_d, irradiance. A significantly smaller μ_d(PAR) was measured prior to snow melt compared to after (0.6 vs. 0.7) when melt ponds covered the ice surface. The impact of the average cosine on primary production estimates, shown in the calculation of depth-integrated daily production, was 16% larger under light-limiting conditions when E_{0d} was used instead of E_d. Under light-saturating conditions, daily production was only 3% larger. Conversion of underwater irradiance data also plays a role in the ratio of total quanta to total energy (E_Q/E_W,

found to be 4.25), which reflects the spectral shape of the under-ice light field. We use these observations to provide factors for converting irradiance measurements between irradiance detector types and units as a function of surface type and depth under sea ice, towards improving primary production estimates.

4.1. Introduction

Optical studies of the past decade have demonstrated that the inhomogeneous sea ice cover at different stages of melt causes a large spatial variability in the transmission of solar radiation to the underlying Arctic Ocean (e.g. Light et al., 2008; Ehn et al., 2011; Nicolaus et al., 2012; Katlein et al., 2015a). The majority of transmitted light remaining under the sea ice is within the 400 – 700 nm spectral band termed photosynthetically active radiation (PAR) with shorter and longer wavelengths strongly attenuated within the overlying snow and ice cover. Snow depth primarily controls the amount of PAR transmitted to the water column (Nicolaus and Katlein, 2013). In the late spring, lower surface albedos of melting snow, developing melt ponds and white ice areas increase total under-ice PAR levels and drive primary production beneath the ice cover (Arrigo et al., 2014; Mundy et al., 2014). Simultaneously, enhanced differences in transmittance due to variation in surface type create a more complex radiation field beneath the ice cover, which is displayed in the diffuse vertical attenuation coefficient, K_d, and average cosine coefficient, μ_d, of downwelling irradiance in the water column. Frey et al. (2011) observed subsurface transmission peaks under white ice at 5 – 10 m water depth due to an order of magnitude larger light transmission through adjacent melt pond-covered ice. The lateral spreading of radiation also impacts the vertical diffuse attenuation coefficient, K, due to changes to the angular distribution of the under-ice radiation field (Ehn et al., 2011; Katlein et al., 2016; Massicotte et al., 2018). Experiments to determine underwater irradiance distributions have been undertaken by Voss (1989), Berwald et al. (1995) and Leppäranta et al. (2003); however, they have not been examined in detail for ice-covered conditions, where the ice cover plays an important role in the measurements of light availability for primary production estimates, as algal cells indiscriminately absorb light from any direction. Bio-optical models of primary production in the open ocean showed an underestimation of phytoplankton growth by 5 – 13%, if the shape of the underwater light field is ignored and only downwelling planar irradiance is measured (Sathyendranath et al., 1989). Furthermore, a recent ice-ocean radiative transfer modelling study highlighted that scalar

irradiance could be up to 1.85 times greater than downwelling planar irradiance immediately beneath the ice cover (Pavlov et al., 2017).

The average cosine for downwelling irradiance, μ_d, provides a tool to describe the angular distribution of the underwater radiation field (0.5 being isotropic, and 1.0 fully downward directed) and to relate spatial variability of the radiation field to the propagation of radiation in the atmosphere-ice-ocean system. This propagation generally follows an exponential decline with increasing depth from the water surface and can be modelled as a function of scattering and absorption processes (Kirk, 1981; Bannister, 1992; Mobley, 1994; Berwald, 1999). However, the high scattering of radiation while propagating through the sea ice causes the angular distribution of light penetrating the water column to be different from the open water scenario, which is largely controlled by the solar zenith angle (Kirk, 2011). Several studies have assumed that μ_d values beneath the ice cover are similar to those in open water at greater depths (Arrigo et al., 1991; Ehn and Mundy, 2013; Katlein et al., 2014), while others have assumed an isotropic light field (e.g. Frey et al., 2011). The lateral spreading of radiation caused by large-scale sea ice features, such as melt ponds, cracks and leads, is also expected to have an impact on μ_d, underlining the need for an improved understanding of the angular shape of vertical radiative transfer.

Direct observations of the average cosine may also help to classify the impact of the heterogeneous under-ice light field on irradiance readings obtained by different radiometer types. Measurements of photosynthetically active radiation (PAR) for primary production estimates are commonly performed with either scalar or cosine-corrected planar radiometers, although an underestimation of the prevailing light availability is known to occur with the latter (Morel and Gentili, 2004). Although scalar radiometers with a spherical collector that capture PAR from all directions provide a more realistic measurement for primary production, planar irradiance sensors are commonly used. Planar irradiance can be converted into scalar irradiance using the average cosine; however, more knowledge regarding changes to μ_d beneath a sea ice cover is needed. To study alterations of μ_d in the ice-covered water column, simultaneous measurements with both sensor types must be performed at several depth levels.

With increasing primary production over the period of ice melt, differences in light attenuation also alter the spectral composition of the radiant flux within the under-ice water column (Pavlov

et al., 2017). Algal cells, detritus, dissolved organic matter and water itself absorb irradiance at specific wavelengths, which makes spectral irradiance measurements necessary to calculate PAR accurately. Differences in the spectral absorption also have an effect on the conversion of irradiance units (Morel and Smith, 1974). For primary production estimates, PAR data are given in quantum units (μmol photons m^{-2} s^{-1}) instead of energy units (W m^{-2}) because photosynthesis is a photochemical process that depends on the number of photons absorbed rather than their energy content. Sensors for measuring the broad-band PAR quantum flux that can accommodate changes in the spectral shape of the underwater light field are available. However, ice mass balance buoys to measure the bio-optical properties of the surface water layer are equipped with shortwave radiation sensors. These frequently used sensors operate in energy units and need to be converted to quantum units for primary production studies.

Recognizing the need for an improved characterization of the under-ice light field, a dataset of spectral irradiance profiles beneath landfast sea ice was collected during the Green Edge ice-camp campaigns in May–June 2015 and June–July 2016. The objectives of this study were to: (1) describe the impact of the sea ice cover on coefficients to describe the spectral distribution of downwelling irradiance in the water column, particularly the downwelling average cosine, with increasing depth and over the course of spring melt; (2) quantify how changes in these coefficients affect under-ice PAR readings taken with a cosine planar versus a spherical scalar radiometer and stated in energy units versus quanta units; and (3) investigate the impact of different irradiance detector types on primary production estimates. Variations in the diffuse attenuation and average cosine of downwelling PAR are presented over the course of spring melt and related to a potential error that different measurements could have on primary production estimates.

4.2. Methods

4.2.1. Study area

Spectral irradiance measurements were conducted as part of the Green Edge project in 2015 and 2016 on landfast sea ice (67° 28.784' N, 63° 47.372' W) near Qikiqtarjuaq, Nunavut, Baffin Bay (Figure 4.1A). From 5 May to 8 June 2015, surface irradiance and under-ice spectral irradiance were measured prior to melt onset, under different snow depths and mostly overcast sky. The solar zenith angle ranged from 54° to 80° with a mean angle of 61°. In 2016, measurements began after

snow melt onset, and spectral irradiance data were collected beneath sea ice covered with wet snow, shallow melt ponds and white ice between 14 June and 4 July. Sky conditions were characterized as cloudy with sunny intervals to fully overcast, long periods of fog and a solar zenith angle ranging from 45° to 73° with a mean angle of 59°. All measurements were performed around the ice camp in areas with undisturbed surfaces. Snow depth, h_S, melt pond depth, h_{MP}, the height of drained white ice above melt pond surface, h_{BI}, freeboard height of white ice above sea surface, h_{FB}, and ice thickness, h_I, were measured with a ruler at the sea ice surface above the under-ice irradiance measurement after each deployment of optical equipment. Melt pond coverage was estimated from unmanned aerial vehicle (UAV) photographs taken 90 m above the sampling area (Figure 4.1B,C).
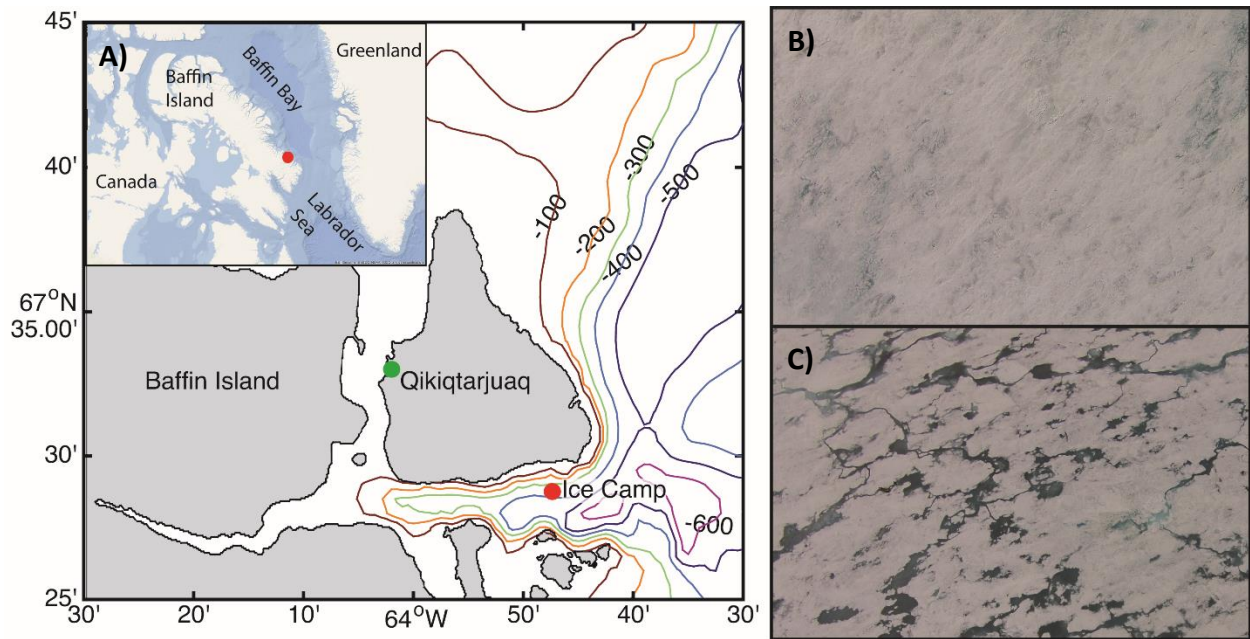
Figure 4.1: Study area. A) Location of ice camp as part of the Green Edge campaign in 2015 and 2016 on landfast sea ice near Qikiqtarjuaq, Southern Baffin Island, NU, Canada (Courtesy of E. Rehm) and UAV photographs showing sea ice surface conditions in the sampling area on B) 16 June and C) 2 July 2016.

4.2.2. Irradiance measurements

At each sampling station, the optical set-up consisted of a surface reference radiometer, which measured incident downwelling planar irradiance, $E_d(0,\lambda)$, and an under-ice arm equipped with three radiometers to measure transmitted downwelling planar irradiance, $E_d(z,\lambda)$, downwelling scalar irradiance, $E_{0d}(z,\lambda)$, and upwelling scalar irradiance, $E_{0u}(z,\lambda,)$ (Figure 4.2). These four hyperspectral radiometers (two planar RAMSES-ACC and two scalar RAMSES-ASC, TriOS

GmbH, Germany) were equipped with internal pressure and tilt sensors and measure irradiance spectra in the wavelength range of 320 to 950 nm at a resolution of 3.3 nm (190 channels).
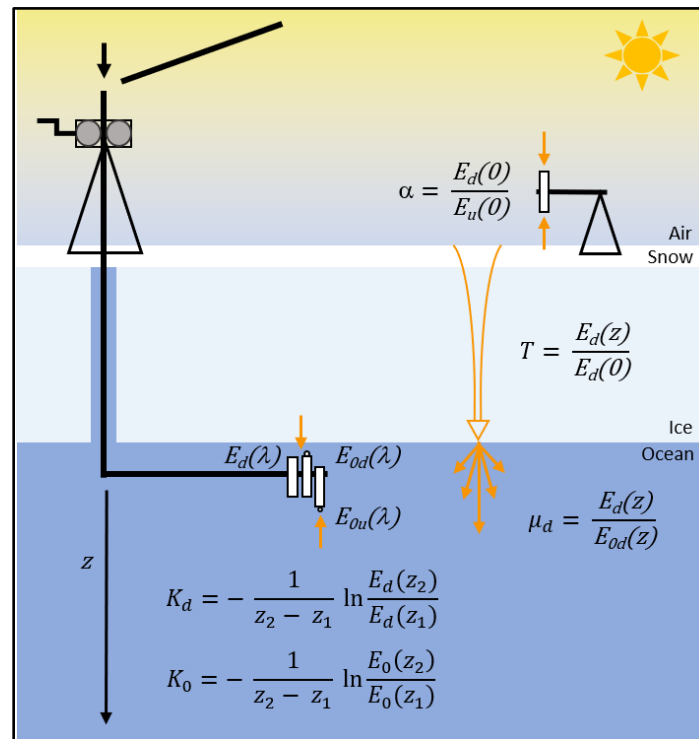
Figure 4.2: Schematic of optical equipment deployment and derived coefficients. Above the air-snow interface: measurement of spectral incident irradiance ($E_d(0)$) and spectral surface albedo (α); beneath the ice bottom via L-arm: measurement of transmitted downwelling planar and scalar irradiance spectra ($E_d(z)$, $E_{0d}(z)$) and upwelling scalar irradiance ($E_{0u}(z)$). Spectral irradiance data were used to calculate transmittance (T), downwelling average cosine (μ_d) and diffuse vertical attenuation coefficient of downwelling (K_d) and scalar irradiance (K_0).

Spectral albedo, $\alpha(\lambda)$, of different sea ice surface features was measured prior to the under-ice light sampling. To achieve this, a planar radiometer was mounted on an aluminum pole 1.5 m away from the tripod and was turned upward to measure downwelling planar irradiance before it was turned downward to measure reflected planar irradiance. Spectral albedo was calculated as the average ratio of five consecutive downwelling and upwelling irradiance readings.

Transmitted irradiance beneath the sea ice cover was recorded using a custom-built double-hinged aluminum pole (hereafter L-arm) connected to a manual winch to lower the instrument array to greater water depths by attaching additional 1.5-m aluminum poles to the arm. The L-arm was deployed through a 20-inch auger hole, and the radiometers were positioned directly beneath the ice bottom 1.5 m south of the hole. Snow or shaved ice was placed back into the hole to minimize the influence of elevated light levels on under-ice measurements. For the investigation of spectral

and PAR transmittance, the two planar radiometers, used as surface reference and under-ice sensor, were cross-calibrated in-air by simultaneously recording incident downward irradiance. Cross-calibration was performed following the equation provided in Antoine et al. (2013). Further steps of pre-analysis included the immersion correction of all under-ice light data due to the larger refractive index of water compared to air, and an exclusion from further analysis of data recorded when the vertical angle of the L-arm exceeded 5° from nadir.

In 2015, 17 vertical profiles of $E_d(0,\lambda)$, $E_{0d}(z,\lambda)$, and $E_{0u}(z,\lambda)$ were collected in 0.4 – 0.5-m steps from approximately 0.1 m below the ice bottom to a water depth of 18 m. Due to no significant changes (Student's T-test) of snow depth and sea ice thickness over the sampling period and much larger vertical angles, only five profiles with a snow depth exceeding 15 cm (thick snow cover) were used in the calculation of changes in transmittance, diffuse attenuation and the downwelling average cosine in the water column. Using the same protocol as that in 2015, in 2016 eleven under-ice irradiance profiles to a water depth of 20 m were recorded under different sea ice surface properties, including four measurements underneath thin snow-covered ice, three measurements below white ice and four measurements below ponded ice.

4.2.3. Chlorophyll *a* measurements

For the analysis of chlorophyll *a* concentration (Chl *a*) in the sea ice bottom, the bottommost 3 cm of at least two ice cores were extracted at a thick snow site in 2015 and thin snow and white ice sites in 2016 in proximity to the optical measurements. No ice cores were collected in melt ponds. The detailed sampling method is described in Galindo et al. (2017). Water samples were taken at 1.5, 5, 10 and 20 m using Niskin bottles, while ice-water interface samples were collected at 0.5 m with a submersible pump (Cyclone®) mounted to an under-ice arm. In the laboratory, melted sea ice and water samples were filtered onto 25 mm GF/F filters using a vacuum pump, wrapped in aluminum foil and stored at –80°C until analysis. Total Chl *a* concentration (TChl *a*) was determined by High Performance Liquid Chromatography (HPLC) following Ras et al. (2008).

4.2.4. Data analysis

In the following calculation of the coefficients, measured irradiance spectra were interpolated to 1-nm steps and vertical profiles of under-ice $E_d(z,\lambda)$, $E_{0d}(z,\lambda)$ and $E_{0u}(z,\lambda)$ were calculated at 0.5-m steps from 1.5-m to 18-m (2015) or 20-m (2016) water depth using linear interpolation. Spectral

irradiance and PAR transmittance through the ice cover at different stages of melt were estimated by dividing E_d measured at the ice bottom by E_d measured simultaneously at the ice surface. For the description of the angular structure of the under-ice light field, $\mu_d(z,\lambda)$ was calculated as the ratio of E_d to E_{0d} for each profile. To provide average μ_d for the four surface types (thick snow, thin snow, white ice, ponded ice), a two-term power series model was fitted through the under-ice $\mu_d(PAR)$ profiles of each surface type. Scalar under-ice irradiance $E_0(z,\lambda)$ was estimated by summing the coincident measurements of E_{0d} and E_{0u}. The vertical diffuse attenuation coefficient for downwelling irradiance $K_d(z,\lambda)$ was estimated by fitting an exponential curve ($R^2 > 0.96$) through the under-ice E_d profiles. To study differences between under-ice K_d and K_0, an exponential curve ($R^2 > 0.96$) was also fitted through the under-ice profile of E_0 to estimate $K_0(z,\lambda)$. All calculations were also performed with the coefficients for PAR, which was integrated over the waveband 400 – 700 nm.

The investigation of a factor to convert under-ice PAR data, given in energy units into values stated in photon density, was undertaken by a spectral conversion of downwelling scalar irradiance measured in W m^{-2} nm^{-1}, $E_{0d}(z)$, into the corresponding quantum irradiance given in µmol photons m^{-2} s^{-1}, $E_{0d-Q}(z)$, as follows

$$E_{0d-W}(z) = \int_{400}^{700} E_{0d}(z)d\lambda \tag{14}$$

$$E_{0d-Q}(z) = \int_{400}^{700} \frac{E_{0d-W}(z)\,\lambda}{c\,h\,N_A}d\lambda \tag{15}$$

including the speed of light (c), Planck's constant (h) and Avogadro's number (N_A). Afterwards, the ratio $E_{0d-Q}(z,\,PAR)$ to $E_{0d-W}(z,\,PAR)$ was calculated for different stages of sea ice melt.

4.2.5. Statistical analysis

A normal distribution of the data set and the homogeneity of variances were confirmed, and a square root transformation was applied, if necessary, before parametric tests were used. To investigate differences in snow depth and ice thickness between the sampling years, a Student's T-test was performed. A one-way ANOVA was used to test for significant differences in PAR transmittance between surface types, followed by Tukey's HSD to identify significantly different

groups. Additionally, differences between planar and scalar irradiance measurements, as well as differences in the downwelling average cosine, $\mu_d(PAR)$, and in the E_Q/E_W ratio with changing surface types and increasing depth were tested using a two-way ANOVA.

4.3. Results and Discussion

4.3.1. Sea ice surface

The conditions on the sea ice surface displayed a strong contrast between sampling years (Table 4.1). Snow depths in 2015 varied between 7 and 32 cm with snowfall events in the end of May and were significantly higher than in 2016 (t = 2.52, df = 18, p <0.05). Measured surface albedo was very high, averaging 0.95 in the PAR range. Ice thickness did not decrease, and no surface flooding was observed in the sampling area during the period of the irradiance measurements in this study. Additional description of the environmental conditions is available elsewhere (Oziel et al., 2019).

In mid-June 2016, air temperatures were above the freezing point, and the ice surface was covered with a relatively wet snow cover displaying a mean albedo of 0.73 in the PAR spectral range, which corresponds to reported albedo values of melting snow (Figure 4.1B; Perovich, 1996). Shortly after, snow melt and a rain event on 22 June acted to rapidly flood the ice surface. Snowfall and freezing surface water due to low air temperatures during the night slowed down surface melt during the following days. By 27 June, large, but shallow melt ponds were visible at the ice surface (Figure 4.1C). Surface PAR albedos of melt ponds and bare ice averaged 0.33 and 0.57, respectively, and lay in the reported range for ponded and white ice (Perovich, 1996). Melt pond coverage of the ice surface reached 17 – 27% within the sampling area; however, melt ponds became smaller at the end of June due to increased surface drainage (Oziel et al., 2019). Ice thickness also began to decrease from >1.2 m at the end of June to <1.0 m by 4 July, but was not significantly different from that of 2015 (t = 1.49, df = 26, p = 0.147).

Table 4.1: Average ± standard deviation snow depth ($\bar{h}_S$), height of white ice above melt pond surface ($\bar{h}_{WI}$), melt pond depth ($\bar{h}_{MP}$), ice thickness ($\bar{h}_I$), and freeboard ($\bar{h}_{FB}$) by sampling year.

Year	$\bar{h}_S$ (cm)	$\bar{h}_{WI}$ (cm)	$\bar{h}_{MP}$ (cm)	$\bar{h}_I$ (m)	$\bar{h}_{FB}$ (cm)
2015	23 ± 8[a]	$-$[b]	$-$	1.24 ± 0.06	4 ± 4
2016	11 ± 6[a]	5 ± 2	5 ± 3	1.19 ± 0.12	9 ± 3

[a] Shared superscripts represent statistically significant differences: $p < 0.05$
[b] Dash indicates no melt ponds or white ice had formed during the sampling period

4.3.2. Spectral and PAR transmittance

The change from a thick snow cover in May 2015 to wet snow in mid-June 2016 to ponded and white ice by the end of June resulted in a significant increase in the transmittance of light through landfast sea ice of the same thickness ($F_{3,12} = 39.64$, $p < 0.001$; Table 4.2). Transmittance profiles for selected spectral bands and PAR in the water column beneath different ice surface types are shown for selected days in the supplemental material (Figure S3.1). In 2015, new snowfall events caused low transmission of surface radiation through the highly reflective snow-covered sea ice, which then decreased monotonically with water depth. Spectral transmittance peaked between 470 and 570 nm reflecting the high absorption of snow and ice in the longer wavelength spectrum. In 2016, transmission through ice with a thin layer of wet snow was significantly larger with a more pronounced peak of spectral transmittance at wavelengths between 470 and 500 nm beneath the ice bottom. Light transmission through white ice was of the same magnitude. However, vertical spectral transmittance profiles showed a small increase in the 400 to 600 nm wavelength spectrum in the first 3 m below the ice bottom due to higher light transmission through adjacent melt ponds. The typical exponential decline of transmittance was observed beneath ponded ice.

Table 4.2: Post-hoc comparison of average PAR transmittance (T) ± standard deviation through landfast sea ice with different surface types in 2015 (thick snow) and 2016 (thin snow, white ice, melt pond).

Group	n	$T(PAR)$	Tukey's HSD comparisons		
			Thick snow	**Thin snow**	**White ice**
Thick snow	5	0.003 ± 0.001	$-$[a]	$-$	$-$
Thin snow	4	0.118 ± 0.05	$p < 0.001$	$-$	$-$
White ice	3	0.121 ± 0.04	$p < 0.001$	$-$	$-$
Melt pond	4	0.264 ± 0.05	$p < 0.001$	$p < 0.05$	$p < 0.05$

[a] Dash indicates no significant differences observed

Observations undertaken in 2016 during melt pond formation showed that the initial increase in under-ice light levels was caused by snow melt onset, which likely caused the surface albedo to be much lower in mid-June 2016 in comparison to very high albedos observed in late-May 2015. PAR transmittance of white and ponded ice corresponded with that presented in the literature (Ehn et al., 2011; Light et al., 2015). PAR transmittance recorded during snow melt was of the same magnitude as the transmission of PAR through the subsequent white ice, although the surface albedo of wet snow was greater. The similarity implies an increased light attenuation within the white ice layer. Ice algae, which were observed in the ice bottom in both years, could have influenced the transmitted light spectra. However, measured ice algae TChl a decreased from 3.476 mg m^{-2} to 0.267 mg m^{-2} over the sampling period. Instead, scattering within the drained surface layer of white ice, which consisted of large melt-grain clusters permeated by void space, could have caused a stronger light attenuation than the likely water-saturated snow layer at the snow-ice-interface (Light et al., 2008).

4.3.3. Vertical diffuse attenuation in the water column

During the 2015 pre-melt study, the thick snow and ice layer was associated with a very diffuse radiation field in the water column and a small $K_d(PAR)$ between 0.08 and 0.14 m^{-1} (Figure 4.3A). Over the sampling period, $K_d(PAR)$ decreased to a relatively constant value at the end of May, while the difference between K_0 and K_d increased from 4 to 18% . In the following year, $K_d(PAR)$ increased by a factor of two from 0.09 m^{-1} to 0.23 m^{-1} (Figure 4.3B). The difference between the two coefficients decreased from 8 to 3%.
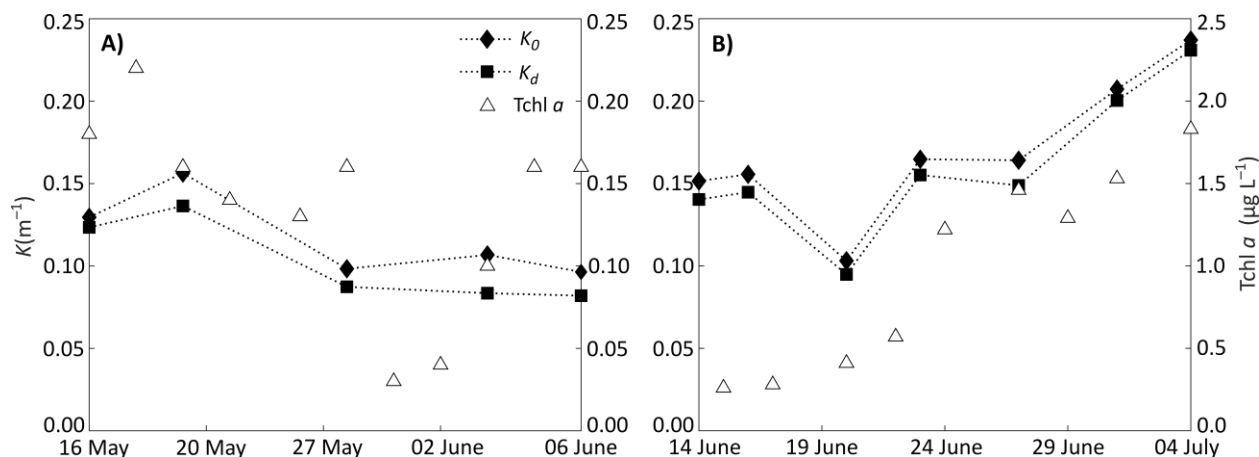
Figure 4.3: Vertical diffuse attenuation of downwelling planar PAR (K_d) and scalar PAR (K_0). Coefficients were measured beneath landfast sea ice in A) 2015 and B) 2016. Total chlorophyll a (TChl a) is given as average concentration in the first 20-m depth.

The variations in $K_d(PAR)$, and $K_0(PAR)$ with depth and ongoing melt progression may have been related to change in the absorption of PAR by algae cells in the water column. In 2015, average TChl a in the first 20 m of the surface water layer varied between 0.177 µg L^{-1} and 0.135 µg L^{-1} until it dropped to 0.035 µg L^{-1} on 29 May. Afterwards TChl a increased again to a value of 0.159 µg L^{-1} on 6 June. PAR attenuation in the water column only decreased slightly with the decline in TChl a. In 2016, vertical diffuse attenuation increased with ongoing melt progression due to enhanced absorption and scattering caused by an increase in average TChl a from 0.258 µg L^{-1} on 15 June to 1.828 µg L^{-1} on 4 July in the upper 20-m water column. Furthermore, phytoplankton cells are mainly forward-scattering, which could have influenced a decrease of the difference between K_d and K_0.

To study differences in diffuse attenuation of transmitted irradiance with increasing depth, K_d and K_0 were calculated between 3 and 6 m and between 6.5 and 18 m for the 2015 dataset (Table S4.1), as well as between 1.5 and 6 m and between 6.5 and 20 m for the 2016 dataset (Table S2), based on an observed smaller decrease in transmittance in the water column below 6-m depth (data not shown). The difference between K_0 and K_d was 22%, whereas in 2016, the melting ice cover displayed a 9% greater K_0 in the first 6-m water depth. In both years, the radiant flux became more downward-directed and less impacted by differences in light transmission through the sea ice cover with greater water depths resulting in only an 11% greater K_0 than K_d between 6.5- and 18-m depths in 2015 and 4% greater K_0 between 6.5 and 20 m in 2016.

Diffuse attenuation coefficients largely varied directly beneath the ice bottom with the change in ice surface from a wet snow cover to a mixture of bare ice and melt ponds. Light exiting the snow-covered ice layer in 2015 was more diffuse due to the highly scattering dry snow conditions (see next section), leading to a greater difference between K_d and K_0. Leppäranta et al. (2003) reported a 10% larger K_0 in snow- and ice-covered lakes, as well as a decrease in the difference between the two coefficients after the artificial removal of the scattering snow cover. Our results show the same trend with ongoing surface melt, whereby the large portion of longer wavelengths, which penetrate through the ponded ice cover and are absorbed strongly in the surface water layer, may have also contributed to a decrease between K_d and K_0.

4.3.4. Differences between under-ice planar and scalar irradiance profiles

Comparing irradiance profiles recorded with planar versus scalar radiometers, surface type ($F_{3,24} = 14.25$, p <0.001) and depth ($F_{1,24} = 43.97$, p <0.001) had a significant effect on the discrepancy between the recorded downwelling planar and scalar irradiance profiles in both years. Summarizing the 2015 dataset, measurements of $E_{0d}(PAR)$ at 3-m and at 18-m water depths were on average 38% and 32% larger, respectively, than simultaneous $E_d(PAR)$ readings. Upwelling scalar irradiance, $E_{0u}(PAR)$, was an order of magnitude less, resulting in a slightly higher $E_0(PAR)$ of 3% compared to $E_{0d}(PAR)$ throughout the entire water column. In 2016, the difference between $E_{0d}(PAR)$ and $E_d(PAR)$ was lower, between 31 and 34% at 3 m and between 25 and 28% at 20-m depth, due to overall greater light transmission through the sea ice cover. $E_{0u}(PAR)$ was again within 3% of that of $E_{0d}(PAR)$.

The under-ice irradiance levels were low under the snow-covered sea ice in 2015 with downwelling scalar PAR never exceeding 4.9 µmol photons m^{-2} s^{-1} (Figure S4.2A). Under-ice PAR levels were 30 times higher after the beginning of surface melt in June 2016, reaching mean $E_{0d}(PAR)$ values of 151.8 µmol photons m^{-2} s^{-1} during snow melt, and 105.5 and 280.3 µmol photons m^{-2} s^{-1} beneath white and ponded ice at 1.5-m depth, respectively (Figure S4.2B–D). Fog events became more frequent by the end of June, which caused lower incident radiation levels. Irradiance profiles recorded below white and ponded ice shortly after each other also illustrated a decreasing impact of the heterogeneous light transmission on the under-ice PAR levels with increasing depth (Figure 4.4). The decrease in PAR with depth was greater under melt ponds than

that under white ice until 10 m where the curves became parallel and, therefore, PAR propagation was no longer influenced by the sea ice cover.
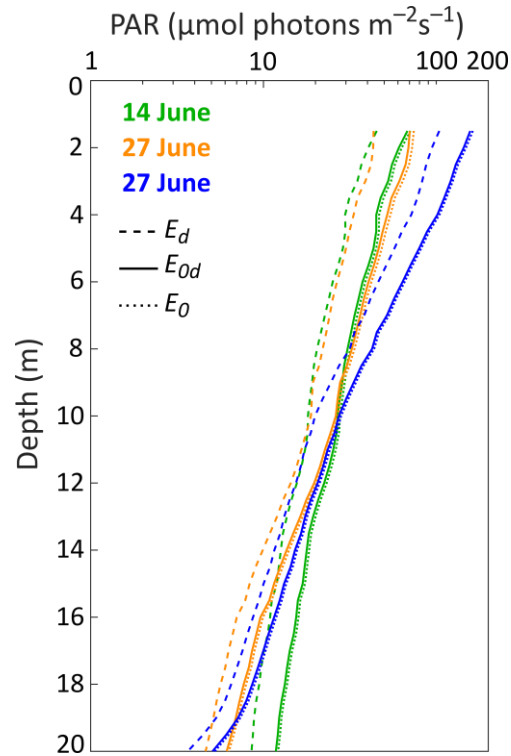
Figure 4.4: Interpolated profiles of measured under-ice PAR. Plotted as downwelling planar irradiance E_d (dashed lines), downwelling scalar irradiance E_{0d} (solid lines) and scalar irradiance E_0 (dotted lines) beneath snow-covered sea ice on 14 June (green), white ice on 27 June (orange), and ponded ice on 27 June (blue) 2016.

4.3.5. Under-ice downwelling average cosine

The measured irradiance spectra, $E_d(\lambda)$ and $E_{0d}(\lambda)$, and the calculated spectral downwelling average cosine, $\mu_d(\lambda)$, are shown for specified depths in Figure 4.5. Changes in the spectral shape of downwelling radiation with increasing depth had an impact on $\mu_d(\lambda)$. On 16 May 2015, light levels were exceedingly low and diffuse due to the thick snow cover, which resulted in relatively constant $\mu_d(\lambda)$ values between 400 and 600 nm with a low at 490 nm (Figure 4.5A). Above 600 nm, irradiance was rapidly attenuated in the water column. In 2016, the spectral shape of $\mu_d(\lambda)$ demonstrated a wavelength dependence. Beneath snow-covered sea ice at 1.5-m depth, the lowest $\mu_d(\lambda)$ of 0.65 was measured at 431 nm and slightly increased to 0.66 at 400 nm on 14 June. A much stronger increase in $\mu_d(\lambda)$ was measured towards longer wavelengths (indicating a more downwards directed irradiance field) with ratios of 0.72 at 700 nm. Enhanced noise for $\mu_d(\lambda)$ was

observed below 10-m depth due to the reduction in irradiance levels. With ongoing surface melt, the smallest $\mu_d(\lambda)$ values of 0.69 shifted from the blue towards the green part of the spectrum at 487 nm at 1.5 m on 4 July (Figure 4.5B–D). The low transmission and strong attenuation of spectral irradiance >600 nm caused uncertainty in the calculation of the average cosine above 600 nm due to the detection limit of the sensor. However, irradiance values of the red spectrum were so low that they were not expected to have an impact on the calculation of $\mu_d(PAR)$.
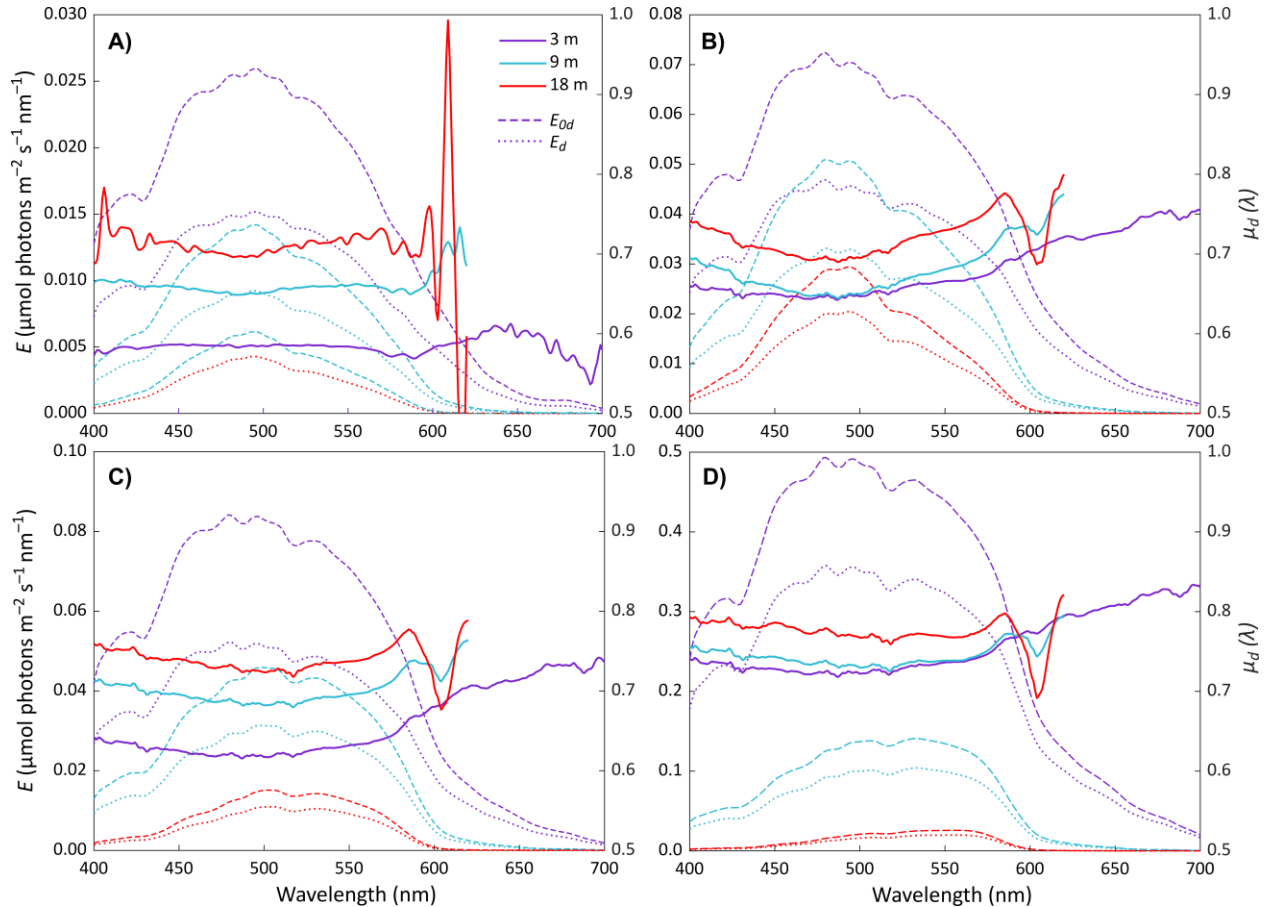
Figure 4.5: Spectral downwelling under-ice irradiance and downwelling average cosine of spectral irradiance. Measurements of spectral E_d (dashed lines) and E_{0d} (dotted lines) were performed A) beneath snow-covered ice on 16 May 2015, B) beneath snow-covered ice on 14 June 2016, C) beneath white ice on 27 June 2016, and D) beneath ponded ice on 4 July 2016. Spectral irradiance and spectral μ_d (solid lines) are plotted for three depths.

The angular distribution of downwelling radiation in the photosynthetic waveband below landfast ice cover varied significantly with surface type ($F_{3,24} = 15.54$, p <0.001) as well as with the change in the shape of the spectra with depth ($F_{1,24} = 62.38$, p <0.001; Fig. 4.6). In 2015, the PAR light field was nearly isotropic displaying significantly lower downwelling average cosines, $\mu_d(PAR)$,

at 3-m depth below ice that was covered with a >15-cm thick snow layer than in 2016 (Table 4.3). The snow layer as a highly scattering medium caused the most diffuse light field directly beneath the ice bottom. With increasing depth, $\mu_d(PAR)$ significantly increased, similarly to those observed in the following year at the same depth level. In 2016, the PAR light field was more downward-directed associated with a greater light transmission through the sea ice cover. At the ice bottom, μ_d values for PAR did not vary significantly between ice surface properties, but continuously increased with depth; $\mu_d(PAR)$ measured at 18 m beneath ponded ice was significantly greater than that at 3 m. Furthermore, $\mu_d(PAR)$ in the water column beneath snow-covered ice showed substantially less change with depth below 10 m than those under white and ponded ice.
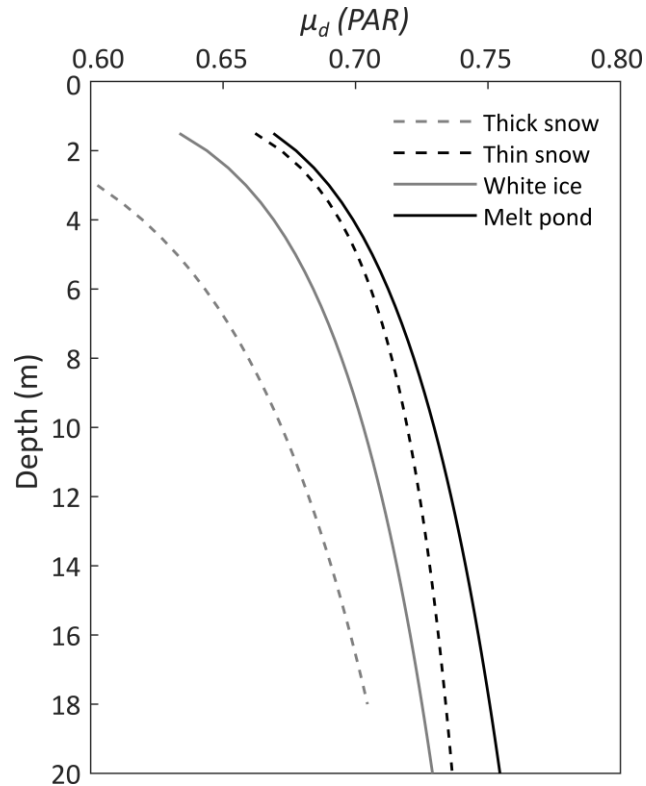
Figure 4.6: Downwelling average cosine ($\mu_d(PAR)$) beneath different sea ice surface types. Mean $\mu_d(PAR)$ was calculated from vertical irradiance profiles beneath sea ice with a thick snow cover in 2015 and beneath ice with a thin snow cover, ponded and white ice in 2016.

Table 4.3: Post-hoc comparison of mean downwelling average cosine ($\mu_d(PAR)$) ± standard deviation beneath landfast sea ice with different surface types: thick snow (TkS) in 2015 and thin snow (TnS), white ice (WI), and melt pond (MP) in 2016.

Surface type	Depth (m)	$\mu_d(PAR)$	Tukey's HSD comparisons			
			$\mu_{d\text{-}TkS}$ (PAR, 3 m)	$\mu_{d\text{-}TnS}$ (PAR, 3 m)	$\mu_{d\text{-}WI}$ (PAR, 3 m)	$\mu_{d\text{-}MP}$ (PAR, 3 m)
Thick snow	3	0.61 ± 0.01	–	–	–	–
	18	0.70 ± 0.02	$p < 0.001$	–	–	–
Thin snow	3	0.69 ± 0.02	$p < 0.001$	–	–	–
	18	0.73 ± 0.01	$p < 0.001$	–	–	–
White ice	3	0.66 ± 0.02	$p < 0.05$	–	–	–
	18	0.72 ± 0.02	$p < 0.001$	–	–	–
Melt pond	3	0.69 ± 0.03	$p < 0.001$	–	–	–
	18	0.75 ± 0.01	$p < 0.001$	$p < 0.05$	$p < 0.001$	$p < 0.01$

Light propagation became more downward-directed ($\mu_d > 0.7$) with the transition from a thick snow cover to a mosaic of white ice and melt ponds due to an increased light transmission. Downwelling average cosine values, stated in the literature, range from 0.56 to 0.7 directly beneath the sea ice bottom, which corresponds well with our field observations (Arrigo et al., 1991; Ehn and Mundy, 2013; Katlein et al., 2014). Diffuse incoming radiation caused by clouds and fog also play a role in the under-ice light propagation. The frequent fog events in late June 2016 could have had an effect on the lower μ_d beneath white ice compared to sea ice with a thin snow layer.

Variations in the propagation of downwelling irradiance with increasing depth were recently examined numerically for an ice-covered water column north of Svalbard as the ratio of E_0/E_d in the PAR spectrum. In the model, the sea ice was covered with a thin snow layer. Ratios of E_0/E_d are presented for pre-bloom and bloom conditions based on the output from a radiative transfer model (Pavlov et al., 2017). A reversal of this ratio allows for a reasonable comparison against our μ_d results, as E_0 is not expected to be much larger than E_{0d} in the water column. Modelled values stated by Pavlov et al. (2017) were a near constant 0.55 at the ice bottom (indicating that the model produces a nearly isotropic light field at the base of the ice cover independent of irradiance level), and then increased with depth to 0.7 during pre-bloom conditions and to 0.65 during a

phytoplankton bloom at 40-m depth. Based on measured under-ice irradiance, our results showed the same trend of a decreasing $\mu_d(PAR)$ with depth. However, measured $\mu_d(PAR)$ was higher and varied between 0.61 and 0.69 directly beneath the ice bottom.

In the ice-covered water column, scattering and absorption processes control the propagation of light. Both processes determine changes in the angular distribution of light, while absorption alone impacts the spectral shape and creates a downward-directed light field weighted toward blue-green wavelengths with increasing depth. Measurements in 2015 recorded very low under-ice irradiance levels and only small changes in $\mu_d(PAR)$, which indicate a low impact of PAR-absorbing and -scattering particles in the water column. Hence, light attenuation was mainly influenced by the high absorption coefficient of water itself, which dominated the rate of change in the average cosine mainly in the red portion of the spectrum. Blue-green light is weakly absorbed by water and, therefore, shows a greater reflectance, which overlaps with the observed low of $\mu_d(\lambda)$ at 490 nm (Morel and Gentili, 2004).

In 2016, measured under-ice irradiance profiles showed an enhanced attenuation of light between 400 and 500 nm toward the end of June, influenced by an increase in phytoplankton biomass in the surface water layer. The implications on the under-ice light field can be seen in an increased rate of change of $\mu_d(PAR)$ below white and ponded ice compared to the mean $\mu_d(PAR)$ profile measured in the beginning of June beneath ice with a thin snow layer (Table 4.3, Fig. 4.5B–D). Furthermore, the increased concentration of phytoplankton and absorption of wavelengths at the chlorophyll maxima led photons of the green spectrum to penetrate deepest and caused the observed depression in spectral μ_d at 487 nm due to a greater reflectance in the water column (Morel and Gentili, 2004). Pavlov et al. (2017) also postulated an increase in E_0 compared to E_d under bloom conditions due to enhanced backscattering of algal cells. Although eukaryotic cells are described as weak backward-scatterers due to their large cell size (Kirk, 2011), the unique colonial aspect of *Phaeocystis pouchetii*, the nanoflagellate observed in Pavlov et al. (2017), could potentially influence backscatter more. More research on the subject is required. Our results showed a decline in the differences between E_{0d} and E_d with negligible E_{0u} over sea ice melt progression and increased TChl *a*, which suggests a stronger impact of the overall larger light transmission to the ocean rather than the elevated scattering by particles on the under-ice light

propagation in spring. Note, however, that average TChl a in the water column only reached 1.8 µg L^{-1} during our study in 2016, in comparison to 7.5 ug L^{-1} in Pavlov et al. (2017).

Discrepancies between E_d and E_{0d} are dependent on the relative importance of scattering versus absorption. A very diffuse underwater light field due to a low sun angle and/or multiple scattering in the overlying snow and ice cover increases the discrepancy between planar and scalar measurements, which can cause a large error in the measurement of light availability for the estimation of polar primary production. Hence, the use of planar irradiance E_d instead of scalar irradiance E_0 in primary production studies will always represent an underestimate of the prevailing underwater light conditions that needs to be corrected (Morel and Gentili, 2004; Kirk, 2011; Pavlov et al., 2017). To show percentage difference in primary production estimates resulting from planar vs. scalar PAR input, depth-integrated daily production was calculated for light-limiting conditions in surface waters on 14 June and light-saturating conditions on 1 July 2016. Averaged hourly surface irradiance, recorded over a period of 24 hours, together with the presented coefficients of light transmission through snow-covered, ponded and bare ice and with $K_d(PAR)$, were used to calculate vertical under-ice profiles of planar and, by using an average cosine of 0.7, scalar irradiance. Hourly photosynthetic rate was calculated with parameters gained from photosynthesis vs. irradiance (PvsE) curves of phytoplankton communities sampled at the ice camp. A maximum photosynthetic rate, P_{max}^B, of 0.83 (0.25) mg C Chl a^{-1} h^{-1}, light saturation point, E_k, of 59 (102) µmol m^{-2} s^{-1} and photoinhibition, β^B, of 7.9 x 10^{-4} (9.4 x 10^{-5}) of communities sampled on 14 June (1 July) were applied in the equation stated in Platt et al. (1980) and normalized to the Chl a concentration measured from 0.5-m to 60-m depth. Afterwards, primary production rates were integrated over a depth of 60 m and over 24 hours.

Results indicate that once photosynthesis is saturated, the impact of the average cosine on calculated primary production rates is minimal. Figure 4.7 shows a 3% higher daily carbon production calculated with E_{0d} instead of E_d on 1 July. The importance of using the scalar irradiance for production estimates is more pronounced in the pre-bloom period when light availability is still limiting photosynthesis and under-ice phytoplankton communities are acclimated to low-light conditions. Depth-integrated daily carbon production was 16% lower using E_d instead of E_{0d} due to the linear relationship between the rate of photosynthesis and increasing light levels before reaching saturation levels. We note these estimates fall slightly below and above

the range of 5 – 13% modelled by Sathyendranath et al. (1989). To avoid possible discrepancies in production estimates, scalar radiometers should be utilized, particularly in studies investigating the timing of under-ice blooms. If only downwelling planar irradiance is measured, an average cosine of 0.6 beneath snow-covered sea ice and 0.7 beneath ponded and white ice can be used to convert these under-ice measurements into downwelling scalar irradiance.
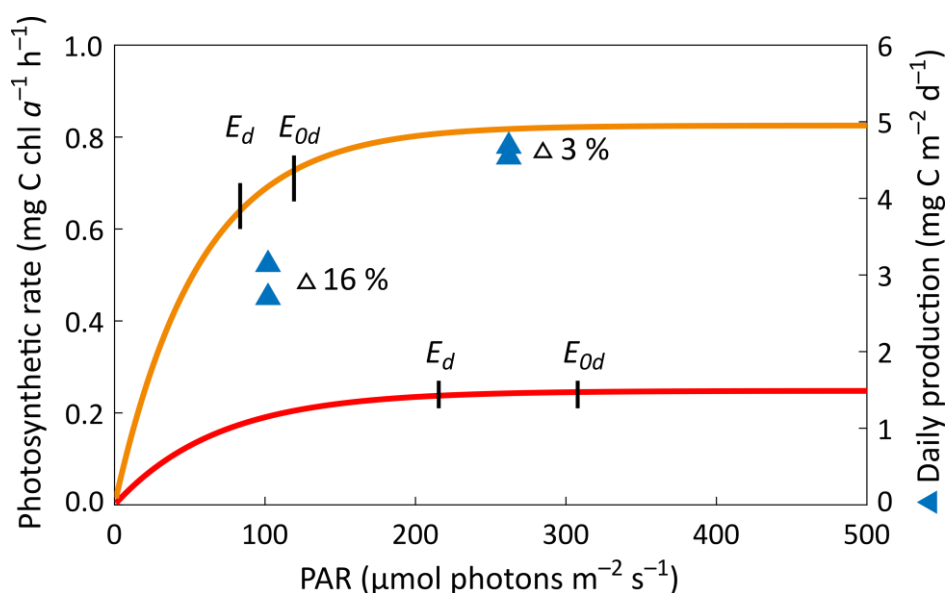
Figure 4.7: PvsE curves of phytoplankton and calculated daily carbon production in the ice-covered water column. Depth-integrated primary production at the sampling site down to 60 m was derived from PvsE curves of phytoplankton communities sampled on 14 June (orange, 16 %) and on 1 July 2016 (red, 3%). Black lines show $E_d(PAR)$ and $E_{0d}(PAR)$ values at 2-m depth at 12:00 pm.

4.3.6. PAR unit conversion factors

Knowledge about the relation between total quanta and total energy at different depths also plays a relevant role in the conversion of underwater irradiance data. In biological studies, PAR data are commonly stated in units of µmol photons m^{-2} s^{-1} (E_Q), while energy balance studies use units of W m^{-2} (E_W). Often the comparison between results from the two disciplinary fields is unclear because irradiance data are usually converted spectrally and conversion ratios for PAR data are lacking. The E_Q/E_W ratio for PAR is dependent on water transparency and depth and was studied for several open water bodies (Morel and Smith, 1974; Reinart et al., 1998). This study investigated variations in the ratio spectrally and was used to study changes in the conversion factor of $E_{0d}(PAR)$ values directly.

The highest and significantly different ratios were observed in profiles near the ice bottom ($F_{1,24}$ = 16.16, p <0.001) due to spectral narrowing as light propagates downward in the water column (Table 4.4). With increasing TChl a in the water column, profiles became C-shaped with a minimum between 6- and 10-m depth before again increasing at further depth. Figure 4.8A presents the calculated E_Q/E_W ratio of $E_{0d}(PAR)$ with increasing depth in 2015. Below the ice bottom at 3-m depth, mean ratios of 4.24 were reached while a mean ratio of 4.14 was measured at 18-m depth. The observed differences in the ratios over time were related to variations in the spectral shape of transmitted irradiance (Fig. 4.8B). The greatest ratio of 4.32, measured on 6 June at 3-m depth, was caused by a high transmission of longer wavelengths between 550 and 600 nm with a lower energy content. In contrast, on 16 May noticeably less irradiance between 550 and 600 nm, but more between 450 and 500 nm (photons with a higher energy content), were transmitted, which resulted in a smaller ratio of 4.16 at the same depth level. The reason for a spectral shift in transmitted irradiance is likely a change in the ice algal biomass in the bottom-ice layer. Within the sampling period, the TChl a in the last 3 cm of the ice bottom varied from 3.8 mg m^{-2} on 16 May to over 31.8 mg m^{-2} on 27 May and 0.5 mg m^{-2} on 2 June (Galindo et al., 2017), which contributed to the decrease in the transmission of wavelengths between 400 and 500 nm at the end of May and, thus, caused lower ratios. Water column TChl a was low (<0.2 µg L^{-1}) throughout the sampling period and had only a small impact on the spectral composition of PAR.
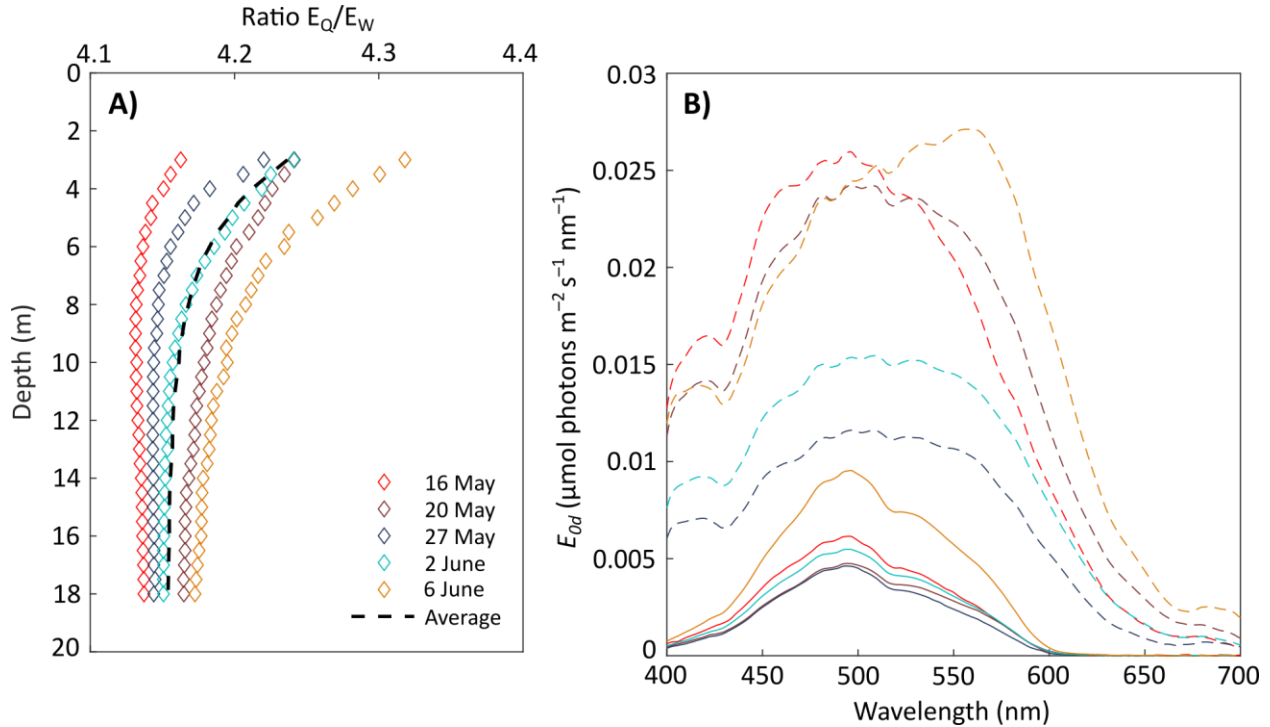
Figure 4.8: The ratio E_Q/E_W and spectral shape of scalar under-ice irradiance. A) Vertical profile of ratio E_Q/E_W and B) transmitted spectral scalar irradiance at depths of 3 m (dashed lines) and 18 m (solid lines) measured beneath snow-covered sea ice in 2015. Mean ratio stated as calculated average of 5 days.

In 2016, measured E_Q/E_W ratios varied less beneath the ice bottom (Table 4.4), which could have been related to a low TChl a in the bottommost 3 cm of the ice layer never exceeding 3.5 mg m^{-2} throughout the sampling period. However, only beneath sea ice with a thin snow cover, the ratio decreased significantly with depth likely due to a low light absorption by algal cells in the water column (Fig. 4.9A). The TChl a was less than 0.3 µg L^{-1}. Beneath white and ponded ice (Fig. 4.9B,C), the water column showed characteristics of blue-green waters (Morel and Smith, 1974). The increase in light attenuation by increased phytoplankton biomass altered the spectral composition of the radiant flux, so that photons of the green spectrum traveled deepest causing a greater ratio. The increase in the ratio with depth, observed beneath ponded ice, also emphasizes a chlorophyll maximum at greater depths. Generally, the E_Q/E_W ratio of 4.25 can be used to convert PAR given in watt units and measured directly beneath the ice. Morel and Smith (1974) provide an E_Q/E_W ratio of 4.15 ± 10% for a PAR unit conversion in the open water, which encompasses with our observations. Another aspect that can be drawn from the spectral composition of downwelling irradiance is the observed change in the quality of PAR. The efficiency of photosynthetic processes depends on how well the spectral composition of PAR matches the

absorption spectrum of algal pigments, so that a shift of the radiant flux towards the green spectrum results in a lower quality of PAR and, thus, lower efficiency in the utilization of radiant energy by phytoplankton (Morel, 1978; 1991). As shown, the spectral shape of transmitted irradiance varied with increasing TChl *a* and must be considered in the discussion of light availability for primary production.

Table 4.4: Average ratio E_Q/E_W ± standard deviation beneath landfast sea ice with different surface types at two depth levels (3 m, 18 m).

Depth (m)	Ratio $E_{Q}/E_{W\text{-Surface type}}$			
	Thick snow	**Thin snow**	**White ice**	**Melt pond**
3 m	4.24 ± 0.05	4.26 ± 0.03^{a}	4.24 ± 0.01	4.26 ± 0.02
18 m	4.15 ± 0.01	4.14 ± 0.01^{a}	4.20 ± 0.04	4.26 ± 0.07

[a] Shared superscripts represent statistically significant differences: $p < 0.05$
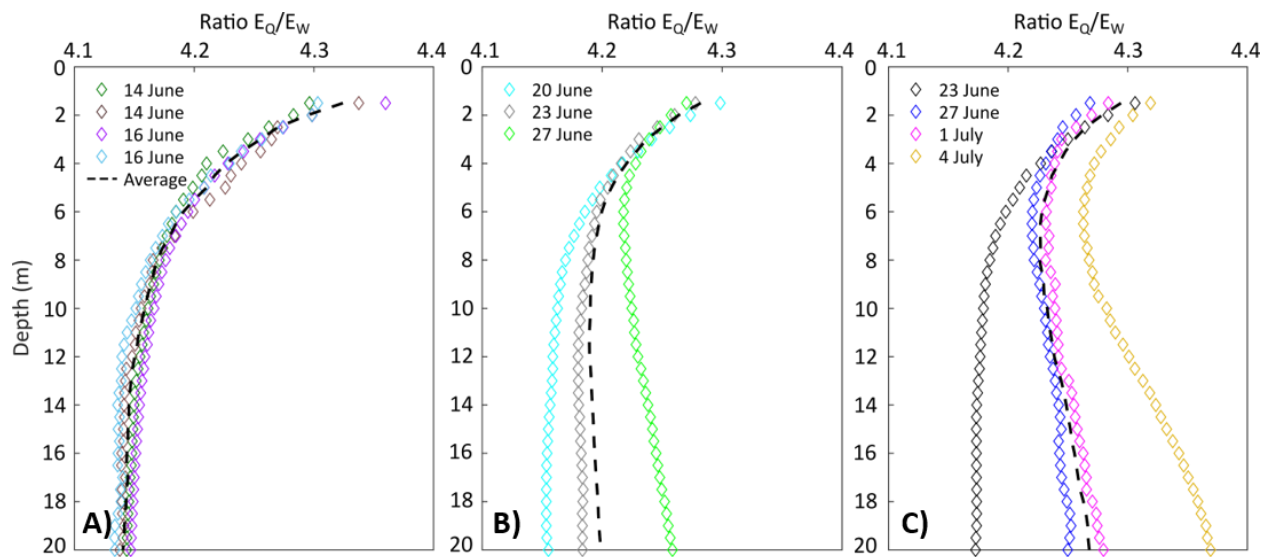
Figure 4.9: The ratio E_Q/E_W beneath sea ice with different surface types. Vertical profiles of the ratio measured A) beneath snow-covered sea ice, B) white ice and C) ponded ice in 2016. Mean coefficient stated as calculated average for each surface type.

Understanding the spring bloom of phytoplankton in the Arctic is of key importance to understanding biological productivity in the Arctic marine environment. A significant fraction of the primary production takes place beneath a sea ice cover and commences during the spring–summer transition, when the sea ice cover starts to melt, and lasts until nutrients become limiting (Mundy et al., 2014; Barber et al., 2015). To understand and predict the timing and intensity of the spring bloom under Arctic sea ice, knowing how much PAR is available in the surface layer of the

water column is important. Whereas energy balance studies require the flux of solar radiation energy incident onto the surface for calculating, e.g., radiative heating or melting rates, estimates of primary production require information of the total flux of photons in the PAR wavelength range from all directions at a given point in the water column or, in other words, the scalar irradiance, $E_{0-Q}(PAR)$.

The dependence of transmitted PAR propagation in the under-ice water column (e.g., transmission, vertical diffuse attenuation and downwelling average cosine) on the state of surface melt have been summarized in Figure 4.10 to assist with parametrization of the under-ice light field in polar primary production studies. The schematic figure presents the coefficients required to link PAR measured (1) above and below a melting landfast sea ice cover in spring, (2) in different units and (3) with different radiometer types. Spectral irradiance measurements were a requirement to derive these coefficients and to convert between units. However, irradiance data in biological studies are often measured using integrated PAR band sensors, in units of quanta, with sometimes little consideration of the prevailing light field (e.g., use of only a planar sensor). The presented results show variations of each coefficient in relation to the prevailing surface conditions to describe the propagation and attenuation of PAR in the water column.

In the next step, these coefficients can be applied in primary production studies as well as in models to calculate PAR availability beneath Arctic landfast sea ice, even if only incident solar irradiance is known. Information about the sea ice surface from drone or satellite imagery can be used to assess the spatial heterogeneity of the surface, so that regional PAR transmittance can be calculated following Equation 16 of bulk transmittance ($\bar{T}$), first presented by Perovich (2005) and later confirmed in a model exercise of ponded first year sea ice by Taskjelle et al. (2017)

$$\bar{T}(PAR, t) = \bar{T}_S(PAR, t)\, A_S(t) + \bar{T}_{WI}(PAR, t)\, A_{WI}(t) + \bar{T}_{MP}(PAR, t)\, A_{MP}(t) + (1 - \alpha_W(PAR))\, A_W(t) \quad (16)$$

Average values of PAR transmittance, as presented in this paper, for snow-covered ($\bar{T}_S$), melt pond-covered ($\bar{T}_{MP}$) and white ice ($\bar{T}_{WI}$), their area fraction (A) as well as the surface albedo of water (α_W) can be used to calculate regional PAR transmittance at a given time (t). The subsequently gained, still planar under-ice PAR values (E_d), together with the average cosine $\mu_d(PAR)$ and vertical diffuse attenuation coefficient $K_d(PAR)$ from Figure 4.8, can now be applied to estimate vertical profiles of downwelling scalar irradiance (E_d) following

$$E_{0d}(PAR, z_2) = \frac{1}{\mu_d(PAR)} E_d(PAR, z_1)e^{-K_d(PAR)(z_2-z_1)} \tag{17}$$
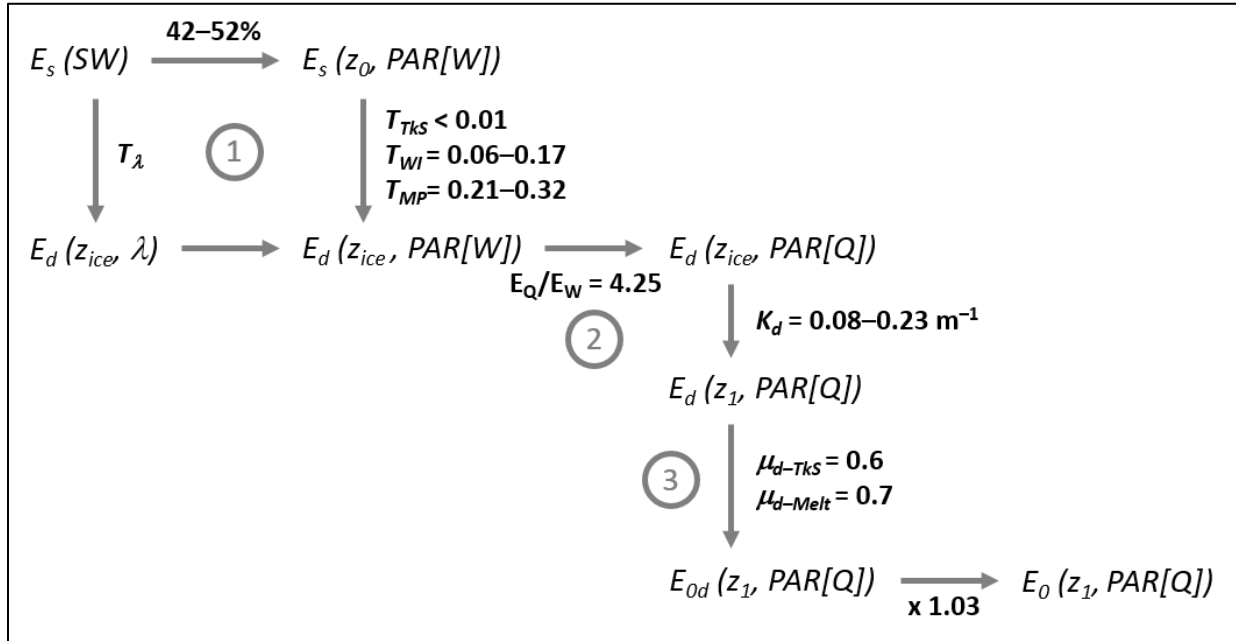
Figure 4.10: Parametrization of the under-ice light field. Flow chart of attributes to describe the transmittance (*T*) of incident shortwave (SW) and PAR irradiance through sea ice with a thick snow cover (TkS), white ice (WI) and ponded ice (MP), and the under-ice propagation of PAR: downwelling vertical diffuse attenuation coefficient (K_d), downwelling average cosine (μ_d) and ratio (E_Q/E_W) to convert PAR stated in energy units [W] into photon flux density [Q]. Transmittance and the change in K_d over the sampling period are given as ranges. PAR-fraction of incident shortwave radiation taken from Yu et al. (2015).

4.4. Conclusion

During melt season, changes in the under-ice light field can occur over a relatively short time period and, in turn, can cause a large error in the measurement of radiation available for photosynthesis. Our investigation aimed to minimize the error by providing new information about coefficients to describe the propagation of transmitted PAR below the sea ice cover in spring. Large variation in the apparent optical properties were shown over time and water depth due to a decreased surface albedo with the melting of snow and the appearance of melt ponds as well as an increase in scattering and absorption processes in the water column. The presented measurements of the downwelling average cosine are the first reported beneath sea ice and are in good agreement with modelled values. Significant differences in $\mu_d(PAR)$ were observed directly beneath the ice bottom, but not with increasing depth. Hence, error in the calculation of under-ice primary

production can be avoided if measured downwelling irradiance is converted into scalar irradiance by using an average cosine of 0.7 (0.6 beneath snow-covered sea ice).

For future statements about the timing of primary production beneath the thinning Arctic ice pack, more information is still needed on the evolution of the angular distribution of the underwater light field over a diurnal cycle. With continuing melt progression, low sun angles, longer daylight and refreezing of the melting sea ice surface caused by low night temperatures are likely to have a strong impact on the transmission and angular distribution of the radiant flux penetrating the ice-covered ocean. Here, the use of Monte-Carlo simulations to create a 3D model of the average cosine will be beneficial to characterize the heterogeneous light climate in spring.

Supplemental material
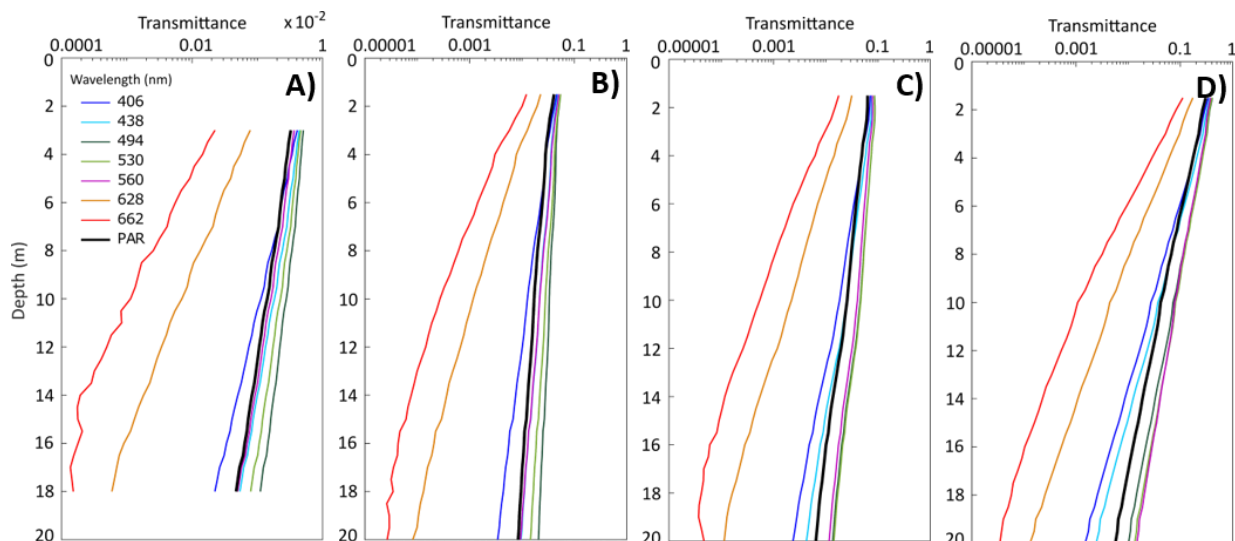
Figure S4.11: Planar transmittance (PAR) profiles at selected wavelengths. Profiles were measured in the water column beneath landfast sea ice with A) thick snow cover (h_S = 29 cm) on 16 May 2015, B) a thin wet snow cover (h_S = 11 cm) on 16 June 2016, C) bare surface on 27 June 2016 and D) ponded surface (h_{MP} = 4 cm) on 4 July 2016. Note the different transmittance scales.
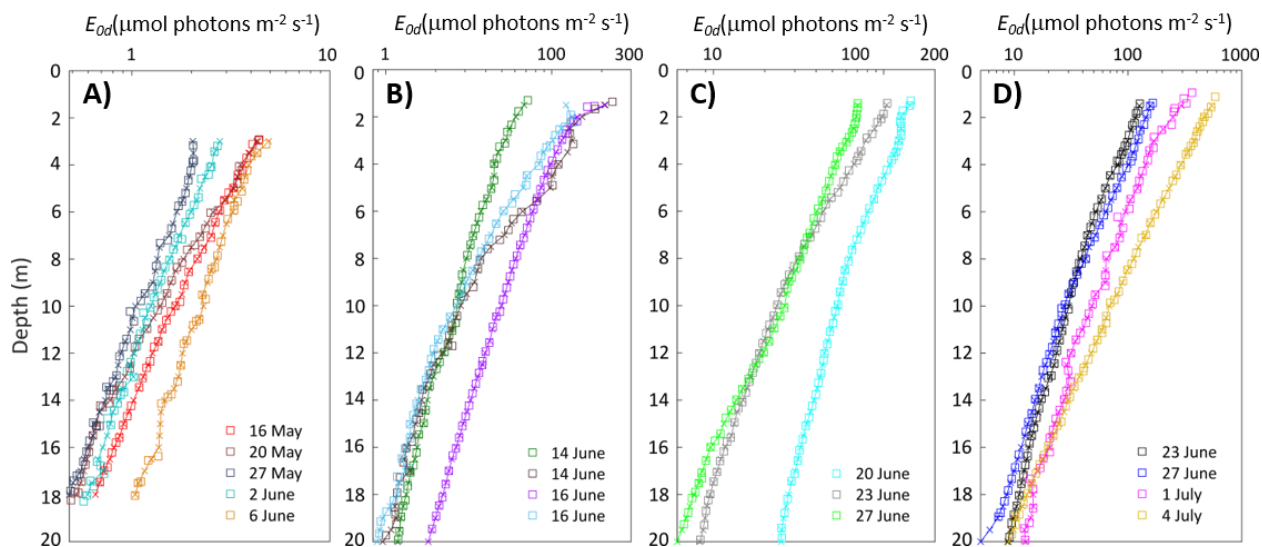
Figure S4.12: Vertical profiles of downwelling PAR. Interpolated (x) and measured (square) downwelling scalar PAR beneath A) snow-covered sea ice in 2015, and B) snow-covered ice, C) white ice and D) ponded ice in 2016.

Table S4.5: Diffuse attenuation coefficient of downwelling PAR (K_d) and scalar PAR (K_0) obtained beneath snow-covered landfast sea ice in 2015.

Date	K_0 (PAR, m^{-1})		K_d (PAR, m^{-1})	
	3 – 6 m	6.5 – 18 m	3 – 6 m	6.5 – 18 m
16 May	0.14	0.12	0.11	0.13
20 May	0.15	0.14	0.09	0.13
27 May	0.06	0.10	0.04	0.10
2 June	0.11	0.10	0.11	0.07
6 June	0.13	0.09	0.12	0.08

Table S4.6: Diffuse attenuation coefficient of downwelling PAR (K_d) and scalar PAR (K_0) obtained beneath melting landfast sea ice in 2016.

Date	K_0 (PAR, m^{-1})		K_d (PAR, m^{-1})	
	1.5 – 6 m	6.5 – 20 m	1.5 – 6 m	6.5 – 20 m
14 June	0.16	0.11	0.14	0.11
16 June	0.20	0.12	0.18	0.11
20 June	0.11	0.08	0.09	0.08
23 June	0.19	0.13	0.17	0.12
27 June	0.16	0.16	0.14	0.15
1 July	0.26	0.16	0.28	0.16
4 July	0.24	0.22	0.23	0.22

5. Chapter – Environmental drivers of spring primary production in Hudson Bay

This manuscript was submitted to the peer-reviewed journal *Elementa: Science of the Anthropocene* and was reviewed by two anonymous reviewers. This chapter represents the revised manuscript. The citation for this manuscript is:

Abstract

Pertinent environmental factors influencing the microalgal bloom during sea-ice breakup in Hudson Bay were investigated in June 2018, producing the first observations of late spring primary production in the offshore waters of this vast inland sea. Phytoplankton production was found to commence at the onset of ice melt, with surface nutrient depletion leading to the formation of a subsurface chlorophyll maximum in the open waters of western Hudson Bay. Concurrently, the melting mobile ice cover in central Hudson Bay created favorable conditions for a diatom-dominated under-ice bloom, with photosynthetic characteristics and relatively high production confirming that phytoplankton cells were able to acclimate to increasing light levels. Lower mean values of phytoplankton production and total chlorophyll *a* concentration observed under the sea ice (414 mg C m^{-2} d^{-1} and 33.7 mg TChl *a* m^{-2}) than those observed in open waters during the late-bloom stage in the western region (460 mg C m^{-2} d^{-1} and 53.5 mg TChl *a* m^{-2}) were attributed to reduced under-ice light levels and low surface concentrations of dissolved inorganic nitrogen (<2 μmol L^{-1}) in central Hudson Bay. However, the highly abundant sub-ice diatom, *Melosira arctica,* was estimated to contribute an additional 378 mg C m^{-2} d^{-1} to under-ice production in this region. Therefore, this sub-ice algal bloom appears to play a similar role in the seasonally ice-covered sub-Arctic as in the central Arctic Ocean where it significantly contributes to local production. Updating historical total production estimates of Hudson Bay ranging between 21.5 – 39 g C m^{-2} yr^{-1} with our late spring observations including the novel observation of *M. arctica*, annual production was recalculated to be 72 g C m^{-2} yr^{-1}, which equates to mean values for interior Arctic shelves.

5.1. Introduction

Over the past decades, the Arctic Ocean has undergone a significant decline in the previously dominant thick multi-year ice cover leading to predictions of an ice-free (sea-ice area <1 million km^2) Arctic summer before 2050 (Notz et al., 2020). This loss in the sea ice cover has decreased habitat availability for Arctic top predators while increasing light availability for primary producers in the ice bottom and water column. Observations of high relative contributions of bottom- and sub-ice algal communities to total annual production in the central Arctic Ocean (e.g. Gosselin et al., 1997; Boetius et al., 2013; Fernández-Méndez et al., 2014, 2015; Leu et al., 2015), followed by large under-ice phytoplankton blooms in spring (e.g. Mundy et al., 2014; Assmy et al., 2017; Oziel et al., 2019), and an increasing occurrence of secondary fall blooms (Ardyna et al., 2014) outline a productive polar ecosystem. However, these features are often localized and show high interannual variability making predictions of the future timing and magnitude of primary production and its impacts on higher trophic levels in the changing Arctic Ocean on a pan-Arctic scale difficult. It also highlights the need to assess current seasonal primary production patterns in several regions of the Arctic and sub-Arctic seas.

Hudson Bay, the world's largest inland sea, at the southern margin of the Canadian Arctic, has so far received little attention during the spring peak of microalgal growth, although it holds 10% of the seasonal ice cover found in the Arctic Ocean and provides a habitat for large populations of migratory birds and marine mammals (Ferguson et al., 2010). Furthermore, the summer ice extent has declined at a rate of $-10.4 \pm 3.2\%$ per decade between 1968 and 2009, increasing the open water season by 3.1 weeks (Tivy et al., 2011; Hochheim and Barber, 2014). The current concentration and thickness distribution of the sea ice cover, which is generally present from December to July, is mainly controlled by air temperature and wind forcing (Gagnon and Gough, 2005; Hochheim et al., 2011; Andrews et al., 2018; Kirillov et al., 2020). Especially strong northwesterly winds regularly open up a polynya in the northwest (NW polynya), which enhances ice formation in winter (Saucier et al., 2004; Landy et al., 2017; Bruneau et al., in review), but also makes northwestern Hudson Bay the first area to become ice-free during spring (Andrews et al., 2018). Due to the dominant northwesterly wind direction, sea ice is generally advected eastward, causing the ice cover along the east coast to dynamically grow to a thickness above 2 m

(Landy et al., 2017; Prinsenberg, 1986). The last remaining sea ice is typically found offshore of the Hudson Bay lowlands in the southern part of the Bay (Landy et al., 2017; Kirillov et al., 2020).

Hudson Bay is furthermore expected to undergo rapid changes in the influx of freshwater with predicted increases in precipitation and freshwater discharge from the surrounding watershed in response to the projected warming climate (Brown, 2010; Stadnyk et al., 2019; Clair et al., 1998), with major implications for primary production (Fouest et al., 2013; Hopwood et al., 2020). The inland sea already receives a river discharge of $630 – 870$ km^3 yr^{-1} which corresponds to 12% of the total pan-Arctic runoff (Saucier et al., 2004; Déry et al., 2011b; St-Laurent et al., 2011). This large runoff forms a strong pycnocline dividing the warmer and fresher surface layer from the underlying colder and saltier water (Prinsenberg, 1986).

In summary, together these environmental conditions (ice dynamics, freshwater fluxes, water circulation and stratification) cause large spatial variations in phytoplankton production and biomass in Hudson Bay. Coastal areas as well as the entrance into Hudson Bay from Foxe Basin, hereafter called the Narrows, are $2 – 3$ times more productive than the central Hudson Bay in late summer, early fall (Bursa, 1961; Anderson and Roff, 1980; Harvey et al., 1997; Ferland et al., 2011; Heikkilä et al., 2014). Due to the inaccessibility of central Hudson Bay during spring, there are no previous observations of ice algal and phytoplankton production during the spring bloom. Based on historical post-bloom measurements, annual production of Hudson Bay has been estimated to range from $21.5 – 39$ g C m^{-2} (Roff and Legendre, 1986; Jones and Anderson, 1994; Ferland et al., 2011; Bélanger et al., 2013). However, these studies likely underestimate total production, as recent observations of satellite-derived surface chlorophyll *a* concentration (Chl *a*) by Barbedo et al. (2020) found the highest phytoplankton biomass to occur in the NW polynya during the spring season. Additionally, ice algal blooms with intermediate <40 mg Chl *a* m^{-2} (Gosselin et al., 1986; Michel et al., 1993) to very high biomass of up to 170 mg Chl *a* m^{-2} (Welch et al., 1991) have been observed under the stable landfast ice at several locations around the Bay between March and May. Furthermore, after the ice algal bloom has sloughed off the ice, under-ice blooms have been observed below the landfast ice in June with Chl *a* of 2.5 mg m^{-3} (Legendre et al., 1981; Michel et al., 1993). Hence, by not accounting for the spring bloom, previous estimates likely significantly underestimate total annual production of Hudson Bay, and further analysis of this period are required.

This study addresses this shortcoming by providing the first ever measurements of ice-algal and pelagic primary production (PP) in Hudson Bay during the late spring season, when incoming solar irradiance is at its seasonal maximum. We used a combination of physical and biogeochemical parameters collected during the Hudson Bay System Study (BaySys) scientific cruise onboard the Canadian Coast Guard icebreaker *CCGS Amundsen* in June 2018. Our objectives are to: 1) characterize the environmental parameters driving spring primary production, 2) investigate the community structure and photoacclimation of microalgae in the different habitats, and 3) estimate the onset and magnitude of primary production by the different algal communities in relation to the melting sea ice cover in central Hudson Bay. Both sea ice and pelagic primary production are presented, which demonstrate a high spatiotemporal variability of microalgal biomass and production in late spring.

5.2. Material and methods

5.2.1. BaySys sampling overview

The present study was conducted from 2 June to 1 July 2018 as part of the BaySys project, which aimed to understand the relative contributions of river regulation, to generate hydroelectric power, and climate change to freshwater-marine coupling in Hudson Bay. At the time of the cruise, the seasonal ice cover was still in place and unregulated river discharge was near its seasonal maximum. Water samples were collected in three regions: 1) the Narrows near the confluence of Foxe Basin, Hudson Bay and Hudson Strait, 2) western Hudson Bay including the NW polynya and 3) ice-covered central Hudson Bay (Fig. 5.1). Ice cores from mobile sea ice were collected from drifting ice floes in the Narrows and central Hudson Bay. Sampling in eastern Hudson Bay was not possible due to heavy ice conditions. Additional long-term chlorophyll fluorescence data were recorded at ~32 m (2016/17) and 28 m (2017/18) by a mooring (AN01), which was deployed in southwestern Hudson Bay (59° 58.156' N, 91° 57.144' W) in September 2016, redeployed in September 2017 and recovered during our June 2018 cruise. At sampling stations, water depths ranged from 104 – 321 m in the Narrows and 31 – 185 m in Hudson Bay. At open water stations, sampling was comprised of vertical profiles of physical and biological variables including light measurements while ice stations further included remotely piloted airborne system (RPAS) surveys of the ice floe surface, ice core and melt pond water sampling for physical and biological variables as well as optical measurements above and beneath the sampled ice floe.

5.2.2. Ice sampling

Sampled mobile ice floes were selected based on both spatial representation and suitability for bringing the *Amundsen* alongside to safely disembark the research team by an ice cage or their suitability to land a helicopter. On the ice, three to four areas of different ice surface types were first identified for optical measurements to ensure an undisturbed snow or ice surface. The radiometer set-up consisted of a surface reference for measuring incident downwelling planar irradiance, $E_d(0,\lambda)$, and an under-ice arm equipped with a similar radiometer to measure transmitted downwelling planar irradiance, $E_d(z,\lambda)$. Both hyperspectral radiometers (RAMSES-ACC, TriOS GmbH) were equipped with internal pressure and tilt sensors and measured irradiance spectra in the wavelength range of 320 to 950 nm at a resolution of 3.3 nm (190 channels). Surface albedo and light transmittance were determined for the different surface types of snow, melt ponds and white ice (i.e., snow free ice with a white surface scattering layer). Transmitted irradiance was recorded via a hyperspectral radiometer that was attached to a custom-built double-hinged aluminum pole (hereafter L-arm, Ehn et al., 2008; Matthes et al., 2019). The L-arm was deployed through a 10-inch auger hole and positioned the radiometer directly beneath the ice bottom 1.5 m south of the hole. Snow and, or shaved ice were placed back into the hole to minimize the influence of elevated light levels on under-ice measurements.

For additional optical data processing, the fractional area for each surface type was estimated from RPAS surveys using a DJI Phantom 4, equipped with a 12 MP optical camera. Details on post-processing mosaic image generation and surface type classification can be found in Harasyn et al. (2020). The surveys covered an area of 0.12 km^2 producing classified images of melt pond, snow-covered, white ice, and open ocean classes with 2.5-cm pixel resolution. Fractional area of melt ponds is expressed as a value of melt ponded area over total sea ice area (sea ice plus melt pond area).

Sea-ice sampling was performed with a 9-cm core barrel (Mark II, Kovacs Enterprises) on snow-covered and white ice areas. No ice cores were collected in melt ponds. Sea ice thickness and freeboard were measured with an ice thickness gauge at each drilled hole through the ice floe. At each sampling location, two ice cores were extracted for vertical salinity and temperature profiles following Eicken et al. (2014). For biological sampling, the 5-cm bottom section of three ice cores were collected, pooled immediately in a dark isothermal container and melted in 0.2-μm filtered

seawater (FSW) at a ratio of 3:1 (three parts FSW, one part ice core volume) in the dark over 24 h to reduce osmotic stress (Campbell et al., 2019). Two additional independent 5-cm bottom sections were collected for bulk-ice nutrient analysis. One 5-cm section was melted slowly in the dark without dilution for the analysis of silicic acid ($Si(OH)_4$) concentration. The other bottom section was melted rapidly in a sterile bag, which was submersed in 40°C to determine the concentration of nitrate (NO_3), nitrite (NO_2) and phosphate (PO_4). If melt ponds were present, water for the analysis of the same biological parameters was collected with a submersible pump (Cyclone®). Nutrient concentration of pond water was not determined.

Additionally, weekly Canadian Ice Service (CIS) ice charts provided for June 2018 were used to determine total ice concentration by different stages of development in the Narrows and central Hudson Bay at the time of ice sampling. Ice charts delineate different ice regimes with polygons that present the partial concentration (in tenths) of up to three different stages of development according to the World Meteorological Organizations egg code. Stages of development considered within this study are new and young ice (<30 cm), thin (30 – 70 cm), medium (70 – 120 cm) and thick (>120 cm) first-year ice (FYI). Daily fields of sea ice concentration were retrieved from passive microwave data (10-km OSI-430 global sea ice concentration; http://www.osi-saf.org) and used to determine the number of days between ice concentration falling below 15% and the day that location was sampled (this is hereafter referred to as the days of open water (DOW)). It is worth noting that sea ice concentration is generally underestimated from passive microwave datasets during the melt period (Kern et al., 2020), which will introduce a slight positive bias to our estimates of DOW. We further estimated the average open water period throughout Hudson Bay from 2008 – 2018 to calculate annual primary production in the open water. The number of melt days, defined as time period of surface air temperatures (SAT) >0°C and ice concentrations >15%, were estimated from SAT over central Hudson Bay extracted from ERA interim reanalysis (Dee et al., 2011).

5.2.3. Water sampling

At each open water and ice station, vertical profiles of physical and biological parameters were collected with the ship's CTD-Rosette system. Temperature, salinity and photosynthetically active radiation (PAR, 400 – 700 nm) were measured with a conductivity, temperature and depth (CTD) probe (SBE-911, Sea-Bird Scientific) and a spherical (scalar) radiometer (QSP-2300, Biospherical

Instruments). A surface reference (QCR-2200, Biospherical Instruments), measuring incoming scalar PAR, was mounted to the ship's main mast. *In situ* chlorophyll *a* fluorescence, measured with the fluorometer (SCF, Seapoint) attached to the Rosette, was calibrated against *ex situ* Chl *a* measured in discrete water samples (see below). Additional chlorophyll fluorescence data was recorded every 15 minutes by ECO-Triplets (Sea-Bird Scientific), attached to the mooring AN01, which were installed at ~32 m (2016/17) and 28 m (2017/18), and were averaged over a 24-hours period.

The mixed layer depth, Z_m, was determined by finding the depth of the maximum buoyancy frequency (Brunt–Väisälä frequency, N^2) following Carvalho et al. (2017). Before the Rosette deployment, the optical depths at 100 (i.e. sea surface), 30, 15, 5, 1, and 0.2% for the water sampling were determined deploying a profiling natural fluorometer (PNF-300A, Biospherical Instruments) at the bow of the ship following Ferland et al. (2011). Afterwards, water samples for the analysis of bulk nutrients, algal pigments, particulates, primary production rates and taxonomic composition were collected at each optical depth with 12-L Niskin bottles. Bulk nutrients were collected every 10 m between 0 and 100 m water depth and every 20 m below 100 m water depth. Water samples were prefiltered with a 200-μm mesh to avoid the influence of large grazers (meso-zooplankton) and stored in the dark containers at air temperatures of 0°C until laboratory analyses.

5.2.4. Optical data processing

Collected hyperspectral irradiance data from ice sampling were interpolated to 1-nm steps and integrated over 400 to 700 nm to calculate surface albedo (or reflectance), R, and transmittance, T, for PAR. *R(PAR)* was calculated as the average ratio of five consecutive downwelling, $E_d(0^+, PAR,$ μmol photons m^{-2} $s^{-1})$, and upwelling, $E_u(0^+, PAR$, μmol photons m^{-2} $s^{-1})$, irradiance readings. T(PAR) was calculated as the ratio of $E_d(z_1, PAR)$ and $E_d(0^+, PAR)$, measured simultaneously at the ice bottom and surface, respectively. Under-ice light data were previously corrected for the larger refractive index of water compared to air.

To provide more accurate estimates of PAR availability at the ice bottom, regional surface albedo, $\bar{R}(PAR)$, and regional transmittance, $\bar{T}(PAR)$, which considers the spatial heterogeneity of the surface, were calculated. Following Matthes et al. (2020), $\bar{R}(PAR)$ and $\bar{T}(PAR)$ were calculated for each ice station with known fractions of open water, A_W, snow-covered ice, A_S, white ice, A_{WI}, and melt pond-covered ice, A_{MP}, $(\Sigma A_i = 1)$ as

$$\bar{R} = R_W A_W + R_S A_S + R_{WI} A_{WI} + R_{MP} A_{MP} \tag{18}$$

$$\bar{T} = T_W A_W + T_S A_S + T_{WI} A_{WI} + T_{MP} A_{MP} \tag{19}$$

where R and T are the measured coefficients for each surface type. For open water, $R_W(PAR)$ was set to the value of surface reflection at 5% (Kirk, 2011).

In the water column, the depth of the euphotic zone, Z_{eu}, was set at 0.2% of incident surface PAR (Ferland et al., 2011). The diffuse vertical attenuation coefficient for scalar irradiance, $K_{d0}(PAR, m^{-1})$ in the euphotic zone was determined by the slope of the linear regression between the natural logarithm of the measured vertical scalar Rosette PAR profiles and depth. For the estimation of primary production vertical scalar PAR profiles, $E_{d0}(z_2, PAR)$, from 1 to 100 m, were calculated by applying Beer-Lambert's Law

$$E_{d0}(z_2, PAR) = E_{d0}(0^-, PAR) * e^{(-K_{d0}(PAR) * \Delta z)} \tag{20}$$

including $K_{d0}(PAR)$ and the measured downwelling scalar PAR beneath the surface, $E_{d0}(0^-, PAR)$. Note that Beer-Lambert's Law is a commonly used approximation of PAR attenuation despite the spectral nature of the downwelling irradiance in water (Wei and Lee, 2013), that we considered valid for the purpose of this study. Due to the artificially created open water area for the rosette deployment at ice stations, under-ice vertical PAR profiles were derived as follow

$$E_{d0}(z_2, PAR) = \frac{1}{\mu_{d(z_1)}} * \bar{T}(PAR) * E_d(0^+, PAR) * e^{(-K_{d0}(PAR) * \Delta z)} \tag{21}$$

including incident downwelling planar PAR, $E_d(0^+, PAR)$, from the surface TriOS measurement at the ice surface, calculated regional $\bar{T}(PAR)$, $K_{d0}(PAR)$ from the vertical rosette profiles and the average cosine for downwelling irradiance, μ_d, of 0.7 to convert planar PAR into scalar PAR at the ice bottom (z_1), following Matthes et al. (2019).

5.2.5. Laboratory analysis of seawater samples

Water samples for dissolved inorganic nutrients ($Si(OH)_4$, NO_3, NO_2, and PO_4) were collected into acid-washed 15-ml polyethylene tubes after a filtration through a 25-mm Whatman GF/F filter inserted into a filter holder to remove large particles. Nutrient concentrations were immediately measured onboard with a continuous-flow AutoAnalyzer III (Bran and Luebbe) using a routine colorimetric method adapted from Hansen and Koroleff (1999). Analytical detection limits were

0.05 and 0.02 µmol L^{-1} for NO_3 and NO_2, respectively, and 0.05 and 0.1 µmol L^{-1} for PO_4 and $Si(OH)_4$, respectively. Nutrient ratios were calculated for different water depths and collected ice bottom sections at each station. The N:P and N:Si ratios are defined here as the molar ratio of nitrate+nitrite to phosphate and silicic acid, respectively. Contour plots of nutrient and chlorophyll *a* fluorescence were drawn using the ODV 5.1.5 software (Schlitzer, 2018).

Particulate organic carbon (POC) was analyzed from water samples filtered onto pre-combusted (450°C for 5h) 25-mm Whatman GF/F filters. Filter blanks for each sampling station were produced by filtering 500 mL of FSW through a Whatman GF/F filter. Filters were then wrapped in tinfoil and stored at –80°C for later analysis of POC following acidification of filters to remove particulate inorganic carbon at the University of British Columbia following the protocol of Glaz et al. (2014).

Extracted Chl *a* was measured with a fluorometer (10AU Field Fluorometer, Turner Designs) onboard while the identification and concentration of selected algal pigments were determined by reverse-phase high-performance liquid chromatography (HPLC) after the cruise. Onboard, samples were filtered onto 25-mm Whatman GF/F filters using a vacuum pump. For fluorometric analysis, filters were subsequently soaked in 10 mL of 90% acetone at 5°C for 18 – 24 h to extract Chl *a*. Fluorescence was measured before and after acidifying the sample with 5% hydrochloric acid (HCl, 1N) (Parsons et al., 1984) and Chl *a* was determined from these measurements using the equations of Holm-Hansen et al. (1965). For HPLC analysis, filters were stored in 2-mL cryovials, wrapped in tinfoil and flash-frozen in liquid nitrogen. Samples were then stored at –80°C until analysis following Kilias et al. (2013). Pigments were extracted in 1.5 mL 100% acetone at –20°C, homogenized (Precellys, Bertin Intruments) with glass beads and centrifuged for 5 min at 12,500 rpm in a cooled centrifuge (0°C). The supernatant was filtered through 0.2-µm PTFE-filters and samples were stored in Eppendorf tubes at –80°C prior to analysis. Subsamples of the pigment extracts were measured with reverse-phase HPLC with a VARIAN Microsorb-MV3 C8 column (4.6 mm x 100 mm), using HPLC-grade solvents (Merck), a Waters 1525 binary pump equipped with an autosampler (OPTIMAS^{TM}), a Waters 2996 PDA (photodiode array detector) and the EMPOWER software. Chlorophyll, derivate and carotenoid absorption peaks were detected at 440 nm, while phaeopigments were detected at 410 nm. Pigments and derivates were identified based on retention time and the spectral properties of external pigment standards. In this

study, total chlorophyll *a* concentration (TChl *a*) corresponds to the sum of Chl *a* and chlorophyllide *a*. The ratios of photoprotective carotenoids (PPC; including Diadinoxanthin, Diatoxanthin, Violaxanthin, Antheraxanthin, Zeaxanthin, Lutein, β,β-carotene) to photosynthetic carotenoids (PSC; including fucoxanthin, peridinin, neoxanthin, alloxanthin, 19'-butanoyl-oxy-fucoxanthin, 19'-hexanoyl-oxy-fucoxanthin) was also calculated following the pigment clustering of Kauko et al. (2019).

The taxonomic structure of the main protist groups for all water stations, collected ice bottom and melt pond water samples was calculated from marker pigment ratios using the CHEMTAX software V1.95 (Mackey et al., 1996; Wright, 2008). Initial pigment ratios were constrained as suggested by Higgins et al. (2011) based on microscopic examination of representative samples during the cruise, and published input matrices for ice algae (Alou-Font et al., 2013) and Arctic phytoplankton (Coupel et al., 2015; Fragoso et al., 2017) were applied. Following Coupel et al. (2015), phytoplankton samples were divided into high-light surface samples (0 – 15 m) and low-light deep samples (16 – 50 m) to account for variations in pigment ratios due to light acclimation of the present phytoplankton groups. Melt pond and bottom-ice algal samples were grouped together to increase the number of samples for a successful CHEMTAX run. In the used CHEMTAX version, the initial matrices were optimized by generating 60 variants of the input ratio using the random function $F = 1 + S * (R – 0.5)$ with a scaling factor $S = 0.7$ and R as a random number between 0 and 1 generated using the RAND function in Microsoft Excel as described in Wright et al. (2009). The best 10% of output matrices (n = 6) were averaged and used as new input matrix for a successive run of 60 variants of the new input matrix with $S = 0.4$ to reduce the standard deviation of results as recommended by Latasa (2007). The result of these six best output matrices were used to calculate the averages of the relative abundance estimates of the main protist groups. The final ratio matrices for bottom-ice algae and melt ponds (Table S5.5), and phytoplankton (Tables S5.6, S5.7) are displayed in the supplemental material.

Additionally, identification and enumeration of ice-bottom communities and phytoplankton at the subsurface chlorophyll maximum, hereafter called SCM, was performed on 250 mL subsamples from melted bottom-ice scrapes and water samples. For the analysis of ice-bottom communities, the bottommost 1 cm of three ice cores was scraped off with a pocketknife into a container with filtered seawater. Subsamples were preserved in acidic Lugol's solution (Parsons et al., 1984) and

stored in the dark at 4°C until analysis. Cells were identified with a light microscope (40x-objective, Zeiss Axiovert 10 and Leica DMIL LED), following the inverted microscope method (Lund et al., 1958). Cell identification was performed to the lowest rank possible (groups, genus or species; >2 µm) and primarily referring to Poulin and Cardinal (1982a; 1982b), Medlin and Priddle (1990), Tomas (1997), von Quillfeldt (2001). Cell abundance was corrected for filtered seawater dilution of ice bottom samples.

5.2.6. Photosynthesis-irradiance relationships

Net primary production (NPP) of ice algal (from bottom-ice scrapes), melt pond and phytoplankton communities were determined using the ^{14}C assimilation method and applying photosynthesis-irradiance (PE) relationships. Water samples in 1000-mL opaque Nalgene bottles were inoculated with initial $NaH^{14}CO_3$ concentrations between 0.2 and 1.0 µCi mL^{-1} depending on the strength of the Chl a fluorescence signal during the rosette cast and the length of the incubation. Out of each sampling bottle, sub-samples of 50 mL were transferred to 12 clear culture flasks and one opaque flask, which were placed in a custom-made incubation chamber adapted after Babin et al. (1994). In the incubator, bottles were arranged in a row with the first bottle closest to the light source (7/9/15W EIKO LED light bulb) and the dark bottle the furthest to provide a light gradient from 860 to 0 µmol photons m^{-2} s^{-1}. They were incubated at –1.6°C for 2 – 4 h. Three vials were also filled with 20 µL of the sample, 50 µL of ethanolamine and 500 µL of MilliQ water to measure the initial activity and to determine the exact concentration of ^{14}C in the samples. At the end of the incubation, samples were filtered onto 0.2-µm Millipore filters and filters were transferred into 20-mL scintillation vials to be spiked with 300 µL of 3.16% HCl. Vials were placed open on an orbital shaker for 2 h to evaporate the remaining inorganic ^{14}C on the filter under a fume hood. Afterwards, vials were filled with 10 mL EcoLume Scintillation Cocktail (MP Biomedicals). The particulate radioactive carbon uptake was counted after the cruise at Université Laval using a PerkinElmer Tri-Carb 2910 TR scintillation counter. The carbon uptake values in the opaque flask were subtracted from the corresponding clear flask carbon uptake values.

Samples for dissolved inorganic carbon (DIC), which was needed in the calculation of the amount of labelled carbon incorporation into the cell, were taken directly from the Niskin bottles and melt ponds into 250-mL or 500-mL borosilicate glass bottles with ground-glass stoppers and secured with electrical tape. All DIC samples were poisoned with 100 µL of a saturated $HgCl_2$ solution to

halt biological activity and were stored in the dark at room temperature until being processed ashore. DIC was measured with a SOMMA (Single-Operator Multiparameter Metabolic Analyzer). The DIC concentration in the collected 5-cm ice bottom core sections was not measured. Instead, DIC was calculated using the measured salinity of the core section and the equation presented in Parsons et al. (1984). Calculated carbon fixation rates (P^B, mg C mg^{-1} Chl a h^{-1}) were normalized to measured Chl a and photosynthesis-irradiance relationships (P-E curves) were fitted by minimizing the sum of differences between the measured carbon uptake and the model proposed by Platt et al. (1980)

$$P^B = P_s^B * \left(1 - e^{\left(\frac{-\alpha^B * E}{P_s^B}\right)}\right) * e^{\left(\frac{-\beta^B * E}{P_s^B}\right)} \tag{22}$$

where P_s^B (mg C mg^{-1} Chl a h^{-1}) is the maximum carbon fixation rate if there is no photoinhibition β^B (mg C mg^{-1} Chl a h^{-1} (µmol photons m^{-2} s^{-1})$^{-1}$), α^B (mg C mg^{-1} Chl a h^{-1} (µmol photons m^{-2} s^{-1})$^{-1}$) is the photosynthetic efficiency, defined as the initial slope of the P-E curve, and E (µmol photons m^{-2} s^{-1}) is the irradiance measured in the incubation chamber. Only P-E curves with a $R^2 = 0.9$ were included in the further analysis. Maximum carbon fixation rate P_{max}^B was calculated as

$$P_{max}^B = P_s^B * \left(\frac{\alpha^B}{\alpha^B + \beta^B}\right) * \left(\frac{\beta^B}{\alpha^B + \beta^B}\right)^{\frac{\beta^B}{\alpha^B}} \tag{23}$$

The photoacclimation parameter, E_k, was calculated as P_{max}^B/α^B. Production rates (mg C m^{-3} h^{-1}) for each station were calculated by multiplying the P-E parameters of six optical depths with the vertical profiles of $E_{d0}(z_2, PAR)$ for each hour of the day (24 h), which were generated from the performed light measurements and the change of the sun's position over the day. Hourly production rates were then integrated over Z_{eu} and over the day using trapezoidal integration to calculate daily production rates (mg C m^{-2} d^{-1}). Although short incubation times of 2 – 4 h were used to measure production, which does not account for respiration during nighttime and recycling of ^{14}C fixed by photosynthesis, we consider our results to be only slightly different from NPP due to the integration of production over the euphotic zone. Prior studies have shown that the ^{14}C-method with short incubation times provides good estimates of NPP at low growth rates, which was likely the case in the light-limited lower euphotic zone (Pei and Laws, 2013, and citations

therein). Furthermore, short-term incubations minimize the potential for algae to acclimate to the constant light conditions in the incubator (Lewis and Smith, 1983). TChl *a* and nutrients were also integrated over Z_{eu} using trapezoidal integration. Mean integrated nutrient concentrations in the euphotic layer were obtained by dividing depth-integrated values by the integration depth.

Total annual primary production of microalgal communities was estimated from historic field measurements and results from this study. Due to a lack of direct primary production measurements in early spring, Chl *a* of bottom-ice algae and under-ice phytoplankton was extracted from the literature and production was calculated as net accumulation over the sampling period with a POC:Chl *a* ratio of 54 (Irwin, 1990). It is also worth noting that the incubation times of direct primary production measurements differ between this study and historic estimations (24 h on-deck incubations in Ferland et al. (2011), 10 h on-deck incubations in Lapoussière et al. (2013). In the next calculation step of annual PP, seasonal production for early spring was calculated by multiplying the daily average of total production by ice algae and phytoplankton with 92 days. Late spring production during the sea ice melt was calculated by multiplying the daily average of total production by phytoplankton, bottom-ice algae and *Melosira arctica*, measured in this study, with 34 melt days (i.e., where surface air temperatures were above 0°C and ice concentration was >15%). Seasonal production in the ice-free water in summer and fall was calculated by multiplying the daily average of phytoplankton production with the average of 146 open water days between 2008 – 2018. Primary production during the winter (December – February) is assumed to be negligible and was not included in the annual estimate.

5.2.7. Statistical analysis

A principal component analysis (PCA) was carried out on collected physical data to identify clusters of regions within Hudson Bay with similar physical environmental parameters. Included parameters were $K_{d0}(PAR)$, Z_{eu}, Z_m, mean temperature, T_m, and salinity, S_m, in the mixed layer, integrated nutrient concentration ($Si(OH)_4$, NO_3+NO_2, PO_4) in the euphotic zone, ice concentration gained from the CIS ice charts for June 2018 and the DOW prior to sampling. The principal component analysis was performed with the stats package in the R 5.5.1 software. Significant differences between the photosynthetic (P-E curve) parameters of phytoplankton communities in the different environments (open water, under-ice) and at different depths (surface: 0 – 15 m, deep: 16 – 50 m) were investigated using a two-way ANOVA in the R software packages 'car' and

'dplyr'. A log-transformation was performed to achieve normal distribution of the dataset and the homogeneity of variances for the use of parametric tests. Differences in P-E parameters of ice-associated communities were not statistically tested due to the low number of measured P-E curves. A two-way ANOVA was also used to investigate differences between the ratios of POC:Chl *a* and PPC:PSC of phytoplankton in the different environments and depths. A TukeyHSD test was performed to investigate the interaction between the groups further if significant results were identified during the ANOVA. Differences between the ratios of POC:Chl *a* and PPC:PSC of ice-associated communities (bottom-ice algae, melt pond) were tested with a Student's T-test.

5.3. Results

5.3.1. Spatial variability and sea ice conditions

Based on the geographical location of sampling stations and the presence/absence of an ice cover, all sampling stations were grouped into three regions with distinct environmental conditions: 1) the partially ice-covered Narrows, 2) open water in western Hudson Bay, including the NW polynya, and 3) ice-covered central Hudson Bay (Fig. 5.1). Open water stations close to the coast and in the NW polynya in western Hudson Bay were characterized by a depleted nutrient concentration in the upper euphotic zone, and a warmer and deeper surface mixed layer (Table S5.4). Inshore stations also had the lowest surface salinities due to their proximity to river estuaries with the PCA analysis outlier, station 46, being located in front of the large and turbid estuaries of the Nelson and Hayes rivers (Fig. 5.1). Stations in central Hudson Bay showed a higher nutrient concentration in the euphotic zone as well as a colder and shallower mixed layer compared to western Hudson Bay. An increased light attenuation ($K_{d0}(PAR)$) was also observed at stations 32, 34 and 40, which were located east of the estuary.
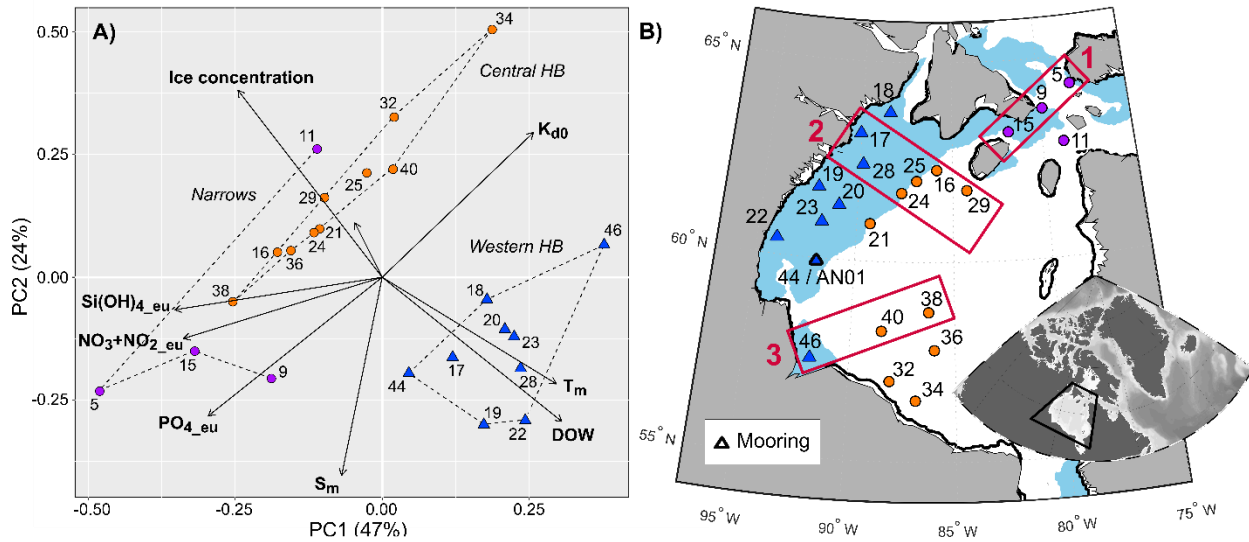
Figure 5.1: Principal component analysis (PCA) of 23 stations sampled in Hudson Bay. The environmental parameters displayed in the (A) PCA are the ice concentration (%) from CIS ice charts, open water days prior sampling (DOW), diffuse vertical attenuation coefficient for downwelling scalar PAR (K_{d0}), depth of the euphotic zone (Z_{eu}), depth of mixed layer (Z_m), mean temperature of the mixed layer (T_m), mean salinity of the mixed layer (S_m), and integrated concentration of nitrate plus nitrite ($NO_3+NO_{2\_eu}$), phosphate (PO_{4_eu}), and silicic acid ($Si(OH)_{4\_eu}$) over the euphotic zone. The dashed lines in the PCA distinguish stations sampled in the Narrows (purple circles), central (orange circles) and western (blue triangles) Hudson Bay (HB). Location of sampling stations and extend of ice cover (white) in early June are displayed in the (B) map. Red rectangles in the map indicate transects (1 – 3) shown in Figure 5.4.

To highlight the varying ice conditions in Hudson Bay, ice stations were separated into three sub-regions: 1) the Narrows, stations sampled in early June, 2) north-central Hudson Bay, stations sampled in mid-June, and 3) south-central Hudson Bay, stations sampled in late-June (red polygons Fig. 5.2A). The Narrows had an ice concentration of 67%, mainly composed of thick FYI that had no visible signs of surface melt (Fig. 5.2B). Ice in the Narrows had a mean thickness of 114 ± 29 cm (herein and after representing the mean $\pm$ standard error), a freeboard of 9 ± 1 cm and a snow depth of 13 ± 6 cm, along with the coldest (-1.7 ± 0.1°C) and saltiest (5.8 ± 0.2) ice observed. In comparison, sea ice concentrations were higher in north- and south-central Hudson Bay with more medium and thinner FYI being present (Fig. 5.2C, D). Mean ice thickness was lowest in north-central Hudson Bay (75 ± 7 cm and freeboard of 5 ± 1 cm) where negative freeboard was observed at a few floes. Sea ice concentration and thickness (128 ± 17 cm and a freeboard of 16 ± 2 cm) was highest in south-central Hudson Bay where the ice was much more deformed, and several ice floes were thicker than 2 m. Additionally, the ice in central Hudson Bay was in an advanced melt stage with a high melt pond coverage and the ice itself was warmer and

111

less salty with mean ice temperatures of –0.9 ± 0.1°C and –0.8 ± 0.1°C as well as mean bulk salinities of 3.6 ± 0.2 and 1.9 ± 0.2, respectively.

The differences in ice thickness and state of decay directly impact the optical parameters of the ice cover in the Narrows and central Hudson Bay. The observed decrease in $\bar{R}(PAR)$ and increase in $\bar{T}(PAR)$ throughout the sampling period matched the observed ice surface melt progression (Fig. 5.2). Although the areal fraction of more transparent melt ponds increased, $\bar{T}(PAR)$ remained in the same range in south-central (0.01 – 0.40) compared to north-central (0.07 – 0.27) Hudson Bay due to the thicker ice cover.
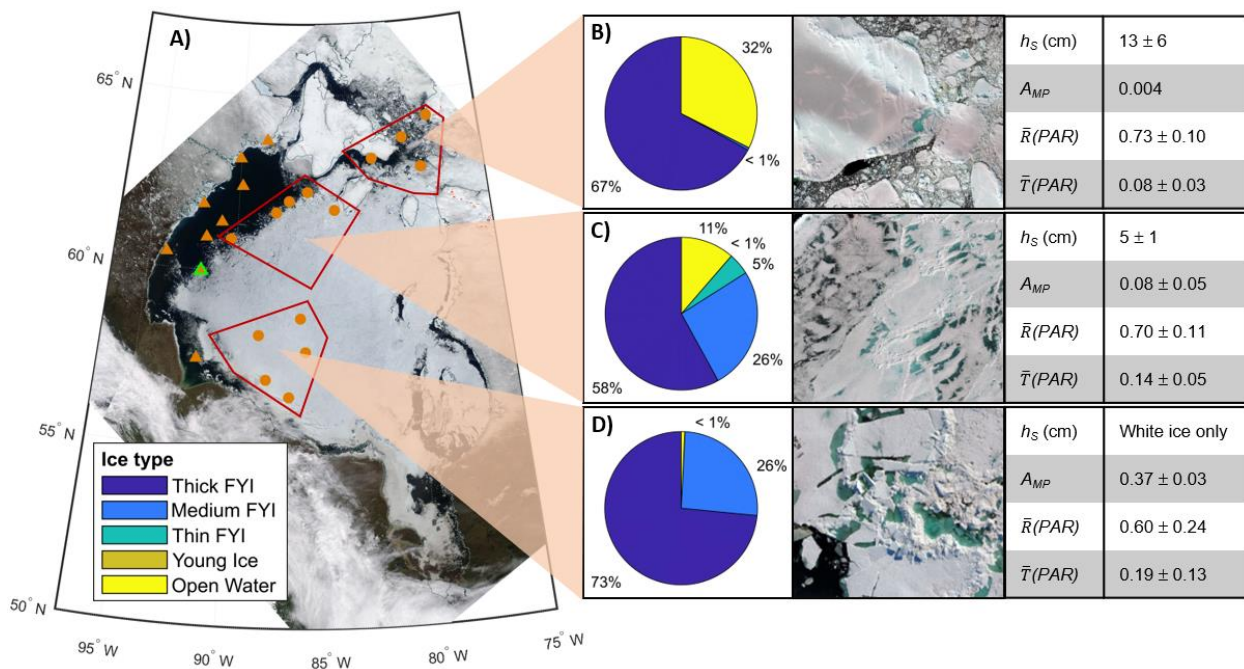
Figure 5.2: Sea ice concentration and ice surface properties in Hudson Bay in June 2018. Sea ice concentration in (A) MODIS image from 13 June 2018 and ice types (pie charts), sea ice surface appearance (RPAS images), mean snow depth, h_S, (± standard error), area fraction of melt ponds, A_{MP}, regional PAR albedo, $\bar{R}(PAR)$, and regional PAR transmittance, $\bar{T}(PAR)$, are shown for sampled ice floes in the (B) Narrows, (C) north-central, and (D) south-central Hudson Bay. Open water sampling stations (orange triangles), ice stations (orange dots), mooring location (green outline) and input area for pie charts (red rectangles) are shown in the MODIS image.

5.3.2. Water column properties

Differences in the water column structure between the regions are presented as potential temperature-salinity (TS) diagrams of the vertical CTD profiles (Fig. 5.3) and along transects in the three regions (Fig. 5.4; temperature (B, I, P), salinity (C, J, Q)). The Narrows were characterized by a surface water layer with S_m and T_m of 31.9 ± 0.4 and –1.5 ± 0.1°C, respectively

(Fig. 5.3A). The deep water (>100 m) was saltier, but in the same temperature range, resulting in a weakly stratified water column with a Z_m at 22 ± 5 m. In western Hudson Bay, the mixed layer shoaled from 20 ± 4 m, measured in the center of the NW polynya, to 10 ± 2 m, measured inshore. This surface mixed layer was characterized by a S_m and T_m of 31.9 ± 0.3 and $0.4 \pm 0.3°C$, respectively, and was ice free (<15% ice concentration) for an averaged 25 days prior to sampling. The deep water in the center of the NW polynya was the coldest and saltiest observed in entire Hudson Bay with S >33.1 and T <–1.7°C below100 m (Fig. 5.3B). In central Hudson Bay, the observed vertical salinity gradient followed the seawater freezing point (Fig. 5.3C). Similar S_m and T_m of 31.2 ± 0.2 and $–1.4 \pm 0.1°C$, respectively, were measured throughout central Hudson Bay, while the mixed layer of 23 ± 4 m was deeper in the north compared to the mixed layer of 13 ± 2 m in the south.
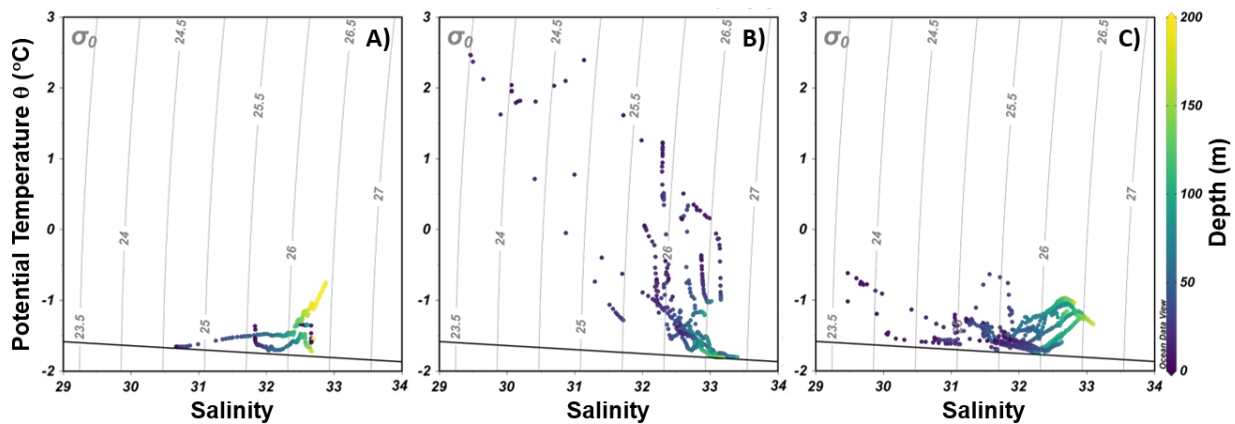
Figure 5.3: Water masses determined from salinity, potential temperature and depth. Potential temperature-salinity diagrams of rosette stations with biological sampling in the (A) Narrows, (B) western and (C) central Hudson Bay. Points of vertical profiles in the diagrams are colored according to depth. Freezing point of saltwater is displayed as black solid line.

5.3.3. Nutrients

Nutrient concentrations in the euphotic zone and in the deep waters differed between the three regions and are shown along a transect in each region (Fig. 5.1B, 5.4). Transect 1 in the Narrows extends across the mouth of Foxe Basin and the strait between Southampton Island and Coats Island. Transect 2 in western Hudson Bay extends from the western shore of Hudson Bay across the area of open water (NW polynya) and into the western edge of the ice pack. Transect 3 in central Hudson Bay extends from the outer Nelson River estuary into the thicker ice pack of central Hudson Bay.

Along transect 1, the NO_3+NO_2 concentration ranged $3.34 - 9.09$ µmol L^{-1}, with highest concentrations in the bottom waters of the Narrows (measured 10 m above the sea floor, Fig. 5.4E; Table 5.1). Concentrations of PO_4 and $Si(OH)_4$ ranged $0.85 - 1.07$ µmol L^{-1} and $9.03 - 16.1$ µmol L^{-1}, respectively (Fig. 5.4F, G). Overall, nutrient concentrations in the euphotic zone were higher in Narrows with mean surface N:P and N:Si molar ratios of 5.05 and 0.44, respectively, compared to the euphotic zone across Hudson Bay with mean surface N:P molar ratios between 0.16 and 1.73, and N:Si molar ratios between 0.03 and 0.22 (Table 5.1).

In the euphotic zone of the NW polynya along transect 2 in western Hudson Bay, concentrations of NO_3+NO_2, PO_4 and $Si(OH)_4$ ranged $0.01 - 3.22$ µmol L^{-1}, $0.41 - 0.90$ µmol L^{-1}, and $0.01 - 9.01$ µmol L^{-1}, respectively, (Fig. 5.4L–N, Table 5.1) with inshore $Si(OH)_4$ concentrations near the detection limit. The nitracline depth (NO_3+NO_2 <1 µmol L^{-1}) largely tracked the depth of the mixed layer (Fig. 5.4L), extending to 30 m at station 28 in the polynya and shoaling towards the ice edge. Nutrient concentrations in the deep waters below 100 m remained high along the transect with NO_3+NO_2, PO_4 and $Si(OH)_4$ concentrations ranging $4.47 - 12.9$ µmol L^{-1}, $0.75 - 1.62$ µmol L^{-1}, and $9.21 - 35.7$ µmol L^{-1}, respectively. Concentrations of NO_3+NO_2 in the deep water at stations 20, 21 and 24 in western and central Hudson Bay were even higher than the observed nitrogen inventory of the deep waters in the Narrows (Fig. 5.4E, L).

Along transect 3 in central Hudson Bay, the nitracline depth exhibited a similar pattern to transect 2, being deepest in the open water and shoaled towards the ice edge (Fig. 5.4S). In the euphotic zone, integrated NO_3+NO_2 concentration increased from 0.52 µmol L^{-1} at station 46 to 2.05 µmol L^{-1} at station 38. Concentrations of NO_3+NO_2, PO_4 and $Si(OH)_4$ in ice-covered euphotic zone ranged $0.44 - 5.73$ µmol L^{-1}, $0.64 - 1.01$ µmol L^{-1}, and $3.16 - 13.0$ µmol L^{-1}, respectively (Fig. 5.4 S–U, Table 5.1). Concentrations of NO_3+NO_2 and $Si(OH)_4$ in the bottom water were difficult to compare across transect 3 as water depth greatly varied from 31 m at station 32 to 178 m as station 38. In general, concentrations of NO_3+NO_2 ($Si(OH)_4$) of 13.1 (38.5) µmol L^{-1} in the deepest waters were comparable to those observed in western Hudson Bay (Fig. 5.4L, N, S, U).
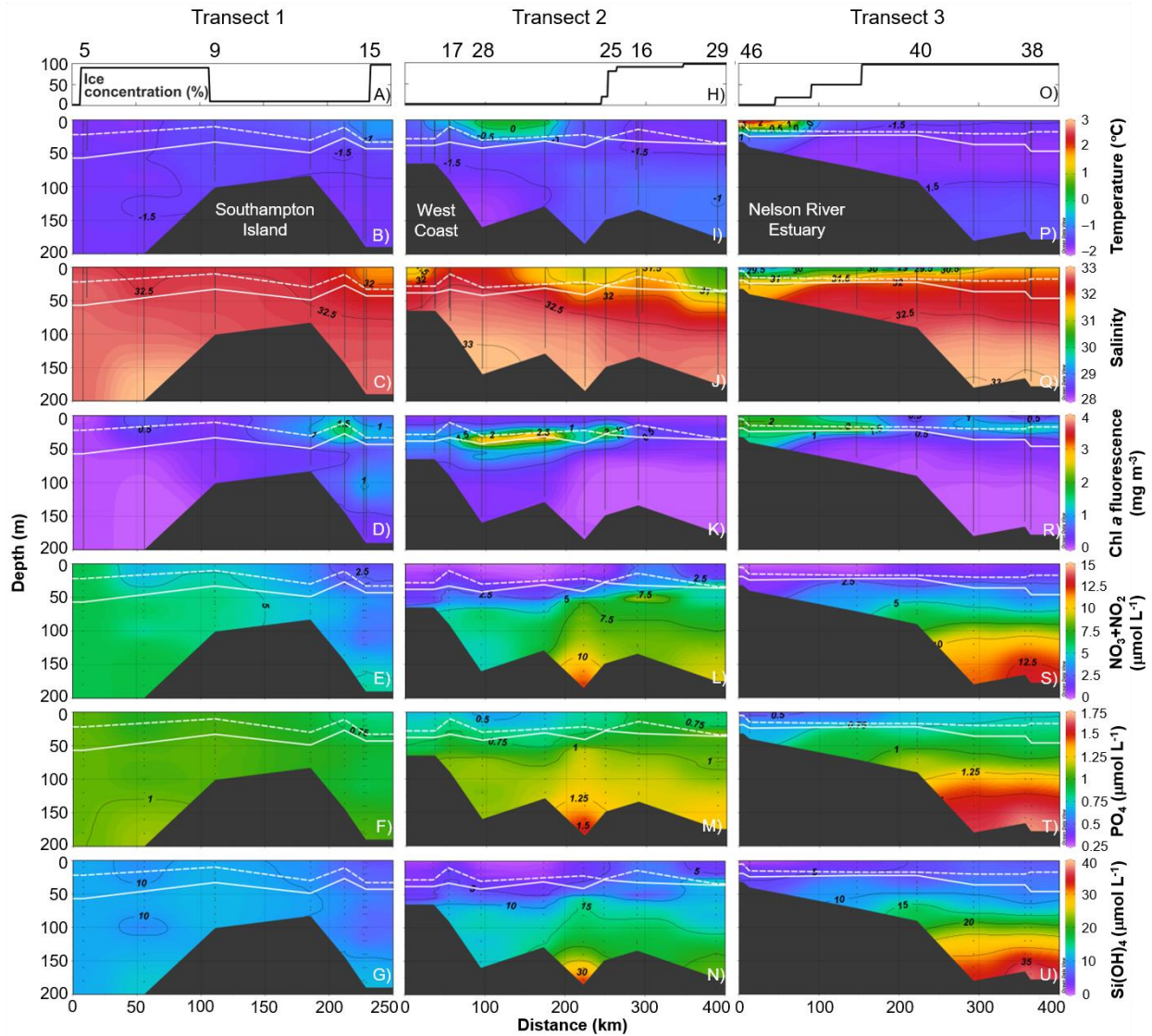
Figure 5.4: Spatial distribution of sea ice, chlorophyll *a* and nutrient concentrations, salinity and water temperature along three transects. Ice concentration from CIS ice charts (A, H, O), temperature (B, I, P), salinity (C, J, Q), *in situ* chlorophyll *a* fluorescence (D, K, R), nitrate plus nitrite (E, L, S), phosphate (F, M, T) and silicic acid (G, N, U) concentration are plotted along a transect in 1) the Narrows, 2) western and 3) central Hudson Bay as shown in Figure 1b. White lines indicate the depth of the mixed layer (dashed) and the euphotic zone (solid). Only station numbers with a complete physical and biological sampling are labelled above each panel. Additional nutrient rosette stations are shown as dotted lines in each sub-plot.

Concentrations of NO_3+NO_2, PO_4 and $Si(OH)_4$ in the ice bottom of the mobile ice cover were higher in the Narrows compared to central Hudson Bay (Table 5.1). Ice stations within central Hudson Bay further showed a spatial gradient of 2-times higher bottom-ice nutrient concentrations in the north compared to the south. Overall, bottom-ice nutrient concentrations were low with smaller N:P and N:Si molar ratios of 1.04 and 0.50, respectively, than N:P and N:Si molar ratios in the underlying surface water (Table 5.1).

1 **Table 5.1:** Measured nutrient concentrations and ratios in the Narrows and Hudson Bay. Nutrient concentrations
2 (mean ± standard error) at 2 m water depth, at 10 m above the sea floor (Z_{bot}) and in the 5 cm-ice bottom sections are
3 given for nitrate plus nitrite (NO_3+NO_2), phosphate (PO_4) and silicic acid ($Si(OH)_4$). Nutrient ratios are stated for 2
4 m, Z_{eu}, Z_{bot} and the ice-bottom section. Number of sampling stations are shown for each region with the number of ice
5 sampling sites in parentheses.

Region	Depth	NO_3+NO_2 (μmol L^{-1})	PO_4 (μmol L^{-1})	$Si(OH)_4$ (μmol L^{-1})	N:P	N:Si
Narrows **n = 4 (3)**	**2 m**	4.65 ± 0.65	0.91 ± 0.03	10.6 ± 0.4	5.04 ± 0.55	0.44 ± 0.06
	Z_{eu}	4.74 ± 0.62	0.92 ± 0.03	10.4 ± 0.35	5.13 ± 0.50	0.46 ± 0.05
	Z_{bot}	6.40 ± 0.97	0.99 ± 0.04	12.3 ± 1.3	6.40 ± 1.48	0.52 ± 0.06
	Ice bottom	1.40 ± 0.41	0.43 ± 0.02	1.82 ± 0.18	3.22 ± 0.80	0.91 ± 0.20
Western HB **n = 9**	**2 m**	0.10 ± 0.06	0.51 ± 0.02	1.83 ± 0.73	0.16 ± 0.09	0.03 ± 0.01
	Z_{eu}	1.61 ± 0.49	0.70 ± 0.04	4.67 ± 1.21	2.61 ± 0.61	0.27 ± 0.05
	Z_{bot}	4.26 ± 1.14	0.92 ± 0.09	10.3 ± 2.7	4.01 ± 0.93	0.34 ± 0.05
Central HB **n = 10 (6)**	**2 m**	1.26 ± 0.25	0.70 ± 0.02	5.77 ± 0.58	1.73 ± 0.28	0.22 ± 0.03
	Z_{eu}	3.24 ± 0.45	0.83 ± 0.03	8.03 ± 0.73	3.75 ± 0.33	0.39 ± 0.03
	Z_{bot}	7.32 ± 1.37	1.16 ± 0.11	19.0 ± 3.8	5.77 ± 0.71	0.38 ± 0.02
	Ice bottom	0.21 ± 0.10	0.19 ± 0.08	0.90 ± 0.32	1.04 ± 0.17	0.50 ± 0.29

6

5.3.4. Total chlorophyll *a* concentration and primary production

8 The spatial distribution of TChl *a* and primary production in the water column largely reflected

9 the vertical gradients of nutrient concentration in the different regions with high production

10 estimates being associated with low nutrient concentrations. Within the Narrows, TChl *a* was low

11 in the euphotic zone with values <1 mg m^{-3}, although Z_{eu} reached down to 41 ± 7 m (Fig. 5.4D,

12 Table 2.2). Integrated daily NPP of phytoplankton in this region were the lowest observed during

13 the study with a mean value of 98.4 ± 18.2 mg C m^{-2} d^{-1}.

14 In western Hudson Bay, a strong SCM, was observed between 9 and 50 m, usually between Z_m

15 and Z_{eu} (Fig. 5.4K, Table 5.2). The strongest SCM with TChl *a* between 2.6 and 4.7 mg m^{-3} was

16 observed in the center of the NW polynya, resulting in a higher $K_{d0}(PAR)$ and a slightly shallower

17 Z_{eu} of 38 ± 4 m compared to that of the Narrows (labelled 'Integration depth' in Table 2). However,

18 inshore stations 19 and 22 were characterized by a low $K_{d0}(PAR)$ of 0.12 m^{-1}, a deep Z_{eu} of 49 m

19 and low TChl *a* <1 mg m^{-3}. Inshore station 46, which was located near the Nelson River estuary,

20 differed from these characteristics with a $K_{d0}(PAR)$ of 0.23 m^{-1}, a Z_{eu} of 24 m and TChl *a* >1 mg

21 m^{-3}. NPP varied largely in the open water between 170 mg C m^{-2} d^{-1} at station 22 and 803 mg C

22 m^{-2} d^{-1} at station 17 with a mean NPP of 460 ± 70 mg C m^{-2} d^{-1} (Table 5.2).

23   Phytoplankton TChl *a* measured beneath the ice cover in central Hudson Bay exceeded 0.5 mg m^{-}

24   ^{3} throughout the euphotic zone with highest concentrations between 2.7 and 4.0 mg m^{-3} at station

25   25. These high TChl *a* in the north-central Hudson Bay resulted in high $K_{d0}(PAR)$ similar to those

26   in the NW polynya (Table S5.4) and the highest estimated NPP of 1400 mg C m^{-2} d^{-1}. Mean

27   phytoplankton NPP in central Hudson Bay was calculated at 414 ± 146 mg C m^{-2} d^{-1} with lowest

28   NPP in the south due to TChl *a* that only exceeded 1 mg m^{-3} in the shallow surface mixed layer

29   (Fig. 5.4R). However, NPP increased further into the ice from 128 mg C m^{-2} d^{-1} at station 40 to

30   391 mg C m^{-2} d^{-1} at station 36.

31   NPP measured in the ice bottom in the Narrows and central Hudson Bay and in the evolving melt

32   ponds on the ice surface within Hudson Bay were minimal due to low TChl *a* (Table 5.2). Mean

33   NPP was highest in the ice bottom in the Narrows. Overall, the combined contribution of ice algal

34   and melt pond communities to late spring primary production in Hudson Bay accounted for less

35   than 1% during this study. In contrast, the observed sub-ice diatom *Melosira arctica* contributed

36   30% to late spring production (Table 5.2). *M. arctica* was visibly observed in long strands attached

37   to the ice bottom at stations in the Narrows and north-central Hudson Bay, and present as small

38   chains in the ice-bottom in south-central Hudson Bay, except for long strands observed at station

39   38. Samples of *M. arctica* for biological analysis were collected at station 25 and 38. The measured

40   TChl *a* of 13.7 ± 0.8 mg m^{-2} and an assumed *M. arctica* mat thickness of 5 cm resulted in a NPP

41   of 378 ± 119 mg C m^{-2} d^{-1}. It is noted that these estimates are believed conservative since much

42   of *M. arctica* biomass sloughed from the ice bottom upon extraction of an ice core, making it

43   difficult to obtain a quantitative sample (Fig. S5.9). Furthermore, the NPP estimate does not

44   account for the observed patchiness of *M. arctica* aggregates due to limited sampling.

Table 5.2: Spatial variations in underwater light attenuation, integrated total chlorophyll *a* concentration and integrated net primary production rates. Mean values (± standard error) of the diffuse vertical attenuation coefficient for downwelling scalar PAR (K_{d0}), the integration depth (given as depth of euphotic zone for phytoplankton, length of bottom core for ice-algae and melt pond depth), the depth of the sub-surface chlorophyll *a* maximum (Z_{SCM}), integrated total chlorophyll *a* concentration (TChl *a*) and integrated daily net primary production rates of microalgal communities are provided for the Narrows, western and central Hudson Bay. Number of sampling stations are shown for each region with the number of ice sampling sites in brackets. *Melosira arctica* was sampled at two stations.

Region		$K_{d0}(PAR)$ (m^{-1})	Integration depth (m)	Z_{SCM} (m)	Integrated TChl *a* (mg m^{-2})	Integrated net production (mg C m^{-2} d^{-1})
Narrows **n = 4 (3)**	Phytoplankton	0.12 ± 0.01	41 ± 7	15 ± 2	13.0 ± 2.7	98.4 ± 18.2
	Bottom-ice algae	–	0.05	–	2.45 ± 0.72	2.72 ± 0.81
	*Melosira arctica**	–	–	–	–	–
	Melt pond**	–	–	–	–	–
Western HB **n = 9**	Phytoplankton	0.16 ± 0.01	38 ± 4	31 ± 4	53.5 ± 9.3	460 ± 70
Central HB **n = 10 (6)**	Phytoplankton	0.15 ± 0.02	34 ± 4	17 ± 3	33.7 ± 7.8	414 ± 146
	Bottom-ice algae	–	0.05	–	1.06 ± 0.62	1.76 ± 1.40
	Melosira arctica	–	0.05	–	13.7 ± 0.8	378 ± 119
	Melt pond	–	0.11 ± 0.02	–	0.04 ± 0.02	0.64 ± 0.27

* *Melosira arctica* was observed in the Narrows, but not sampled; **Melt ponds had not formed yet

5.3.5. Species composition of microalgal communities

CHEMTAX results, which calculate the relative contribution of each algal group to Chl *a*, and results from the inverted light microscopy suggest a flagellate-dominated phytoplankton community in the Narrows, with a particularly high relative abundance of unclassified flagellates (including prymnesiophytes, raphidophytes and choanoflagellates) in the deeper water layers of the euphotic zone between 16 and 50 m (Fig. 5.5). Diatoms made up less than 33% of the relative contribution to the main protist groups in the Narrows. Within Hudson Bay, the open and ice-covered water column was dominated by diatoms with a relative contribution of more than 61% in the surface and 64% in the deeper layers of the euphotic zone in the CHEMTAX analysis. The relative contribution of unclassified flagellates decreased to less than 17% in surface water between 0 and 15 m and 13% between 16 and 50 m. Cryptophytes, chrysophytes and prasinophytes were present in relative contributions below 14%, 7%, and 19%, respectively, at all stations while chlorophytes were only sparsely detected in the calculated pigment ratios. The microscopic analysis showed that centric and pennate diatoms were similarly abundant at the SCM with 28 and 26%, respectively, in western Hudson Bay and 19 and 24%, respectively, in central Hudson Bay. In western Hudson Bay, the most abundant centric diatoms were *Chaetoceros gelidus* (3.9 x 10^6

cells L^{-1}) and *Thalassiosira nordenskioeldii* (2.3 x 10^6 cells L^{-1}), while *Fragilariopsis cylindrus* (5.0 x 10^6 cells L^{-1}) and *Fragilariopsis oceanica* (6.5 x 10^6 cells L^{-1}) were the most abundant pennate diatoms. In central Hudson Bay, the most abundant centric diatoms were *Chaetoceros* spp. (0.8 x 10^6 cells L^{-1}) and *Thalassiosira nordenskioeldii* (0.7 x 10^6 cells L^{-1}). The most abundant pennate diatoms were *Fragilariopsis cylindrus* (1.1 x 10^6 cells L^{-1}) and *Nitzschia frigida* (1.2 x 10^6 cells L^{-1}).

Bottom-ice algal communities within Hudson Bay were dominated by diatoms with a mean relative contribution of 92% (Fig. 5.5) to Chl *a* of the major algal groups in the CHEMTAX analysis. The microscopic analysis of the bottom-ice community revealed a similar high mean relative abundance of diatoms with 82% of all cells enumerated. Pennate diatoms were especially abundant with a mean relative abundance of 66%. The most abundant pennate diatom was *Nitzschia frigida* (261.8 x 10^6 cells L^{-1}), while *Chaetoceros* spp. (75.3 x 10^6 cells L^{-1}), *Thalassiosira* spp. (29.0 x 10^6 cells L^{-1}) and *Melosira arctica* (31.2 x 10^6 cells L^{-1}) were abundant centric diatoms, Melt pond communities were also dominated by diatoms with a relative contribution of 53% in the CHEMTAX analysis but were overall more divers with a larger relative contribution of cryptophytes (18%), unclassified flagellates (15%) and prasinophytes (14%) compared to their relative contribution to Chl *a* in the bottom-ice algal communities. It is noted that sampled melt ponds were not connected to the underlying water column and salinities were between 0.2 and 4.1.
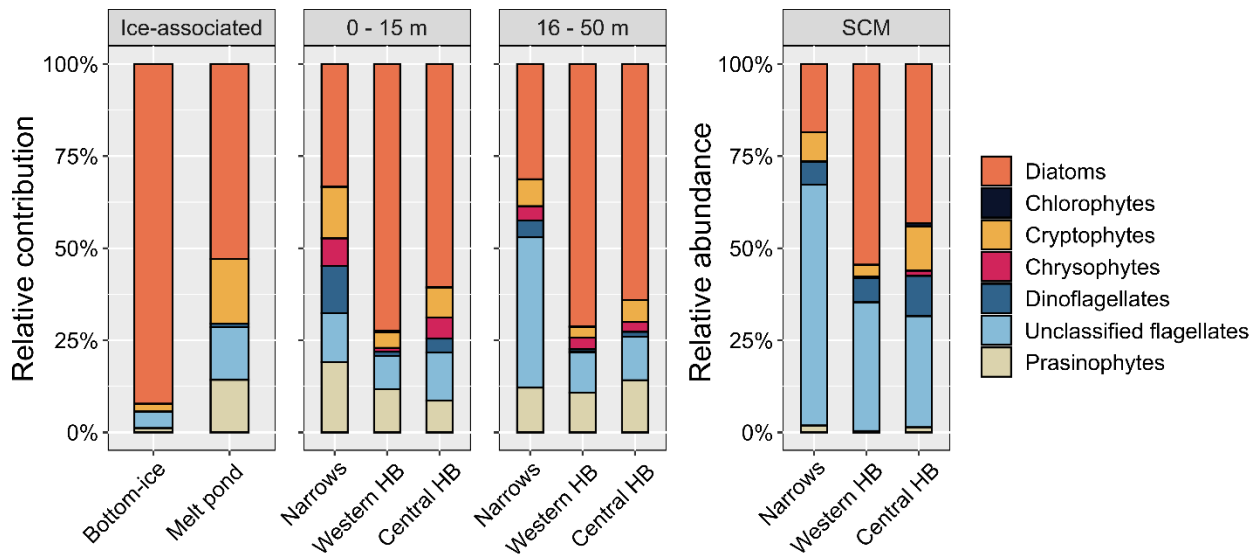
Figure 5.5: Relative contribution and abundance of the main algae groups in the Narrows and Hudson Bay. Composition of protist communities from CHEMTAX analysis (relative contribution) are presented for bottom-ice and melt pond communities (ice-associated), and phytoplankton collected between 0 – 15 m and 16 – 50 m in the Narrows, western and central Hudson Bay (HB). Phytoplankton community composition (relative abundance) at the subsurface chlorophyll maximum (SCM) was determined in microscopic analysis.

5.3.6. Photophysiology of microalgal communities

The P-E parameters varied between the microalgal communities in the different habitats (Table 5.3). P_{max}^B of phytoplankton in the open water was significantly higher ($F_{1,75} = 4.53$, p <0.05) than that beneath the ice cover. E_k and α^B were not significantly different and photoinhibition was only observed in a few under-ice surface samples. Depth influenced all three P-E parameters with significantly higher P_{max}^B ($F_{1,75} = 5.55$, p <0.05), significantly lower α^B ($F_{1,75} = 5.29$, p <0.05), and significantly higher E_k ($F_{1,75} = 36.49$, p <0.001) in the surface water. E_k was significantly higher in the open (p <0.05) and in the ice-covered surface water (p <0.001) compared to those of the deeper water layers in the respective environments.

P-E parameters of *Melosira arctica* were in the same range of phytoplankton in the ice-covered surface water. However, P_{max}^B and α^B of bottom-ice algae and melt pond communities were 3–10 times lower compared to under-ice phytoplankton. Only E_k of the bottom-ice algae was similar to that of the under-ice communities. Melt pond communities at the ice surface showed the highest and lowest E_k and α^B, respectively, and high β^B, which was not measured in other ice-associated communities.

Table 5.3: Photosynthetic parameters of microalgal communities. Maximum photosynthetic rate (P^B_{max}, mg C mg^{-1} Chl a h^{-1}, mean ± standard error), photosynthetic efficiency (α^B, mg C mg^{-1} Chl a h^{-1} (µmol photons m^{-2} s^{-1})$^{-1}$) and photoacclimation parameter (E_k, µmol photons m^{-2} s^{-1}) are given for phytoplankton in the open water and beneath the ice cover between 0 – 15 m and 16 – 50 m, for bottom-ice algae, *Melosira arctica* and melt pond communities. The number (n) of included PE curves is provided for each group.

Group	Depth	P^B_{max}	α^B	E_k	β^B
Open water **n = 13**	**0 – 15 m**	2.07 ± 0.22	0.022 ± 0.002	101 ± 12.7	0.000 ± 0.000
	16 – 50 m	1.40 ± 0.15	0.024 ± 0.002	61.0 ± 7.84	0.000 ± 0.000
Under-ice **n = 27**	**0 – 15 m**	1.50 ± 0.11	0.018 ± 0.001	84.6 ± 4.76	0.001 ± 0.001
	16 – 50 m	1.30 ± 0.21	0.026 ± 0.003	51.3 ± 4.98	0.000 ± 0.000
Bottom-ice algae **n = 8**	–	0.15 ± 0.09	0.002 ± 0.001	66.6 ± 14.0	0.000 ± 0.000
Melosira arctica **n = 2**	–	1.41 ± 0.34	0.017 ± 0.001	83.5 ± 16.3	0.000 ± 0.000
Melt pond **n = 3**	–	0.47 ± 0.22	0.004 ± 0.002	151 ± 27.5	0.008 ± 0.007

Water column POC:Chl a ratios (wt:wt) were significantly different between different environments ($F_{1,94}$ = 5.27, p <0.05) and depths ($F_{1,94}$ = 8.15, p <0.01). Mean open water ratios were 175 ± 38 (median = 134, Fig. 5.6) in the surface and 134 ± 39 (67) in the deeper layer. Under-ice POC:Chl a ratios were significantly lower at 87 ± 9.0 (72) in the surface and 67.4 ± 11.3 (52.2) in the deeper layer. The regression of POC versus Chl a (data not presented) showed no statistically significant relationships between POC and Chl a in western Hudson Bay. The y-intercept of POC versus Chl a relationships of stations in south-central HB, although significantly different from zero, were low or even negative. Mean POC:Chl a ratios of 341 ± 123 (153) for ice-bottom and 401 ± 105 (312) for melt ponds were not significantly different.

The ratio of photoprotective to photosynthetic carotenoids (PPC:PSC, wt:wt) was not significantly different between phytoplankton in the open water and ice-covered water column (Fig. 5.6). However, ratios decreased significantly with depth ($F_{1,97}$ = 43.5, p <0.001) with measured ratios of 0.28 ± 0.04 (median = 0.27, Fig. 5.6) in the open surface water and 0.17 ± 0.01 (0.17) in the deeper water. Mean ratios of under-ice phytoplankton were 0.24 ± 0.10 (0.23) in the surface and 0.16 ± 0.01 (0.16) in the deeper water. PPC:PSC ratios of ice-associated communities were significantly higher ($t_{1,11}$ = –7.14, p <0.001) in melt ponds with a mean ratio of 1.63 ± 0.30 (2.11) compared to in the ice bottom with a mean ratio of 0.27 ± 0.03 (0.27). Furthermore, bottom-ice algal communities had a higher mean PPC:PSC ratio than under-ice phytoplankton communities.
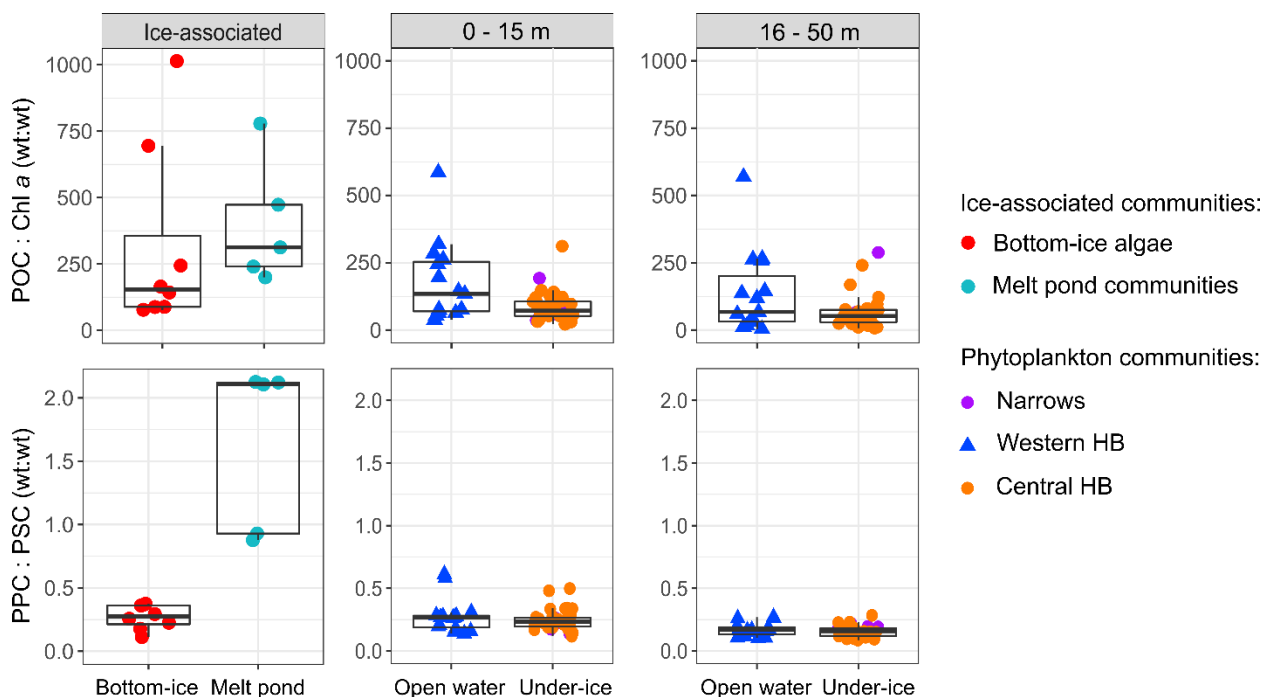
Figure 5.6: Particulate organic matter ratios and pigment ratios of microalgal communities. Ratios (wt:wt) of particulate organic carbon to Chl *a* (POC:Chl *a*) and photoprotective to photosynthetic carotenoids (PPC:PSC) of bottom-ice algal (n = 8) and melt pond communities (n = 5), and phytoplankton collected in the surface (0 – 16 m) and deeper (16 – 50 m) layer of the euphotic zone in in western Hudson Bay (n = 15) and in the Narrows and central Hudson Bay (n = 37). Boxplots show the median, the 25th and 75th percentiles, as well as 1.5 times the interquartile range as whiskers.

5.3.7. Onset of spring primary production at mooring station

Time series of Chl *a* fluorescence at the lower SCM depth (28 – 32 m) was recorded by mooring AN01 (Fig. 5.1) in SW Hudson Bay to gain more information about the timing of primary production in the water column (Fig. 5.7). In 2017, the ice cover (>8/10 concentration, CIS ice charts) was present until early July. Chl *a* fluorescence already increased in the fully ice-covered surface water layer in the beginning of June. During the following open water season of the same year, Chl *a* fluorescence decreased and could have been related to a formation of an SCM, which was observed at 37 m in late June 2018. In 2018, Chl *a* fluorescence also increased while the ice cover was still present. However, maximum Chl *a* fluorescence was measured in the open water column due to an earlier ice breakup in early June at the mooring location.
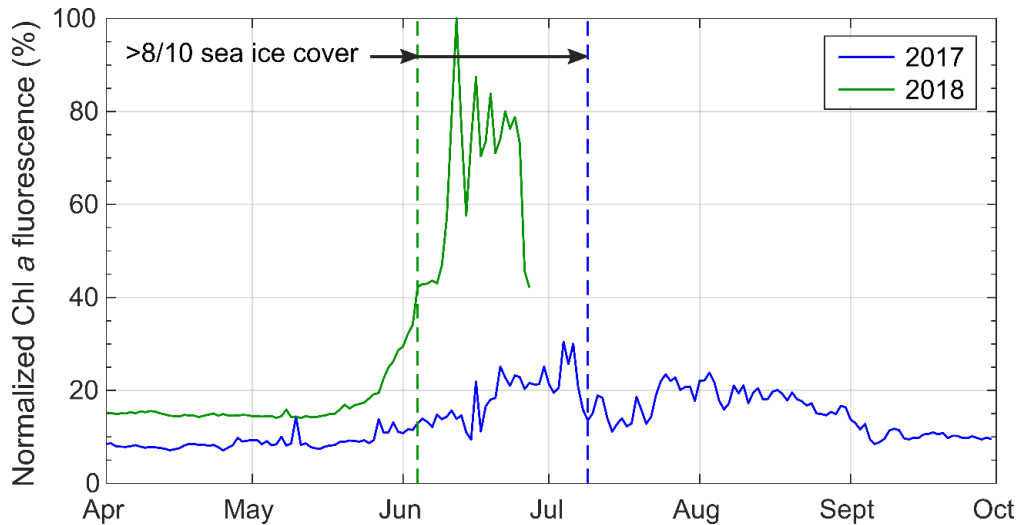
Figure 5.7: Temporal variability of chlorophyll *a* concentration in relation to sea ice cover at mooring station. Monthly change in Chl *a* fluorescence in 2017 (blue) and 2018 (green) at mooring station AN01. The presence of an ice cover with concentrations >8/10 (CIS ice charts) is indicated as dashed line and arrows.

5.4. Discussion

5.4.1. Spatiotemporal patterns of phytoplankton spring primary production

The observed large differences in primary production, biomass (TChl *a*) and phytoplankton community composition between the Narrows, western and central Hudson Bay are in line with previous observations during summer and fall. The main factors influencing these various regions are differences in freshwater input, nutrient concentrations, light conditions and distance from shore (Bursa, 1961; Anderson and Roff, 1980; Harvey et al., 1997; Ferland et al., 2011; Heikkilä et al., 2014).

5.4.1.1. Western Hudson Bay

In western Hudson Bay, surface phytoplankton communities benefitted from a continuously open latent-heat polynya in early May, that thereby increased underwater light availability and promoted strong surface stratification through solar heating as well as contributions from ice melt. Relatively high surface Chl *a* (>1.2 mg m^{-3}) was observed by satellite in late May 2018 within the first three weeks after the ice breakup (Barbedo et al., 2020). At the time of sampling in mid-June 2018, the region had been ice-free for 25 days, providing more than enough time for a surface bloom to nearly deplete $NO_3 + NO_2$ and $Si(OH)_4$ in the surface mixed layer and form a strong SCM (Fig. 5.4). PO_4 was still available throughout the euphotic zone in the entire Hudson Bay following the Redfield ratio of 16N:1P (Redfield, 1963) and, thus, was not limiting algal growth anywhere.

In early spring, primary production in the NW polynya benefits from replenished surface nutrient concentrations brought up by vertical mixing during winter months (Tremblay et al., 2019). The enhanced ice formation and brine production in the NW polynya (Landy et al., 2017; Kirillov et al., 2020; Bruneau et al., in review) can overcome stratification and deeply mix the water column to depths of 100 m by the end of winter in the region (Saucier et al., 2004; Prinsenberg, 1986). Indeed, deep water in the center of the NW polynya was the coldest and saltiest observed during our study. These waters were further characterized by a high concentration of inorganic nutrients (Table 5.1), which likely accumulate in the deep interior of the Bay due to the small water exchange with the adjacent marine water bodies and the long residence time of deep waters between 4 – 14 years within Hudson Bay (Pett and Roff, 1982; Tremblay et al., 2019). With the deep winter mixing potential, it is likely that this pool of nutrients can help increase surface production within the NW polynya.

Rivers draining into western Hudson Bay, with the largest contributors being Chesterfield Inlet in the northwest, and Churchill, Hayes and Nelson Rivers in the southwest, have not been shown to supply substantial additional inorganic nutrients during late spring to summer (Déry et al., 2011b; Tremblay et al., 2019). During our study, several coastal stations (17, 18, 19, 22, 46, Fig. 5.1B) lay within 30 to 75 km from shore and were influenced by the large cyclonic coastal buoyancy current that carries freshwater along the coast (Prinsenberg, 1983; Granskog et al., 2007; Déry et al., 2011b; St-Laurent et al., 2011). Salinities decreased in the surface mixed layer from 32.3 in the north (station 18) to 31.6 and 29.8 at southern stations (22 and 46, respectively). This boundary current reaches up to 100 km offshore and creates a fresh, 5 – 25 m thick summer mixed layer overlaying a colder subsurface layer formed during winter mixing (Granskog et al., 2009). The investigated coastal stations during this study were characterized by a shallow and fresher mixed layer of 12.0 ± 2.9 m thickness and very low nutrient concentrations. In the center of the NW polynya, the mixed layer was 22.5 ± 5.3 m. Thus, it is likely that riverine input decreases the potential of coastal primary production in this region by adding a buoyant, nutrient depleted surface layer, particularly after phytoplankton deplete surface nutrients originally replenished via winter mixing processes.

However, several studies reported an inshore-offshore gradient of higher biomass found inshore with values between $0.2 – 1.0$ mg Chl a m^{-3} versus lower biomass found offshore with values

between 0.1 – 0.5 mg Chl *a* m^{-3} in summer (Anderson and Roff, 1980; Roff and Legendre, 1986; Harvey et al., 1997; Granskog et al., 2007; Ferland et al., 2011). During summer and fall, strong tidal and wind-driven mixing can weaken surface stratification and, in combination with the entrainment of deeper salt water and accompanying nutrients into the freshwater plume via estuarine circulation, lead to increased production inshore (Kuzyk et al., 2009; Ferland et al., 2011). In late spring, the inshore-offshore gradient was reversed with a lower TChl *a* between 0.3 and 1.4 mg m^{-3} in the euphotic zone inshore compared to higher TChl *a* between 1.4 and 4.9 mg m^{-3} in the euphotic zone of the NW polynya.

Although TChl *a* at the SCM was high in the center of the NW polynya, late spring primary production was driven by phytoplankton in the surface layer. Production at the SCM, which generally occurred below the mixed layer depth near the nitracline and was associated with the 0.2 – 1% optical depth at 40 ± 4 m, only contributed 1 – 9% to total production, assuming a SCM thickness of 5 m. A well-developed SCM, often found at similar optical depths and between 20 and 60 m, is characteristic of central Hudson Bay in the summer and fall (Roff and Legendre, 1986; Harvey et al., 1997; Granskog et al., 2007; Ferland et al., 2011; Lapoussière et al., 2013). However, estimated late spring primary production of 460 mg C m^{-2} d^{-1} of the diatom-dominated phytoplankton community in western Hudson Bay was higher than the estimated production of 322 mg C m^{-2} d^{-1} in summer (Ferland et al., 2011) and of 100 mg C m^{-2} d^{-1} in fall (Lapoussière et al., 2013), which was dominated by smaller cells (0.7 – 5 μm). We conclude that the bloom was likely past its peak, although integrated phytoplankton biomass and primary production in the NW polynya were still greater than those in the Narrows and central Hudson Bay (Table 5.2).

5.4.1.2. Narrows and central Hudson Bay

Phytoplankton production in the Narrows and central Hudson Bay was driven by the formation of open water through ice export in the Narrows and by the sea ice melt and increasing melt pond formation at the ice surface in central Hudson Bay, which contributed largely to the increase in under-ice light levels, a deepening of the euphotic zone and surface stratification. Phytoplankton communities within the Narrows appeared to be in a pre- to early bloom stage with observed low biomass and NPP, which were likely the result of density instabilities in surface waters due to freezing air temperatures (Oziel et al., 2019) and stronger tidal mixing at the southern end of Foxe Basin (Drinkwater and Jones, 1987). This early stage had little impact on surface nutrient

concentrations in the Narrows, which remained relatively high throughout the water column. Later in the season, after increasing air temperatures and sea ice melt produce a more stabilized surface mixed layer (Drinkwater and Jones, 1987), these relatively nutrient replete waters create favorable conditions for a phytoplankton bloom (Ferland et al., 2011). Previously observed late summer NPP of 371 mg C m^{-2} d^{-1} (Ferland et al., 2011) in the Narrows were four times higher than our measured early June NPP of 98.4 mg C m^{-2} d^{-1}. Furthermore, the late summer production presented by Ferland et al. (2011) was also driven by a diatom-dominated community while the spring phytoplankton community observed in our study contained a large fraction of flagellates, particularly in the water column below 15 m, which is more typical of a pre-bloom stage (Norrbin et al., 2009).

In central Hudson Bay, a diatom-dominated under-ice phytoplankton bloom was observed. TChl a was high throughout the euphotic zone with no distinct SCM since nutrients were still available in the surface layer with NO_3+NO_2 concentrations just below 2 µmol L^{-1}. Under-ice NPP in the euphotic zone was highly variable with a greater NPP of 612 mg C m^{-2} d^{-1} in north-central Hudson Bay compared to 215 mg C m^{-2} d^{-1} in south-central Hudson Bay. Several environmental conditions may have caused these regional differences. North-central ice stations (16, 21, 24, 25, 29) were in proximity of the incoming polar surface and Atlantic water through Foxe Basin and Hudson Strait, respectively, which represents an external nutrient source for an ice-edge/under-ice bloom. Satellite observations suggested moderate surface Chl a (0.2 to 0.5 mg m^{-3}) immediately after the break-up followed by a decreasing trend as the season progressed (Barbedo et al., 2020). This is consistent with our *in situ* observations.

The south-central ice stations 32 and 34 were only 44 – 65 km away from shore and were characterized by a shallow mixed layer with a low surface salinity (Table S5.4) indicating the influence of the previously mentioned coastal buoyancy current. This current also carries an elevated CDOM concentration, particularly in the south (Granskog et al., 2009), which could explain the observed high PAR attenuation of 0.19 and 0.27 m^{-1} at stations 32 and 42, respectively. The high K_{d0}(PAR) in combination with measured low $\overline{T}$(PAR) of 0.01 through ice floes thicker than 2 m resulted in a shallow Z_{eu} and, subsequently, low NPP. (Barber et al., in press) further described a vast area of thick (>10 m), heavily deformed sediment-laden sea ice in this region, which, with its thickness, prolongs ice melt till August and could limit light availability and

ultimately primary production during spring and summer in this area. Additionally, the calculated low integrated surface nutrient concentrations over the euphotic zone in south-central Hudson Bay (Fig. 5.4) indicate an overall lower potential for under-ice production compared to the ice-covered northern region. This phenomenon of low surface nutrient concentrations at the beginning of the sea ice melt could be a function of the localized cyclonic circulation of water with lower nutrient concentrations in this region (Ridenour et al., 2019).

Previous studies on landfast ice in southeastern Hudson Bay reported the formation of under-ice blooms after freshwater from snow and ice melt stabilized the water column in late May (Legendre et al., 1981; Runge et al., 1991; Michel et al., 1993). The observed blooms reached maximum Chl a between 1.5 and 2.7 mg m^{-3} in the surface water, which is similar to the TChl a of 1.8 mg m^{-3} that we observed in the ice-covered surface mixed layer in June 2018. The Chl a fluorescence sensor attached to mooring AN01 at 30 m detected an increase in Chl a fluorescence at the beginning of June 2018, highlighting an early onset of under-ice primary production (Fig. 5.7). A similar trend of an under-ice Chl a accumulation was observed at the mooring site in 2018. However, the ice broke up a month earlier in early June, which fuelled a phytoplankton bloom in the open water at the ice edge (Barbedo et al., 2020). Under-ice blooms occur in Hudson Bay as evidenced from our and the historical record of blooms beneath landfast ice. However, considering the calculated mean integrated TChl a of 35.10 mg m^{-2} over the ice-covered euphotic zone in central Hudson Bay (Table 5.2), phytoplankton biomass was comparable to the central Arctic Ocean, but much lower than under-ice blooms in the Arctic shelf regions (Ardyna, Mundy, Mayot, et al., 2020).

5.4.1.3. Phytoplankton photophysiology

The investigation of the state of photoacclimation of the phytoplankton communities showed that communities displayed greater light (shade) acclimation near the surface (deeper waters). In the open water, surface communities synthesized more photoprotective carotenoids, displayed in the significantly greater PPC:PSC ratio, that dissipate excess light energy via nonphotochemical quenching (Hill et al., 2005; Alou-Font et al., 2016; Joy-Warren et al., 2019; Kauko et al., 2019) compared to communities in the deeper layer of the euphotic zone. However, the significantly greater POC:Chl a in the open water surface layer cannot necessarily be attributed to a lower amount of light-absorbing pigments due to the potential for increased contribution of detritus to

POC during late-bloom stages. Nevertheless, these acclimation mechanisms help explain the greater P_{max}^B of surface communities than that at the SCM. Our observations are also consistent with Huot et al. (2013) who found decreasing P_{max}^B with depth in the Beaufort Sea and in the Canadian Archipelago.

In the ice-covered surface layer, the phytoplankton community was acclimated to the reduced light, however increasing light levels displaying a greater E_k, lower α^B and a higher PPC:PSC ratio compared to phytoplankton found in the deeper ice-covered water. P_{max}^B as well as POC:Chl a ratios of the surface community were similar to those observed during the large under-ice phytoplankton bloom in the Chukchi Sea (Palmer et al., 2013; Arrigo et al., 2014). This observed capacity to acclimate to the variable light conditions in the different environments demonstrates a considerable plasticity of the photosynthetic apparatus of phytoplankton over large spatial scales and is in line with observations of Arctic phytoplankton by Palmer et al. (2011) and Lewis et al. (2019).

5.4.2. Ice-associated primary production in central Hudson Bay

In late spring, three ice-associated communities, namely melt-pond algae, bottom-ice algae and the sub-ice algae with varying contributions to the late spring primary production were identified in central Hudson Bay. NPP of bottom-ice algal and melt pond communities were insignificant compared to NPP of the sub-ice algae *Melosira arctica*, which was found in large, but patchy quantities growing attached to the bottom of ice floes mainly in the north-central region and the Narrows. This sub-ice algal species benefits from relatively high light transmission through melting sea ice, while having access to surface water nutrients through its large filaments. It has also been found to significantly increase local primary production in the otherwise marginally productive central Arctic (Gutt, 1995; Gosselin et al., 1997; Fernández-Méndez et al., 2014; 2015). Sub-ice algae could play a similar key role in carbon export in central Hudson Bay since our conservative estimates of NPP were on the same order of magnitude as the rates of the observed under-ice phytoplankton bloom. Filament samples showed a biomass of 13.7 ± 0.8 mg Chl a m^{-2}, which corresponds to the lower end of the *Melosira* aggregate biomass of $14 - 44$ mg Chl a m^{-2} sampled in the central Arctic (Fernández-Méndez et al., 2014). However, due to the sporadic sampling, it was not possible to quantify the biomass and production of *M. arctica* in central

Hudson Bay. Images from the ice edge showed extensive coverage, highlighting the need for future investigation of the role of *M. arctica* during the spring bloom (Fig. S5.9).

Bottom-ice algal communities had a much lower biomass compared to previous observations in landfast sea ice (Gosselin et al., 1986; Welch et al., 1991; Michel et al., 1993) and were likely already in a post-bloom state with partial biomass loss through ice bottom melt, reflected also in the relatively high sea ice temperatures. The measured low molar nutrient ratios of N:P and N:Si of 1.04 and 0.50, respectively, in the ice bottom as well as the high POC:Chl *a* ratios of ice algal cells suggest a strong nitrogen depletion (Gosselin et al., 1990; Campbell et al., 2016; Dalman et al., 2019) and are typical of a post-bloom scenario in the Canadian Arctic (Niemi and Michel, 2015). Much higher biomass was previously observed between March and May in landfast ice with Chl *a* between 27.0 and 170.0 mg m^{-2} in northwestern Hudson Bay near Chesterfield Inlet (Bergmann et al., 1991; Welch et al., 1991) and between 23.6 and 39.7 mg m^{-2} in southeastern Hudson Bay (Freeman, 1982; Gosselin et al., 1986; Michel et al., 1993), suggesting that sea ice can play an important role in the overall carbon budget of Hudson Bay.

Despite being in a nutrient-limited post-bloom stage, bottom-ice algae were well acclimated to the high light levels during melt pond formation at the ice surface. Elevated concentrations of photoprotective carotenoids with PPC:PSC ratios even higher than in under-ice phytoplankton communities in the surface water as well as a significantly higher E_k were found throughout the sampled mobile ice cover and correspond to acclimated Arctic ice algal communities during advanced melt stages (Michel et al., 1988; Mundy et al., 2011; Galindo et al., 2017). However, the observed mean PPC:PSC ratios of 0.27 during the post-bloom stage were much lower than previously reported post-bloom ratios in the Canadian Arctic (up to 1 – 3.5, Alou-Font et al., 2013; up to 0.81, Galindo et al., 2017) and were only found in the melt pond samples. Since our bottom-ice algal communities were not photoinhibited despite the relatively high under-ice light levels, we conclude that ice algae have the opportunity to photoacclimate and reduce susceptibility to photoinhibition (Michel et al., 1988; Juhl and Krembs, 2010). Nevertheless, P_{max}^B was much lower than previously observed in the landfast ice (Gosselin et al., 1985; Gosselin et al., 1986; Michel et al., 1988; Bergmann et al., 1991), and could be explained by an additional nitrogen limitation (Campbell et al., 2016).

Melt pond communities were subject to even higher light levels near the ice surface and, therefore, showed the highest E_k and PPC:PSC ratios of all microalgal communities in this study and increased photoinhibition. P^B_{max} and E_k were in the range of P-E parameters measured in melt pond algae in the Arctic Ocean (Lee et al., 2012; Fernández-Méndez et al., 2015). During melt pond formation, sea ice algae can get trapped at the surface and need to rapidly adapt to the changing conditions of high light levels, variable salinities and a potential nutrient limitation as observed elsewhere (Mundy et al., 2011; Fernández-Méndez et al., 2015; Sørensen et al., 2017). Mundy et al. (2011) further observed a high abundance of flagellates, which overlaps with the findings of this study. Overall, the contribution of melt pond communities to late spring primary production in Hudson Bay was inconsequential due to a low biomass and low NPP. This conclusion is in contrast to observations on MYI and FYI in the central Arctic, where measured melt pond algal biomass was up to eight times higher with daily production rates of $0.8 - 60$ mg C m^{-2} (Fernández-Méndez et al., 2015) resulting in a contribution of $1 - 10\%$ to total NPP in the central Arctic (Lee et al., 2012; Fernández-Méndez et al., 2015).

5.4.3. Estimation of annual primary production

Figure 8 summarizes existing data on ice algal and phytoplankton production in the open and ice-covered water column from direct field measurements and satellite-derived Chl *a* (data can be found in Table S5.8). Total particulate annual production of microalgal communities was estimated at 72 g C m^{-2} yr^{-1} in Hudson Bay and represents the sum of seasonal production in early spring (March – May) and during the spring melt (June) and ice-free period (July – November; Table S5.9). Growth season of bottom-ice algae in the peripheral landfast sea ice starts in March, while an increase in under-ice phytoplankton Chl *a* was measured in May. Primary production during the sea ice melt is driven by phytoplankton in the open and ice-covered water column with a significant contribution of *Melosira arctica* in central Hudson Bay. Our estimate shows that 32% to annual biomass is produced during the 34-day melt period.

Seasonal production in the ice-free water represents 57% of annual production and is supported by a lengthening of the growth season to 146 open water days between 2008 – 2018 compared to an estimated growth season of 120 days in previous annual primary production estimates (Ferland et al., 2011). This is in line with observation of an increase in primary production found on a pan-Arctic scale (Arrigo and van Dijken, 2015). Satellite-derived daily production rates were not

included in the estimation of seasonal production as these rates seem to largely underestimate production in the open water (Fig. 5.8). Overall, our updated estimate of annual production is almost twice as high as annual estimates of 24 – 39 g C m^{-2} yr^{-1} based on post-bloom summer and fall measurements (Roff and Legendre, 1986; Jones and Anderson, 1994; Ferland et al., 2011) and satellite-derived annual rates of ~20 – 25 g C m^{-2} yr^{-1} for the open water season (Bélanger et al., 2013), but in the range of modelled annual primary production of 50 – 80 g C m^{-2} yr^{-1} (Sibert et al., 2011).
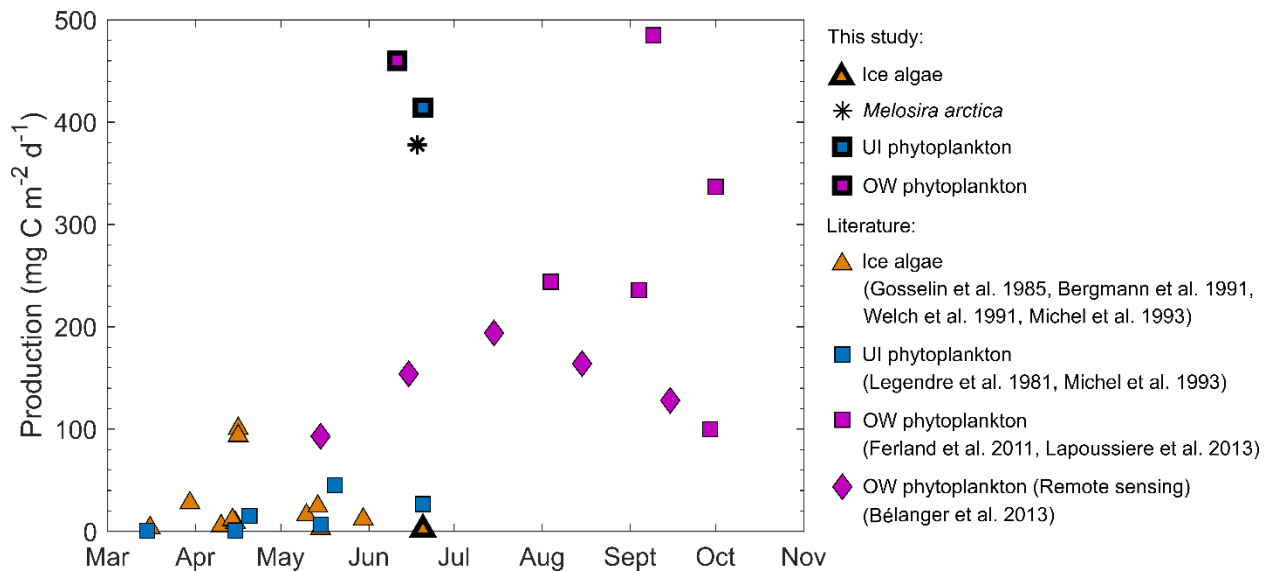
Figure 5.8: Seasonal production of microalgal communities in Hudson Bay. Daily primary production of bottom-ice algae (orange triangles), under-ice phytoplankton (UI, blue squares), open-water phytoplankton (OW, purple squares) and satellite-derived phytoplankton production in the open water (purple diamonds) was extracted from the literature. Production of bottom-ice algae (thick black outlined orange triangles), *Melosira arctica* (asterisk), under-ice phytoplankton (thick black outlined blue square) and open-water phytoplankton (thick black outlined purple squares) in June were measured in this study.

5.5. Conclusion

This study has revised the total estimated annual primary production in Hudson Bay from 21.5 – 39 g C m^{-2} yr^{-1} to 72 g C m^{-2} yr^{-1} by including the first measurements of primary production in late spring. This estimate includes the first scientific observations of the sub-ice diatom *Melosira arctica* in Hudson Bay. The diatom-dominated spring bloom is driven by phytoplankton production in the surface layer beneath the melting ice cover in central Hudson Bay and at the SCM in the open water of western Hudson Bay. The measured high production rates in the ice-covered and open water thereby highlight the considerable plasticity of phytoplankton photosynthetic performance in the variable light environment of the Hudson Bay Complex.

However, capturing the peak in production and biomass by the different microalgal communities is challenging due to the spatiotemporal variability in the environmental factors. In this study, we were not able to quantify the contribution of bottom-ice algae to primary production in central Hudson Bay because, by the time we reached the sampling area in mid-June, the ice-algal community was already in a post-bloom state. Instead, our observations have shown that the thin mobile ice cover in the north-central region provides a favourable habitat for *M. arctica*, which has the potential to significantly contribute to spring primary production in Hudson Bay.

Climate induced trends towards earlier sea ice breakup and delayed freeze-up will likely have a negative impact on habitat availability for ice-associated communities such as *M. arctica* and may shift peak production earlier in Hudson Bay. An extended open water season will further increase the amount of light and heat received in the surface water in spring and will lead to changes in the timing of the phytoplankton bloom. While the spring bloom may develop earlier in the year, the longer open water season in fall combined with the projected increase in wind speeds in the Hudson Bay region (Steiner et al., 2013) could enhance mixing and result in greater access to the deep nutrient pool in the Bay. Freshwater discharge into Hudson Bay is projected to increase considerably, particularly in winter and spring, due to increased air temperature and precipitation (Stadnyk et al., 2019). This freshwater addition in winter counters the addition of brine from sea ice formation in polynyas and leads (Eastwood et al., 2020), resulting in reduced mixing and thus a reduced replenishment of the surface nutrient inventory during winter. Ultimately, such a change could lead to a decrease in spring primary production in the NW polynya, which we have shown is the largest regional contributor to annual production in Hudson Bay. It also highlights the possibility to use Hudson Bay as a small-scale model system for the entire Arctic Ocean to investigate the interplay of increasing freshwater buoyancy input and the increase in turbulent mixing processes caused by an intensification of storms, strong tides and brine rejection during sea ice formation, and their impact on future nutrient availability and primary production potential in Arctic surface waters.

To gain more knowledge about the response of microalgal communities to the rapidly changing environmental conditions, the marine environment of Hudson Bay needs to be monitored more frequently with annual resolution. In the future, more autonomous observing systems such as moorings, autonomous underwater vehicles (e.g. gliders) or drifting buoy systems should be

deployed in the three key regions presented here, which can collect year-round and multiannual datasets of biogeochemical cycles especially in the winter-spring and summer-fall transitions when sea ice is present

Supplemental material

Table S5.4: Physical parameters of 23 stations sampled in Hudson Bay in June 2018. Parameters were used in the principal component analysis (PCA) to cluster stations into regions. The environmental parameters are the ice concentration (%) retrieved from ice charts, days of open water days prior to sampling (DOW), diffuse vertical attenuation coefficient for downwelling scalar PAR (K_{d0}), depth of the euphotic zone ($Z_{eu,}$ not used in PCA), depth of mixed layer (Z_m), average temperature of the mixed layer (T_m), average salinity of the mixed layer (S_m), and integrated concentration of nitrate plus nitrite (NO_{X_eu}), phosphate ($PO_{4\_eu,}$) and silicic acid ($Si(OH)_{4\_eu}$) over the euphotic zone.

Station	Ice conc. (tenth)	DOW	K_{d0} (m^{-1})	Z_{eu} (m)	Z_m (m)	T_m (°C)	S_m	NO_{x_eu} ($mmol\ m^{-2}$)	PO_{4_eu} ($mmol\ m^{-2}$)	$Si(OH)_{4\_eu}$ ($mmol\ m^{-2}$)
5	9	0	0.10	54	22	-1.57	32.7	345	53.3	581
9	1	0	0.11	33	10	-1.32	32.5	188	32.1	389
11	9.7	0	0.15	26	35	-1.65	30.7	87.9	22.5	277
15	5	1	0.10	52	22	-1.58	31.9	213	45.8	487
16	9.7	0	0.11	34	14	-1.51	31.6	128	29.2	296
17	0	23	0.18	31	10	-0.65	32.4	50.6	23.7	204
18	0.3	23	0.17	23	21	-0.90	32.2	18.0	8.97	153
19	0	30	0.12	49	10	-0.42	32.9	1.44	28.1	4.16
20	0	24	0.19	34	15	0.03	32.0	17.5	19.3	127
21	9.7	0	0.12	38	17	-1.36	31.5	74.8	27.9	202
22	0	27	0.12	53	4	1.76	31.6	0.41	32.3	0.65
23	0	23	0.16	37	33	0.16	32.6	1.53	17.2	1.77
24	9	0	0.09	44	22	-1.33	31.1	56.3	31.5	178
25	9	0	0.17	31	27	-1.22	31.3	46.3	22.3	181
28	0	31	0.16	40	30	0.72	32.3	21.0	21.0	51.5
29	9.7	9	0.13	38	34	-1.54	30.8	83.6	29.2	225
32	9.7	0	0.19	30	15	-1.50	30.4	29.0	18.9	151
34	9.7	0	0.27	9	11	-0.80	29.8	11.1	5.8	71.4
36	9.7	0	0.13	38	4	-1.57	31.5	90.2	31.6	324
38	9.7	0	0.08	50	17	-1.54	31.9	102	40.8	374
40	9.7	0	0.19	24	17	-1.56	31.9	27.4	17.1	118
44	0.3	14	0.11	54	12	0.83	31.0	48.7	37.9	246
46	0	30	0.23	24	15	1.92	29.8	12.6	14.1	84.4

Table S5.5: Initial and final (after CHEMTAX optimization) pigment to chlorophyll a ratios for sea-ice algae. The initial matrix was taken from Alou-Font et al. (2013). Pigment abbreviations: Chl *c3* = chlorophyll *c3*; Chl *c2* = chlorophyll *c2*; Peri = peridinin; But-Fuco = 19-butanoyl-oxy-fucoxanthin; Fuco = fucoxanthin; Allo = alloxanthin; Lut = lutein; Chl *b* = chlorophyll *b*; Neo = neoxanthin and Chl *a* = chlorophyll *a*. RMS: root mean square error.

Class / Pigment	Chl *c3*	Chl *c2*	Peri	But-Fuco	Fuco	Allo	Lut	Chl *b*	Neo	Chl *a*
Initial ratio matrix										
Diat1	0	0.189	0	0	0.7	0	0	0	0	1
Diat2	0.066	0.299	0	0	1.1	0	0	0	0	1
Crypto	0	0.2	0	0	0	0.229	0	0	0	1
Dino	0	0.162	0.675	0	0	0	0	0	0	1
Prasino2	0	0	0	0	0	0	0.049	0.418	0.017	1
Flagel	0.145	0.08	0	0.039	0.125	0	0	0	0	1
Final ratio matrix (RMS = 0.12)										
Diat1	0	0.069	0	0	0.654	0	0	0	0	1
Diat2	0.050	0.363	0	0	1.101	0	0	0	0	1
Crypto	0	0.072	0	0	0	0.303	0	0	0	1
Dino	0	0.180	0.713	0	0	0	0	0	0	1
Prasino2	0	0	0	0	0	0	0.061	0.367	0.018	1
Flagel	0.014	0.058	0	0.150063	0.142	0	0	0	0	1

Table S5.6: Initial pigment to chlorophyll a ratio for each phytoplankton group. The initial matrix was taken from Coupel et al. (2015) and Fragoso et al. (2017). Pigment abbreviations: Chl c3 = chlorophyll c3; Chl c2 = chlorophyll c2; Peri = peridinin; But-Fuco = 19-butanoyl-oxy-fucoxanthin; Fuco = fucoxanthin; Pras = Prasinoxanthin; Hex-fuco = 19-hexanoyl-oxy-fucoxanthin; Zea = Zeaxanthin; Allo = alloxanthin; Lut = lutein; Chl b = chlorophyll b; Neo = neoxanthin and Chl a = chlorophyll a. RMS: root mean square error.

Class / Pigment	Depth	Chl c3	Chl c2	Peri	But-fuco	Fuco	Pras	Hex-fuco	Zea	Allo	Lut	Chl b	Neo	Chl a
Initial ratio matrix														
Diat	0 – 15 m	0	0.192	0	0	0.495	0	0	0	0	0	0	0	1
	16 – 50 m	0	0.171	0	0	0.424	0	0	0	0	0	0	0	1
Chloro	0 – 15 m	0	0	0	0	0	0	0	0	0	0.12	0.217	0.023	1
	16 – 50 m	0	0	0	0	0	0	0	0	0	0.143	0.037	0.035	1
Crypto	0 – 15 m	0	0.075	0	0	0	0	0	0	0.201	0	0	0	1
	16 – 50 m	0	0.079	0	0	0	0	0	0	0.162	0	0	0	1
Chryso	0 – 15 m	0.044	0.111	0	0.324	0.131	0	0	0	0	0	0	0	1
	16 – 50 m	0.038	0.105	0	0.386	0.141	0	0	0	0	0	0	0	1
Dino	0 – 15 m	0	0	0.285	0	0	0	0	0	0	0	0	0	1
	16 – 50 m	0	0	0.375	0	0	0	0	0	0	0	0	0	1
Flagel	0 – 15 m	0.145	0.08	0	0.039	0.125	0	0.056	0	0	0	0	0	1
	16 – 50 m	0.133	0.072	0	0.046	0.171	0	0.11	0	0	0	0	0	1
Prasino2	0 – 15 m	0	0	0	0	0	0	0	0.035	0	0.049	0.418	0.017	1
	16 – 50 m	0	0	0	0	0	0	0	0	0	0.02	0.424	0.03	1
Prasino3	0 – 15 m	0	0	0	0	0	0.136	0	0.057	0	0.005	0.222	0.043	1
	16 – 50 m	0	0	0	0	0	0.209	0	0	0	0.004	0.271	0.054	1
Phaeocys	0 – 15 m	0.167	0	0	0	0.188	0	0	0	0	0	0	0	1
	16 – 50 m	0.276	0.167	0	0.373	0.476	0	0.684	0	0	0	0	0	1

Table S5.7: Final (after CHEMTAX optimization) pigment to chlorophyll a ratio for each phytoplankton group. The initial matrix was taken from Coupel et al. (2015) and Fragoso et al. (2017). Pigment abbreviations: Chl *c3* = chlorophyll *c3*; Chl *c2* = chlorophyll *c2*; Peri = peridinin; But-Fuco = 19-butanoyl-oxy-fucoxanthin; Fuco = fucoxanthin; Pras = Prasinoxanthin; Hex-fuco = 19-hexanoyl-oxy-fucoxanthin; Zea = Zeaxanthin; Allo = alloxanthin; Lut = lutein; Chl *b* = chlorophyll *b*; Neo = neoxanthin and Chl *a* = chlorophyll *a*. RMS: root mean square error.

Class / Pigment	Depth	Chl *c3*	Chl *c2*	Peri	But-fuco	Fuco	Pras	Hex-fuco	Zea	Allo	Lut	Chl *b*	Neo	Chl *a*
Final ratio matrix (RMS = 0.11 (0 – 15 m), RMS = 0.07 (16 – 50 m))														
Diat	0 – 15 m	0	0.174	0	0	0.590	0	0	0	0	0	0	0	1
	16 – 50 m	0	0.156	0	0	0.534	0	0	0	0	0	0	0	1
Chloro	0 – 15 m	0	0	0	0	0	0	0	0	0	0.148	0.179	0.020	1
	16 – 50 m	0	0	0	0	0	0	0	0	0	0.151	0.037	0.036	1
Crypto	0 – 15 m	0	0.092	0	0	0	0	0	0	0.256	0	0	0	1
	16 – 50 m	0	0.078	0	0	0	0	0	0	0.188	0	0	0	1
Chryso	0 – 15 m	0.039	0.107	0	0.276	0.127	0	0	0	0	0	0	0	1
	16 – 50 m	0.033	0.110	0	0.455	0.157	0	0	0	0	0	0	0	1
Dino	0 – 15 m	0	0	0.365	0	0	0	0	0	0	0	0	0	1
	16 – 50 m	0	0	0.361	0	0	0	0	0	0	0	0	0	1
Flagel	0 – 15 m	0.106	0.084	0	0.038	0.130	0	0.112	0	0	0	0	0	1
	16 – 50 m	0.339	0.064	0	0.010	0.154	0	0.016	0	0	0	0	0	1
Prasino2	0 – 15 m	0	0	0	0	0	0	0	0.032	0	0.037	0.579	0.016	1
	16 – 50 m	0	0	0	0	0	0	0	0	0	0.018	0.542	0.025	1
Prasino3	0 – 15 m	0	0	0	0	0	0.158	0	0.059	0	0.005	0.261	0.049	1
	16 – 50 m	0	0	0	0	0	0.201	0	0	0	0.004	0.286	0.052	1
Phaeocys	0 – 15 m	0.265	0	0	0	0.160	0	0	0	0	0	0	0	1
	16 – 50 m	0.259	0.158	0	0.394	0.521	0	0.760	0	0	0	0	0	1
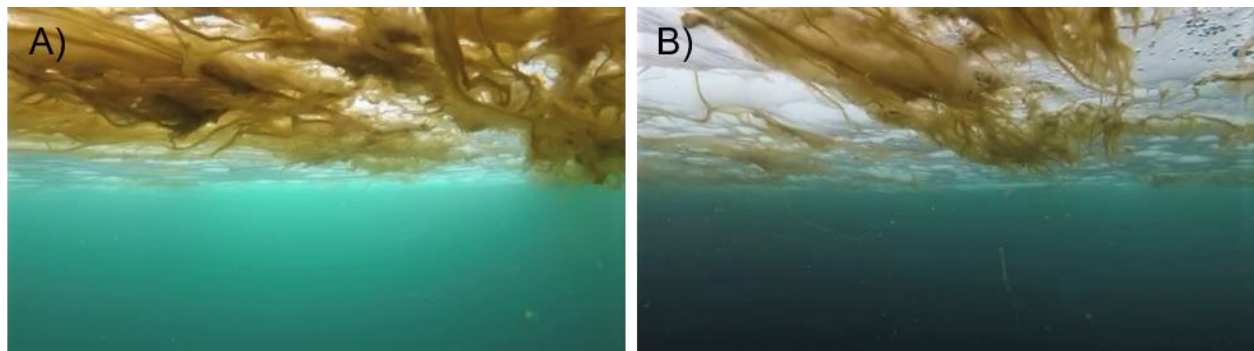
Figure S5.9: *Melosira arctica* growing attached to the bottom of first-year sea ice in central Hudson Bay at Station 25. (Photo credit: L. Dalman).

Table S5.8: Historical and measured seasonal primary production of microalgal communities in Hudson Bay. Historical data and data from this study presented in Figure 5.8. Daily production rates were extracted from the stated references or were calculated as net accumulation from provided Chl *a* in the references (*).

Reference	Community	Region	Date	Primary production $(mg\ m^{-2}\ d^{-1})$
Gosselin et al 1985*	Bottom-ice algae	East	10-Apr-1982	5.5
	Bottom-ice algae	East	10-May-1982	15.9
Michel et al. 1993*	Bottom-ice algae	East	15-Apr-1986	8.6
	Bottom-ice algae	East	15-May-1986	2.8
Welch et al. 1991*	Bottom-ice algae station 1	West	14-Mar-1988	3.6
	Bottom-ice algae station 1	West	14-Apr-1988	11.4
	Bottom-ice algae station 1	West	14-May-1988	24.6
	Bottom-ice algae station 2	West	30-Mar-1988	27.8
	Bottom-ice algae station 2	West	16-Apr-1988	101
	Bottom-ice algae station 2	West	16-May-1988	93.5
Bergmann et al. 1991	Bottom-ice algae	West	30-May-1988	12.0
Legendre et al. 1981*	Under-ice phytoplankton	East	15-Feb-1978	1.3
	Under-ice phytoplankton	East	15-Mar-1978	0.7
	Under-ice phytoplankton	East	15-Apr-1978	1.0
	Under-ice phytoplankton	East	15-May-1978	6.6
Michel et al. 1993*	Under-ice phytoplankton	East	20-Apr-1986	15.3
	Under-ice phytoplankton	East	20-May-1986	45.1
	Under-ice phytoplankton	East	20-Jun-1986	26.8
This study	Open-water phytoplankton	West	11-Jun-2018	460
	Under-ice phytoplankton	West	20-Jun-2018	414
	Bottom-ice algae	West	20-Jun-2018	1.8
	Melosira arctica	West	18-Jun-2018	378
Bélanger et al. 2013	Open-water phytoplankton	Entire Bay	May 1998 – 2010	93
	Open-water phytoplankton	Entire Bay	Jun 1998 – 2010	154
	Open-water phytoplankton	Entire Bay	Jul 1998 – 2010	194
	Open-water phytoplankton	Entire Bay	Aug 1998 – 2010	164
	Open-water phytoplankton	Entire Bay	Sep 1998 – 2010	128
Ferland et al. 2011	Open-water phytoplankton	West	04-Aug-2004	244
	Open-water phytoplankton	West	04-Sep-2005	236
	Open-water phytoplankton	West	09-Sep-2006	485
Lapoussiere et al. 2013	Open-water phytoplankton	West	29-Sep-2005	100
	Open-water phytoplankton	East	01-Oct-2005	337

Table S5.9: Seasonal and annual primary production in Hudson Bay. Seasonal production was calculated for early spring by multiplying 92 days with the mean daily rate of this season, for the spring melt by multiplying 34 melt days with the mean daily rate, and for the ice-free period by multiplying 146 open water days with the mean daily rate. Total annual production is calculated as the sum of seasonal production.

Season	Mean daily primary production (mg C m^{-2} d^{-1})	Seasonal primary production (g C m^{-2})
Winter (Dec – Feb)	0.0	0.0
Early spring (Mar – May)	85.5	7.9
Spring melt (Jun)	680	23.1
Ice-free (Jul – Nov)	280	40.9
Total annual production (g C m^{-2} yr^{-1})		**71.9**

6. Chapter – Summary and conclusions

6.1. Summary of major contributions

This thesis made three main contributions to knowledge in marine optics and Arctic primary production bringing together detailed spectral irradiance measurement in the ice-covered water column and biological measurements of different microalgal communities during the sea ice melt in late spring. Figure 6.1 summarizes the important findings of **Chapters 3 (contribution 1)** and **4 (contribution 2)** about the dependence of PAR propagation on the state of ice surface melt. These findings were integrated in the estimation and interpretation of spatially variable primary production in Hudson Bay during the spring ice melt in **Chapter 5 (contribution 3)**. As demonstrated in **Chapter 3**, regional estimates of surface albedo and PAR transmittance that account for the spatially heterogeneous sea and ice surface provide a more representative estimate of underwater light availability over larger spatial scales. Hence, areal fractions of open water, snow-covered or white ice and melt ponds gained from RPAS images in combination with single point irradiance measurements above and beneath these ice surface types were used to calculate weighted averages of PAR albedo and transmittance in the ice-covered sub-regions in **Chapter 5**. The measured decrease in albedo and increase in transmittance throughout the sampling period matched the observed ice surface melt progression with increasing melt pond formation in Hudson Bay.
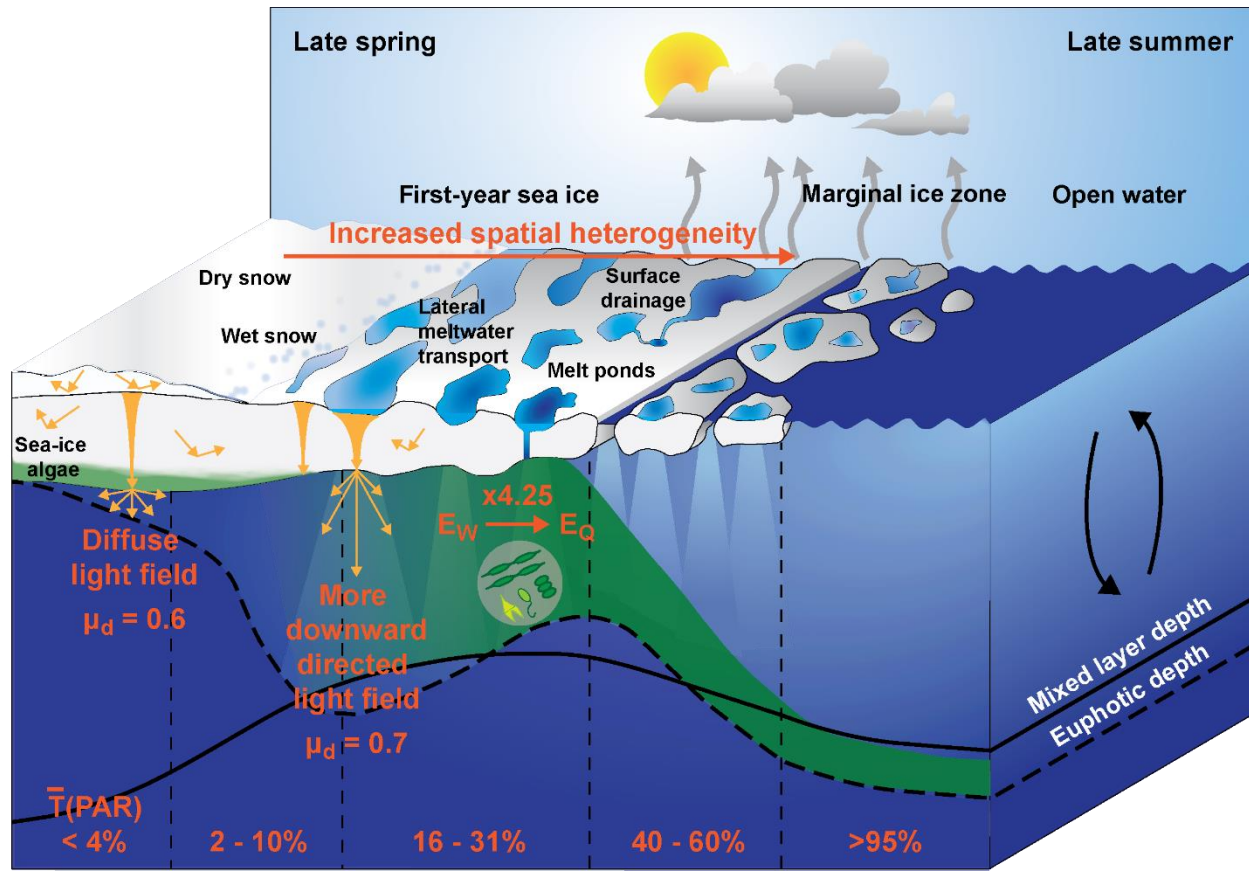
Figure 6.1: Thesis contribution to knowledge of the under-ice light field (in red) showing the increase in average PAR transmittance, $\bar{T}(PAR)$, and its spatial heterogeneity with progressing ice surface melt, the change in the angular distribution of the under ice field, $\mu_d(PAR)$, and the coefficient to link under-ice PAR data given in different units.

The calculated regional averages of PAR transmittance as well as the conversion of measured planar PAR into scalar PAR values to account for the shape of the under-ice light field as recommended in **Chapters 3** and **4** were applied in the calculation of the euphotic depth in **Chapter 5**. Results showed a deepening of the euphotic zone below the mixed layer depth and an increased nutrient accessibility, which helped to explain favorable conditions for the observed under-ice phytoplankton bloom in central Hudson Bay. Additionally, following the recommendations in **Chapter 4**, scalar PAR input was used in the calculation of depth-integrated daily production in **Chapter 5** to minimize the error in estimated phytoplankton production in the deeper layer of the euphotic zone, including the SCM, under light-limiting conditions. In summary, the improved understanding of the increase in PAR transmittance and deepening of the euphotic zone throughout the melt period was crucial in the interpretation of environmental drivers of late spring primary production in Hudson Bay.

Contribution 1 – Thesis objectives 1.1. & 1.2.: An improved understanding of the increase in spatial heterogeneity of light transmission in relation to changing sea ice surface properties

In **Chapter 3** I present a detailed data set on the spatial and temporal melt progression of transmitted UVR and PAR in relation to the changing quantities of snow, ice and melt ponds throughout the spring-summer transition (Fig. 6.1). I observed a close link between the temporal increase in under-ice PAR and UVR levels, classified as stage I – III, and the phases of melt pond evolution presented in studies by Eicken et al. (2002) and Landy et al. (2014):

Stage I prior to melt pond onset: Less than 4% of incoming PAR and UV(A)R (320 – 400 nm) were transmitted through the snow-covered ice, and spatial variability of light transmission did not change noticeably.

Stage II of increasing melt pond coverage: Once melt water became visible in large stretches at the ice surface, PAR and UV(A)R transmission increased by an order of magnitude to 31% and 26%, respectively, while under-ice irradiance became increasingly variable. UV(B)R (305 nm) became detectable beneath the ice cover with a transmission of 1%. The widespread ponding during this stage matched the described second phase of melt pond evolution, which starts with the complete removal of snow and an accelerated ice surface melt.

Stage III of discrete areas of white ice and melt ponds: PAR and UV(A)R transmission and their spatial variability did not increase further during this stage. In fact, PAR transmission decreased in the continuously monitored area due to surface drainage of melt water through cracks, seal breathing holes, enlarged brine drainage channels. This led to a decrease in melt pond sizes and an increase in more reflective white ice patches. Only UV(B)R transmission increased to 7% during this stage.

This evolving spatially heterogeneous light transmission through ponded and white ice created a complex under-ice light field including edge effects at the ice bottom and subsurface maxima as observed elsewhere (Ehn et al., 2011; Frey et al., 2011; Katlein et al., 2016; Laney et al., 2017; Massicotte et al., 2018). Measurements showed that the depth of the surface layer, which is influenced by this heterogeneity and is defined as 'aggregate-scale-depth' in **Chapter 3**, increased from 2.0 – 13.8 m prior to melt pond onset to depths of 14.4 – 29.0 m after melt water became

visible on the ice surface. Within the water layer, drifting phytoplankton has been found to be exposed to variations in PAR availability of up to 43%.

Furthermore, I highlight that the spatial heterogeneity in light transmission through melting sea ice needs to be taken into account for the estimation of light availability and the depth of the euphotic zone during the Arctic spring when a phytoplankton bloom commences beneath a still fully closed ice cover. I demonstrate that regional averages of PAR transmission provide more representative estimates of under-ice light availability relative to single point irradiance measurements. These regional PAR transmission averages can be a) calculated from large-scale continuous measurements via ROVs or b) calculated as length-weighted transmission averages from representative single point measurements beneath white and ponded ice combined with known melt pond coverage from aerial UAV surveys.

Contribution 2 – Thesis objectives 1.3. & 1.4.: An improved characterization of parameters that describe the under-ice light field and are frequently used in the estimation of primary production

In **Chapter 4** I investigated the impact of the increasing spatial heterogeneity in light transmission on the angular and spectral shape of the under-ice light field and on irradiance readings obtained by different radiometer types. Measurements of the underwater irradiance distribution with increasing depth and over the course of the spring melt represent the first *in situ* measurements of the downwelling average cosine (μ_d) in ice-covered conditions. Beneath ice with thick snow cover in 2015, the light field was very diffuse with a $\mu_d(PAR)$ of 0.6 due to high scattering in the snow layer. This led to the largest differences between planar and scalar PAR values. During melt season in 2016, PAR propagation became more downward-directed, which contradicts the previous assumption of a diffuse under-ice light field lasting throughout the melt season (Fig. 6.1). A significantly higher $\mu_d(PAR)$ of 0.7 was measured at the ice bottom after melt pond onset and the difference between planar and scalar PAR values decreased. These significant changes in the spectral shape of the under-ice light field, which affects the conversion of PAR data from energy units (W m^{-2}, E_W), frequently used in energy balance studies, into quantum units (μmol photons m^{-2} s^{-1}, E_Q), more commonly used in biological studies, were not observed over the spring melt progression. Generally, the E_Q/E_W ratio of 4.25 can be used to convert PAR that was measured

143

directly beneath the ice (Fig. 6.1). Morel and Smith (1974) provide an E_Q/E_W ratio of 4.15 ± 10% for a PAR unit conversion in the open water, which encompasses with my observations.

Contribution 3 – Thesis objectives 2.1. & 2.2.: First measurements of late spring primary production in Hudson Bay

Due to inaccessibility in spring, observations of ice algal and phytoplankton production prior and during sea ice melt are still lacking for central Hudson Bay. Data presented in **Chapter 5** are the first *in situ* measurements of microalgal biomass and production in the western and central region when the mobile ice cover was still largely present in late spring. The refined parametrization of light propagation through melting seasonal sea ice presented in Figure 6.1 was applied in the calculation of primary production. Figure 6.2 summarizes the contribution of phytoplankton, melt pond communities, bottom-ice algae and *Melosira arctica* to late spring primary production to the three regions: 1) Narrows, 2) Western Hudson Bay including the northwestern polynya, and 3) central Hudson Bay.
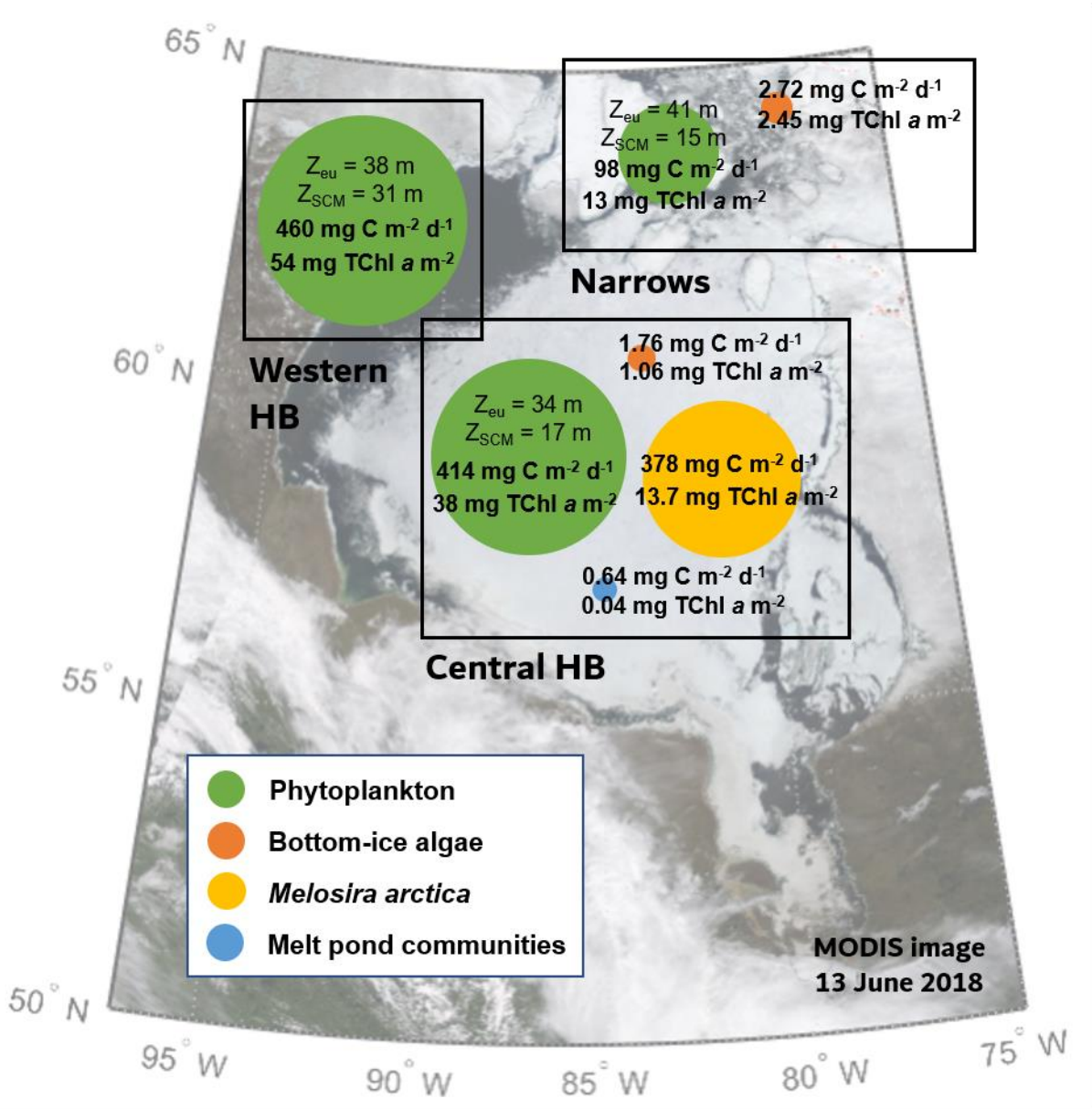
Figure 6.2: Summary of contribution of different microalgal communities to late spring primary production in the Narrows, western and central Hudson Bay (HB). Total chlorophyll *a* (mg TChl *a* m^{-2}) and primary production (mg C m^{-2} d^{-1}) is provided for each community in the corresponding circle as well as the euphotic depth (Z_{eu}) and depth of the subsurface chlorophyll maximum (Z_{SCM}) is provided for each region.

Based on historical measurements on landfast sea ice, spring primary production is initiated by a bottom-ice algal bloom between March and May reaching a biomass between 27.0 and 170.0 mg Chl *a* m^{-2} in northwestern Hudson Bay near Chesterfield Inlet (Bergmann et al., 1991; Welch et al., 1991) and between 23.6 – 39.7 mg Chl *a* m^{-2} in southeastern Hudson Bay (Freeman, 1982; Gosselin et al., 1986; Michel et al., 1993). **Chapter 5** provided post-bloom stage observations of bottom-ice algal communities with a low mean biomass of 1.06 mg TChl *a* m^{-2} and a negligible

145

contribution of 1.76 mg C m^{-2} d^{-1} to estimated total under-ice NPP of 794 mg C m^{-2} d^{-1} in central Hudson Bay in June. Instead, large, but patchy quantities of the sub-ice diatom *Melosira arctica* contributed up to 48% to total under-ice production. These novel observations of the species in the seasonal ice cover of the Canadian sub-Arctic indicate a similar key role in under-ice PP in central Hudson Bay to that in the central Arctic Ocean where *M. arctica* has demonstrated to significantly increase local PP (Gutt, 1995; Gosselin et al., 1997; Fernández-Méndez et al., 2014; 2015).

Similar to the interior Arctic Ocean, central Hudson Bay has been considered to be a nutrient-limited sea where a strongly stratified water column and vertical mixing processes control the replenishments of inorganic nutrients in the surface layer and therefore the magnitude of primary production (Anderson and Roff, 1980; Ferland et al., 2011; Tremblay et al., 2019; Tremblay and Gagnon, 2009). Our first measurements of *in situ* late spring PP further highlight the role of nutrient availability in the spatial distribution of phytoplankton production. The weak stratification in the Narrows prevented a large spring bloom with low biomass and NPP (98 mg C m^{-2} d^{-1}, 13 mg TChl *a* m^{-2}), although nutrients were available throughout the water column. In the open water of western Hudson Bay, nutrients were nearly depleted in the surface layer leading to the formation of a distinct SCM. However, mean values of phytoplankton production and biomass observed in open waters during the late-bloom stage (460 mg C m^{-2} d^{-1}, 53.5 mg TChl *a* m^{-2}) were higher than those observed under the sea ice during the early- to mid-bloom stage (414mg C m^{-2} d^{-1}, 33.7 mg TChl *a* m^{-2}), which were attributed to reduced under-ice light levels and low surface concentrations of inorganic nitrogen (<2 μmol L^{-1}) in central Hudson Bay. These results highlight the role of the NW polynya as largest regional contributor to annual production. In the central region, a diatom-dominated under-ice phytoplankton bloom was observed with high TChl *a* throughout the euphotic zone. Phytoplankton profited from the increased light transmission through the increasingly ponded ice and the still available nutrients in the surface layer. Additionally, phytoplankton communities showed a high plasticity to acclimate to the high(low)-light conditions in the open (ice-covered) surface layer through adjustments of the ratio of photosynthetic to photoprotective pigments and modulations in PE parameters.

Refining the historical total production estimates of Hudson Bay with the novel late spring observations, annual NPP was estimated at 72 g C m^{-2}. This updated estimate is almost twice as high as previous NPP estimates of 21.5 – 39 g C m^{-2} based on post-bloom summer and fall

146

measurements (Roff and Legendre, 1986; Jones and Anderson, 1994; Ferland et al., 2011; Bélanger et al., 2013) and highlights the importance of ice-associated and under-ice microalgal communities in central Hudson Bay. Seasonal production during the 34-day ice melt period represents 32% of annual production, which strongly contributed to the large increase in the updated estimate. The presented dataset in **Chapter 5** can be also used as a baseline to assess the response of marine primary producers to changes in river runoff, sea ice dynamics (increase in open water season), and water mass characteristics (strength of stratification, vertical mixing) in Hudson Bay.

6.2 Limitations and recommendations for future work

This thesis provides a detailed discussion on the complexity of the under-ice light field and its apparent optical parameters during the sea ice melt progression in late spring. Optical measurements in a remote and ice-covered location are challenging due to the limited infrastructure and natural barriers in the sea ice topography such as ridges, leads and very thin ice. This chapter will describe the limitations of various optical sensor set-ups and discusses available remote sensing tools that can be used to estimate under-ice light levels in the Arctic Ocean. Additionally, challenges in the sampling of bottom-ice and sub-ice algal communities during the hard-to-access early months of spring will be discussed. Finally, recommendations for future research on another more frequently observed Arctic phytoplankton growth pattern, fall blooms, are provided.

6.2.1. Remote sensing of under-ice light availability

As presented in **Chapter 3**, point measurements of transmitted irradiance beneath different sea ice surface types combined with drone imagery of the ice surface allow a good estimate of spatially averaged light transmission. However, image processing of pixel brightness relies on the strong dichotomy between white ice and melt ponds. If open water is also present in the image, difficulties to derive melt pond coverage arise. Rösel et al. (2012) applied a machine-learning algorithm, which was trained by defined surface features in photos, to gain the fraction of open water, ice, snow and melt ponds from MODIS images. The authors were able to track the increase in melt pond fraction throughout the Arctic summer, but could not identify other ice surface features such as wet snow, sediment-laden ice surfaces or refrozen melt ponds, which also impact light

147

transmission. Larger photo libraries of sea ice surface characteristics for the training of machine-learning algorithms could overcome this problem. For future work, these algorithms could be used to upscale the approach of calculating regional light transmission from the areal fraction of different surface types, derived from optical remote sensing, and available transmittance data for each surface type. To support this effort, more data on light transmittance of different surface types such as ridges, refrozen leads and sediment-laden ice is needed and could be collected by remotely operated and autonomous platforms.

However, the deployment of ROVs and AUVs in an ice-covered water column also presents several difficulties. ROVs are connected through a tether to a surface unit, which limits the survey area and increases the risk of entanglement. Therefore, ROVs are usually deployed beneath landfast or smooth mobile FYI without ridges or dynamically grown ice areas, which could block the tether. AUVs, which were deployed in marginal ice zones in Baffin Bay (Green Edge project with glider platforms), north of Svalbard (Johnsen et al., 2018) and offshore of Barrow, Alaska (Kukulya et al., 2010), overcome these problems and can cover areas of tens of kilometers. However, large under-ice surveys have not been performed yet due to the challenges of under-ice navigation. The thick ice cover prevents the use of a GPS system for localization, so that AUVs must rely on on-board sensors and estimation techniques. Acoustic-based navigation with the help of static beacons equipped with a transducer and the AUC carrying a transponder to triangulate the location of the AUV under the ice present an option (Kukulya et al., 2010; Munafò and Ferri, 2017). Another option provides the inertial navigation system (INS) in the Remote Environmental Monitoring Units (REMUS) developed by WHOI Ocean Systems laboratory for a deployment in the Arctic Ocean. This navigation system uses the vehicle's orientation, acceleration, and propeller turns and information from an ADCP capable of bottom tracking to calculate an approximate position over longer distances (20 – 30 km) between acoustic beacons installed at the sea floor (Plueddemann et al., 2008). Developing reliable internal navigation systems for the under-ice deployments of AUVs will allow large-scale physical and bio-optical measurements throughout the ice-covered Arctic Ocean.

Due to the limited range of ROV or AUV under-ice surveys, remote sensing products provide additional data to estimate light levels at the ice bottom on Arctic-wide scales during the phytoplankton growth season. Although satellite sensors cannot penetrate the ice cover, ice surface

properties through optical data and ice thickness through altimeter freeboard measurements can be quantified (Table 6.1).

Table 6.1: Remote sensing products to retrieve sea ice properties.

Parameter	Data input	Reference
Surface albedo	MODIS surface reflectance data	Qu et al. 2016
Snow depth	ICESat-2 LiDAR and CryoSat-2 radar altimeter data	Kwok et al. 2020
Melt pond fraction	MODIS surface reflectance data	Rösel et al. 2012
Sea ice thickness and concentration	ICESat-2 LiDAR altimeter data (2019 – present) CryoSat-2 radar altimeter data (2010 – present) ICESat radar altimeter data (2003 – 2008)	Petty et al. 2020 Landy et al. 2017

An estimate of spectral shortwave surface albedo of the Arctic sea ice cover can be generated from reflectance measurements by sensors attached to MODIS (Zege et al., 2015; Qu et al., 2016). It is an important parameter in the calculation of the Arctic surface energy budget but can be also used to produce an under-ice light time series. However, cloud cover and albedo retrieval errors caused by large sun zenith angles limit optical surface albedo estimations (Laine et al., 2011).

With the launch of ICESat-2 in 2019, the attached LiDAR (Light Detection and Ranging) altimeter can be used to estimate snow depth from differences in the measured freeboard from LiDAR (which measures the height of the air-snow interface above the local sea surface) and the measured freeboard from the radar altimeter of CryoSat-2 (which measures the height of the snow ice interface above the local sea surface, Kwok et al., 2020). However, the quality of snow depth retrievals through this method could be influenced by e.g. snow morphology such as snow density, water content or internal ice layers, and needs to be validated by long-term data series and field programs (e.g. Multidisciplinary drifting Observatory for the Study of Arctic Climate [MOSAiC]). Later during the sea ice spring melt, daily and weekly data sets of melt pond fraction can be retrieved from MODIS data and associated with known melt pond light transmittance. However, optical sea ice data are influenced by the cloud cover and can produce large data gaps during the advanced spring melt when the increase in surface water temperatures and air moisture enhance cloud formation (Schweiger, 2004; Bélanger et al., 2013).

Combining spatially extensive *in situ* measurements (ROV and AUV surveys) with these large-footprint remote sensing products increases the sampling size and reduces the error of primary production estimates in ice-covered waters as demonstrated by Massicotte et al. (2019). However,

large quantities of sea ice constituents such as sediments (Frey et al., 2001; Barber et al., in press), ice algae (Ehn and Mundy, 2013; Mundy et al., 2014) and CDOM (Belzile et al., 2000; Xie and Gosselin, 2005; Hill and Zimmerman, 2016) decrease light transmission through the ice cover and cannot be detected by satellites. Also, models applied to estimate how much of the ice-covered Arctic Ocean permits under-ice blooms in spring/summer (Horvat et al., 2017; Kinney et al., 2020) do not currently account for the impact of ice constituents on under-ice light availability. Gaining more knowledge about light attenuation by each ice impurity is difficult if light measurements are only performed from below the ice. The novel in-ice multispectral light sensor chain presented by Katlein et al. (2021) is capable of autonomous ice internal measurements while frozen into the ice, and could provide more insights into the impact of ice impurities on light propagation within the ice layer.

6.2.2. Spring observations of ice-associated algal communities in Hudson Bay

The assessment of ice algal and sub-ice algal biomass is often limited due to their early growth season when heavy ice conditions hamper large quantitative sampling. During my late spring sampling in central Hudson Bay, the end of the bottom-ice algal bloom was only observed and, thus, I was not able to assess their contribution to spring primary production. Landfast ice observations in Hudson Bay describe an ice algal blooming period between March and May, which makes ship-based sampling in the central region unrealistic. Autonomous observing platforms in form of Ice-Tethered Profilers (ITPs; Berge et al., 2016; Laney et al., 2017) and the Warming and Irradiance Measurements (WARM) buoy system (Hill et al., 2018), which are currently deployed to monitor under-ice phytoplankton biomass, can also be used to position optical sensors and camera systems close to the ice bottom and to monitor ice algae biomass. These observation platforms have the advantage of drifting with the ice instead of being anchored to the sea floor like moorings, which can lose near-surface sensor attachments through ice deformations. During the Ocean Science Meeting in San Diego in February 2020, Hill et al. (2020) presented a 2-month dataset on ice-bottom light availability and ice algal biomass, derived from changes in $K_d(PAR)$, which was collected with the WARM buoy system in drifting pack ice on the Chukchi shelf. The NDI approach (Campbell et al., 2014) can also be used to estimate ice algal biomass from transmitted irradiance spectra. Hence, similar sampling of ice algal phenology and biomass by

autonomous ice-tethered buoys, deployed by Helicopter, could be performed in the mobile pack ice of Hudson Bay.

Biomass accumulation of the sub-ice algae *Melosira arctica*, which was observed in large quantities in central Hudson Bay, could be monitored in a similar fashion. However, it still needs to be investigated if biomass of *M. arctica*, often growing in large strands, can be estimated from transmitted irradiance. Additionally, this species appears to grow in patches (Fig. 6.3), which creates difficulties in monitoring biomass with static sensors and can lead to under- or overestimation of abundance and biomass.
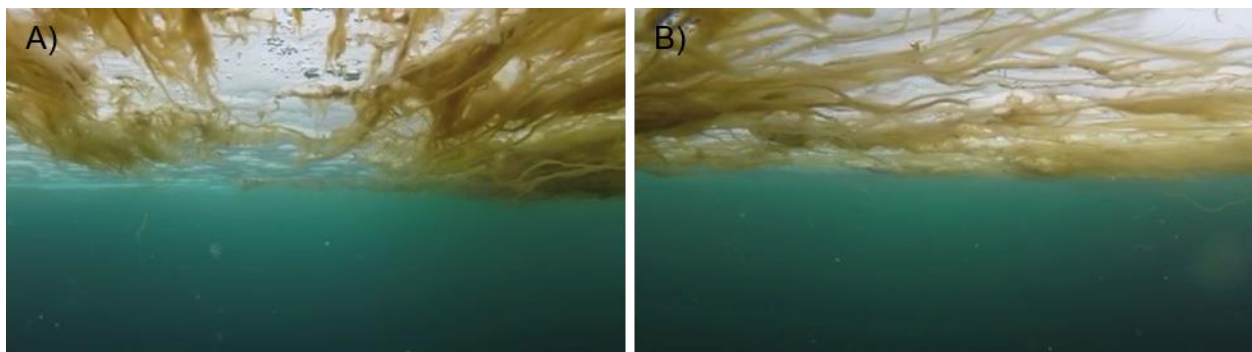
Figure 6.3: *Melosira arctica* growing attached to first-year sea ice in central Hudson Bay (Photo credit: L. Dalman).

A different sampling approach could represent the combination of *in situ* sampling by SCUBA diving and remote abundance mapping by an ROV equipped with an upward-looking camera system. Since *M. arctica* was observed in June when central Hudson Bay was accessible by ice breaker, under-ice sampling can be performed by divers with slurp guns to collected complete strands of this species in a defined area. As mentioned in **Chapter 5**, the collection of strands through the ice-coring method is difficult due to the sloughing of biomass from the ice bottom during extraction. Onboard, biomass in form of Chl *a* and particulate carbon as well as the lengths of strands can be measured from the slurp gun samples. Simultaneously, the spatial distribution of *M. arctica* can be mapped during under-ice ROV surveys in a known area as done so for algal aggregates under summer sea ice by Katlein et al. (2015b). The strong contrast between the brown-green algal strands and the white ice bottom can be used in image processing to quantify the spatial distribution. Subsequently, *M. arctica* biomass of a region can be extrapolated from the *in situ* measured biomass of a known area and the camera footage.

6.2.3. Understanding seasonal algal growth patterns in the Arctic Ocean

The underwater light climate (intensity, spectrum and duration of light) is governed by the spatial and temporal variability in the Arctic sea cover throughout the year. As it is shown in **Chapter 3** and **5**, a phytoplankton bloom can commence in the surface layer in spring when the ice cover is still present due to the increase in light transmission resulting from the formation of less reflective melt ponds at the ice surface. Under-ice blooms were investigated intensively in recent years and information has been published about the environmental drivers of these blooms (e.g., Arrigo et al., 2014; 2017; Mundy et al., 2014; Assmy et al., 2017; Oziel et al., 2019; Ardyna et al., 2020b), their magnitude (e.g. Mundy et al., 2009; Arrigo et al., 2012; Oziel et al., 2019; Boles et al., 2020), their taxonomic composition (e.g. Sherr et al., 2003; Laney and Sosik, 2014; Assmy et al., 2017) and their photoacclimation strategies to the reduced under-ice light levels (e.g. Palmer et al., 2011; 2013; Lewis et al., 2019; Kauko et al., 2019).

Similar detailed observations are still lacking for Arctic fall blooms, whose formation is triggered by the recent extensive loss in Arctic sea ice and the delayed freeze-up (Ardyna et al., 2014). Fall blooms have the potential to increase total production of the Arctic Ocean since they are fuelled by new inorganic nutrients from deeper water layers, to provide a food source for higher trophic levels before polar night and to support an additional carbon export. However, as discussed in section 2.5.4., the replenishment of surface nutrients depends on the interplay between vertical mixing processes and the strength of stratification. If wind-induced or convection mixing, the latter driven by brine rejection during sea ice formation and/or cooling of the surface layer, can overcome stratification, the surface mixed layer deepens. This provides phytoplankton with access to high nutrient concentrations in the deeper water before photosynthesis becomes light-limited (Ardyna et al., 2011). However, these mixing processes can also redistribute algal biomass from a strong SCM, which had developed during the surface-nutrient depleted summer months, and which could appear as a surface bloom in remote sensing observations. Therefore, *in situ* measurements of algal growth rates and primary production in the surface layer are needed.

Furthermore, the window for fall bloom development is short due to the strong reduction in underwater light levels caused by low sun zenith angles and sea ice formation. Newly formed sea ice decreases light levels. However, a study by Kauko et al. (2017) showed that still 5 – 41% of surface PAR were transmitted through a 17 – 27 cm thick refrozen lead with a 1 – 6 cm thick snow

layer in late May. As demonstrated in Chapter 3, these PAR transmission values are enough to trigger an under-ice bloom. Therefore, low sun elevations before winter could potentially play a larger role in bloom termination, particularly if the freeze-up is delayed into fall (Lebrun et al., 2019). Large-scale under-ice surveys by ROVs or AUVS could provide more information on light availability in the surface water layer during the fall freeze-up at decreasing sun elevation. *In situ* observations of the photophysiological response of phytoplankton to decreasing light availability similar to the photoacclimation strategies of phytoplankton during an under-ice spring bloom are also needed.

Appendix A: List of original manuscripts and contributions of collaborating authors

I **Matthes, L.C.**, Mundy, C.J., L.-Girard, S., Babin, M., Verin, G. and Ehn, J.K. (2020). *Spatial heterogeneity as a key variable influencing spring-summer progression in UVR and PAR transmission through Arctic sea ice.* Front Mar Sci 7. Frontiers. doi: 10.3389/fmars.2020.00183

II **Matthes, L.C.**, Ehn, J.K., L.-Girard, S., Pogorzelec, N.M., Babin, M. and Mundy, C.J. (2019). *Average cosine coefficient and spectral distribution of the light field under sea ice: Implications for primary production*. Elem Sci Anth, 7(1), p.25. doi: http://doi.org/10.1525/elementa.363

III **Matthes, L.C.**, Ehn, J.K., Dalman, L.A., Babb, D.G., Peeken, I., Harasyn, M., Kirillov, S., Lee, J., Bélanger, S., Tremblay, J.-É., Barber, D.G., and Mundy, C.J. *Environmental drivers of spring primary production in Hudson Bay*. Elem Sci Anth (BaySys Special Issue). Under review.

Author contributions to the individual manuscripts:

	Manuscript I	**Manuscript II**	**Manuscript III**
Study design & Methods	LM, CJM, JE, SL-G	LM, CJM, JE	LM, CJM
Data collection	LM, SL-G, GV, MB	LM, SL-G, JE, NP	LM, LD, DBabb, MH, SK, JL
Data analysis & Interpretation	LM, SL-G, CJM, JE	LM, JKE, CJM, SL-G	LM, LD, DBabb, CJM, JE, JL, SK, IP
Manuscript preparation*	Everyone	Everyone	Everyone

*Each manuscript was drafted by me and revised by every co-author

Appendix B: Additional contributions to the peer-reviewed literature

In addition to the three manuscripts, which are the body of this thesis, I have co-authored three published peer-reviewed manuscripts and three manuscripts in preparation or under review in a peer-reviewed journal. I have further contributed to the Phase II report of the BaySys project, and smaller quarterly reports and field campaign reports within this project.

Published manuscripts

Massicotte, P., Amiraux, R., […], **Matthes, L**., et al. (2019): *Green Edge ice camp campaigns: understanding the processes controlling the under-ice Arctic phytoplankton spring bloom*, Earth Syst. Sci. Data Discuss., https://doi.org/10.5194/essd-2019-160

This manuscript is an overview of all data that was collected during the Green Edge ice camp campaigns (2015, 2016) in which I had participated in 2016. Additional to the submission of data presented in my two project related manuscripts (Chapter 3 & 4), I have provided a written summary of my optical measurements and figures for the optics section of this manuscript. I also contributed to the review of the manuscript prior to submission and acceptance.

Barber, D.G., Babb, D.G., Ehn, J.K., Chan, W., **Matthes, L.**, et al. (2018). *Increasing mobility of high Arctic Sea ice increases marine hazards off the east coast of Newfoundland*. Geophysical Research Letters, 45. DOI: https://doi.org/10.1002/2017GL076587

In this manuscript I helped collecting and processing ice samples during the cancelled BaySys cruise in 2017. I further edited the manuscript draft before the review process.

Ardyna, M., Mundy, C.J., Mayot, N., **Matthes, L.C.**, Oziel, L., Horvat, C., Leu, E., Assmy, P., Hill, V., Matrai, P. A., Gale, M., Melnikov. I.A. and Arrigo, K.R. *Under-ice phytoplankton blooms: shedding light on the 'invisible' part of Arctic primary production*. Front Mar Sci **7**. Frontiers. DOI: 10.3389/fmars.2020.608032

In this review I wrote the section about the under-ice light field and phytoplankton photoacclimation, and contributed a figure (Figure 5). I further contributed significantly to the writing of Box 1 about technological advancements in under-ice sensor platforms. And I provided comments and suggestions on the entire manuscript draft prior to submission and during the review process.

Jacquemot, L., Kalenitchenko, D., **Matthes, L.C.**, Vigneron, A., Mundy, C.J., Tremblay, J.-É., Lovejoy, C. *Protist communities along Hudson Bay (Canada) freshwater-marine transition zones.* Elem Sci Anth (BaySys Special Issue). In press.

In this manuscript I collected and processed the presented transmissometer (processed only), Chl *a* and POC data for the Nelson River estuary that was all collected during the BaySys cruise in 2018. I also provided written paragraphs for the methods section and edits on the manuscript draft prior to submission.

Barber, D.G., Harasyn, M.L. Babb, D.G., Capelle, D., McCullough, G., Dalman, L.A., **Matthes, L.C.**, Ehn, J.K., Kirillov, S., Basu, A., Fayak, M., Schembri, S., Papkyriakou, T., Ahmed, M., Guéguen, C., Meilleur, C., Dmitrenko, I., Mundy, C.J., Kuzyk, Z., Rysgaard, S., Stroeve J. and Sydor, K. *Sediment-laden sea ice in southern Hudson Bay: entrainment, transport and biogeochemical significance.* Elem Sci Anth (BaySys Special Issue). In press.

In this manuscript I helped processing the collected ice samples during the BaySys cruise in 2018. I contributed to the writing of the section about the biogeochemical significance of sediment-laden sea ice and edited drafts of the manuscript before submission and during the review process.

Manuscripts in preparation and other contributions

Dalman L.A., **Matthes, L.C.**, Barber, D.B., Kuzyk, Z., Tremblay, J.-É., Lee, J., Wiktor, J., Tatarek, A., Lovejoy, C., Jacquemot, L., and Mundy, C.J. *Response of microalgal communities to a seasonal freshwater gradient in southwestern Hudson Bay, Canada.* Elem Sci Anth (BaySys special issue). In preparation.

This manuscript presents the environmental and biogeochemical data collected under the lead of L. Dalman in winter 2017 and under my lead in late spring 2018 in the Nelson River estuary. During the BaySys cruise in 2018, the physical and biological sampling in the open water was carried out in a team effort. I processed the collected dataset (light availability, Chl *a*, POC, PP) as well as the ice algal light data from the winter campaign 2017, significantly helped with the manuscript design and created the plots to present the phytoplankton data. I contributed in writing to the method section and edit the draft during the writing process.

Tremblay, J- É., Swanson, G., Kullman, M., Fortier, L., Maps, F., Lovejoy, C., Bélanger, Archambault, P., Mundy, C.J., Delongchamps, G., Gangon, J., Deschepper, I., PierreJean, M., Schembri, S., Jacquemot, L., Barbedo de Freitas, L., Lee, J., **Matthes, L.**, Dalman, L. Marine Ecosystems. Chapter 3.3 in, *Hudson Bay Systems Study (BaySys) Phase 2 Report: Project Analysis and Results*. In preparation.

For this report myself, L. Dalman and my supervisor CJ Mundy have summarized the results of the ice algal and phytoplankton data collected during the BaySys Nanuk field campaign in 2017 and research cruise in Hudson Bay in 2018. I have contributed an overview of the results that are presented in Chapter 5 of this thesis and several figures. For this report we have also summarized results that will be presented in the publication (in prep.) about the microalgal communities in the Nelson River estuary.

References

Agarwal S, Moon W, Wettlaufer JS. 2011. Decadal to seasonal variability of Arctic sea ice albedo. *Geophys Res Lett* **38**(20). doi: 10.1029/2011GL049109

Alexander V, Niebauer HJ. 1981. Oceanography of the eastern Bering Sea ice-edge zone in spring. *Limnol Ocean* **26**(6): 1111–1125.

Alou-Font E, Mundy C-J, Roy S, Gosselin M, Agustí S. 2013. Snow cover affects ice algal pigment composition in the coastal Arctic Ocean during spring. *Mar Ecol Prog Ser* **474**: 89–104. doi: 10.3354/meps10107

Alou-Font E, Roy S, Agustí S, Gosselin M. 2016. Cell viability, pigments and photosynthetic performance of Arctic phytoplankton in contrasting ice-covered and open-water conditions during the spring-summer transition. *Mar Ecol Prog Ser* **543**: 89–106. doi: 10.3354/meps11562

AMAP. 2017. Snow, Water, Ice and Permafrost in the Arctic (SWIPA) 2017. Arctic Monitoring and Assessment Programme (AMAP).

Ambrose WG, Von Quillfeldt C, Clough LM, Tilney PV, Tucker T. 2005. The sub-ice algal community in the Chukchi sea: large-and small-scale patterns of abundance based on images from a remotely operated vehicle. *Polar Biol* **28**(10): 784–795.

Anderson J, Roff J. 1980. Seston ecology of the surface waters of Hudson Bay. *Can J Fish Aquat Sci* **37**(12): 2242–2253. NRC Research Press. doi: 10.1139/f80-269

Andrews J, Babb D, Barber D. 2018. Climate change and sea ice: Shipping in Hudson Bay, Hudson Strait, and Foxe Basin (1980–2016). *Elem Sci Anth* **6**(1): 19. University of California Press. doi: 10.1525/elementa.281

Antoine D, Hooker S, Bélanger S, Matsuoka A, Babin M. 2013. Apparent optical properties of the Canadian Beaufort Sea–Part 1: Observational overview and water column relationships. *Biogeosciences* **10**(7): 4493–4509.

Apollonio S. 1959. Hydrobiological measurements on IGY drifting station Bravo. *Trans Am Geophys Union* **40**(3): 316–3.

Ardyna M, Arrigo KR. 2020. Phytoplankton dynamics in a changing Arctic Ocean. *Nat Clim Change*: 1–12. Nature Publishing Group.

Ardyna M, Babin M, Gosselin M, Devred E, Rainville L, Tremblay J. 2014. Recent Arctic Ocean sea ice loss triggers novel fall phytoplankton blooms. *Geophys Res Lett* **41**(17): 6207–6212. doi: 10.1002/2014GL061047

Ardyna M, Gosselin M, Michel C, Poulin M, Tremblay J-É. 2011. Environmental forcing of phytoplankton community structure and function in the Canadian High Arctic: contrasting oligotrophic and eutrophic regions. *Mar Ecol Prog Ser* **442**: 37–57.

Ardyna M, Mundy CJ, Mayot N, Matthes LC, Oziel L, Horvat C, Leu E, Assmy P, Hill V, Matrai PA, et al. 2020. Under-Ice Phytoplankton Blooms: Shedding Light on the "Invisible" Part of Arctic Primary Production. *Front Mar Sci* **7**. Frontiers. doi: 10.3389/fmars.2020.608032

Ardyna M, Mundy CJ, Mills MM, Oziel L, Grondin P-L, Lacour L, Verin G, Dijken GV, Ras J, Alou-Font E, et al. 2020. Environmental drivers of under-ice phytoplankton bloom dynamics in the Arctic Ocean. *Elem Sci Anth* **8**(1): 30. University of California Press. doi: 10.1525/elementa.430

Arndt S, Meiners KM, Ricker R, Krumpen T, Katlein C, Nicolaus M. 2017. Influence of snow depth and surface flooding on light transmission through Antarctic pack ice. *J Geophys Res Oceans* **122**(3): 2108–2119. doi: 10.1002/2016JC012325

Arrigo KR, van Dijken GL. 2015. Continued increases in Arctic Ocean primary production. *Prog Oceanogr* **136**: 60–70. doi: 10.1016/j.pocean.2015.05.002

Arrigo KR, Mills MM, Dijken GL van, Lowry KE, Pickart RS, Schlitzer R. 2017. Late Spring Nitrate Distributions Beneath the Ice-Covered Northeastern Chukchi Shelf. *J Geophys Res Biogeosciences* **122**(9): 2409–2417. doi: 10.1002/2017JG003881

Arrigo KR, Mock T, Lizotte MP. 2010. Primary producers and sea ice. *Sea Ice* **2**: 283–325.

Arrigo KR, Perovich DK, Pickart RS, Brown ZW, van Dijken GL, Lowry KE, Mills MM, Palmer MA, Balch WM, Bahr F. 2012. Massive phytoplankton blooms under Arctic sea ice. *Science* **336**(6087): 1408–1408.

Arrigo KR, Perovich DK, Pickart RS, Brown ZW, van Dijken GL, Lowry KE, Mills MM, Palmer MA, Balch WM, Bates NR. 2014. Phytoplankton blooms beneath the sea ice in the Chukchi Sea. *Deep Sea Res Part II Top Stud Oceanogr* **105**: 1–16. doi: 10.1016/j.dsr2.2014.03.018

Arrigo KR, Sullivan CW. 1992. The Influence of Salinity and Temperature Covariation on the Photophysiological Characteristics of Antarctic Sea Ice Microalgae1. *J Phycol* **28**(6): 746–756. doi: 10.1111/j.0022-3646.1992.00746.x

Arrigo KR, Sullivan CW, Kremer JN. 1991. A bio-optical model of Antarctic sea ice. *J Geophys Res Oceans* **96**(C6): 10581–10592.

Årthun M, Eldevik T, Smedsrud L, Skagseth Ø, Ingvaldsen R. 2012. Quantifying the influence of Atlantic heat on Barents Sea ice variability and retreat. *J Clim* **25**(13): 4736–4743.

Asplin MG, Galley R, Barber DG, Prinsenberg S. 2012. Fracture of summer perennial sea ice by ocean swell as a result of Arctic storms. *J Geophys Res Oceans* **117**(C6). doi: 10.1029/2011JC007221

Assmy P, Fernández-Méndez M, Duarte P, Meyer A, Randelhoff A, Mundy CJ, Olsen LM, Kauko HM, Bailey A, Chierici M, et al. 2017. Leads in Arctic pack ice enable early phytoplankton blooms below snow-covered sea ice. *Sci Rep* **7**: 40850. doi: 10.1038/srep40850

Babb DG, Galley RJ, Asplin MG, Lukovich JV, Barber DG. 2013. Multiyear sea ice export through the Bering Strait during winter 2011–2012. *J Geophys Res Oceans* **118**(10): 5489–5503.

Babin M, Bélanger S, Ellingsen I, Forest A, Le Fouest V, Lacour T, Ardyna M, Slagstad D. 2015. Estimation of primary production in the Arctic Ocean using ocean colour remote sensing and coupled physical–biological models: strengths, limitations and how they compare. *Prog Oceanogr* **139**: 197–220. Elsevier.

Babin M, Morel A, Gagnon R. 1994. An incubator designed for extensive and sensitive measurements of phytoplankton photosynthetic parameters. *Limnol Oceanogr* **39**(3): 694–702. doi: 10.4319/lo.1994.39.3.0694

Bannister TT. 1992. Model of the mean cosine of underwater radiance and estimation of underwater scalar irradiance. *Limnol Oceanogr* **37**(4): 773–780. doi: 10.4319/lo.1992.37.4.0773

Barbedo L, Bélanger S, Tremblay J-É. 2020. Climate control of sea-ice edge phytoplankton blooms in the Hudson Bay system. *Elem Sci Anthr* **8**(039). doi: 10.1525/elementa.039

Barber D, Babb D, Ehn J, Chan W, Matthes L, Dalman L, Campbell Y, Harasyn M, Firoozy N, Theriault N. 2018. Increasing mobility of high Arctic sea ice increases marine hazards off the east coast of Newfoundland. *Geophys Res Lett* **45**(5): 2370–2379.

Barber DG, Harasyn ML, Babb DG, Capelle D, McCullough G, Dalman LA, Matthes LC, Ehn JK, Kirillov S, Basu A, et al. in press. Sediment-laden sea ice in southern Hudson Bay: entrainment, transport and biogeochemical significance. *Elem Sci Anth*(BaySys Special Issue).

Barber DG, Hop H, Mundy CJ, Else B, Dmitrenko IA, Tremblay J-E, Ehn JK, Assmy P, Daase M, Candlish LM. 2015. Selected physical, biological and biogeochemical implications of a rapidly changing Arctic Marginal Ice Zone. *Prog Oceanogr* **139**: 122–150.

Barbieri ES, Villafaññ VE, Helbling EW. 2002. Experimental assessment of UV effects on temperate marine phytoplankton when exposed to variable radiation regimes. *Limnol Oceanogr* **47**(6): 1648–1655. doi: 10.4319/lo.2002.47.6.1648

Barnes PW, Reimnitz E, Fox D. 1982. Ice rafting of fine-grained sediment, a sorting and transport mechanism, Beaufort Sea, Alaska. *J Sediment Res* **52**(2): 493–502. SEPM Society for Sedimentary Geology.

Bélanger S, Babin M, Tremblay J-É. 2013. Increasing cloudiness in Arctic damps the increase in phytoplankton primary production due to sea ice receding. *Biogeosciences* **10**(6): 4087.

Belzile C, Johannessen SC, Gosselin M, Demers S, Miller WL. 2000. Ultraviolet attenuation by dissolved and particulate constituents of first-year ice during late spring in an Arctic polynya. *Limnol Oceanogr* **45**(6): 1265–1273.

Berge J, Geoffroy M, Johnsen G, Cottier F, Bluhm B, Vogedes D. 2016. Ice-tethered observational platforms in the Arctic Ocean pack ice. *IFAC-Pap* **49**(23): 494–499. doi: 10.1016/j.ifacol.2016.10.484

Bergmann MA, Welch HE, Butler-Walker JE, Siferd TD. 1991. Ice algal photosynthesis at resolute and saqvaqjuac in the Canadian arctic. *J Mar Syst* **2**(1): 43–52. doi: https://doi.org/10.1016/0924-7963(91)90012-J

Berwald JM. 1999. The relationship between the average cosine of the underwater light field and the inherent optical properties of the ocean. PhD thesis. USC Digtal Library.

Berwald JM, Stramski D, Mobley CD, Kiefer AD. 1995. Influences of absorption and scattering on vertical changes in the average cosine of the underwater light field. *Limnol Oceanogr* **40**(8): 1347–1357. doi: 10.4319/lo.1995.40.8.1347

Blais M, Ardyna M, Gosselin M, Dumont D, Bélanger S, Tremblay J, Gratton Y, Marchese C, Poulin M. 2017. Contrasting interannual changes in phytoplankton productivity and community structure in the coastal Canadian Arctic Ocean. *Limnol Oceanogr* **62**(6): 2480–2497.

Boetius A, Albrecht S, Bakker K, Bienhold C, Felden J, Fernández-Méndez M, Hendricks S, Katlein C, Lalande C, Krumpen T. 2013. Export of algal biomass from the melting Arctic sea ice. *Science* **339**(6126): 1430–1432. doi: 10.1126/science.1231346

Boles E, Provost C, Garçon V, Bertosio C, Athanase M, Koenig Z, Sennéchael N. 2020. Under-Ice Phytoplankton Blooms in the Central Arctic Ocean: Insights From the First Biogeochemical IAOOS Platform Drift in 2017. *J Geophys Res Oceans* **125**(3): e2019JC015608. doi: 10.1029/2019JC015608

Born M, Wolf E. 1999. *Principles of Optics: Electromagnetic Theory of Propagation, Interference and Diffraction of Light*. 7th ed. Cambridge: Cambridge University Press. doi: 10.1017/CBO9781139644181

Boss E, Behrenfeld M. 2010. In situ evaluation of the initiation of the North Atlantic phytoplankton bloom. *Geophys Res Lett* **37**(18).

Brown RD. 2010. Analysis of snow cover variability and change in Québec, 1948–2005. *Hydrol Process* **24**(14): 1929–1954. doi: 10.1002/hyp.7565

Bruneau J, Babb DG, Chan W, Kirillov S, Ehn JK, Hanesiak J, Barber DG. In review. The ice factory of Hudson Bay: spatiotemporal variability of the polynya in northwestern Hudson Bay. *Elem Sci Anthr* (BaySys Special Issue).

Brunet C, Johnsen G, Lavaud J, Roy S. 2011 Oct. Pigments and photoacclimation processes. Phytoplankton Pigments: Characterization, Chemotaxonomy and Applications in Oceanography. Cambridge University Press. doi: 10.1017/CBO9780511732263.017

Brzezinski MA. 1985. The Si:C:N ratio of marine diatoms: interspecific variability and the effect of some environmental variables. *J Phycol* **21**(3): 347–357. doi: 10.1111/j.0022-3646.1985.00347.x

Buck KR, Nielsen TG, Hansen BW, Gastrup-Hansen D, Thomsen HA. 1998. Infiltration phyto-and protozooplankton assemblages in the annual sea ice of Disko Island, West Greenland, spring 1996. *Polar Biol* **20**(6): 377–381. Springer.

Bursa A. 1961. Phytoplankton of the Calanus Expeditions in Hudson Bay, 1953 and 1954. *J Fish Res Board Can* **18**(1): 51–83. NRC Research Press. doi: 10.1139/f61-004

Campbell K, Mundy C, Landy J, Delaforge A, Michel C, Rysgaard S. 2016. Community dynamics of bottom-ice algae in Dease Strait of the Canadian Arctic. *Prog Oceanogr* **149**: 27–39. Elsevier. doi: 10.1016/j.pocean.2016.10.005

Campbell K, Mundy CJ, Barber DG, Gosselin M. 2014. Remote Estimates of Ice Algae Biomass and Their Response to Environmental Conditions during Spring Melt. *ARCTIC* **67**(3): 375–387.

Campbell K, Mundy CJ, Barber DG, Gosselin M. 2015. Characterizing the sea ice algae chlorophyll a–snow depth relationship over Arctic spring melt using transmitted irradiance. *J Mar Syst* **147**: 76–84.

Campbell K, Mundy CJ, Belzile C, Delaforge A, Rysgaard S. 2018. Seasonal dynamics of algal and bacterial communities in Arctic sea ice under variable snow cover. *Polar Biol* **41**(1): 41–58. doi: 10.1007/s00300-017-2168-2

Campbell K, Mundy CJ, Juhl AR, Dalman LA, Michel C, Galley RJ, Else BE, Geilfus NX, Rysgaard S. 2019. Melt Procedure Affects the Photosynthetic Response of Sea Ice Algae. *Front Earth Sci* **7**. doi: 10.3389/feart.2019.00021

Carmack E, Wassmann P. 2006. Food webs and physical–biological coupling on pan-Arctic shelves: Unifying concepts and comprehensive perspectives. *Prog Oceanogr* **71**(2): 446–477. doi: 10.1016/j.pocean.2006.10.004

Carmack EC. 2007. The alpha/beta ocean distinction: A perspective on freshwater fluxes, convection, nutrients and productivity in high-latitude seas. *Deep Sea Res Part II Top Stud Oceanogr* **54**(23): 2578–2598. doi: 10.1016/j.dsr2.2007.08.018

Carvalho F, Kohut J, Oliver MJ, Schofield O. 2017. Defining the ecologically relevant mixed-layer depth for Antarctica's coastal seas. *Geophys Res Lett* **44**(1): 338–345. Wiley Online Library. doi: 10.1002/2016GL071205

Cavalieri D, Parkinson C. 2012. Arctic sea ice variability and trends, 1979-2010. *The Cryosphere* **6**(4): 881.

Clair TA, Warner BG, Robarts R, Murkin H, Lilley J, Mortsch L, Rubec C. 1998. Canadian inland wetlands and climate change. *Can Ctry Study Clim Impacts Adapt Natl Sect Vol Environ Can Ott Ont Can*: 189–218.

Codispoti L, Kelly V, Thessen A, Matrai P, Suttles S, Hill V, Steele M, Light B. 2013. Synthesis of primary production in the Arctic Ocean: III. Nitrate and phosphate based estimates of net community production. *Prog Oceanogr* **110**: 126–150.

Coello-Camba A, Agustí S, Vaqué D, Holding J, Arrieta JM, Wassmann P, Duarte CM. 2015. Experimental Assessment of Temperature Thresholds for Arctic Phytoplankton Communities. *Estuaries Coasts* **38**(3): 873–885. doi: 10.1007/s12237-014-9849-7

Comiso JC. 2012. Large decadal decline of the Arctic multiyear ice cover. *J Clim* **25**(4): 1176–1193.

Comiso JC, Parkinson CL, Gersten R, Stock L. 2008. Accelerated decline in the Arctic sea ice cover. *Geophys Res Lett* **35**(1): L01703. doi: 10.1029/2007GL031972

Consalvey M, Perkins R, Paterson D, Underwood G. 2005. PAM fluorescence: a beginners guide for benthic diatomists. *Diatom Res* **20**: 1–22. doi: 10.1080/0269249X.2005.9705619

Cota GF. 1985. Photoadaptation of high Arctic ice algae. *Nature* **315**(6016): 219–222. Springer.

Cota GF, Smith RE. 1991. Ecology of bottom ice algae: III. Comparative physiology. *J Mar Syst* **2**(3–4): 297–315. Elsevier.

Coupel P, Matsuoka A, Ruiz-Pino D, Gosselin M, Marie D, Tremblay J-É, Babin M. 2015. Pigment signatures of phytoplankton communities in the Beaufort Sea. *Biogeosciences* **12**(4): 991–1006. doi: 10.5194/bg-12-991-2015

Crabeck O, Delille B, Rysgaard S, Thomas DN, Geilfus N, Else B, Tison J. 2014. First "in situ" determination of gas transport coefficients (, and) from bulk gas concentration measurements (O2, N2, Ar) in natural sea ice. *J Geophys Res Oceans* **119**(10): 6655–6668.

Crabeck O, Galley RJ, Mercury L, Delille B, Tison J-L, Rysgaard S. 2019. Evidence of Freezing Pressure in Sea Ice Discrete Brine Inclusions and Its Impact on Aqueous-Gaseous Equilibrium. *J Geophys Res Oceans* **124**(3): 1660–1678. doi: 10.1029/2018JC014597

Crawford AD, Krumhardt KM, Lovenduski NS, van Dijken GL, Arrigo KR. 2020. Summer High-Wind Events and Phytoplankton Productivity in the Arctic Ocean. *J Geophys Res Oceans* **125**(9): e2020JC016565.

Dalman LA, Else BGT, Barber D, Carmack E, Williams WJ, Campbell K, Duke PJ, Kirillov S, Mundy CJ. 2019. Enhanced bottom-ice algal biomass across a tidal strait in the Kitikmeot Sea of the Canadian Arctic. *Elem Sci Anth* **7**(1): 22. University of California Press. doi: 10.1525/elementa.361

Dalpadado P, Arrigo KR, van Dijken GL, Skjoldal HR, Bagøien E, Dolgov AV, Prokopchuk IP, Sperfeld E. 2020. Climate effects on temporal and spatial dynamics of phytoplankton and zooplankton in the Barents Sea. *Prog Oceanogr* **185**: 102320. doi: 10.1016/j.pocean.2020.102320

Darley WM. 1982. *Algal Biology: A Physiological Approach*. Blackwell Scientific Publications.

Dee DP, Uppala SM, Simmons AJ, Berrisford P, Poli P, Kobayashi S, Andrae U, Balmaseda MA, Balsamo G, Bauer P, et al. 2011. The ERA-Interim reanalysis: configuration and performance of the data assimilation system. *Q J R Meteorol Soc* **137**(656): 553–597. doi: 10.1002/qj.828

Degerlund M, Eilertsen HC. 2010. Main species characteristics of phytoplankton spring blooms in NE Atlantic and Arctic waters (68–80 N). *Estuaries Coasts* **33**(2): 242–269. Springer.

Déry SJ, Mlynowski TJ, Hernández-Henríquez MA, Straneo F. 2011a. Interannual variability and interdecadal trends in Hudson Bay streamflow. *J Mar Syst* **88**(3): 341–351. doi: 10.1016/j.jmarsys.2010.12.002

Déry SJ, Mlynowski TJ, Hernández-Henríquez MA, Straneo F. 2011b. Interannual variability and interdecadal trends in Hudson Bay streamflow. *J Mar Syst* **88**(3): 341–351. doi: 10.1016/j.jmarsys.2010.12.002

Diaz A, Ehn J, Landy J, Else B, Campbell K, Papakyriakou T. 2018. The Energetics of Extensive Meltwater Flooding of Level Arctic Sea Ice. *J Geophys Res Oceans* **123**(12): 8730–8748.

Drinkwater K, Jones E. 1987. Density stratification, nutrient and chlorophyll distributions in the Hudson Strait region during summer and their relation to tidal mixing. *Cont Shelf Res* **7**(6): 599–607. doi: 10.1016/0278-4343(87)90025-2

Dukhovskoy DS, Yashayaev I, Proshutinsky A, Bamber JL, Bashmachnikov IL, Chassignet EP, Lee CM, Tedstone AJ. 2019. Role of Greenland Freshwater Anomaly in the Recent Freshening of the Subpolar North Atlantic. *J Geophys Res Oceans*, in press. doi: 10.1029/2018JC014686

Eastwood RA, Macdonald R, Ehn J, Heath J, Arragutainaq L, Myers P, Barber D, Kuzyk Z. 2020. Role of River Runoff and Sea Ice Brine Rejection in Controlling Stratification Throughout Winter in Southeast Hudson Bay. *Estuaries Coasts*: 1–31. Springer. doi: 10.1007/s12237-020-00698-0

Eberhard S, Finazzi G, Wollman F-A. 2008. The dynamics of photosynthesis. *Annu Rev Genet* **42**: 463–515.

Ehn JK, Mundy CJ. 2013. Assessment of light absorption within highly scattering bottom sea ice from under-ice light measurements: Implications for Arctic ice algae primary production. *Limnol Oceanogr* **58**(3): 893–902.

Ehn JK, Mundy CJ, Barber DG, Hop H, Rossnagel A, Stewart J. 2011. Impact of horizontal spreading on light propagation in melt pond covered seasonal sea ice in the Canadian Arctic. *J Geophys Res Oceans* **116**(C9).

Ehn JK, Papakyriakou TN, Barber DG. 2008. Inference of optical properties from radiation profiles within melting landfast sea ice. *J Geophys Res Oceans* **113**(C9): C09024. doi: 10.1029/2007JC004656

Eicken H, Bluhm BA, Collins RE, Haas C, Ingham M, Gradinger R, Mahoney A, Nicolaus M, Perovich DK. 2014. Field techniques in sea-ice research. In: *Cold Regions Science and Marine Technology*. Eolss Publishers. p. 1–20.

Eicken H, Krouse HR, Kadko D, Perovich DK. 2002. Tracer studies of pathways and rates of meltwater transport through Arctic summer sea ice. *J Geophys Res Oceans* **107**(C10): SHE 22-1-SHE 22-20. doi: 10.1029/2000JC000583

Elliott A, Mundy CJ, Gosselin M, Poulin M, Campbell K, Wang F. 2015. Spring production of mycosporine-like amino acids and other UV-absorbing compounds in sea ice-associated algae communities in the Canadian Arctic. *Mar Ecol Prog Ser* **541**: 91–104. doi: 10.3354/meps11540

English T. 1965. Some Biological Oceanographic Observations in the Central North Polar Sed, Drift Station Alpha, 1957-1958. *US-IGY Drift Stn Alpha Arct Ocean 1957-1958*(38): 195. Air Force Cambridge Research Laboratories.

Falkowski P, Raven J. 2007. Photosynthesis and primary production in nature. *Aquat Photosynth 2nd Ed Princet Univ Press Princet*.

Falk-Petersen S, Pavlov V, Berge J, Cottier F, Kovacs KM, Lydersen C. 2015. At the rainbow's end: high productivity fueled by winter upwelling along an Arctic shelf. *Polar Biol* **38**(1): 5–11.

Ferguson SH, Loseto LL, Mallory ML. 2010. *A Little Less Arctic: Top Predators in the World's Largest Northern Inland Sea, Hudson Bay*. Springer.

Ferland J, Gosselin M, Starr M. 2011. Environmental control of summer primary production in the Hudson Bay system: The role of stratification. *J Mar Syst* **88**(3): 385–400. doi: 10.1016/j.jmarsys.2011.03.015

Fernández-Méndez M, Katlein C, Rabe B, Nicolaus M, Peeken I, Bakker K, Flores H, Boetius A. 2015. Photosynthetic production in the central Arctic Ocean during the record sea-ice minimum in 2012. *Biogeosciences* **12**(11): 3525–3549. doi: 10.5194/bg-12-3525-2015

Fernández-Méndez M, Olsen LM, Kauko HM, Meyer A, Rösel A, Merkouriadi I, Mundy CJ, Ehn JK, Johansson AM, Wagner PM, et al. 2018. Algal Hot Spots in a Changing Arctic Ocean: Sea-Ice Ridges and the Snow-Ice Interface. *Front Mar Sci* **5**. Frontiers. doi: 10.3389/fmars.2018.00075

Fernández-Méndez M, Wenzhöfer F, Peeken I, Sørensen HL, Glud RN, Boetius A. 2014. Composition, Buoyancy Regulation and Fate of Ice Algal Aggregates in the Central Arctic Ocean. *PLOS ONE* **9**(9): e107452. doi: 10.1371/journal.pone.0107452

Fetterer F, Knowles K, Meier WN, Savoie M, Windnagel AK. 2017 updated daily. Sea Ice Index, Version 3 (Sea_Ice_Index_Monthly_Data_by_Year_G02135_v3.0). *Boulder Colo USA NSIDC Natl Snow Ice Data Cent*, in press. doi: doi: https://doi.org/10.7265/N5K072F8

Fetterer F, Untersteiner N. 1998. Observations of melt ponds on Arctic sea ice. *J Geophys Res Oceans* **103**(C11): 24821–24835.

Fofonoff NP, Millard Jr RC. 1983. Algorithms for the computation of fundamental properties of seawater. UNESCO. Available at https://repository.oceanbestpractices.org/handle/11329/109.

Fortier M, Fortier L, Michel C, Legendre L. 2002. Climatic and biological forcing of the vertical flux of biogenic particles under seasonal Arctic sea ice. *Mar Ecol Prog Ser* **225**(1): 16.

Fouest VL, Babin M, Tremblay J-É. 2013. The fate of riverine nutrients on Arctic shelves. *Biogeosciences* **10**(6): 3661–3677. Copernicus GmbH.

Fragoso GM, Poulton AJ, Yashayaev IM, Head EJH, Purdie DA. 2017. Spring phytoplankton communities of the Labrador Sea (2005–2014): pigment signatures, photophysiology and elemental ratios. *Biogeosciences* **14**(5): 1235–1259. doi: 10.5194/bg-14-1235-2017

Franks PJS. 2001. Phytoplankton blooms in a fluctuating environment: the roles of plankton response time scales and grazing. *J Plankton Res* **23**(12): 1433–1441. Oxford Academic. doi: 10.1093/plankt/23.12.1433

Freeman M. 1982. An ecological perspective on man-environment research in the Hudson and James Bay region. *Nat Can* **109**(4): 955–963.

Frey K, Eicken H, Perovich DK, Grenfell TC, Light B, Shapiro LH, Stierle AP. 2001. Heat budget and decay of clean and sediment-laden sea ice off the northern coast of Alaska. 2001. Port and Ocean Engineering in the Arctic Conference (POAC'1) Ottawa, Ont., Canada.

Frey KE, Perovich DK, Light B. 2011. The spatial distribution of solar radiation under a melting Arctic sea ice cover. *Geophys Res Lett* **38**(22).

Gagnon AS, Gough WA. 2005. Trends in the Dates of Ice Freeze-up and Breakup over Hudson Bay, Canada. *Arctic* **58**(4): 370–382. Arctic Institute of North America.

Galindo V, Gosselin M, Lavaud J, Mundy CJ, Else B, Ehn J, Babin M, Rysgaard S. 2017. Pigment composition and photoprotection of Arctic sea ice algae during spring. *Mar Ecol Prog Ser* **585**: 49–69. doi: 10.3354/meps12398

Geider RJ, Osborne BA. 1992. The Photosynthesis-Light Response Curve. In: Geider RJ, Osborne BA, editors. *Algal Photosynthesis*. Boston, MA: Springer US. p. 156–191. doi: 10.1007/978-1-4757-2153-9_7

Giles KA, Laxon SW, Ridout AL, Wingham DJ, Bacon S. 2012. Western Arctic Ocean freshwater storage increased by wind-driven spin-up of the Beaufort Gyre. *Nat Geosci* **5**(3): 194.

Glaz P, Sirois P, Archambault P, Nozais C. 2014. Impact of Forest Harvesting on Trophic Structure of Eastern Canadian Boreal Shield Lakes: Insights from Stable Isotope Analyses. *PLOS ONE* **9**(4): e96143. Public Library of Science. doi: 10.1371/journal.pone.0096143

Golden KM, Ackley SF, Lytle VI. 1998. The Percolation Phase Transition in Sea Ice. *Science* **282**(5397): 2238–2241. American Association for the Advancement of Science. doi: 10.1126/science.282.5397.2238

Gordeev VV. 2000. River Input of Water, Sediment, Major Ions, Nutrients and Trace Metals from Russian Territory to the Arctic Ocean. In: Lewis EL, Jones EP, Lemke P, Prowse TD, Wadhams P, editors. *The Freshwater Budget of the Arctic Ocean*. Dordrecht: Springer Netherlands. p. 297–322. doi: 10.1007/978-94-011-4132-1_14

Gosselin M, Legendre L, Demers S, Ingram RG. 1985. Responses of sea-ice microalgae to climatic and fortnightly tidal energy inputs (Manitounuk Sound, Hudson Bay). *Can J Fish Aquat Sci* **42**(5): 999–1006. doi: 10.1139/f85-125

Gosselin M, Legendre L, Therriault J, Demers S. 1990. Light and nutrient limitation of sea-ice microalgae (Hudson Bay, Canadian Arctic). *J Phycol* **26**(2): 220–232. doi: 10.1111/j.0022-3646.1990.00220.x

Gosselin M, Legendre L, Therriault J-C, Demers S, Rochet M. 1986. Physical control of the horizontal patchiness of sea-ice microalgae. *Mar Ecol Prog Ser* **29**(3): 289–298.

Gosselin M, Levasseur M, Wheeler PA, Horner RA, Booth BC. 1997. New measurements of phytoplankton and ice algal production in the Arctic Ocean. *Deep Sea Res Part II Top Stud Oceanogr* **44**(8): 1623–1644. Elsevier. doi: 10.1016/S0967-0645(97)00054-4

Gradinger R. 1996. Occurrence of an algal bloom under Arctic pack ice. *Mar Ecol Prog Ser* **131**: 301–305. doi: 10.3354/meps131301

Gradinger R. 2009. Sea-ice algae: Major contributors to primary production and algal biomass in the Chukchi and Beaufort Seas during May/June 2002. *Deep Sea Res Part II Top Stud Oceanogr* **56**(17): 1201–1212. Elsevier.

Granskog MA, Macdonald RW, Kuzyk ZZA, Senneville S, Mundy C, Barber DG, Stern GA, Saucier F. 2009. Coastal conduit in southwestern Hudson Bay (Canada) in summer: Rapid transit of freshwater and significant loss of colored dissolved organic matter. *J Geophys Res Oceans* **114**(C8). Wiley Online Library. doi: 10.1029/2009JC005270

Granskog MA, Macdonald RW, Mundy C-J, Barber DG. 2007. Distribution, characteristics and potential impacts of chromophoric dissolved organic matter (CDOM) in Hudson Strait and Hudson Bay, Canada. *Cont Shelf Res* **27**(15): 2032–2050. doi: 10.1016/j.csr.2007.05.001

Granskog MA, Vihma T, Pirazzini R, Cheng B. 2006. Superimposed ice formation and surface energy fluxes on sea ice during the spring melt–freeze period in the Baltic Sea. *J Glaciol* **52**(176): 119–127. Cambridge University Press.

Grenfell TC, Perovich DK, Ogren JA. 1981. Spectral albedos of an alpine snowpack. *Cold Reg Sci Technol* **4**(2): 121–127. Elsevier.

Gutt J. 1995. The occurrence of sub-ice algal aggregations off northeast Greenland. *Polar Biol* **15**(4): 247–252. Springer. doi: 10.1007/BF00239844

Ha S-Y, Kim Y-N, Park M-O, Kang S-H, Kim H, Shin K-H. 2012. Production of mycosporine-like amino acids of in situ phytoplankton community in Kongsfjorden, Svalbard, Arctic. *J Photochem Photobiol B* **114**: 1–14. doi: 10.1016/j.jphotobiol.2012.03.011

Haine TWN, Curry B, Gerdes R, Hansen E, Karcher M, Lee C, Rudels B, Spreen G, de Steur L, Stewart KD, et al. 2015. Arctic freshwater export: Status, mechanisms, and prospects. *Glob Planet Change* **125**: 13–35. doi: 10.1016/j.gloplacha.2014.11.013

Hansen HP, Koroleff F. 1999. Determination of nutrients. *Methods Seawater Anal*: 159–228.

Harasyn ML, Isleifson D, Chan W, Barber DG. 2020. Multi-scale observations of the co-evolution of sea ice thermophysical properties and microwave brightness temperatures during the summer melt period in Hudson Bay. *Elem Sci Anth* **8**(1): 16. University of California Press. doi: 10.1525/elementa.412

Harvey M, Therriault J-C, Simard N. 1997. Late-summer distribution of phytoplankton in relation to water mass characteristics in Hudson Bay and Hudson Strait (Canada). *Can J Fish Aquat Sci* **54**(8): 1937–1952. doi: 10.1139/f97-099

Heikkilä M, Pospelova V, Hochheim KP, Kuzyk ZZA, Stern GA, Barber DG, Macdonald RW. 2014. Surface sediment dinoflagellate cysts from the Hudson Bay system and their relation to freshwater and nutrient cycling. *Mar Micropaleontol* **106**: 79–109. doi: 10.1016/j.marmicro.2013.12.002

Higgins HW, Wright SW, Schlüter L. 2011. Quantitative interpretation of chemotaxonomic pigment data. In: *Phytoplankton Pigments: Characterization, Chemotaxonomy and Applications in Oceanography*. Cambridge: Cambridge University Press. p. 257–313.

Hill V, Cota G, Stockwell D. 2005. Spring and summer phytoplankton communities in the Chukchi and Eastern Beaufort Seas. *Deep Sea Res Part II Top Stud Oceanogr* **52**(24): 3369–3385. doi: 10.1016/j.dsr2.2005.10.010

Hill V, Steele M, Light B. 2020. Observation of prolonged ice algae bloom in drifting Arctic pack ice from autonomous buoy [Conference presentation]. Ocean Science Meeting, San Diego.

Hill VJ, Light B, Steele M, Zimmerman RC. 2018. Light availability and phytoplankton growth beneath Arctic sea ice: Integrating observations and modeling. *J Geophys Res Oceans* **123**(5): 3651–3667.

Hill VJ, Matrai PA, Olson E, Suttles S, Steele M, Codispoti L, Zimmerman RC. 2013. Synthesis of integrated primary production in the Arctic Ocean: II. In situ and remotely sensed estimates. *Prog Oceanogr* **110**: 107–125.

Hill VJ, Zimmerman RC. 2016. Characteristics of colored dissolved organic material in first year landfast sea ice and the underlying water column in the Canadian Arctic in the early spring. *Mar Chem* **180**: 1–13. doi: 10.1016/j.marchem.2016.01.007

Hochheim K, Barber DG, Lukovich JV. 2010. Changing sea ice conditions in Hudson Bay, 1980–2005. In: *A Little Less Arctic*. Springer. p. 39–52.

Hochheim K, Lukovich J, Barber D. 2011. Atmospheric forcing of sea ice in Hudson Bay during the spring period, 1980–2005. *J Mar Syst* **88**(3): 476–487. Elsevier. doi: 10.1016/j.jmarsys.2011.05.003

Hochheim KP, Barber DG. 2014. An Update on the Ice Climatology of the Hudson Bay System. *Arct Antarct Alp Res* **46**(1): 66–83. Taylor & Francis. doi: 10.1657/1938-4246-46.1.66

Holmes RM, McClelland JW, Peterson BJ, Tank SE, Bulygina E, Eglinton TI, Gordeev VV, Gurtovaya TY, Raymond PA, Repeta DJ. 2012. Seasonal and annual fluxes of nutrients and organic matter from large rivers to the Arctic Ocean and surrounding seas. *Estuaries Coasts* **35**(2): 369–382. Springer.

Holm-Hansen O, Lorenzen CJ, Holmes RW, Strickland JDH. 1965. Fluorometric Determination of Chlorophyll. *ICES J Mar Sci* **30**(1): 3–15. Oxford Academic. doi: 10.1093/icesjms/30.1.3

Hop H, Vihtakari M, Bluhm BA, Assmy P, Poulin M, Gradinger R, Peeken I, Von Quillfeldt C, Olsen LM, Zhitina L. 2020. Changes in sea-ice protist diversity with declining sea ice in the Arctic Ocean from the 1980s to 2010s. *Front Mar Sci* **7**: 243. Frontiers.

Hopwood MJ, Carroll D, Dunse T, Hodson A, Holding JM, Iriarte JL, Ribeiro S, Achterberg EP, Cantoni C, Carlson DF. 2020. How does glacier discharge affect marine biogeochemistry and primary production in the Arctic? *The Cryosphere* **14**: 1347–1383. Copernicus Publications (EGU). doi: 10.5194/tc-14-1347-2020

Horner R, Schrader GC. 1982. Relative Contributions of Ice Algae, Phytoplankton, and Benthic Microalgae to Primary Production in Nearshore Regions of the Beaufort Sea. *ARCTIC* **35**(4): 485–503. doi: 10.14430/arctic2356

Horvat C, Flocco D, Rees Jones DW, Roach L, Golden KM. 2020. The Effect of Melt Pond Geometry on the Distribution of Solar Energy Under First-Year Sea Ice. *Geophys Res Lett* **47**(4): e2019GL085956. doi: 10.1029/2019GL085956

Horvat C, Jones DR, Iams S, Schroeder D, Flocco D, Feltham D. 2017. The frequency and extent of sub-ice phytoplankton blooms in the Arctic Ocean. *Sci Adv* **3**(3): e1601191. doi: 10.1126/sciadv.1601191

Hsiao SI. 1988. Spatial and seasonal variations in primary production of sea ice microalgae and phytoplankton in Frobisher Bay, Arctic Canada. *Mar Ecol Prog Ser*: 275–285. JSTOR.

Huot Y, Babin M, Bruyant F. 2013. Photosynthetic parameters in the Beaufort Sea in relation to the phytoplankton community structure. *Biogeosciences* **10**(5): 3445–3454. Copernicus GmbH. doi: 0.5194/bg-10-3445-2013

Hwang BJ, Ehn JK, Barber DG. 2006. Relationships between albedo and microwave emissions over thin newly formed sea ice during fall freeze-up. *Geophys Res Lett* **33**(17). Wiley Online Library.

Iacozza J, Barber DG. 1999. An examination of the distribution of snow on sea-ice. *Atmosphere-Ocean* **37**(1): 21–51. doi: 10.1080/07055900.1999.9649620

IOCCG. 2011. Bio-Optical Sensors on Argo Floats. Affiliated Program of the Scientific Committee on Ocean Research (SCOR). Report No.: 11.

Iriberri J, Undurraga A, Muela A, Egea L. 1985. Heterotrophic bacterial activity in coastal waters: Functional relationship of temperature and phytoplankton population. *Ecol Model* **28**(1): 113–120. doi: 10.1016/0304-3800(85)90016-X

Irwin BD. 1990. Primary production of ice algae on a seasonally-ice-covered, continental shelf. *Polar Biol* **10**(4): 247–254. doi: 10.1007/BF00238421

Ito M, Ohshima KI, Fukamachi Y, Hirano D, Mahoney AR, Jones J, Takatsuka T, Eicken H. 2019. Favorable conditions for suspension freezing in an Arctic coastal polynya. *J Geophys Res Oceans* **124**(12): 8701–8719. Wiley Online Library.

Johnsen G, Leu E, Gradinger R. 2020. Marine Micro- and Macroalgae in the Polar Night. In: Berge J, Johnsen G, Cohen JH, editors. *POLAR NIGHT Marine Ecology: Life and Light in the Dead of Night*. Cham: Springer International Publishing. p. 67–112. doi: 10.1007/978-3-030-33208-2_4

Johnsen G, Norli M, Moline M, Robbins I, von Quillfeldt C, Sørensen K, Cottier F, Berge J. 2018. The advective origin of an under-ice spring bloom in the Arctic Ocean using multiple observational platforms. *Polar Biol* **41**(6): 1197–1216. doi: 10.1007/s00300-018-2278-5

Jones EP, Anderson LG. 1994. Northern Hudson Bay and Foxe Basin: water masses, circulation and productivity. *Atmosphere-Ocean* **32**(2): 361–374. Taylor & Francis. doi: 10.1080/07055900.1994.9649502

Joy-Warren HL, Dijken GL van, Alderkamp A-C, Leventer A, Lewis KM, Selz V, Lowry KE, Poll W van de, Arrigo KR. 2019. Light Is the Primary Driver of Early Season Phytoplankton Production Along the Western Antarctic Peninsula. *J Geophys Res Oceans* **124**(11): 7375–7399. doi: 10.1029/2019JC015295

Juhl AR, Krembs C. 2010. Effects of snow removal and algal photoacclimation on growth and export of ice algae. *Polar Biol* **33**(8): 1057–1065. doi: 10.1007/s00300-010-0784-1

Kahru M, Zhongping L, Mitchell BG, Nevison CD. 2016. Effects of sea ice cover on satellite-detected primary production in the Arctic Ocean. *Biol Lett* **12**(11): 20160223. doi: 10.1098/rsbl.2016.0223

Katlein C, Arndt S, Belter H. Jakob, Castellani G, Nicolaus M. 2019. Seasonal Evolution of Light Transmission Distributions Through Arctic Sea Ice. *J Geophys Res Oceans* **124**(8): 5418–5435. doi: 10.1029/2018JC014833

Katlein C, Arndt S, Nicolaus M, Perovich DK, Jakuba MV, Suman S, Elliott S, Whitcomb LL, McFarland CJ, Gerdes R. 2015a. Influence of ice thickness and surface properties on light transmission through Arctic sea ice. *J Geophys Res Oceans* **120**(9): 5932–5944.

Katlein C, Fernández-Méndez M, Wenzhöfer F, Nicolaus M. 2015b. Distribution of algal aggregates under summer sea ice in the Central Arctic. *Polar Biol* **38**(5): 719–731.

Katlein C, Nicolaus M, Petrich C. 2014. The anisotropic scattering coefficient of sea ice. *J Geophys Res Oceans* **119**(2): 842–855.

Katlein C, Perovich DK, Nicolaus M. 2016. Geometric Effects of an Inhomogeneous Sea Ice Cover on the under Ice Light Field. *Front Earth Sci* **4**: 6.

Katlein C, Valcic L, Lambert-Girard S, Hoppmann M. 2021. New insights into radiative transfer within sea ice derived from autonomous optical propagation measurements. *The Cryosphere* **15**(1): 183–198. Copernicus GmbH. doi: https://doi.org/10.5194/tc-15-183-2021

Kauko HM, Pavlov AK, Johnsen G, Granskog MA, Peeken I, Assmy P. 2019 Feb 15. Photoacclimation state of an Arctic under-ice phytoplankton bloom. *J Geophys Res Oceans*, in press. doi: 10.1029/2018JC014777

Kauko HM, Taskjelle T, Assmy P, Pavlov AK, Mundy CJ, Duarte P, Fernández-Méndez M, Olsen LM, Hudson SR, Johnsen G, et al. 2017. Windows in Arctic sea ice: Light transmission and ice algae in a refrozen lead. *J Geophys Res Biogeosciences* **122**(6): 1486–1505. doi: 10.1002/2016JG003626

Kempama E, Reimnitz E, Barnes PW. 1989. Sea ice sediment entrainment and rafting in the Arctic. *J Sediment Res* **59**(2): 308–317. SEPM Society for Sedimentary Geology.

Kilias E, Wolf C, Nöthig E, Peeken I, Metfies K. 2013. Protist distribution in the Western Fram Strait in summer 2010 based on 454-pyrosequencing of 18S rDNA. *J Phycol* **49**(5): 996–1010. Wiley Online Library. doi: 10.1111/jpy.12109

Kinney JC, Maslowski W, Osinski R, Jin M, Frants M, Jeffery N, Lee YJ. 2020. Hidden production: On the importance of pelagic phytoplankton blooms beneath Arctic sea ice. *J Geophys Res Oceans* **n/a**(n/a): e2020JC016211. doi: 10.1029/2020JC016211

Kiørboe T. 2008. *A Mechanistic Approach to Plankton Ecology*. Princeton University Press.

Kirillov S, Babb D, Dmitrenko I, Landy J, Lukovich J, Ehn J, Sydor K, Barber D, Stroeve J. 2020. Atmospheric forcing drives the winter sea ice thickness asymmetry of Hudson Bay. *J Geophys Res Oceans* **125**(2): e2019JC015756. Wiley Online Library. doi: 10.1029/2019JC015756

Kirk JTO. 1981. Monte Carlo study of the nature of the underwater light field in, and the relationships between optical properties of, turbid yellow waters. *Mar Freshw Res* **32**(4): 517–532. doi: 10.1071/mf9810517

Kirk JTO. 2011. *Light and Photosynthesis in Aquatic Ecosystems*. Cambridge Univ Pr: New York.

Kukulya A, Plueddemann A, Austin T, Stokey R, Purcell M, Allen B, Littlefield R, Freitag L, Koski P, Gallimore E. 2010. Under-ice operations with a REMUS-100 AUV in the Arctic. 2010. 2010 IEEE/OES Autonomous Underwater Vehicles. IEEE.

Kuzyk ZZA, Macdonald RW, Tremblay J-É, Stern GA. 2009. Elemental and stable isotopic constraints on river influence and patterns of nitrogen cycling and biological productivity in Hudson Bay. *Cont Shelf Res* **30**(2): 163–176. Elsevier. doi: 10.1016/j.csr.2009.10.014

Kvernvik AC, Hoppe CJM, Lawrenz E, Prášil O, Greenacre M, Wiktor JM, Leu E. 2018. Fast reactivation of photosynthesis in arctic phytoplankton during the polar night1. *J Phycol* **54**(4): 461–470. doi: 10.1111/jpy.12750

Kwok R. 2018. Arctic sea ice thickness, volume, and multiyear ice coverage: losses and coupled variability (1958–2018). *Environ Res Lett* **13**(10): 105005. IOP Publishing.

Kwok R, Cunningham G, Wensnahan M, Rigor I, Zwally H, Yi D. 2009. Thinning and volume loss of the Arctic Ocean sea ice cover: 2003–2008. *J Geophys Res Oceans* **114**(C7).

Kwok R, Kacimi S, Webster MA, Kurtz NT, Petty AA. 2020. Arctic Snow Depth and Sea Ice Thickness From ICESat-2 and CryoSat-2 Freeboards: A First Examination. *J Geophys Res Oceans* **125**(3): e2019JC016008. doi: 10.1029/2019JC016008

Kwok R, Rothrock DA. 1999. Variability of Fram Strait ice flux and North Atlantic oscillation. *J Geophys Res Oceans* **104**(C3): 5177–5189.

Kwok R, Spreen G, Pang S. 2013. Arctic sea ice circulation and drift speed: Decadal trends and ocean currents. *J Geophys Res Oceans* **118**(5): 2408–2425.

Lacour T, Larivière J, Babin M. 2017. Growth, Chl a content, photosynthesis, and elemental composition in polar and temperate microalgae. *Limnol Oceanogr* **62**(1): 43–58. doi: 10.1002/lno.10369

Laine V, Manninen T, Riihelä A, Andersson K. 2011. Shortwave broadband black-sky surface albedo estimation for Arctic sea ice using passive microwave radiometer data. *J Geophys Res Atmospheres* **116**(D16). doi: 10.1029/2011JD015700

Landy J, Ehn J, Shields M, Barber D. 2014. Surface and melt pond evolution on landfast first-year sea ice in the Canadian Arctic Archipelago. *J Geophys Res Oceans* **119**(5): 3054–3075.

Landy JC, Ehn JK, Babb DG, Thériault N, Barber DG. 2017. Sea ice thickness in the Eastern Canadian Arctic: Hudson Bay Complex & Baffin Bay. *Remote Sens Environ* **200**: 281–294. doi: 10.1016/j.rse.2017.08.019

Laney SR, Krishfield RA, Toole JM. 2017. The euphotic zone under Arctic Ocean sea ice: Vertical extents and seasonal trends. *Limnol Oceanogr* **62**(5): 1910–1934. doi: 10.1002/lno.10543

Laney SR, Sosik HM. 2014. Phytoplankton assemblage structure in and around a massive under-ice bloom in the Chukchi Sea. *Deep Sea Res Part II Top Stud Oceanogr* **105**: 30–41. doi: 10.1016/j.dsr2.2014.03.012

Lange BA, Katlein C, Castellani G, Fernández-Méndez M, Nicolaus M, Peeken I, Flores H. 2017. Characterizing Spatial Variability of Ice Algal Chlorophyll a and Net Primary Production between Sea Ice Habitats Using Horizontal Profiling Platforms. *Front Mar Sci* **4**. doi: 10.3389/fmars.2017.00349

Lapoussière A, Michel C, Gosselin M, Poulin M, Martin J, Tremblay J-É. 2013. Primary production and sinking export during fall in the Hudson Bay system, Canada. *Cont Shelf Res* **52**: 62–72. Elsevier. doi: 10.1016/j.csr.2012.10.013

Latasa M. 2007. Improving estimations of phytoplankton class abundances using CHEMTAX. *Mar Ecol Prog Ser* **329**: 13–21. doi: 10.3354/meps329013

Lebret K, Fernández MF, Hagman CHC, Rengefors K, Hansson L-A. 2012. Grazing resistance allows bloom formation and may explain invasion success of Gonyostomum semen. *Limnol Oceanogr* **57**(3): 727–734. doi: 10.4319/lo.2012.57.3.0727

Lebrun M, Vancoppenolle M, Madec G, Massonnet F. 2019. Arctic sea-ice-free season projected to extend into autumn. *The Cryosphere* **13**: 79–96. doi: 10.5194/tc-13-79-2019

Ledley TS, Pfirman S. 1997. The impact of sediment-laden snow and sea ice in the arctic on climate. *Clim Change* **37**(4): 641–664. Springer.

Lee SH, Stockwell DA, Joo H-M, Son YB, Kang C-K, Whitledge TE. 2012. Phytoplankton production from melting ponds on Arctic sea ice. *J Geophys Res Oceans* **117**(C4). doi: 10.1029/2011JC007717

Lee YJ, Matrai PA, Friedrichs MAM, Saba VS, Antoine D, Ardyna M, Asanuma I, Babin M, Bélanger S, Benoît-Gagné M, et al. 2015. An assessment of phytoplankton primary productivity in the Arctic Ocean from satellite

ocean color/in situ chlorophyll-a based models. *J Geophys Res Oceans* **120**(9): 6508–6541. doi: https://doi.org/10.1002/2015JC011018

Legendre L, Gosselin M. 1991. In situ spectroradiometric estimation of microalgal biomass in first-year sea ice. *Polar Biol* **11**(2): 113–115.

Legendre L, Ingram RG, Poulin M. 1981. Physical control of phytoplankton production under sea ice (Manitounuk Sound, Hudson Bay). *Can J Fish Aquat Sci* **38**(11): 1385–1392. doi: 10.1139/f81-185

Leppäranta M, Reinart A, Erm A, Arst H, Hussainov M, Sipelgas L. 2003. Investigation of ice and water properties and under-ice light fields in fresh and brackish water bodies. *Hydrol Res* **34**(3): 245–266.

Letelier RM, Karl DM, Abbott MR, Bidigare RR. 2004. Light driven seasonal patterns of chlorophyll and nitrate in the lower euphotic zone of the North Pacific Subtropical Gyre. *Limnol Oceanogr* **49**(2): 508–519. Wiley Online Library.

Leu E, Mundy C, Assmy P, Campbell K, Gabrielsen T, Gosselin M, Juul-Pedersen T, Gradinger R. 2015. Arctic spring awakening–steering principles behind the phenology of vernal ice algal blooms. *Prog Oceanogr* **139**: 151–170. doi: 10.1016/j.pocean.2015.07.012

Lewis KM, Arntsen AE, Coupel P, Joy-Warren H, Lowry KE, Matsuoka A, Mills MM, Dijken GL van, Selz V, Arrigo KR. 2019. Photoacclimation of Arctic Ocean phytoplankton to shifting light and nutrient limitation. *Limnol Oceanogr* **64**(1): 284–301. doi: 10.1002/lno.11039

Lewis KM, Dijken GL van, Arrigo KR. 2020. Changes in phytoplankton concentration now drive increased Arctic Ocean primary production. *Science* **369**(6500): 198–202. American Association for the Advancement of Science. doi: 10.1126/science.aay8380

Lewis MR, Smith JC. 1983. A small volume, short-incubation-time method for measurement of photosynthesis as a function of incident irradiance. *Mar Ecol Prog Ser* **13**: 99–102.

Li WKW, McLaughlin FA, Lovejoy C, Carmack EC. 2009. Smallest Algae Thrive As the Arctic Ocean Freshens. *Science* **326**(5952): 539–539. doi: 10.1126/science.1179798

Light B, Eicken H, Maykut GA, Grenfell TC. 1998. The effect of included particulates on the spectral albedo of sea ice. *J Geophys Res* **103**(C12): 27739–27752.

Light B, Grenfell TC, Perovich DK. 2008. Transmission and absorption of solar radiation by Arctic sea ice during the melt season. *J Geophys Res Oceans* **113**(C3).

Light B, Maykut G, Grenfell T. 2003. Effects of temperature on the microstructure of first-year Arctic sea ice. *J Geophys Res Oceans* **108**(C2). Wiley Online Library.

Light B, Perovich DK, Webster MA, Polashenski C, Dadic R. 2015. Optical properties of melting first-year Arctic sea ice. *J Geophys Res Oceans* **120**(11): 7657–7675.

Long Z, Perrie W. 2012. Air-sea interactions during an Arctic storm. *J Geophys Res Atmospheres* **117**(D15).

Lowry KE, Pickart RS, Mills MM, Brown ZW, van Dijken GL, Bates NR, Arrigo KR. 2015. The influence of winter water on phytoplankton blooms in the Chukchi Sea. *Deep Sea Res Part II Top Stud Oceanogr* **118**: 53–72. doi: 10.1016/j.dsr2.2015.06.006

Lowry KE, Pickart RS, Selz V, Mills MM, Pacini A, Lewis KM, Joy-Warren HL, Nobre C, Dijken GL van, Grondin P-L, et al. 2018. Under-Ice Phytoplankton Blooms Inhibited by Spring Convective Mixing in Refreezing Leads. *J Geophys Res Oceans* **123**(1): 90–109. doi: 10.1002/2016JC012575

Lu P, Leppäranta M, Cheng B, Li Z. 2016. Influence of melt-pond depth and ice thickness on Arctic sea-ice albedo and light transmittance. *Cold Reg Sci Technol* **124**: 1–10. doi: 10.1016/j.coldregions.2015.12.010

Lund J, Kipling C, Le Cren E. 1958. The inverted microscope method of estimating algal numbers and the statistical basis of estimations by counting. *Hydrobiologia* **11**(2): 143–170. Springer. doi: 10.1007/BF00007865

Lund-Hansen LC, Juul T, Eskildsen TD, Hawes I, Sorrell B, Melvad C, Hancke K. 2018. A low-cost remotely operated vehicle (ROV) with an optical positioning system for under-ice measurements and sampling. *Cold Reg Sci Technol* **151**: 148–155. doi: 10.1016/j.coldregions.2018.03.017

Macdonald RW, Anderson LG, Christensen JP, Miller LA, Semiletov IP, Stein R. 2010. The Arctic Ocean. In: *Carbon and Nutrient Fluxes in Continental Margins*. Springer, Heidelberg. p. 291–303.

Mackey M, Mackey D, Higgins H, Wright S. 1996. CHEMTAX - a program for estimating class abundances from chemical markers: application to HPLC measurements of phytoplankton. *Mar Ecol Prog Ser* **144**: 265–283. doi: 10.3354/meps144265

Markus T, Stroeve JC, Miller J. 2009. Recent changes in Arctic sea ice melt onset, freezeup, and melt season length. *J Geophys Res Oceans* **114**(C12). Wiley Online Library.

Martin J, Tremblay J-É, Gagnon J, Tremblay G, Lapoussière A, Jose C, Poulin M, Gosselin M, Gratton Y, Michel C. 2010. Prevalence, structure and properties of subsurface chlorophyll maxima in Canadian Arctic waters. *Mar Ecol Prog Ser* **412**: 69–84.

Massicotte P, Amiraux R, Amyot M-P, Archambault P, Ardyna M, Arnaud L, Artigue L, Aubry C, Ayotte P, Bécu G, et al. 2020. Green Edge ice camp campaigns: understanding the processes controlling the under-ice Arctic phytoplankton spring bloom. *Earth Syst Sci Data* **12**(1): 151–176. Copernicus GmbH. doi: https://doi.org/10.5194/essd-12-151-2020

Massicotte P, Bécu G, Lambert-Girard S, Leymarie E, Babin M. 2018. Estimating Underwater Light Regime under Spatially Heterogeneous Sea Ice in the Arctic. *Appl Sci* **8**(12): 2693. doi: 10.3390/app8122693

Massicotte P, Peeken I, Katlein C, Flores H, Huot Y, Castellani G, Arndt S, Lange BA, Tremblay J-É, Babin M. 2019. Sensitivity of phytoplankton primary production estimates to available irradiance under heterogeneous sea-ice conditions. *J Geophys Res Oceans*, in press. doi: 10.1029/2019JC015007

Mathis JT, Pickart RS, Hansell DA, Kadko D, Bates NR. 2007. Eddy transport of organic carbon and nutrients from the Chukchi Shelf: Impact on the upper halocline of the western Arctic Ocean. *J Geophys Res Oceans* **112**(C5). doi: 10.1029/2006JC003899

Matthes LC, Ehn JK, L.-Girard S, Pogorzelec NM, Babin M, Mundy CJ. 2019. Average cosine coefficient and spectral distribution of the light field under sea ice: Implications for primary production. *Elem Sci Anth* **7**(1): 25. doi: 10.1525/elementa.363

Matthes LC, Mundy CJ, L. -Girard S, Babin M, Verin G, Ehn JK. 2020. Spatial Heterogeneity as a Key Variable Influencing Spring-Summer Progression in UVR and PAR Transmission Through Arctic Sea Ice. *Front Mar Sci* **7**. Frontiers. doi: 10.3389/fmars.2020.00183

Maykut GA, Untersteiner N. 1971. Some results from a time-dependent thermodynamic model of sea ice. *J Geophys Res* **76**(6): 1550–1575.

McMinn A, Ashworth C, Ryan K. 2005. Growth and Productivity of Antarctic Sea Ice Algae under PAR and UV Irradiances. *Bot Mar* **42**(4): 401–407. doi: 10.1515/BOT.1999.046

Medlin LK, Priddle J. 1990. *Polar Marine Diatoms*. British Antarctic Survey.

Melnikov A. 1997. *Arctic Sea Ice Ecosystem*. CRC Press.

Michel C, Hamilton J, Hansen E, Barber D, Reigstad M, Iacozza J, Seuthe L, Niemi A. 2015. Arctic Ocean outflow shelves in the changing Arctic: A review and perspectives. *Prog Oceanogr* **139**: 66–88. doi: 10.1016/j.pocean.2015.08.007

Michel C, Ingram RG, Harris LR. 2006. Variability in oceanographic and ecological processes in the Canadian Arctic Archipelago. *Prog Oceanogr* **71**(2): 379–401. doi: 10.1016/j.pocean.2006.09.006

Michel C, Legendre L, Demers S, Therriault J-C. 1988. Photoadaptation of sea-ice microalgae in springtime: photosynthesis and carboxylating enzymes. *Mar Ecol Prog Ser* **50**(1/2): 177–185. Inter-Research Science Center.

Michel C, Legendre L, Therriault J-C, Demers S, Vandevelde T. 1993. Springtime coupling between ice algal and phytoplankton assemblages in southeastern Hudson Bay, Canadian Arctic. *Polar Biol* **13**(7): 441–449.

Mizobata K, Saitoh S, Shiomoto A, Miyamura T, Shiga N, Imai K, Toratani M, Kajiwara Y, Sasaoka K. 2002. Bering Sea cyclonic and anticyclonic eddies observed during summer 2000 and 2001. *Prog Oceanogr* **55**(1–2): 65–75. Elsevier.

Mobley CD. 1994. *Light and Water: Radiative Transfer in Natural Waters*. Academic press.

Mock T, Gradinger R. 1999. Determination of Arctic ice algal production with a new in situ incubation technique. *Mar Ecol Prog Ser* **177**: 15–26.

Moore G, Schweiger A, Zhang J, Steele M. 2018. Collapse of the 2017 winter Beaufort High: A response to thinning sea ice? *Geophys Res Lett* **45**(6): 2860–2869.

Morel A. 1978. Available, usable, and stored radiant energy in relation to marine photosynthesis. *Deep Sea Res* **25**(8): 673–688. doi: 10.1016/0146-6291(78)90623-9

Morel A. 1991. Light and marine photosynthesis: a spectral model with geochemical and climatological implications. *Prog Oceanogr* **26**(3): 263–306. doi: 10.1016/0079-6611(91)90004-6

Morel A, Gentili B. 2004. Radiation transport within oceanic (case 1) water. *J Geophys Res Oceans* **109**(C6). doi: 10.1029/2003JC002259

Morel A, Smith RC. 1974. Relation between total quanta and total energy for aquatic photosynthesis. *Limnol Oceanogr* **19**(4): 591–600.

Morison J, Kwok R, Peralta-Ferriz C, Alkire M, Rigor I, Andersen R, Steele M. 2012. Changing arctic ocean freshwater pathways. *Nature* **481**(7379): 66.

Munafò A, Ferri G. 2017. An acoustic network navigation system. *J Field Robot* **34**(7): 1332–1351. Wiley Online Library.

Mundy C, Gosselin M, Ehn JK, Belzile C, Poulin M, Alou E, Roy S, Hop H, Lessard S, Papakyriakou TN. 2011. Characteristics of two distinct high-light acclimated algal communities during advanced stages of sea ice melt. *Polar Biol* **34**(12): 1869–1886. Springer. doi: 10.1007/s00300-011-0998-x

Mundy CJ, Barber DG, Michel C. 2005. Variability of snow and ice thermal, physical and optical properties pertinent to sea ice algae biomass during spring. *J Mar Syst* **58**(3): 107–120.

Mundy CJ, Gosselin M, Ehn J, Gratton Y, Rossnagel A, Barber DG, Martin J, Tremblay J-É, Palmer M, Arrigo KR. 2009. Contribution of under-ice primary production to an ice-edge upwelling phytoplankton bloom in the Canadian Beaufort Sea. *Geophys Res Lett* **36**(17).

Mundy CJ, Gosselin M, Gratton Y, Brown K, Galindo V, Campbell K, Levasseur M, Barber D, Papakyriakou T, Bélanger S. 2014. Role of environmental factors on phytoplankton bloom initiation under landfast sea ice in Resolute Passage, Canada. *Mar Ecol Prog Ser* **497**: 39Á49. doi: 10.3354/meps10587

Neeley AR, Harris LA, Frey KE. 2018. Unraveling Phytoplankton Community Dynamics in the Northern Chukchi Sea Under Sea-Ice-Covered and Sea-Ice-Free Conditions. *Geophys Res Lett* **45**(15): 7663–7671. doi: 10.1029/2018GL077684

Nicolaus M, Hudson SR, Gerland S, Munderloh K. 2010. A modern concept for autonomous and continuous measurements of spectral albedo and transmittance of sea ice. *Cold Reg Sci Technol* **62**(1): 14–28. doi: 10.1016/j.coldregions.2010.03.001

Nicolaus M, Katlein C. 2013. Mapping radiation transfer through sea ice using a remotely operated vehicle (ROV). *The Cryosphere* **7**(3): 763–777. doi: 10.5194/tc-7-763-2013

Nicolaus M, Katlein C, Maslanik J, Hendricks S. 2012. Changes in Arctic sea ice result in increasing light transmittance and absorption. *Geophys Res Lett* **39**(24).

Nicolaus M, Petrich C, Hudson SR, Granskog M. 2013. Variability of light transmission through Arctic land-fast sea ice during spring. , in press.

Niebauer HJ, Alexander V. 1985. Oceanographic frontal structure and biological production at an ice edge. *Cont Shelf Res* **4**(4): 367–388. doi: 10.1016/0278-4343(85)90001-9

Niemi A, Michel C. 2015. Temporal and spatial variability in sea-ice carbon: nitrogen ratios on Canadian Arctic shelves. *Elem Sci Anth* **3**. University of California Press. doi: 10.12952/journal.elementa.000078

Nomura D, Nishioka J, Granskog MA, Krell A, Matoba S, Toyota T, Hattori H, Shirasawa K. 2010. Nutrient distributions associated with snow and sediment-laden layers in sea ice of the southern Sea of Okhotsk. *Mar Chem* **119**(1–4): 1–8. Elsevier.

Norrbin F, Eilertsen HChr, Degerlund M. 2009. Vertical distribution of primary producers and zooplankton grazers during different phases of the Arctic spring bloom. *Deep Sea Res Part II Top Stud Oceanogr* **56**(21): 1945–1958. doi: 10.1016/j.dsr2.2008.11.006

Nöthig E-M, Bracher A, Engel A, Metfies K, Niehoff B, Peeken I, Bauerfeind E, Cherkasheva A, Gäbler-Schwarz S, Hardge K, et al. 2015. Summertime plankton ecology in Fram Strait—a compilation of long- and short-term observations. *Polar Res* **34**(1): 23349. doi: 10.3402/polar.v34.23349

Nöthig E-M, Ramondenc S, Haas A, Hehemann L, Walter A, Bracher A, Lalande C, Metfies K, Peeken I, Bauerfeind E. 2020. Summertime Chlorophyll a and Particulate Organic Carbon Standing Stocks in Surface Waters of the Fram Strait and the Arctic Ocean (1991–2015). *Front Mar Sci*, in press. Frontiers Research Foundation.

Notz D, Dörr J, Bailey DA, Blockley E, Bushuk M, Debernard JB, Dekker E, DeRepentigny P, Docquier D, Fučkar NS, et al. 2020. Arctic Sea Ice in CMIP6. *Geophys Res Lett* **47**(10). doi: 10.1029/2019GL086749

O'Brien MC, Melling H, Pedersen TF, Macdonald RW. 2011. The role of eddies and energetic ocean phenomena in the transport of sediment from shelf to basin in the Arctic. *J Geophys Res Oceans* **116**(C8). Wiley Online Library.

Olsen LM, Laney SR, Duarte P, Kauko HM, Fernández-Méndez M, Mundy CJ, Rösel A, Meyer A, Itkin P, Cohen L, et al. 2017. The seeding of ice algal blooms in Arctic pack ice: The multiyear ice seed repository hypothesis. *J Geophys Res Biogeosciences* **122**(7): 1529–1548. doi: 10.1002/2016JG003668

Oziel L, Baudena A, Ardyna M, Massicotte P, Randelhoff A, Sallée J-B, Ingvaldsen RB, Devred E, Babin M. 2020. Faster Atlantic currents drive poleward expansion of temperate phytoplankton in the Arctic Ocean. *Nat Commun* **11**(1): 1705. Nature Publishing Group. doi: 10.1038/s41467-020-15485-5

Oziel L, Massicotte P, Randelhoff A, Ferland J, Vladoiu A, Lacour L, Galindo V, Lambert-Girard S, Dumont D, Cuypers Y, et al. 2019. Environmental factors influencing the seasonal dynamics of spring algal blooms in and beneath sea ice in western Baffin Bay. *Elem Sci Anth* **7**(1): 34. doi: 10.1525/elementa.372

Oziel L, Massicotte P, Randelhoff A, Vladoiu A, Lacour L, Lambert-Girard S, Dumont D, Cuypers Y, Bouruet-Aubertot P, Babin M. n.d. Seasonal dynamic of environmental factors influencing under-ice spring bloom in the Baffin Bay. *Elementa*, in press.

Oziel L, Neukermans G, Ardyna M, Lancelot C, Tison J-L, Wassmann P, Sirven J, Ruiz-Pino D, Gascard J-C. 2017. Role for Atlantic inflows and sea ice loss on shifting phytoplankton blooms in the Barents Sea. *J Geophys Res Oceans* **122**(6): 5121–5139. doi: 10.1002/2016JC012582

Oziel L, Sirven J, Gascard J-C. 2016. The Barents Sea frontal zones and water masses variability (1980–2011). *Ocean Sci*(12): 169–184. doi: 10.5194/os-12-169-2016

Palmer MA, Arrigo KR, Mundy C, Ehn JK, Gosselin M, Barber DG, Martin J, Alou E, Roy S, Tremblay J-É. 2011. Spatial and temporal variation of photosynthetic parameters in natural phytoplankton assemblages in the Beaufort Sea, Canadian Arctic. *Polar Biol* **34**(12): 1915–1928. doi: 10.1007/s00300-011-1050-x

Palmer MA, Dijken GL van, Mitchell BG, Seegers BJ, Lowry KE, Mills MM, Arrigo KR. 2013. Light and nutrient control of photosynthesis in natural phytoplankton populations from the Chukchi and Beaufort seas, Arctic Ocean. *Limnol Oceanogr* **58**(6): 2185–2205. doi: 10.4319/lo.2013.58.6.2185

Parsons TR, Maita Y, Lalli CM. 1984. *A Manual of Chemical & Biological Methods for Seawater Analysis*. New York: Pergamon Press.

Pavlov AK, Taskjelle T, Kauko HM, Hamre B, Stephen HR, Assmy P, Duarte P, Fernández-Méndez M, Mundy CJ, Granskog MA. 2017. Altered inherent optical properties and estimates of the underwater light field during an Arctic under-ice bloom of Phaeocystis pouchetii. *J Geophys Res Oceans* **122**(6): 4939–4961. doi: 10.1002/2016JC012471

Pei S, Laws EA. 2013. Does the 14C method estimate net photosynthesis? Implications from batch and continuous culture studies of marine phytoplankton. *Deep Sea Res Part Oceanogr Res Pap* **82**: 1–9. Elsevier. doi: 10.1016/j.dsr.2013.07.011

Perovich DK. 1996. The Optical Properties of Sea Ice. US Army Corps of Engineers.

Perovich DK. 2005. On the aggregate-scale partitioning of solar radiation in Arctic sea ice during the Surface Heat Budget of the Arctic Ocean (SHEBA) field experiment. *J Geophys Res Oceans* **110**(C3). doi: 10.1029/2004JC002512

Perovich DK. 2006. The interaction of ultraviolet light with Arctic sea ice during SHEBA. *Ann Glaciol* **44**: 47–52. doi: 10.3189/172756406781811330

Perovich DK, Govoni JW. 1991. Absorption coefficients of ice from 250 to 400 nm. *Geophys Res Lett* **18**(7): 1233–1235. doi: 10.1029/91GL01642

Perovich DK, Gow AJ. 1996. A quantitative description of sea ice inclusions. *J Geophys Res Oceans* **101**(C8): 18327–18343. Wiley Online Library.

Perovich DK, Light B, Eicken H, Jones KF, Runciman K, Nghiem SV. 2007. Increasing solar heating of the Arctic Ocean and adjacent seas, 1979–2005: Attribution and role in the ice-albedo feedback. *Geophys Res Lett* **34**(19). doi: 10.1029/2007GL031480

Perovich DK, Polashenski C. 2012. Albedo evolution of seasonal Arctic sea ice. *Geophys Res Lett* **39**(8).

Petrich C, Eicken H. 2010. Growth, Structure and Properties of Sea Ice. In: *Sea Ice*Second. United Kingdom: Wiley-Blackwell, John Wiley & Sons Ltd. p. 23–78.

Pett RJ, Roff JC. 1982. Some observations and deductions concerning the deep waters of Hudson Bay. *Nat Can* **109**: 767–774.

Pfirman S, Wollenburg I, Thiede J, Lange MA. 1989. Lithogenic sediment on Arctic pack ice: Potential aeolian flux and contribution to deep sea sediments. In: *Paleoclimatology and Paleometeorology: Modern and Past Patterns of Global Atmospheric Transport*. Springer. p. 463–493.

Pickart RS, Spall MA, Mathis JT. 2013. Dynamics of upwelling in the Alaskan Beaufort Sea and associated shelf–basin fluxes. *Deep Sea Res Part Oceanogr Res Pap* **76**: 35–51. Elsevier.

Piiparinen J, Enberg S, Rintala J-M, Sommaruga R, Majaneva M, Autio R, Vähätalo AV. 2015. The contribution of mycosporine-like amino acids, chromophoric dissolved organic matter and particles to the UV protection of sea-ice organisms in the Baltic Sea. *Photochem Photobiol Sci* **14**(5): 1025–1038.

Platt T, Gallegos C, Harrison W. 1980. Photoinhibition of photosynthesis in natural assemblages of marine phytoplankton. *J Mar Res* **38**: 687–701.

Plueddemann A, Packard G, Lord J, Whelan S. 2008. Observing Arctic coastal hydrography using the REMUS AUV. 2008. 2008 IEEE/OES Autonomous Underwater Vehicles. IEEE.

Polashenski C, Perovich D, Courville Z. 2012. The mechanisms of sea ice melt pond formation and evolution. *J Geophys Res Oceans* **117**(C1).

Polyakov IV, Alkire MB, Bluhm BA, Brown KA, Carmack EC, Chierici M, Danielson SL, Ellingsen I, Ershova EA, Gårdfeldt K, et al. 2020. Borealization of the Arctic Ocean in Response to Anomalous Advection From Sub-Arctic Seas. *Front Mar Sci* **7**. Frontiers. doi: 10.3389/fmars.2020.00491

Poulin M, Cardinal A. 1982a. Sea ice diatoms from Manitounuk Sound, southeastern Hudson Bay (Quebec, Canada). III. Cymbellaceae, Entomoneidaceae, Gomphonemataceae, and Nitzschiaceae. *Can J Bot* **61**(1): 107–118. NRC Research Press. doi: 10.1139/b83-010

Poulin M, Cardinal A. 1982b. Sea ice diatoms from Manitounuk Sound, southeastern Hudson Bay (Quebec, Canada). II. Naviculaceae, genus Navicula. *Can J Bot* **60**(1): 2825–2845. NRC Research Press. doi: 10.1139/b82-343

Poulin M, Daugbjerg N, Gradinger R, Ilyash L, Ratkova T, von Quillfeldt C. 2011. The pan-Arctic biodiversity of marine pelagic and sea-ice unicellular eukaryotes: a first-attempt assessment. *Mar Biodivers* **41**(1): 13–28. doi: 10.1007/s12526-010-0058-8

Poulin M, Underwood GJ, Michel C. 2014. Sub-ice colonial Melosira arctica in Arctic first-year ice. *Diatom Res* **29**(2): 213–221.

Prinsenberg S. 1983. Effects of the hydroelectric developments on the oceanographic surface parameters of Hudson Bay. *Atmosphere-Ocean* **21**(4): 418–430. Taylor & Francis. doi: 10.1080/07055900.1983.9649177

Prinsenberg SJ. 1986. The circulation pattern and current structure of Hudson Bay. *Can Inland Seas*: 187–204.

Prisendorfer RW. 1961. Application of radiative transfer theory to light measurements in the sea. *Union Geod Geophys Inst Monogr* **10**: 11–30.

Proshutinsky A, Dukhovskoy D, Timmermans M-L, Krishfield R, Bamber J. 2015. Arctic circulation regimes. *Philos Transact A Math Phys Eng Sci* **373**. doi: 10.1098/rsta.2014.0160

Qu Y, Liang S, Liu Q, Li X, Feng Y, Liu S. 2016. Estimating Arctic sea-ice shortwave albedo from MODIS data. *Remote Sens Environ* **186**: 32–46. doi: 10.1016/j.rse.2016.08.015

Ralph PJ, Ryan KG, Martin A, Fenton G. 2007. Melting out of sea ice causes greater photosynthetic stress in algae than freezing in1. *J Phycol* **43**(5): 948–956. doi: 10.1111/j.1529-8817.2007.00382.x

Randelhoff A, Holding J, Janout M, Sejr MK, Babin M, Tremblay J-É, Alkire MB. 2020a. Pan-Arctic Ocean Primary Production Constrained by Turbulent Nitrate Fluxes. *Front Mar Sci* **7**. Frontiers. doi: 10.3389/fmars.2020.00150

Randelhoff A, Lacour L, Marec C, Leymarie E, Lagunas J, Xing X, Darnis G, Penkerc'h C, Sampei M, Fortier L, et al. 2020b. Arctic mid-winter phytoplankton growth revealed by autonomous profilers. *Sci Adv* **6**(39): eabc2678. American Association for the Advancement of Science. doi: 10.1126/sciadv.abc2678

Randelhoff A, Sundfjord A. 2018. Short commentary on marine productivity at Arctic shelf breaks: upwelling, advection and vertical mixing - ProQuest. *Ocean Sci* **14**(2): 293.

Ras J, Claustre H, Uitz J. 2008. Spatial variability of phytoplankton pigment distributions in the Subtropical South Pacific Ocean: comparison between in situ and predicted data. *Biogeosciences* **5**(2): 353–369.

Redfield AC. 1963. The influence of organisms on the composition of seawater. *The Sea* **2**: 26–77.

Reigstad M, Wassmann P, Wexels Riser C, Øygarden S, Rey F. 2002. Variations in hydrography, nutrients and chlorophyll a in the marginal ice-zone and the central Barents Sea. *J Mar Syst* **38**(1): 9–29. doi: 10.1016/S0924-7963(02)00167-7

Reimnitz E, Kempema E, Barnes P. 1987. Anchor ice, seabed freezing, and sediment dynamics in shallow Arctic seas. *J Geophys Res Oceans* **92**(C13): 14671–14678. Wiley Online Library.

Reinart A, Arst H, Blanco-Sequeiros A, Herlevi A. 1998. Relation between underwater irradiance and quantum irradiance in dependence on water transparency at different depths in the water bodies. *J Geophys Res Oceans* **103**(C4): 7749–7752.

Renaut S, Devred E, Babin M. 2018. Northward Expansion and Intensification of Phytoplankton Growth During the Early Ice-Free Season in Arctic. *Geophys Res Lett* **45**(19): 10,590-10,598. doi: 10.1029/2018GL078995

Ridenour NA, Hu X, Sydor K, Myers PG, Barber DG. 2019. Revisiting the Circulation of Hudson Bay: Evidence for a Seasonal Pattern. *Geophys Res Lett* **46**(7): 3891–3899. doi: 10.1029/2019GL082344

Roff J, Legendre L. 1986. Physico-chemical and biological oceanography of Hudson Bay. *Can Inland Seas* **44**: 265–292.

Rösel A, Kaleschke L. 2011. Comparison of different retrieval techniques for melt ponds on Arctic sea ice from Landsat and MODIS satellite data. *Ann Glaciol* **52**(57): 185–191.

Rösel A, Kaleschke L. 2012. Exceptional melt pond occurrence in the years 2007 and 2011 on the Arctic sea ice revealed from MODIS satellite data. *J Geophys Res Oceans* **117**(C5). doi: 10.1029/2011JC007869

Rösel A, Kaleschke L, Birnbaum G. 2012. Melt ponds on Arctic sea ice determined from MODIS satellite data using an artificial neural network. *The cryosphere* **6**: 431–446.

Rothrock D, Zhang J. 2005. Arctic Ocean sea ice volume: What explains its recent depletion? *J Geophys Res Oceans* **110**(C1). Wiley Online Library.

Runge JA, Therriault J-C, Legendre L, Ingram RG, Demers S. 1991. Coupling between ice microalgal productivity and the pelagic, metazoan food web in southeastern Hudson Bay: a synthesis of results*. *Polar Res* **10**(2): 325–338. doi: 10.1111/j.1751-8369.1991.tb00657.x

Sathyendranath S, Platt T, Caverhill CM, Warnock RE, Lewis MR. 1989. Remote sensing of oceanic primary production: computations using a spectral model. *Deep Sea Res Part Oceanogr Res Pap* **36**(3): 431–453.

Saucier F, Senneville S, Prinsenberg S, Roy F, Smith G, Gachon P, Caya D, Laprise R. 2004. Modelling the sea ice-ocean seasonal cycle in Hudson Bay, Foxe Basin and Hudson Strait, Canada. *Clim Dyn* **23**(3–4): 303–326. Springer. doi: 10.1007/s00382-004-0445-6

Scharien RK, Yackel JJ, Granskog MA, Else BGT. 2007. Coincident high resolution optical-SAR image analysis for surface albedo estimation of first-year sea ice during summer melt. *Remote Sens Environ* **111**(2): 160–171. doi: 10.1016/j.rse.2006.10.025

Schlitzer R. 2018. Ocean Data View. odv.awi.de.

Schweiger AJ. 2004. Changes in seasonal cloud cover over the Arctic seas from satellite and surface observations. *Geophys Res Lett* **31**(12). Wiley Online Library.

Serreze MC, Barry RG. 2011. Processes and impacts of Arctic amplification: A research synthesis. *Glob Planet Change* **77**(1–2): 85–96. Elsevier.

Sherr EB, Sherr BF, Wheeler PA, Thompson K. 2003. Temporal and spatial variation in stocks of autotrophic and heterotrophic microbes in the upper water column of the central Arctic Ocean. *Deep Sea Res Part Oceanogr Res Pap* **50**(5): 557–571. Elsevier.

Shimada K, Kamoshida T, Itoh M, Nishino S, Carmack E, McLaughlin F, Zimmermann S, Proshutinsky A. 2006. Pacific Ocean inflow: Influence on catastrophic reduction of sea ice cover in the Arctic Ocean. *Geophys Res Lett* **33**(8).

Sibert V, Zakardjian B, Gosselin M, Starr M, Senneville S, LeClainche Y. 2011. 3D bio-physical model of the sympagic and planktonic productions in the Hudson Bay System. *J Mar Syst* **88**(3): 401–422. doi: 10.1016/j.jmarsys.2011.03.014

Simmonds I, Keay K. 2009. Extraordinary September Arctic sea ice reductions and their relationships with storm behavior over 1979–2008. *Geophys Res Lett* **36**(19).

Slagstad D, Ellingsen I, Wassmann P. 2011. Evaluating primary and secondary production in an Arctic Ocean void of summer sea ice: an experimental simulation approach. *Prog Oceanogr* **90**(1–4): 117–131. Elsevier.

Smith R, Gosselin M, Taguchi S. 1997. The influence of major inorganic nutrients on the growth and physiology of high arctic ice algae. *J Mar Syst* **11**(1–2): 63–70. Elsevier.

Søreide JE, Carroll ML, Hop H, Ambrose Jr WG, Hegseth EN, Falk-Petersen S. 2013. Sympagic-pelagic-benthic coupling in Arctic and Atlantic waters around Svalbard revealed by stable isotopic and fatty acid tracers. *Mar Biol Res* **9**(9): 831–850.

Sørensen HL, Thamdrup B, Jeppesen E, Rysgaard S, Glud RN. 2017. Nutrient availability limits biological production in Arctic sea ice melt ponds. *Polar Biol* **40**(8): 1593–1606. doi: 10.1007/s00300-017-2082-7

Spencer RGM, Aiken GR, Butler KD, Dornblaser MM, Striegl RG, Hernes PJ. 2009. Utilizing chromophoric dissolved organic matter measurements to derive export and reactivity of dissolved organic carbon exported to the Arctic Ocean: A case study of the Yukon River, Alaska. *Geophys Res Lett* **36**(6). doi: 10.1029/2008GL036831

Spielhagen RF, Werner K, Sørensen SA, Zamelczyk K, Kandiano E, Budeus G, Husum K, Marchitto TM, Hald M. 2011. Enhanced Modern Heat Transfer to the Arctic by Warm Atlantic Water. *Science* **331**(6016): 450–453. American Association for the Advancement of Science. doi: 10.1126/science.1197397

Stadnyk T, Déry S, McDonald M, Koenig K. 2019. The Freshwater System. In: *From Science to Policy in the Greater Hudson Bay Marine Region: An Integrated Regional Impact Study (IRIS) of Climate Change and Modernization.* Québec City: ArcticNet. p. 113–154.

Steele M, Zhang J, Ermold W. 2010. Mechanisms of summertime upper Arctic Ocean warming and the effect on sea ice melt. *J Geophys Res Oceans* **115**(C11). Wiley Online Library.

Steiner N, Azetsu-Scott K, Galbraith P, Hamilton J, Hedges K, Hu X, Janjua M, Lambert N, Larouche P, Lavoie D. 2013. *Climate Change Assessment in the Arctic Basin Part 1: Trends and Projections: A Contribution to the Aquatic Climate Change Adaptation Services Program.* Fisheries and Oceans Canada.

Stewart D, Lockhart W. 2005. An overview of the Hudson Bay marine ecosystem. *Dep Fish Oceans Ott Can.*

St-Laurent P, Straneo F, Dumais J-F, Barber DG. 2011. What is the fate of the river waters of Hudson Bay? *J Mar Syst* **88**(3): 352–361. doi: 10.1016/j.jmarsys.2011.02.004

Stoyneva MP, Descy J-P, Vyverman W. 2007. Green algae in Lake Tanganyika: is morphological variation a response to seasonal changes? *Hydrobiologia* **578**(1): 7–16. doi: 10.1007/s10750-006-0428-1

Strass VH, Nöthig E-M. 1996. Seasonal shifts in ice edge phytoplankton blooms in the Barents Sea related to the water column stability. *Polar Biol* **16**(6): 409–422.

Stroeve J, Notz D. 2018. Changing state of Arctic sea ice across all seasons. *Environ Res Lett* **13**(10): 103001. IOP Publishing.

Stroeve JC, Serreze MC, Holland MM, Kay JE, Malanik J, Barrett AP. 2012. The Arctic's rapidly shrinking sea ice cover: a research synthesis. *Clim Change* **110**(3): 1005–1027.

Sturm M, Massom RA. 2009. Snow and sea ice. *Sea Ice Oxf Wiley-Blackwell*: 153–204.

Sverdrup H. 1953. On conditions for the vernal blooming of phytoplankton. *J Cons Int Explor Mer* **18**(3): 287–295.

Syvertsen EE. 1991. Ice algae in the Barents Sea: types of assemblages, origin, fate and role in the ice-edge phytoplankton bloom. *Polar Res* **10**(1): 277–288.

Taskjelle T, Hudson SR, Granskog MA, Hamre B. 2017. Modelling radiative transfer through ponded first-year Arctic sea ice with a plane-parallel model. *The Cryosphere* **11**(5): 2137–2148. doi: https://doi.org/10.5194/tc-11-2137-2017

Taylor RL, Semeniuk DM, Payne CD, Zhou J, Tremblay J-É, Cullen JT, Maldonado MT. 2013. Colimitation by light, nitrate, and iron in the Beaufort Sea in late summer. *J Geophys Res Oceans* **118**(7): 3260–3277. doi: 10.1002/jgrc.20244

Tedesco L, Vichi M, Scoccimarro E. 2019. Sea-ice algal phenology in a warmer Arctic. *Sci Adv* **5**(5): eaav4830. doi: 10.1126/sciadv.aav4830

Tivy A, Howell SE, Alt B, McCourt S, Chagnon R, Crocker G, Carrieres T, Yackel JJ. 2011. Trends and variability in summer sea ice cover in the Canadian Arctic based on the Canadian Ice Service Digital Archive, 1960–2008 and 1968–2008. *J Geophys Res Oceans* **116**(C3). Wiley Online Library. doi: 10.1029/2009JC005855

Tomas C. 1997. Identifying Marine Phytoplankton Academic Press. *Acad Press*, in press.

Tremblay J, Bélanger S, Barber D, Asplin M, Martin J, Darnis G, Fortier L, Gratton Y, Link H, Archambault P. 2011. Climate forcing multiplies biological productivity in the coastal Arctic Ocean. *Geophys Res Lett* **38**(18).

Tremblay J-É, Anderson LG, Matrai P, Coupel P, Bélanger S, Michel C, Reigstad M. 2015. Global and regional drivers of nutrient supply, primary production and CO2 drawdown in the changing Arctic Ocean. *Prog Oceanogr* **139**: 171–196. doi: 10.1016/j.pocean.2015.08.009

Tremblay J-É, Gagnon J. 2009. The effects of irradiance and nutrient supply on the productivity of Arctic waters: a perspective on climate change. *SpringerLink*: 73–93. doi: 10.1007/978-1-4020-9460-6_7

Tremblay J-É, Hattori H, Michel C, Ringuette M, Mei Z-P, Lovejoy C, Fortier L, Hobson KA, Amiel D, Cochran K. 2006. Trophic structure and pathways of biogenic carbon flow in the eastern North Water Polynya. *Prog Oceanogr* **71**(2): 402–425. doi: 10.1016/j.pocean.2006.10.006

Tremblay J-É, Lee J, Gosselin M, Bélanger S. 2019. Nutrient Dynamics and Marine Biological Productivity in the Greater Hudson Bay Marine Region. In: *From Science to Policy in the Greater Hudson Bay Marine Region: An Integrated Regional Impact Study (IRIS) of Climate Change and Modernization*. Québec City: ArcticNet. p. 424 pp.

Tremblay J-É, Raimbault P, Garcia N, Lansard B, Babin M, Gagnon J. 2014. Impact of river discharge, upwelling and vertical mixing on the nutrient loading and productivity of the Canadian Beaufort Shelf. *Biogeosciences* **11**(17): 4853–4868.

Tremblay J-É, Robert D, Varela DE, Lovejoy C, Darnis G, Nelson RJ, Sastri AR. 2012. Current state and trends in Canadian Arctic marine ecosystems: I. Primary production. *Clim Change* **115**(1): 161–178. doi: 10.1007/s10584-012-0496-3

Tremblay J-E, Smith WO. 2007. Chapter 8 Primary Production and Nutrient Dynamics in Polynyas. In: Smith WO, Barber DG, editors. *Elsevier Oceanography Series*. Elsevier. p. 239–269. doi: 10.1016/S0422-9894(06)74008-9

Trodahl HJ, Buckley RG. 1990. Enhanced ultraviolet transmission of Antarctic sea ice during the austral spring. *Geophys Res Lett* **17**(12): 2177–2179. doi: 10.1029/GL017i012p02177

Uusikivi J, Vähätalo AV, Granskog MA, Sommaruga R. 2010. Contribution of mycosporine-like amino acids and colored dissolved and particulate matter to sea ice optical properties and ultraviolet attenuation. *Limnol Oceanogr* **55**(2): 703–713. doi: 10.4319/lo.2010.55.2.0703

Villafañe VE, Barbieri ES, Helbling EW. 2004. Annual patterns of ultraviolet radiation effects on temperate marine phytoplankton off Patagonia, Argentina. *J Plankton Res* **26**(2): 167–174. doi: 10.1093/plankt/fbh011

Von Quillfeldt C. 2001. Identification of some easily confused common diatom species in Arctic spring blooms. *Bot Mar* **44**(4): 375–389. De Gruyter. doi: 10.1515/BOT.2001.048

Voss KJ. 1989. Use of the radiance distribution to measure the optical absorption coefficient in the ocean. *Limnol Oceanogr* **34**(8): 1614–1622.

Warren SG. 1982. Optical properties of snow. *Rev Geophys* **20**(1): 67–89.

Weeks WF. 1998. Growth conditions and the structure and properties of sea ice. In: *Physics of Ice_Covered Seas*Editor: M. Leppäranta. Helsinki: Helsinki University Press. p. 25–104.

Weeks WF, Ackley SF. 1986. *The Growth, Structure, and Properties of Sea Ice*. Springer.

Wei J, Lee Z. 2013. Model of the attenuation coefficient of daily photosynthetically available radiation in the upper ocean. *Methods Oceanogr* **8**: 56–74. doi: 10.1016/j.mio.2013.12.001

Welch H, Bergmann M, Siferd T, Amarualik P. 1991. Seasonal development of ice algae near Chesterfield Inlet, NWT, Canada. *Can J Fish Aquat Sci* **48**(12): 2395–2402. doi: 10.1139/f91-280

Williams WJ, Carmack EC. 2015. The 'interior' shelves of the Arctic Ocean: Physical oceanographic setting, climatology and effects of sea-ice retreat on cross-shelf exchange. *Prog Oceanogr* **139**: 24–41. doi: 10.1016/j.pocean.2015.07.008

Woodgate RA, Weingartner TJ, Lindsay R. 2012. Observed increases in Bering Strait oceanic fluxes from the Pacific to the Arctic from 2001 to 2011 and their impacts on the Arctic Ocean water column. *Geophys Res Lett* **39**(24). doi: 10.1029/2012GL054092

Wright S. 2008. *Chemtax Version 1.95 for Calculating the Taxonomic Composition of Phytoplankton Populations*. 10.4225/15/59fff1c5ea8fc. Available at https://researchdata.ands.org.au/chemtax-version-195-phytoplankton-populations/700780.

Wright SW, Ishikawa A, Marchant HJ, Davidson AT, van den Enden RL, Nash GV. 2009. Composition and significance of picophytoplankton in Antarctic waters. *Polar Biol* **32**(5): 797–808. doi: 10.1007/s00300-009-0582-9

Xie H, Gosselin M. 2005. Photoproduction of carbon monoxide in first-year sea ice in Franklin Bay, southeastern Beaufort Sea. *Geophys Res Lett* **32**(12). Wiley Online Library.

Yamamoto-Kawai M, McLaughlin F, Carmack E, Nishino S, Shimada K, Kurita N. 2009. Surface freshening of the Canada Basin, 2003–2007: River runoff versus sea ice meltwater. *J Geophys Res Oceans* **114**(C1).

Yang J. 2009. Seasonal and interannual variability of downwelling in the Beaufort Sea. *J Geophys Res Oceans* **114**(C1).

Yoshida K, Seger A, Kennedy F, McMinn A, Suzuki K. 2020. Freezing, Melting, and Light Stress on the Photophysiology of Ice Algae: Ex Situ Incubation of the Ice Algal diatom Fragilariopsis cylindrus (Bacillariophyceae) Using an Ice Tank. *J Phycol* **n/a**(n/a). doi: 10.1111/jpy.13036

Yu X, Wu Z, Jiang W, Guo X. 2015. Predicting daily photosynthetically active radiation from global solar radiation in the Contiguous United States. *Energy Convers Manag* **89**: 71–82. doi: 10.1016/j.enconman.2014.09.038

Zacher K, Rautenberger R, Hanelt D, Wulff A, Wiencke C. 2009. The abiotic environment of polar marine benthic algae. *Bot Mar* **52**(6): 483–490. doi: 10.1515/BOT.2009.082

Zege E, Malinka A, Katsev I, Prikhach A, Heygster G, Istomina L, Birnbaum G, Schwarz P. 2015. Algorithm to retrieve the melt pond fraction and the spectral albedo of Arctic summer ice from satellite optical data. *Remote Sens Environ* **163**: 153–164.

Zhang J, Ashjian C, Campbell R, Spitz YH, Steele M, Hill V. 2015. The influence of sea ice and snow cover and nutrient availability on the formation of massive under-ice phytoplankton blooms in the Chukchi Sea. *Deep Sea Res Part II Top Stud Oceanogr* **118**: 122–135. doi: 10.1016/j.dsr2.2015.02.008

Zhang Q, Gradinger R, Spindler M. 1999. Experimental study on the effect of salinity on growth rates of Arctic-sea-ice algae from the Greenland Sea. *Boreal Environ Res* **4**: 1–8.